

ADAPTATION OF IMAGE RECONSTRUCTION ALGORITHM FOR PURPOSES OF ULTRASOUND TRANSMISSION TOMOGRAPHY (UTT)

A.B. DOBRUCKI and K.J. OPIELIŃSKI

Wrocław University of Technology
Institute of Telecommunication and Acoustics
(50-370 Wrocław, Wybrzeże Wyspiańskiego 27, Poland)
e-mail: ado@zakus.ita.pwr.wroc.pl, popi@zakus.ita.pwr.wroc.pl

In this research, the convolution and backprojection method has been adapted for the purposes of image reconstruction in ultrasound transmission tomography (UTT). In particular, a complete computer algorithm enabling the use of different convolving and interpolation functions has been developed. A technique of reducing and scaling the tomographic measuring data to minimize the reconstruction errors is proposed. The convolution and backprojection method was optimized through a choice of a versatile convolving function and a simple interpolation function, and it was tested using simulated and actual tomographic measuring data. After reconstruction, good-quality images were obtained. It has been found that the number of measuring rays determines the resolution of an image, the accuracy with which the size of structures is imaged and the accuracy with which the image point values are reconstructed, whereas the number of measuring projections determines the dynamics and distortion of an image. Because of computation time and image blur, an optimum reconstruction grid size, according to the visualization quality criterion, should be chosen. The convolution and backprojection algorithm optimized in this research can be applied directly to the UTT visualization of the internal structure of objects as a distribution of local sound velocities in this structure, reconstructed on the basis of measurements of mean times of the passage of an ultrasonic wave through a cross-section of an object immersed in water, in a parallel ray projection geometry.

1. Introduction

In ultrasound transmission tomography (UTT) measurements in a parallel ray projection geometry, ultrasonic transducers: the sending one and the receiving one, are positioned opposite each other with the investigated object inbetween (1st generation of measuring data acquisition) [13]. A packet of measurements is obtained while moving the two transducers over distance s and rotating them at the same time by angle ψ along and around the object (Fig. 1). The measuring cycle ends after a rotation by an angle of 180° . Each shift of the transducers is called a ray and each rotation of them — a projection. A result of the measurement is a set of mean values of a certain acoustic parameter in the measured cross-section of an object for M rays and N projections. The values constitute basic data for the image reconstruction.

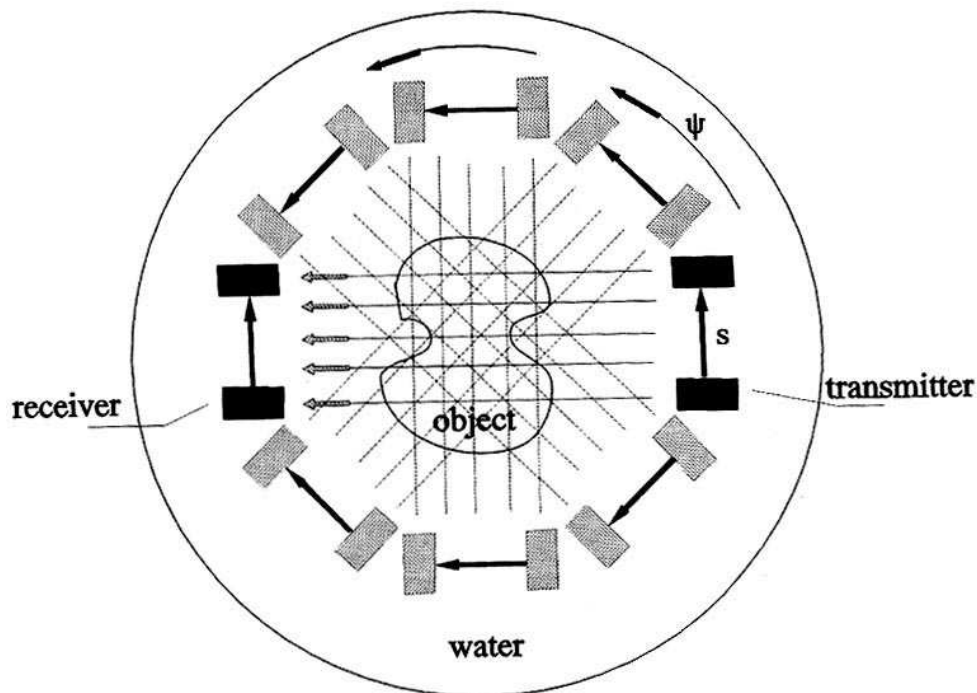


Fig. 1. Technique of measurement in UTT by means of parallel ray projection method.

An image reconstruction algorithm provides a mathematical basis for tomography. To visualize the internal structures of objects one must be absolutely certain that image reconstruction from the measuring data is correct. Therefore it is highly important that a proper reconstruction algorithm is selected, adapted to the particular measuring data, optimized and tested. These operations make it possible to detect and minimize any calculation errors which, compounded by measuring errors included in the tomographic data, could distort the reconstructed image even more.

In the present research, an image reconstruction algorithm was selected and made suitable for entering of the measuring data in the form of ultrasonic wave propagation mean velocities in a parallel ray projection geometry. Then the algorithm was optimized to minimize the calculation errors, tested and implemented as a computer program.

2. Choice of algorithm

An important problem in UTT, requiring a thorough survey of the existing reconstruction methods, is the choice of an image reconstruction algorithm. First, one must choose from the two types of algorithms: the transform method [6] or the finite series-expansion reconstruction method [1], considering their advantages and disadvantages. The first computer-assisted X-ray tomograph, invented by Hounsfield and produced by EMI, used the algebraic reconstruction technique (ART) [1] and the expansion- into-series

concept, whereas the present commercially available tomographs for medical applications do not use the series-expansion concept any longer. Series-expansion methods are iterative algorithms characterized by slow convergence and thus they reconstruct images much slower than the transform methods. However, the development of very fast and efficient computers may make it possible to shorten the computation time, which will give an advantage to series-expansion methods [1] because of:

- their wide application range regardless of the measurement geometry and the kind of data,
- the possibility of reconstructing high-contrast images of the structure of objects characterized by sudden changes in density, which is essential for the application of tomography to industrial non-destructive testing,
- the possibility of reconstructing an image in the case of a small number of illumination angles or incomplete projections.

But at the moment, the long computation time required by series-expansion methods makes it impossible to increase the number of iterations significantly (it is still not possible to implement series-expansion methods on PCs) and so the images reconstructed by these methods are often obscured by noise and distorted [2, 5]. The much bigger errors occurring here than in the case of transform methods are due to the assumption of a linear energy propagation path between the source and the detector, which for UTT is a serious shortcoming because of refraction. Thus one can say that at the moment, the transform algorithm is the most suitable for UTT.

Among transform algorithms one can distinguish two basic types: operating in the space domain (the convolution and backprojection algorithm [6]) and operating in the domain of spatial frequencies (the Fourier inversion and the filtered backprojection algorithm [6]). Considering that the two types have a common origin, it is surprising that they differ radically in their operation. The convolution and backprojection algorithm is highly versatile. Being currently one of the most effective algorithms, it is used in the latest models of computer X-ray tomographs. It has been superseding the Fourier versions. The reason for its dominance is mainly the ease with which it can be implemented in both the software and hardware applications and the fact that it makes it possible to obtain sharp high-quality images from noise-free measuring data [6]. Algorithms based on the Fourier transform are not so easy to implement because of two-dimensional interpolation which lowers the quality of the image [6, 7]. Whereas calculation of the Fourier transforms have this advantage that they require a potentially smaller number of computations to reconstruct an image. Unfortunately, calculation of Fourier transforms, whose efficiency makes this method attractive, are also a source of its shortcomings [2]. Fourier algorithms require direct estimates of the complex amplitude of image harmonic components and an error in one of the components degrades the whole image [6]. The cause of such errors may be inaccurate interpolation. In the convolution and backprojection algorithm inaccurate interpolation is harmless — it causes only smoothing of the image [6].

To take a final decision about the choice of an algorithm, the reconstruction of a simple object by means of the Fourier inversion algorithm and the convolution and backprojection algorithm was considered. Let the object be described by a function which

assumes the value of 1 within a circle with radius a and 0 outside this circle. The Fourier transform of such an object is an oscillating function with the oscillation becoming faster as the object's size increases or when the object is far away from the origin of the image co-ordinates. Faster oscillations of the function result in a bigger error introduced by simple interpolation between the function samples. In the convolution and backprojection method interpolation takes place for convolved data. For the sampled projections of the considered object it can be stated that the sampled convolved data are close to theoretical results. This means that, regardless of the size of an object or its position relative to the origin of the image co-ordinates, a negligible interpolation error appears in the reconstructed values within the circle.

To sum up, the convolution and backprojection algorithm, adapted and tested in this research, is the most suitable one for UTT purposes.

3. Convolution and backprojection algorithm

The convolution and backprojection algorithm was brought out by RAMACHANDRAN and LAKSHMINARAYANAN in 1971 [11] and later popularized by SHEPP and LOGAN [12]. The reconstruction method here is similar to the filtered backprojection algorithm [5, 6], except that filtration takes place in the space domain (as a convolution) and not in the domain of spatial frequencies, which naturally eliminates the problems connected with FFT. The initial convolution and backprojection algorithm formula has this form [6]:

$$f_B(x, y) = \int_0^\pi \int_{-1}^1 p(s, \psi) q(x \cos \psi + y \sin \psi - s) ds d\psi, \quad (1)$$

where

$$q(s) = \int_{-1/2\Delta s}^{1/2\Delta s} |R|W(R)e^{j2\pi Rs} dR, \quad (2)$$

and $p(s, \psi) = p_\psi(s)$ are the measuring data collected in a parallel ray projection geometry (Fig. 1), $W(R)$ is a window function, f_B — band-limited approximation of function $f(x, y)$, and s is normalized to area $[-1, 1]$. Formula (1) can be separated into two parts:

$$\tilde{p}(s', \psi) = \int_{-1}^1 p(s, \psi) q(s' - s) ds, \quad (3)$$

$$f_B(x, y) = \int_0^\pi \tilde{p}(x \cos \psi + y \sin \psi, \psi) d\psi. \quad (4)$$

Formula (3) is an outcome of the convolution of projections at an angle of ψ and convolving function $q(s)$ defined by general formula (2) (different convolving functions are obtained for different window functions). Formula (4) is known as backprojection and it has a simple geometric interpretation. The arguments of the function described by

equation (3) are parameters of a ray passing through point (x, y) at angle ψ , which means that function $f(x, y)$ is created by integrating values of the convolved projection accompanying all the rays passing through point (x, y) .

In practical reconstruction-from-projection applications, the measuring data correspond to estimates $p(s, \psi)$ for many discrete values s and ψ and the reconstructed image is generated in the form of a two-dimensional table of numbers. The principles which apply to the optimization of a reconstruction algorithm on the basis of discrete data should be considered for a case when p is sampled cocurrently for s and ψ . If we have a set of projections measured at N angles spaced at $\Delta\psi$ by means of M rays spaced at Δs , then for each of N projections we can determine constant integers M^+ and M^- :

$$\left. \begin{aligned} M^+ &= (M - 1)/2 \\ M^- &= -(M - 1)/2 \end{aligned} \right\} \text{ for odd } M, \tag{5}$$

$$\left. \begin{aligned} M^+ &= (M/2) - 1 \\ M^- &= -M/2 \end{aligned} \right\} \text{ for even } M. \tag{6}$$

To make sure that set of rays $\{(m\Delta s, n\Delta\psi) : M^- \leq m \leq M^+, 1 \leq n \leq N\}$ covers a unit circle (a normalized measuring area), one should choose $\Delta\psi = \pi/N$ and $\Delta s = 1/M^+$ from the whole range of directions. In this way one can refer to set $p(m\Delta s, n\Delta\psi)$ as to parallel-ray data. A Cartesian grid of image point values is defined as set $\{(k\Delta x, l\Delta y) : K^- \leq k \leq K^+, L^- \leq l \leq L^+\}$ where numbers K^-, K^+, L^-, L^+ are defined in the same way as M^- and M^+ (formulas (5), (6)). A reconstruction algorithm should generate estimates $f(k\Delta x, l\Delta y)$ for $K \times L$ image points from $M \times N$ measurements $p(m\Delta s, \psi_n)$ for $\psi_n = n\Delta\psi$. Thus an algorithm performing approximation $f_B(k\Delta x, l\Delta y)$ on the basis of projection data $p(m\Delta s, \psi_n)$ is needed. The simplest way in which backprojection integrals (formula (4)) can be determined is to apply the trapezoid rule [6]:

$$f_B(k\Delta x, l\Delta y) \cong \Delta\psi \sum_{n=1}^N \tilde{p}(k\Delta x \cos \psi_n + l\Delta y \sin \psi_n, \psi_n). \tag{7}$$

Then for each angle ψ_n one should find convolved projection values $\tilde{p}(s', \psi_n)$ for set $K \times L$ of values s' . A practical approach to this problem is to estimate $\tilde{p}(s', \psi_n)$ for $M^- \leq m \leq M^+$ projections and then to apply reasonable interpolation to calculate $K \times L$ values \tilde{p} on the basis of only M calculated convolved values. Thus the convolution (formula (3)) should be expressed in two stages: a discrete convolution whose result is written as \tilde{p}_C , followed by interpolation \tilde{p}_I . These operations are represented by a pair of equations [6]:

$$\tilde{p}_C(m' \Delta s, \psi_n) = \Delta s \sum_{m=M^-}^{M^+} p(m\Delta s, \psi_n) q((m' - m)\Delta s) \quad \text{for } M^- \leq m' \leq M^+, \tag{8}$$

$$\tilde{p}_I(s', \psi_n) = \Delta s \sum_{m'} \tilde{p}_C(m' \Delta s, \psi_n) I(s' - m' \Delta s), \tag{9}$$

where $s' = k\Delta x \cdot \cos \psi_n + l\Delta y \cdot \sin \psi_n$ and $I(s)$ is an interpolation function. If linear interpolation of convolved values is assumed, function $I(s)$ can be written as:

$$I_L(s) = \begin{cases} \frac{1}{\Delta s}(1 - |s|/\Delta s), & |s| \leq \Delta s, \\ 0, & |s| \geq \Delta s. \end{cases} \quad (10)$$

There are many convolving functions which can be used in a convolution and backprojection algorithm. One of the most often used is the following function [6]:

$$q(m\Delta s) = \begin{cases} \frac{3 - 2E}{12(\Delta s)^2} & \text{for } m = 0, \\ -\frac{E}{\pi^2(m\Delta s)^2} & \text{for even } m, \\ -\frac{1 - E}{\pi^2(m\Delta s)^2} & \text{for odd } m, \end{cases} \quad (11)$$

where $0 \leq E \leq 1$ is a convolving function parameter. A special case of this convolving function is the Ram-Lak (Ramachandran and Lakshminarayanan) function [4]:

$$q_{RL}(m\Delta s) = \begin{cases} \frac{1}{4\Delta s^2} & \text{for } m = 0, \\ -\frac{\sin^2(\pi m/2)}{\pi^2 m^2 \Delta s^2} & \text{for } m \neq 0, \end{cases} \quad (12)$$

obtained from formula (11) for parameter $E = 0$. Another frequently used function is the Shepp-Logan function [4]:

$$q_{SL}(m\Delta s) = \frac{2}{\pi^2 \Delta s^2 (1 - 4m^2)}. \quad (13)$$

The convolution and backprojection algorithm is simple to implement, quite accurate and fast. It is currently used in the latest models of computer X-ray tomographs as one of the most effective algorithms.

4. Measuring data fitting

For the convolution and backprojection algorithm four basic assumptions, which must be satisfied to obtain a correctly reconstructed image, hold good:

- 1) parameter values measured in projections (entered into the algorithm) constitute an integral of local values over the ultrasonic beam's path,
- 2) the path between the source and the detector is a straight line,
- 3) values measured outside the measuring area are zero,
- 4) measuring data entered into the algorithm operating on a measuring circle having a radius of 1, placed in the centre of the co-ordinate system must be re-scaled appropriately.

For the measurement of the time t_p in which an ultrasonic wave passes through the object, the local values are the inverses of sound velocity $1/c(x, y)$ (condition 1)):

$$t_p = \int_L dt_p = \int_L \frac{dt_p}{dl} dl = \int_L \frac{1}{c(x, y)} dl. \quad (14)$$

Condition **2**) can be satisfied only approximately by assuming that for the measured objects, the elongation (as a result of refractions) of the ultrasonic wave propagation path from the transmitter to the receiver is negligible. Measurement of the circle diameter d_p in a parallel ray projection geometry is determined either by the tracking range or by sending transducer-receiving transducer distance l_o :

$$d_p = \begin{cases} (M-1)\Delta s & \text{for } (M-1)\Delta s < l_o, \\ l_o & \text{for } (M-1)\Delta s \geq l_o, \end{cases} \quad (15)$$

where M stands for a number of measuring rays spaced at Δs . According to condition **3**), measurement values outside a circle of diameter d_p should be zero. This condition can be fulfilled in the simplest way by entering reduced time T_d , i.e. difference $t_p - t_{\text{med}}$, instead of the measured transition time values t_p , into the algorithm, where time t_{med} is the time in which an ultrasonic wave passes through a measuring medium (water) at distance l_o (assuming that $t_{\text{med}} \cong \text{const}$). To satisfy condition **4**), let us consider scaling two different parameters entered into the convolution and backprojection algorithm, specified as method *A*: T_d and method *B*: $-c_{\text{med}} \cdot T_d$, when for the two parameters assumptions **1**)–**3**) hold good. If the reduced time measured over path l_o is T_d , the reduced time over path **2** is:

$$\widehat{T}_d = \widehat{t}_p - \widehat{t}_{\text{med}} = \frac{2t_p}{l_o} - \frac{2t_{\text{med}}}{l_o} = \frac{2}{c_p} - \frac{2}{c_{\text{med}}}, \quad (16)$$

where c_p stands for mean ultrasonic wave propagation values measured in a parallel ray projection geometry at distance l_o , and c_{med} is a mean ultrasonic wave propagation velocity in a measuring medium, measured at distance l_o . It is easy to prove that

$$\begin{aligned} \widehat{T}_d &= \frac{2}{c_p} - \frac{2}{c_{\text{med}}} = \int_{-1}^1 (d\widehat{t}_p - d\widehat{t}_{\text{med}}) = \int_{-1}^1 \left(\frac{d\widehat{t}_p}{dl} - \frac{d\widehat{t}_{\text{med}}}{dl} \right) dl \\ &= \int_{-1}^1 \left(\frac{1}{c(x,y)} - \frac{1}{c_{\text{med}}} \right) dl = \int_{-1}^1 f^{(A)}(x,y) dl. \end{aligned} \quad (17)$$

In the case of method *A*, to reproduce, after reconstruction, the local ultrasonic wave propagation velocities, values $2/c_p - 2/c_{\text{med}}$ should be entered into the convolution and backprojection algorithm and the following recalculation should be done for each reconstructed value $f^{(A)}(x,y)$:

$$c(x,y) = \frac{1}{f^{(A)}(x,y) + \frac{1}{c_{\text{med}}}}. \quad (18)$$

In method *B* the difference lies in the fact that after re-scaling as above, we enter values $2 \cdot (1 - c_{\text{med}}/c_p) = 2 \cdot (1 - n_p)$ (where n_p is a mean value of the refraction index [5]) into the algorithm and after reconstruction and recalculation we get:

$$c(x,y) = \frac{c_{\text{med}}}{-f^{(B)}(x,y) + 1}. \quad (19)$$

The two above methods were verified by reconstructing an image on the basis of simulated tomographic measurements of the mean velocity of the propagation of an ultrasonic wave in a cross-section of a homogenous cylinder immersed in water (Fig. 2): identical results were obtained.

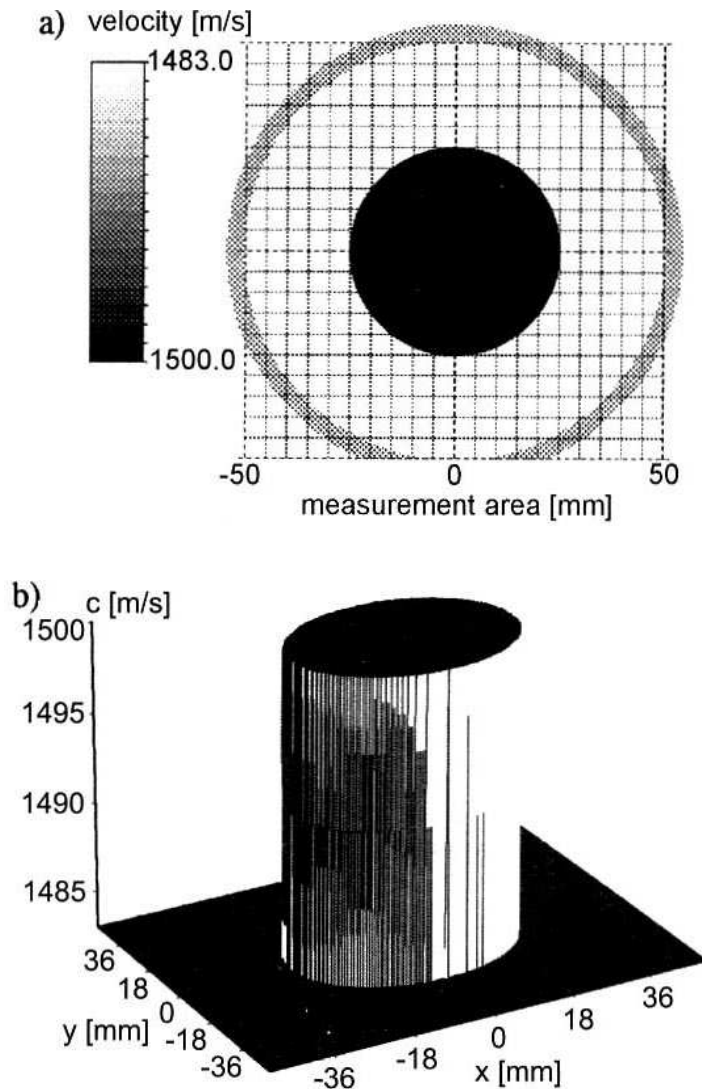


Fig. 2. Image of assigned cylinder cross-section in: a) gray scale, b) pseudo-3D. The following parameters were assigned: sound velocity in cylinder — 1500 m/s, sound velocity in water — 1483 m/s, cylinder's diameter — 50 mm, measuring circle's diameter — $d_p = l_o = 100$ mm.

In the further research method B was used for reconstruction calculations because of shorter computation time.

5. Optimization

The convolution and backprojection algorithm was subjected to optimization through the selection of a convolving function. Two functions: $q(m\Delta s)$ [6] for several values of parameter E and Shepp-Logan function $q_{SL}(m\Delta s)$ (formulas (11), (13)) were tested. The considered convolving functions are shown in Fig. 3 for discrete values $m \cdot \Delta s$. In the case of function $q(m\Delta s)$, calculation were done for seven values of parameter $E = 0, 0.2, 0.4, 0.5, 0.6, 0.8, 1$.

Images of an assigned cylinder cross-section (Fig. 2) were reconstructed by means of the convolution and backprojection algorithm using each of the convolving functions shown in Fig. 3. The obtained images in pseudo-3D are shown in Fig. 4.

If one compares the shapes of the convolving functions (Fig. 3), one can notice that the Shepp-Logan function is very similar to function q with parameter $E = 0.2, 0.4$. The similarity is also visible in the case of the reconstructed images of the cylinder cross-section (Fig. 4). This means that convolving function $q(m \cdot \Delta s)$, presented in a paper by R.M. LEWITT [6] (formula (11)), is a highly versatile function. Thus there is no need to use many different convolving functions in the convolution and backprojection algorithm since the effects which they produce can be brought about by changing the value of parameter $0 \leq E \leq 1$ of function q . Being able to change the value of parameter E , one can reconstruct images differing in contrast.

For low values of parameter $E \leq 0.4$ one can obtain very sharp images with clearly visible edges at structural boundaries (Fig. 4 a–c), in which local sound velocities are meticulously reconstructed in comparison with the object (Fig. 4a). A drawback of this kind of reconstruction are oscillations of the reconstructed values close to the measuring-area boundary (Fig. 4a–c) and interference in the imaging of any discontinuities manifesting itself in overstated reconstructed values at boundaries (Fig. 4 a–c).

For high values of parameter $E \geq 0.6$ images are less contrasty, which manifests itself in blurring of the boundaries of any discontinuities in the reconstructed structure (Fig. 4 e–g). Thus the reconstructed values close to such boundaries contain significant errors. This kind of reconstruction has, however, an advantage: no oscillation in image values close to the measuring area boundary and no interference in the imaging of discontinuities (Fig. 4 e–g). For parameter $E = 0.5$ the above effects for low and high values are balanced (Fig. 4d).

Reconstruction errors along image line $y = 0$ for parameter $E = 0$ and $E = 1$ at $M = 101$ rays and $N = 160$ projections are given in Fig. 5. As regards the image sharpness, it is more advantageous to use low values of E but if the aim is to minimize the offset of reconstructed image point values relative to the assigned values, it is better to use high values of E .

A nonlinear interpolation function can be used to improve the quality of imaging since if linear interpolation is adopted (formula (10)) in the convolution and backprojection algorithm, two kinds of interference occur [6]:

- the reconstructed function is a locally smooth version of the original object function,

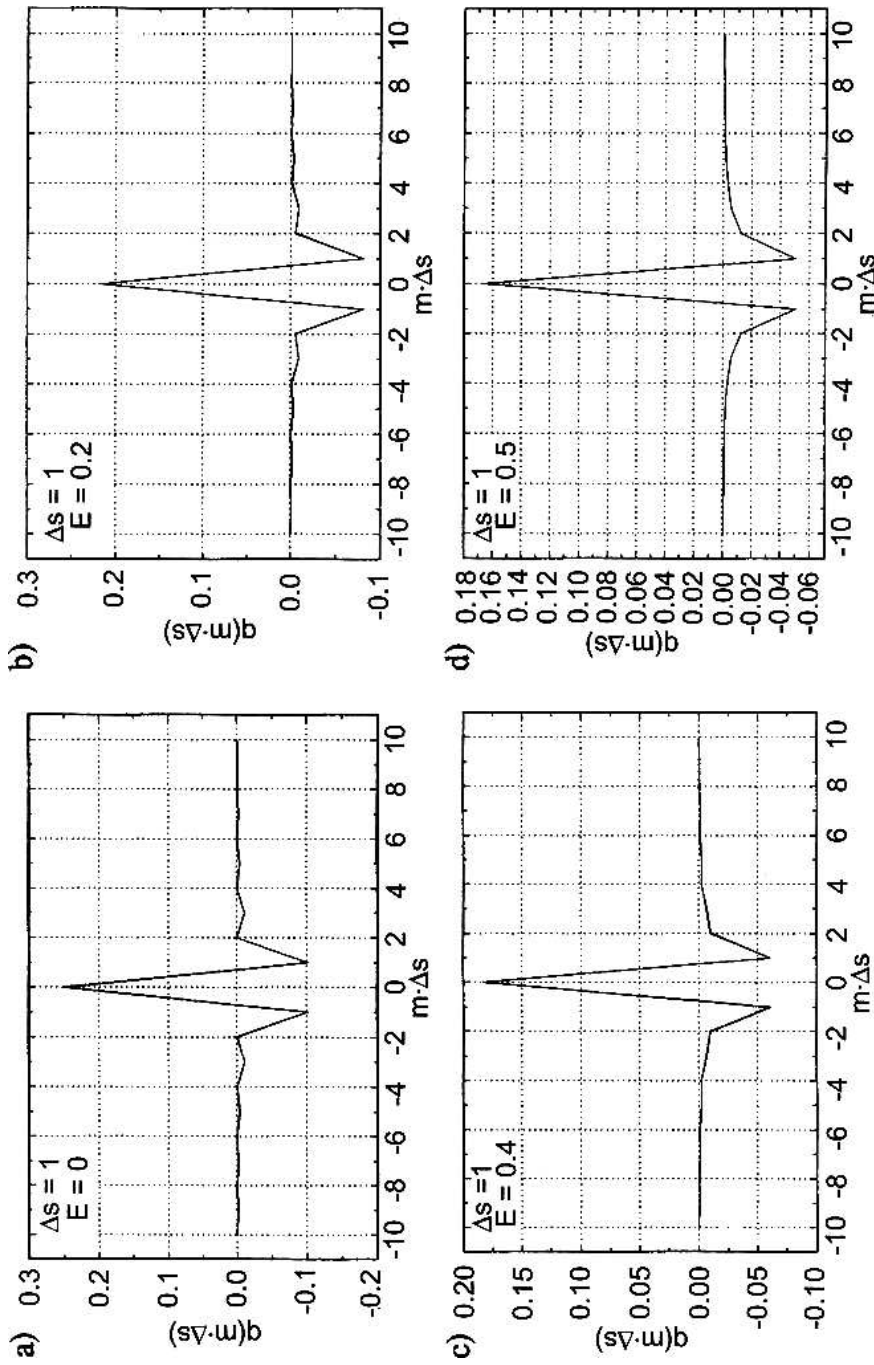


[Fig. 3]

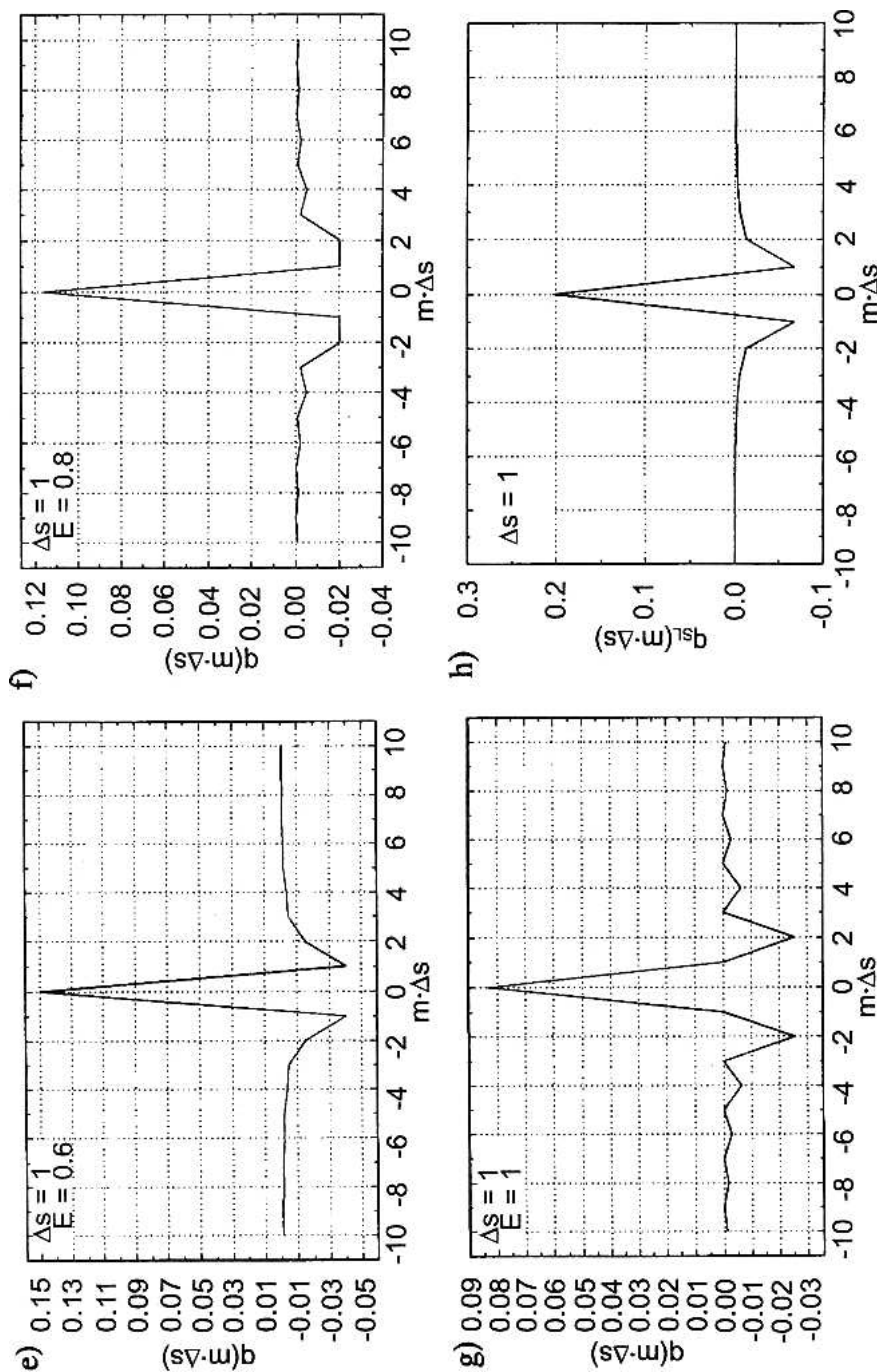
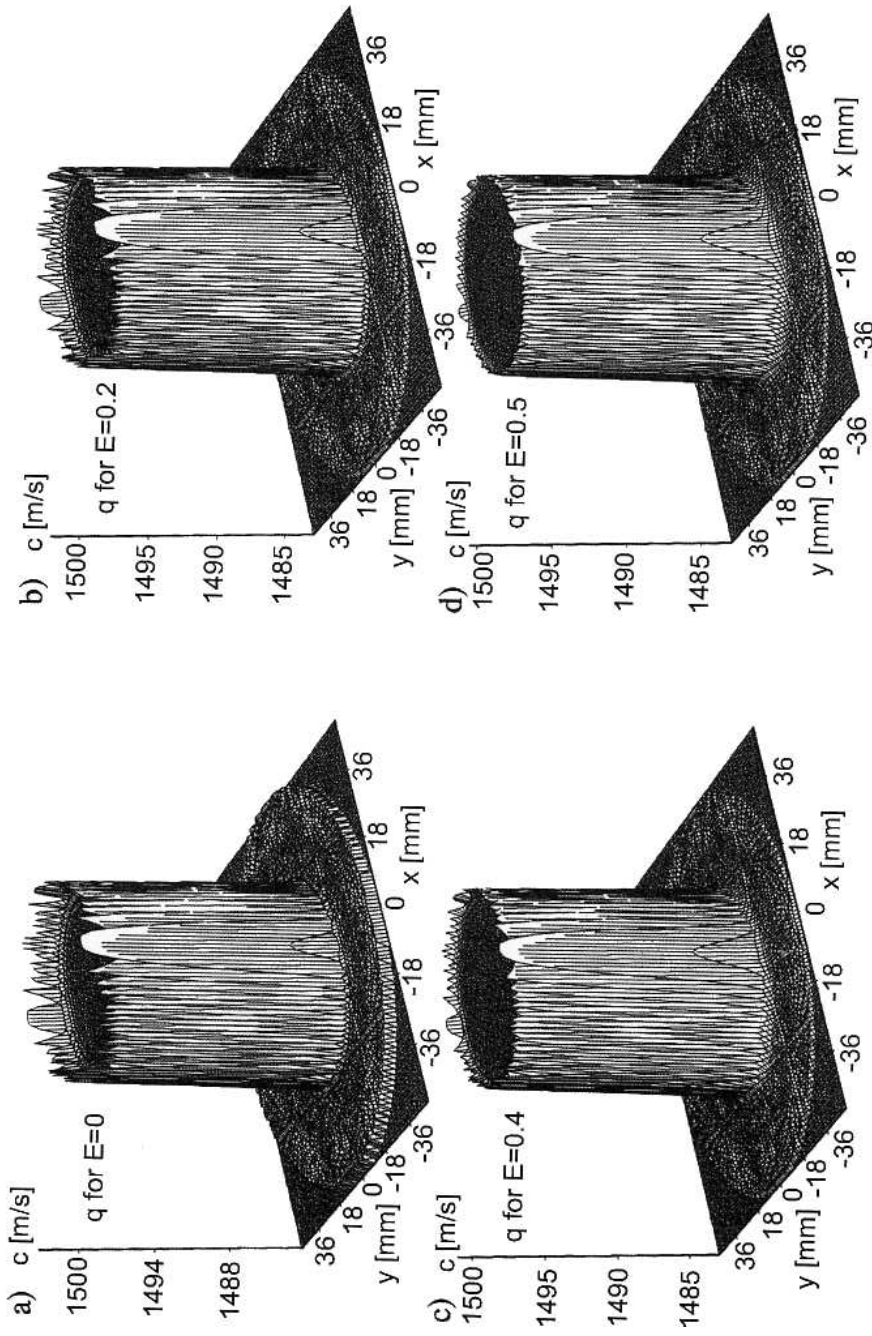


Fig. 3. Convolving functions for discrete data, function q acc. to formula (11) for parameter: a) $E = 0$ (Ram-Lak function, formula (12)), b) $E = 0.2$, c) $E = 0.4$, d) $E = 0.5$, e) $E = 0.6$, f) $E = 0.8$, g) $E = 1$, h) Shepp-Logan function (formula (13)).



[Fig. 4]

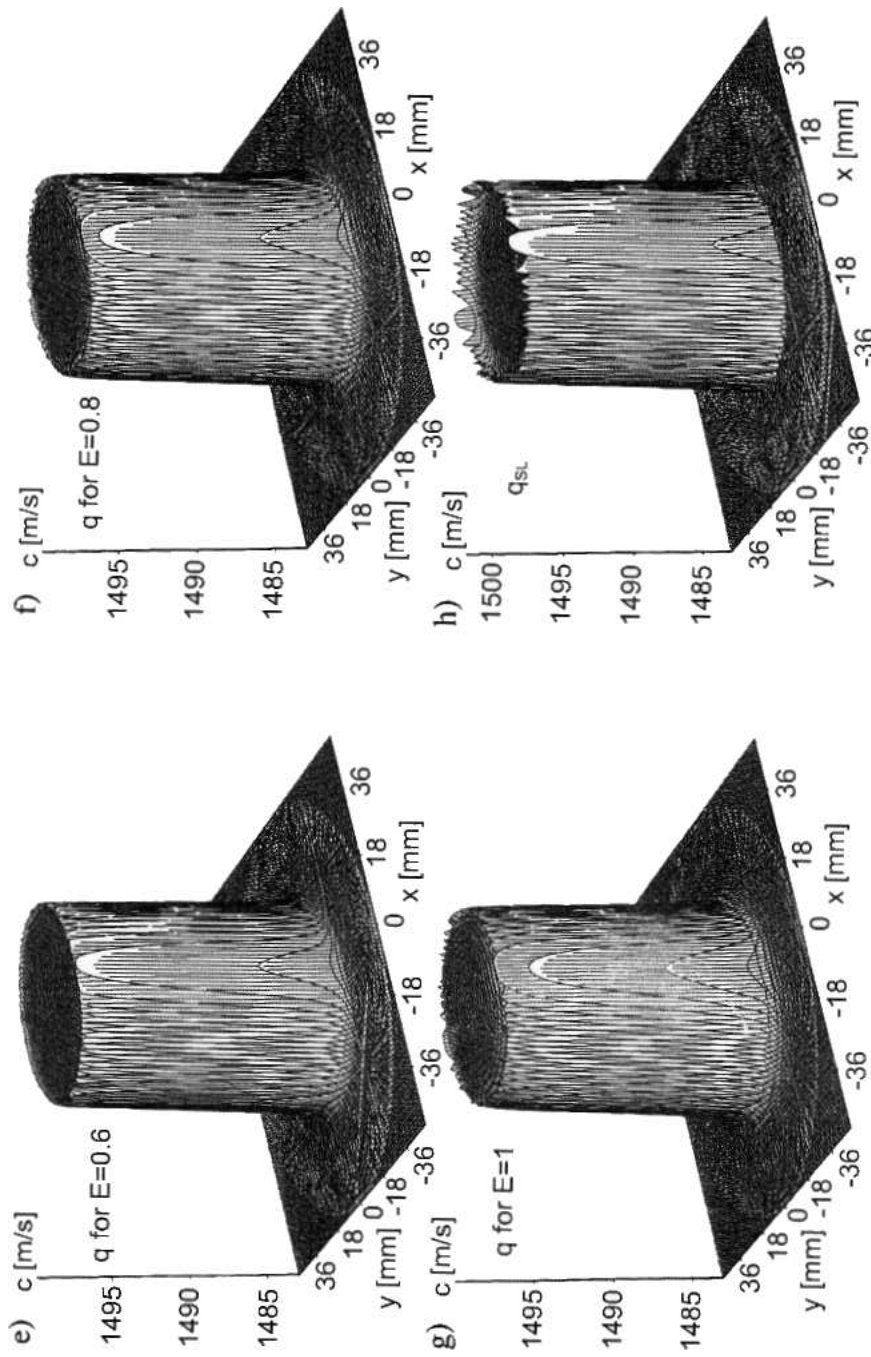


Fig. 4. Cylinder cross-section (from Fig.2) images reconstructed by means of convolution and backprojection algorithm for different convolving functions, presented in pseudo-3D: a) $q_{E=0}$; b) $q_{E=0.2}$; c) $q_{E=0.4}$; d) $q_{E=0.5}$; e) $q_{E=0.6}$; f) $q_{E=0.8}$; g) $q_{E=1}$; h) q_{SL} .

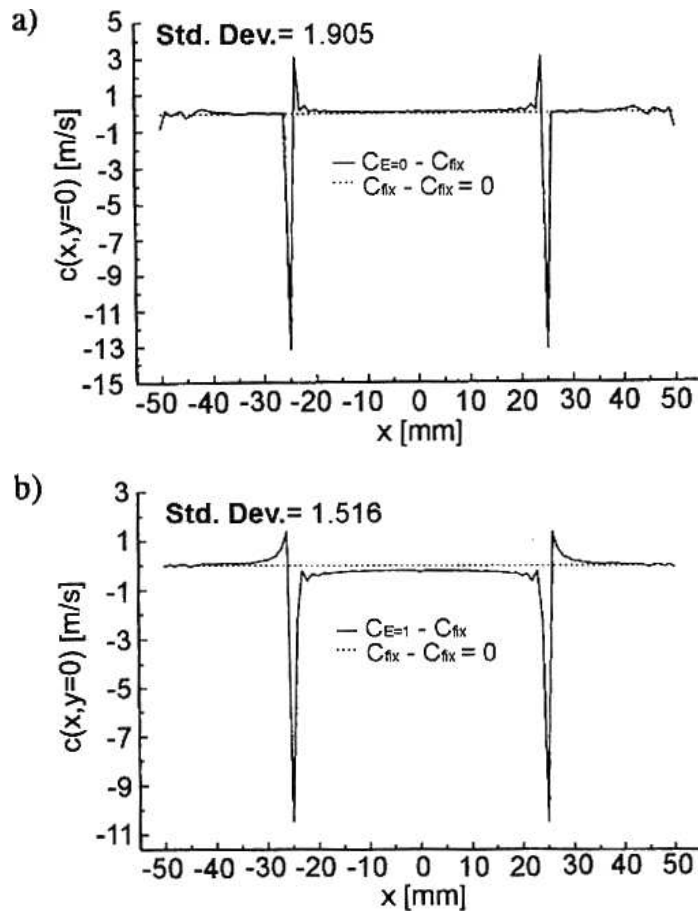


Fig. 5. Reconstruction errors along image line $y = 0$: a) for parameter $E = 0$, b) for parameter $E = 1$, at $M = 101$ rays and $N = 160$ projections (standard deviations have been marked).

— the reconstructed function is characterized by rapid variation of values and their derivatives.

Nevertheless, the smoothing effect is relatively harmless since it is equivalent, in principle, to the modification of convolving function q by increasing the value of parameter E . Thus it can be eliminated by lowering the value of E . The oscillation effect in the reconstructed image manifests itself as streaks radiating from sharp edges (Fig. 4 a–f, h). This interference is not serious enough to justify the introduction of a complicated non-linear interpolation function since this would extend the reconstruction computation time considerably.

In the further research only the convolution and backprojection algorithm in conjunction with convolving function $q(m \cdot \Delta s)$ (formula (11)) and linear interpolation function $I_L(s)$ (formula (10)) is used. Such a value of the convolving function parameter was chosen which ensured images of the best possible quality (in most cases: $E = 0$ and $E = 1$).

6. Testing

To determine a minimum number of measuring data (rays and projections) and to choose an optimum reconstruction grid size — the parameters which determine the quality of an image — the convolution and backprojection algorithm was tested by simulated tomographic measurements of a cylinder cross-section (Fig. 2). For the convolution and backprojection algorithm it is possible to derive a formula for the interrelationship between the number of rays M and the number of projections N , which is necessary in order to minimize the reconstructed image distortions introduced by the algorithm [6]:

$$N - 1 > \frac{\pi M}{2}. \quad (20)$$

This criterion provides many useful guidelines for many applications, considering that the effects of sampling in domain s and in domain ψ interact in a complicated way.

Figure 6 shows image distortions due to an insufficient number of projections relative to the number of rays (Fig. 6 a–c). It is enough to satisfy condition (20) to obtain good-quality images (Fig. 6f). By further increasing the number of projections only slight smoothing of image point value oscillations is obtained (Figs. 6 g, h). It is surprising that a quite clear image can be obtained already for the number of projections smaller by half than the number of rays (Fig. 6d). It should be noted, however, that the tested object is homogenous and large. In the case of objects with complex internal structure, it may become necessary to use the maximum number of projections determined by condition (20) in order to obtain a good-quality image [8–10].

Figures 7 and 8 show how the reconstructed image of the object's cross-section changes depending on the number of measuring rays if condition (20) is fulfilled. In the case of the tested object, a highly accurate image can be obtained already for 101 rays (Figs. 7 e, 8 e) and an undisturbed shape of the object's cross-section — for about 30 rays (Figs. 7 c, d and 8 c, d). By further increasing the number of rays only the interference at structural boundaries is minimized (Figs. 7 f–h and 8 f–h). Thus the cross-section of each homogenous structure can be visualized with high accuracy by means of the convolution and backprojection algorithm, assuming $M \geq 51$ rays for its largest dimension and $N \geq 81$ projections, if we have error-free measurements of the mean values of the acoustic parameter being determined, obtained in a parallel ray projection geometry.

The convolution and backprojection algorithm reconstructs an image as set $K \times L$ of values. This set is called a Cartesian image reconstruction grid. Grid size can be chosen depending on needs. Normally, an equal number of points K in the horizontal plane and points L in the vertical plane is assumed to obtain an area of the image without any differentiation of its resolution along axis X or Y . If the reconstructed image is presented in the gray scale, its resolution is determined by the monitor's or the printer's resolution. Grid size also depends on number M of measuring rays. If grid size $K = L$ is larger than number M of the rays, then the reconstructed image becomes blurred (Fig. 9 b–d) due to the considerable influence of the interpolation of the convolved values. For grid size equal to the number of measuring rays, each pixel of the reconstructed image is a square with

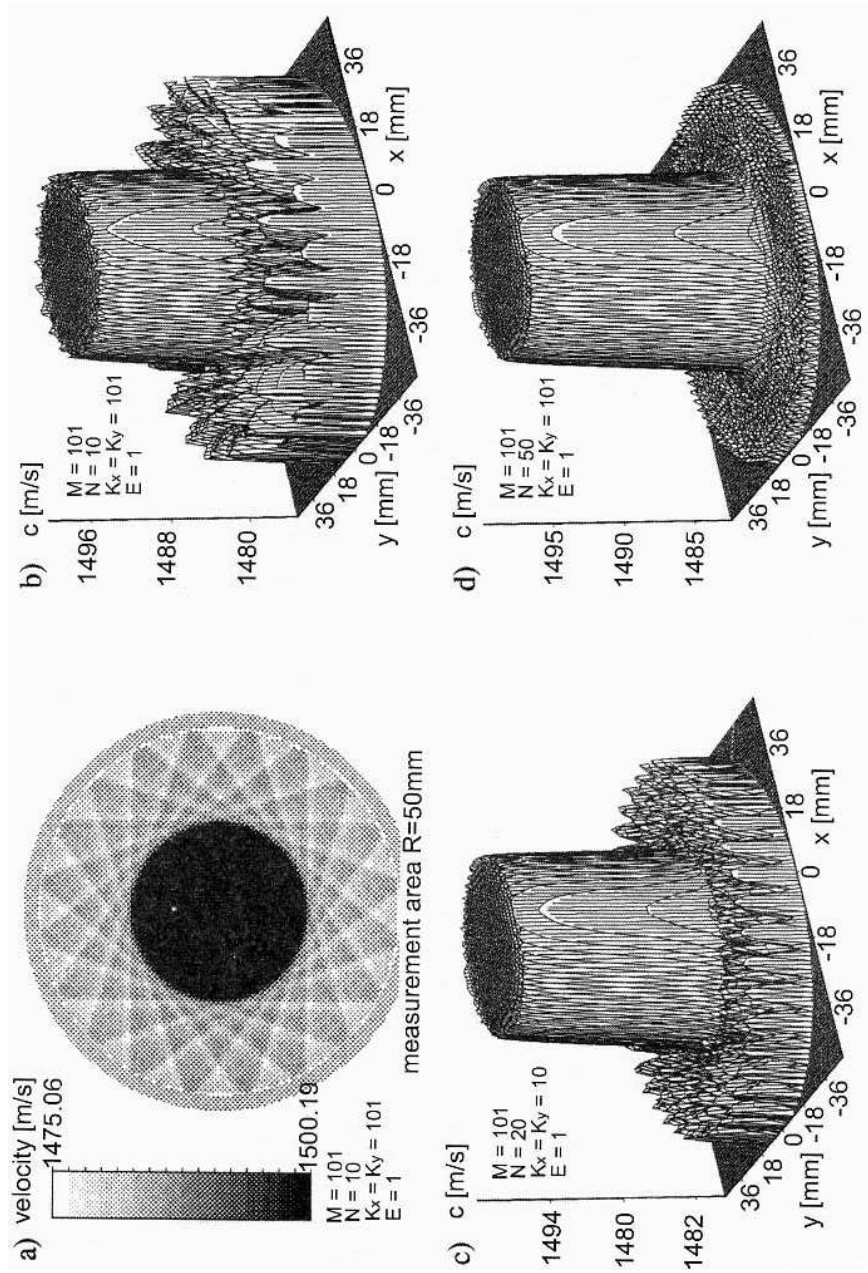


[Fig. 6]

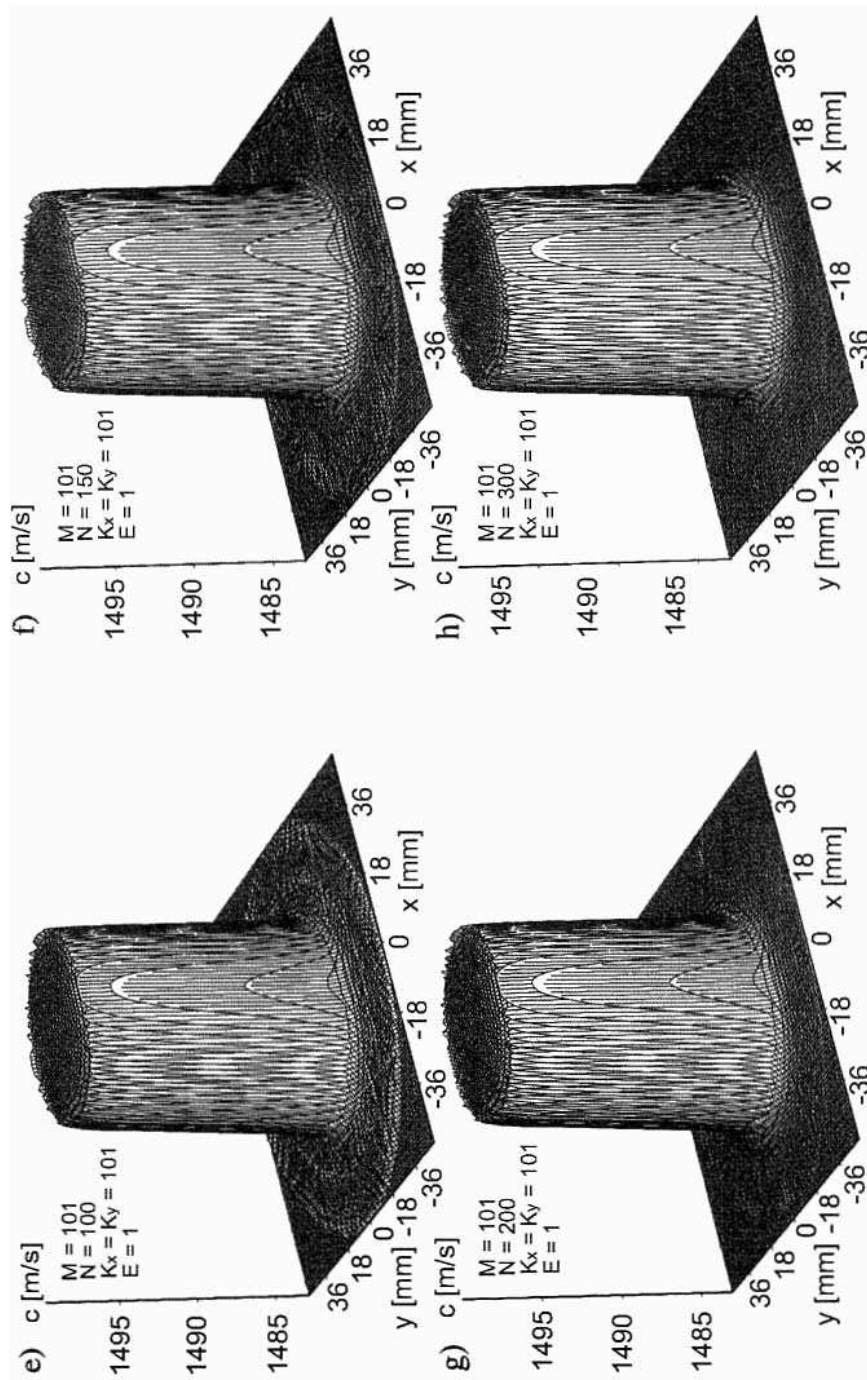
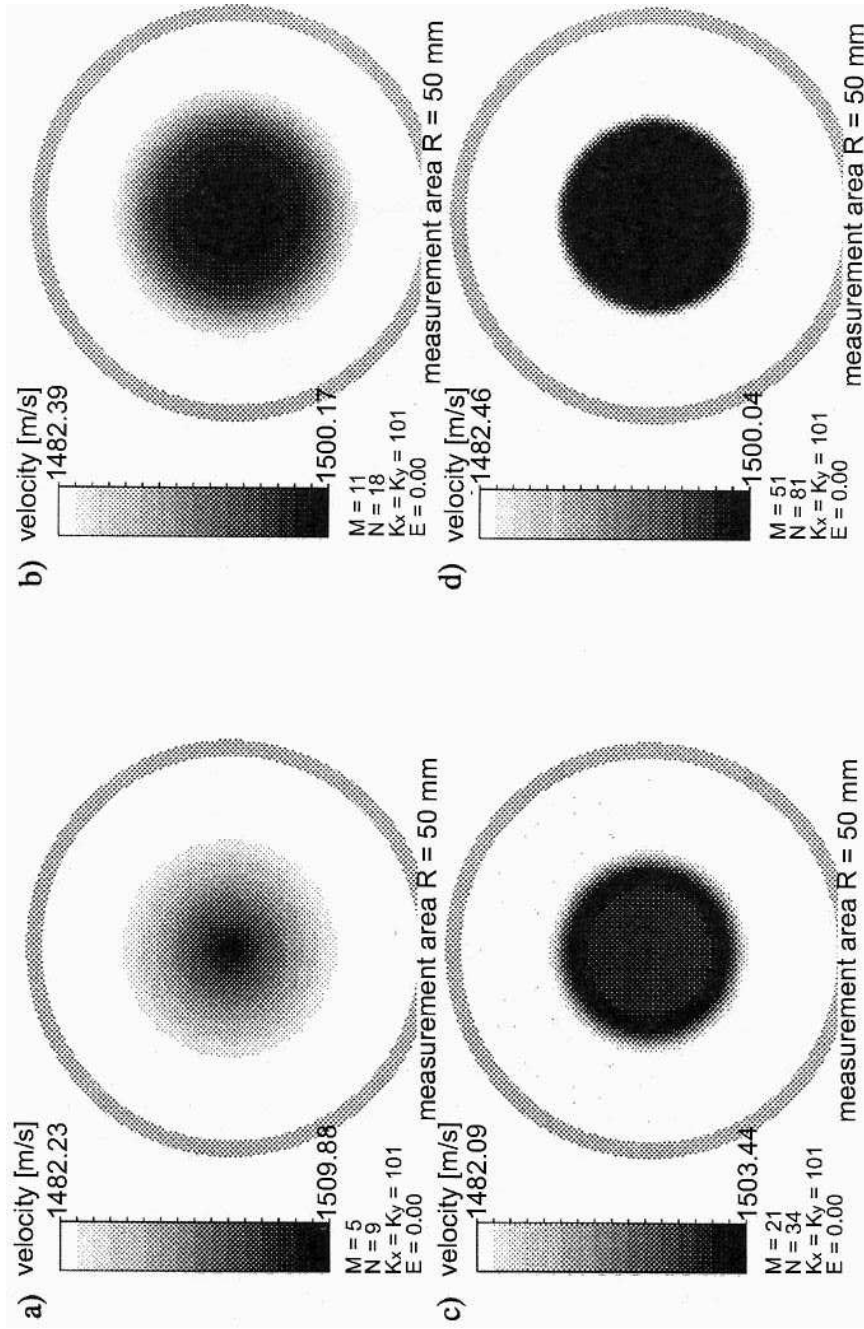


Fig. 6. Cylinder cross-section (from Fig. 2) images reconstructed by means of convolution and backprojection algorithm for $M = 101$ rays and different number of measuring projections N , shown in gray scale a) and in pseudo-3D b)-h) for $E = 1$.



[Fig. 7]

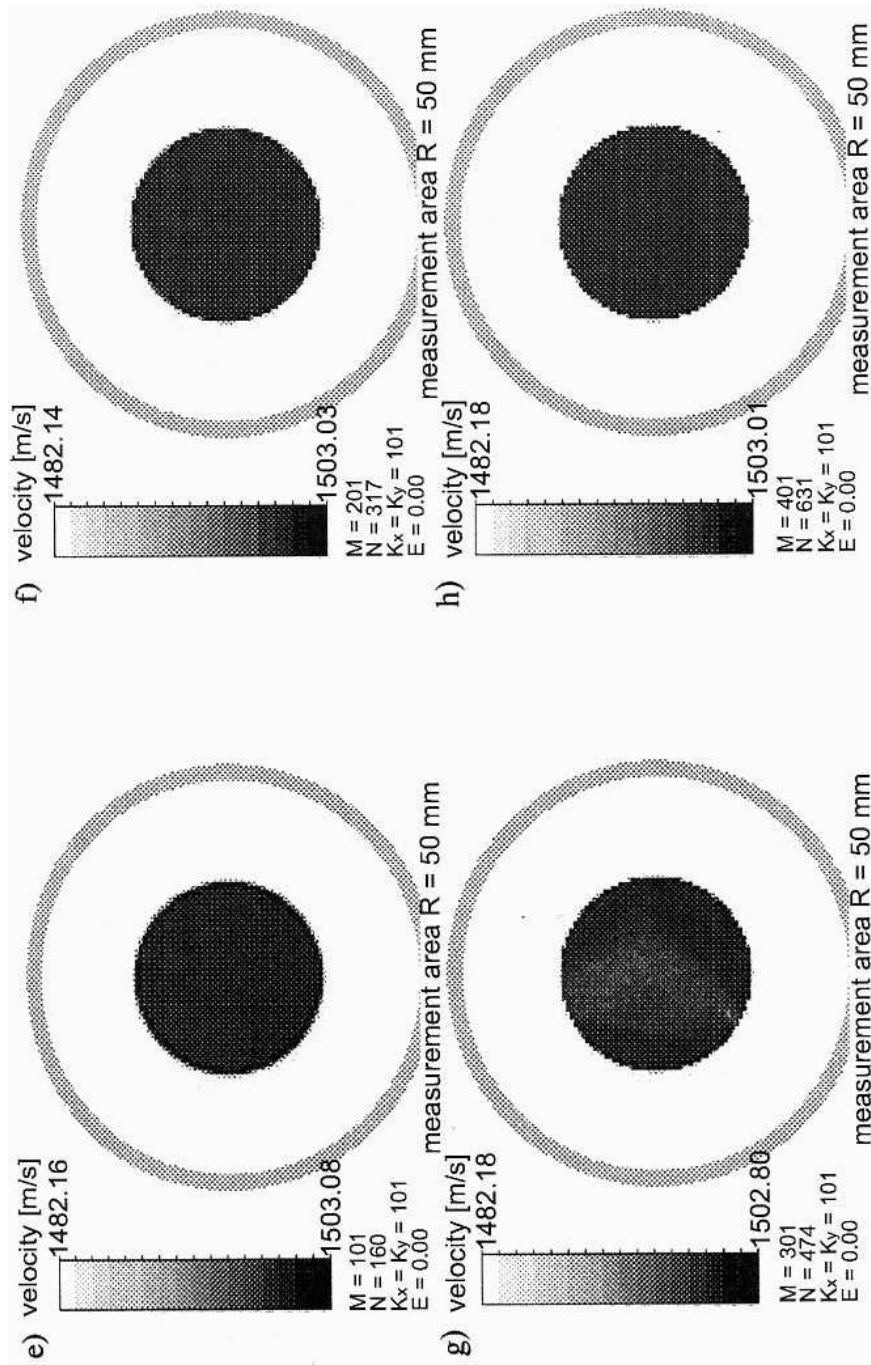
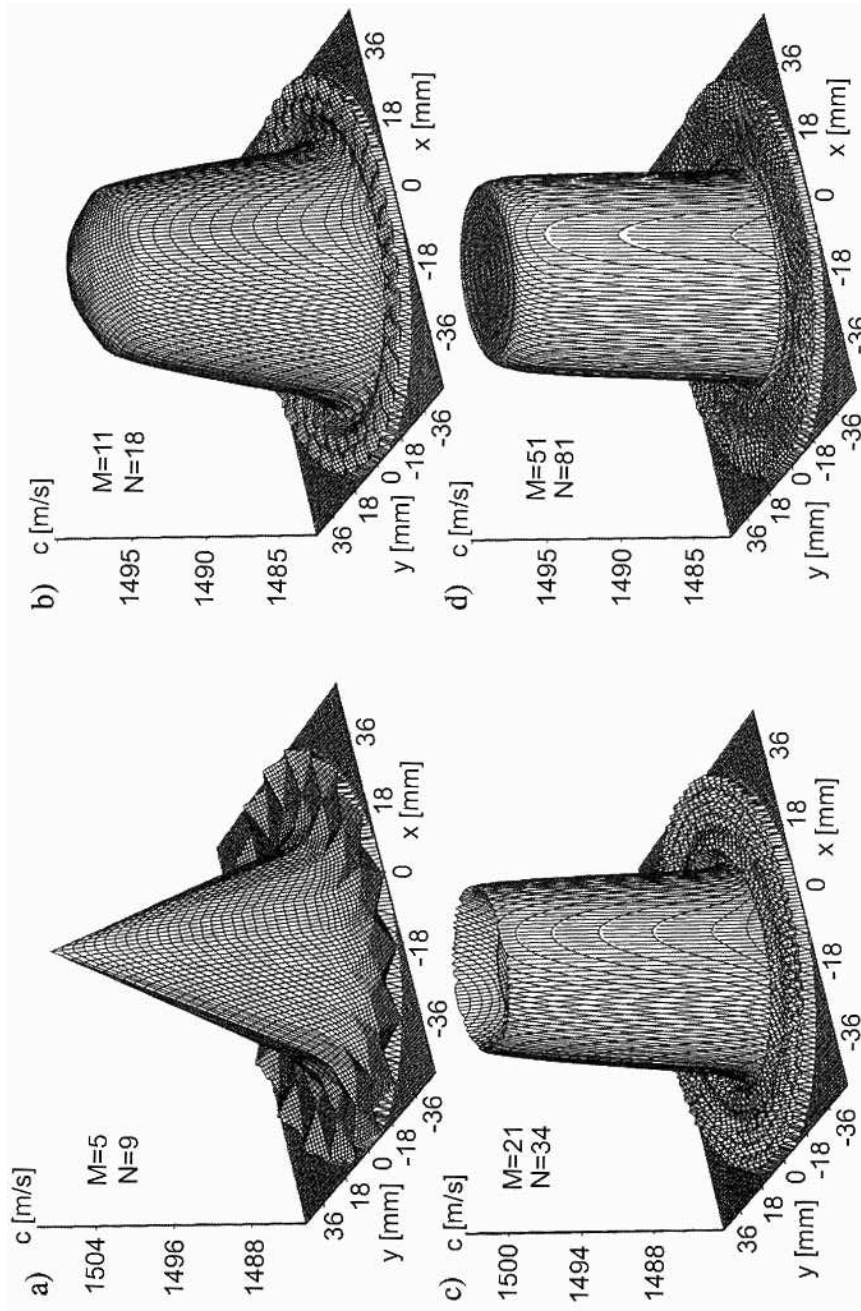


Fig. 7. Cylinder cross-section (from Fig. 2) images reconstructed by means of convolution and backprojection algorithm for different number of measuring rays and minimum required number of projections (acc. to formula (20)), shown in gray-scale for $E = 0$.



[Fig. 8]

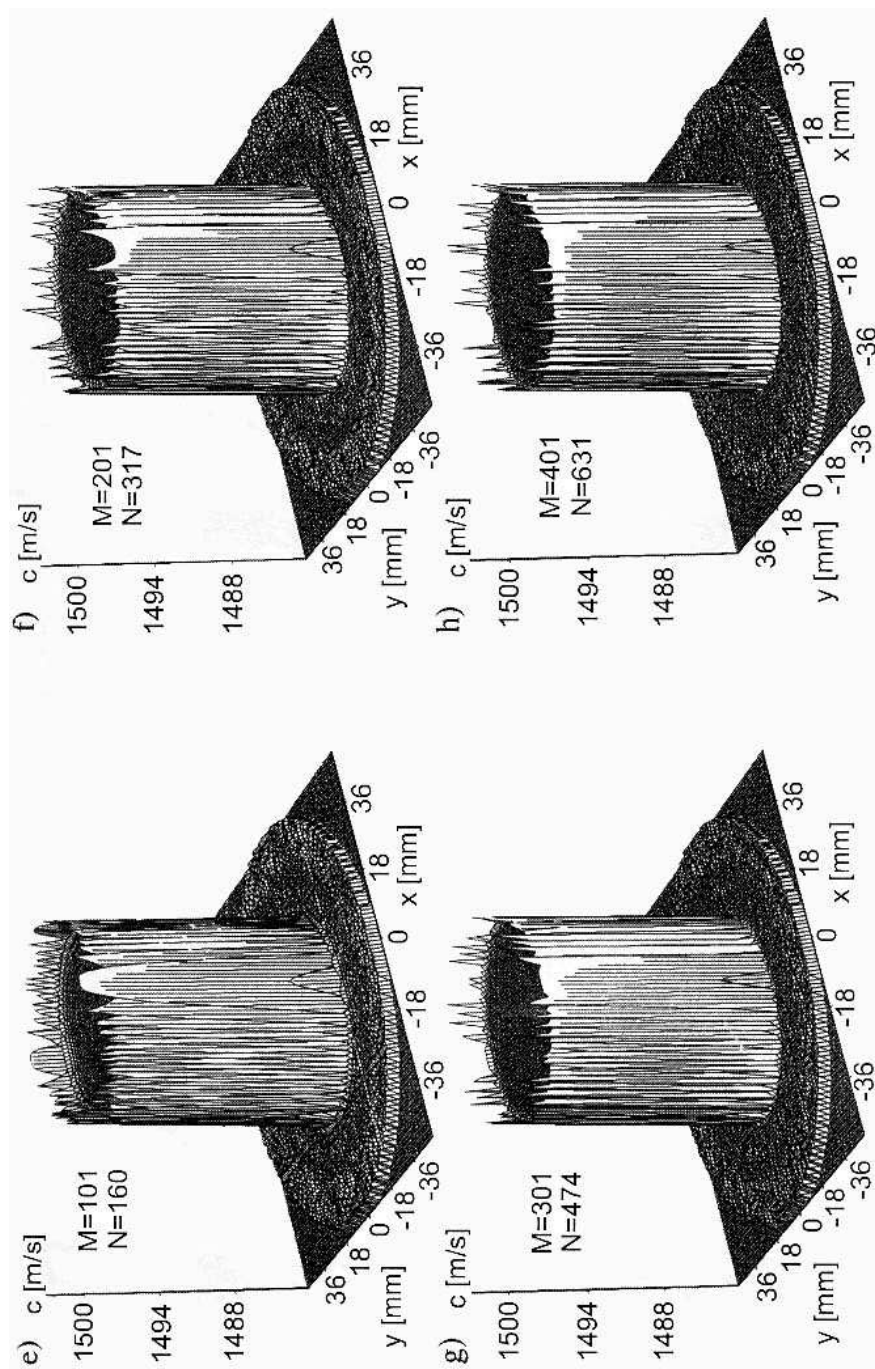


Fig. 8. Cylinder cross-section (from Fig. 2) images reconstructed by means of convolution and backprojection algorithm for different number of measuring rays and minimum required number of projections (acc. to formula (20)), shown in pseudo-3D for $E = 0$.

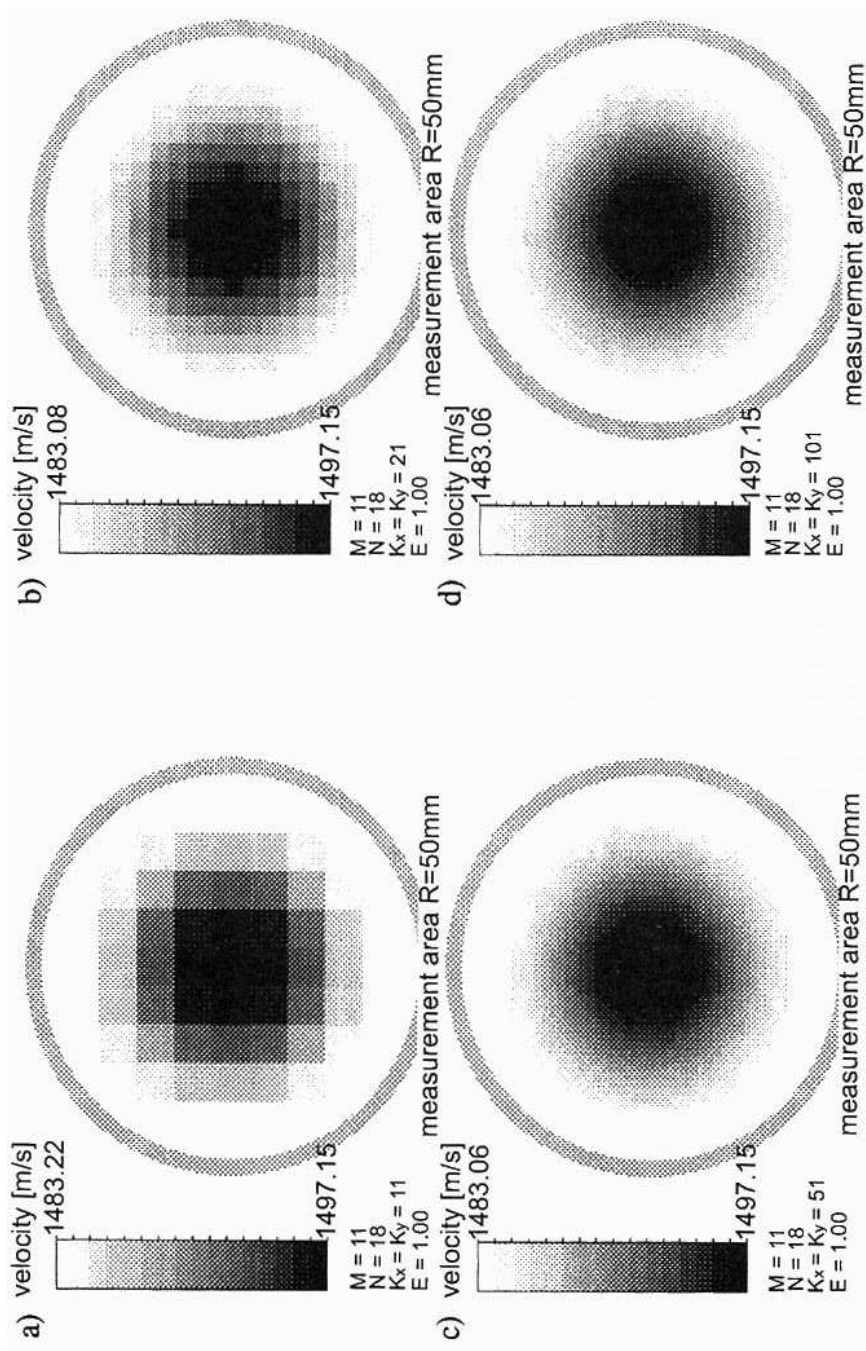


Fig. 9. Cylinder cross-section (from Fig.2) images reconstructed by means of convolution and backprojection algorithm, shown in gray scale for different image reconstruction grid sizes ($E = 0$).

side Δs (Fig. 9 a) where Δs stands for a transducer tracking jump. The larger the grid size (small size of pixels), the longer the reconstruction computation time. Therefore a reasonable grid size should be chosen, adopting the quality of image as the basic criterion (a compromise between resolution and image blur), which is particularly important in the case of a small number M of rays (Fig. 9).

7. Experimental verification

To verify the reconstruction performance of the convolution and backprojection algorithm optimized in this research, actual measurements were made using a UTT experimental setup [3]. To measure transition time, a computer flaw detector card with a resolution of 14 ns (this resolution is determined by card's sampling rate — 72 MHz) and a pair of ultrasonic transducers: a sending one and a receiving one, operating at frequency of 2.5 MHz, were used. A quasi-homogenous cylinder 50 mm in diameter and 70 mm high, formed from agar gel and immersed in water, was measured. The sound velocity in the cylinder was about 1505 m/s and in water — 1491 m/s. A measuring area whose diameter was equal to the sending transducer–receiving transducer distance $l_o = 100$ mm was assumed. A set of measuring data — mean times of passage through the circular cross-section of the cylinder — in a parallel ray projection geometry was obtained (Fig. 1) for $M = 101$ rays and $N = 100$ projections. The obtained data were recalculated to mean noise velocities for the distance of 100 mm and, after reduction and re-scaling according to method B (Sec. 4), they were entered into the convolution and backprojection algorithm in order to reconstruct an image of the distribution of local sound velocities in the investigated cylinder cross-section. During reconstruction 6 different values of parameter E for applied convolving function q (formula (11)): 0, 0.2, 0.4, 0.6, 0.8, 1 were assumed in turn. The data obtained immediately after reconstruction were recalculated to sound velocity using formula (19) and imaged in a 16-degree gray scale (Fig. 10) and in pseudo-3D (Fig. 11).

The cylinder cross-section images reconstructed on the basis of the actual measurements (Figs. 10 and 11) are very similar to images reconstructed from simulations (Fig. 4). This shows that the optimized convolution and backprojection algorithm operation is correct. The oscillations of sound velocities in the images (Figs. 10, 11) are caused by the agar gel heterogeneity.

For low values of parameter E of convolving function q (formula (11)) one can obtain sharp images with clearly visible edges along discontinuities (Figs. 10 a, b, c and 11 a, b, c). A shortcoming of this kind of reconstruction are oscillations of the reconstructed values close to all, even small, discontinuities.

For high values of parameter E reconstructed images are less contrasty — the boundaries of non-homogenous structures are blurred and the small discontinuities are not visible (Figs. 10 d, e, f and 11 d, e, f). But the advantage of such reconstructions is that there are no oscillations or interference which in the case of the visualization of slightly heterogeneous structures may falsify the image.

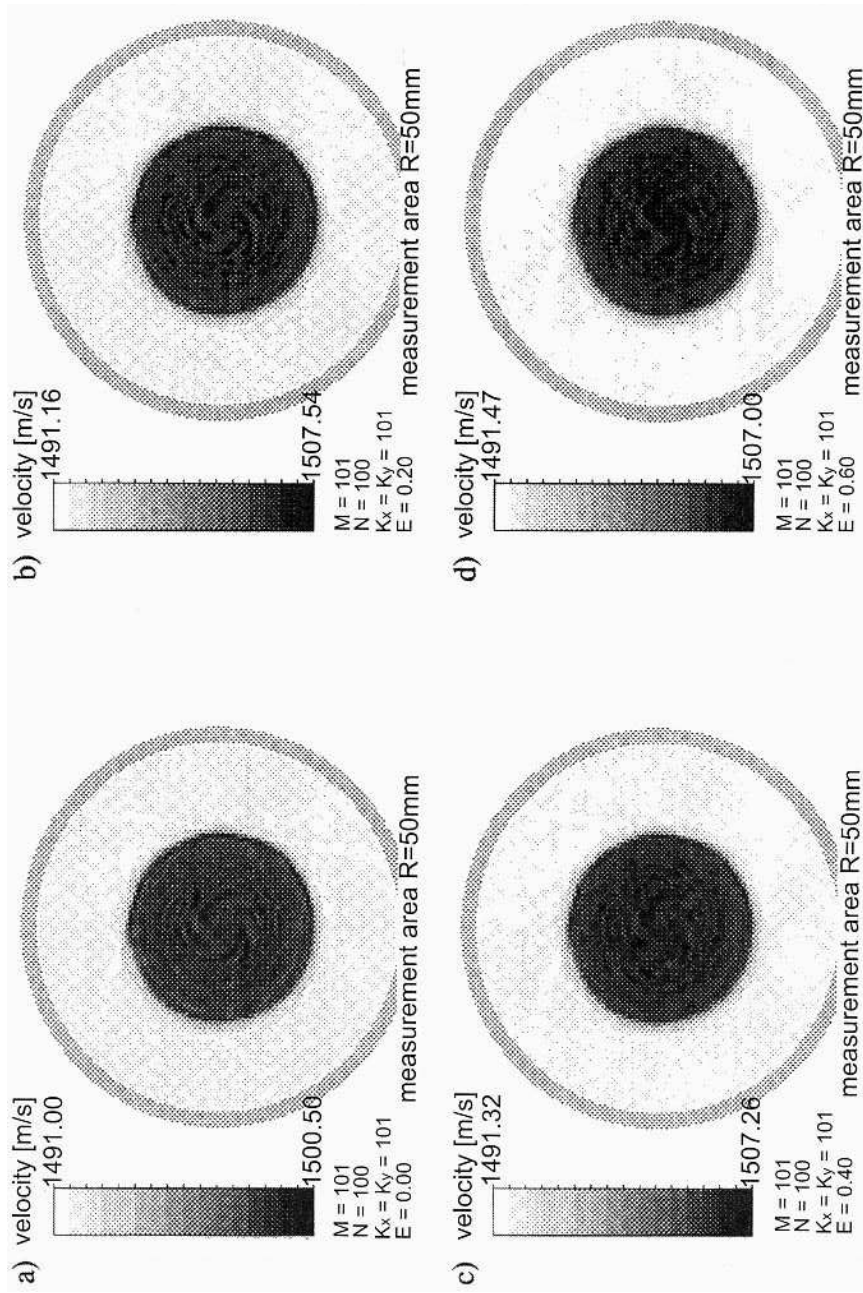


[Fig. 10]

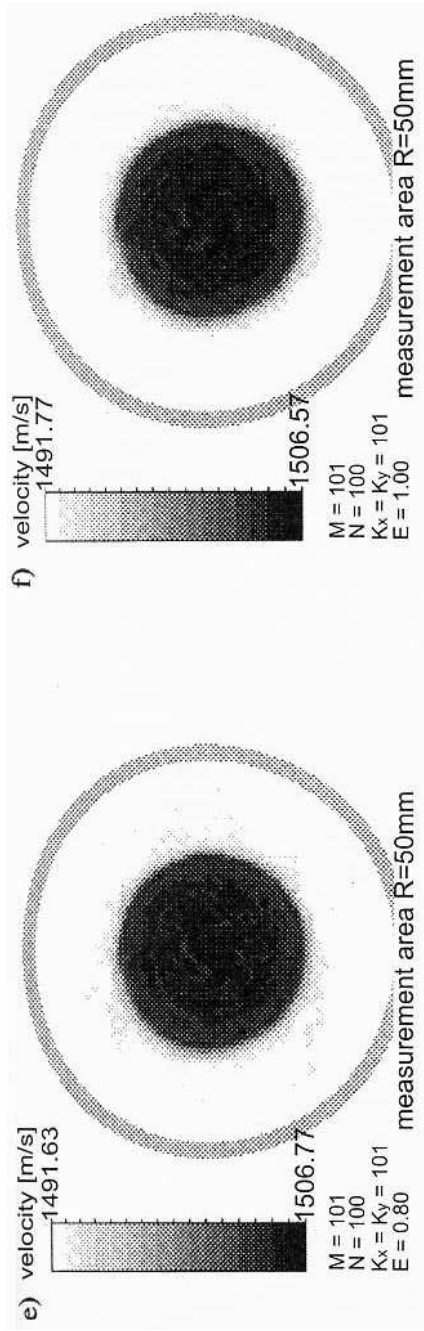
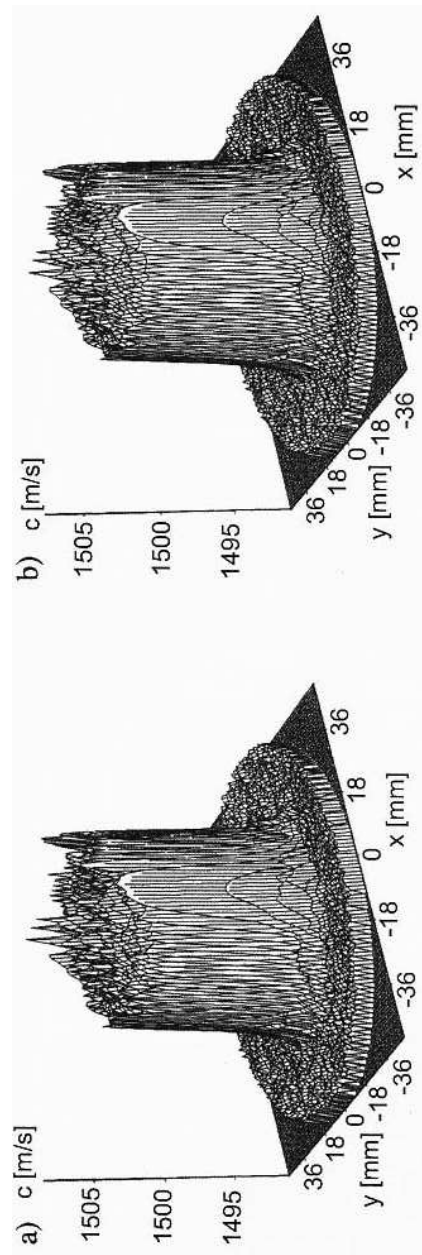


Fig. 10. Agar gel cylinder cross-section images reconstructed on the basis of actual measurements by means of convolution and backprojection algorithm for different values of parameter E of convolving function $q(m, \Delta s)$ (acc. to formula (11)): a) $q_E=0$, b) $q_E=0.2$, c) $q_E=0.4$, d) $q_E=0.6$, e) $q_E=0.8$, f) $q_E=1$, shown in 16-degree gray scale.



[Fig. 11]

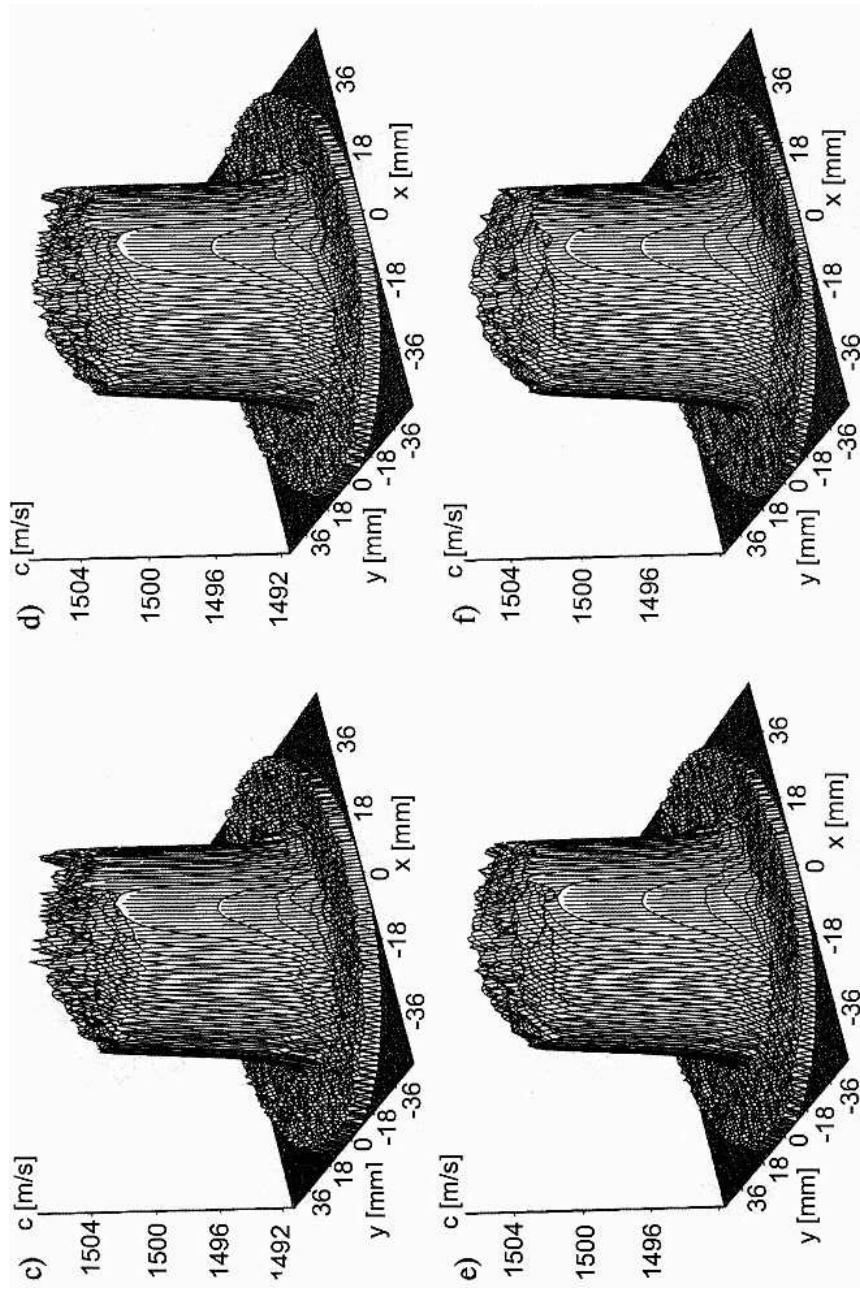


Fig. 11. Agar gel cylinder cross-section images reconstructed on the basis of actual measurements by means of convolution and backprojection algorithm for different values of parameter E of convolving function $q(m, \Delta s)$ (acc. to formula (11)): a) $q_E=0$, b) $q_E=0.2$, c) $q_E=0.4$, d) $q_E=0.6$, e) $q_E=0.8$, f) $q_E=1$, shown in pseudo-3D.

8. Conclusions

After appropriate optimization, the convolution and backprojection algorithm is perfectly suitable for UTT purposes because of its application versatility and the compromise between the imaging accuracy and the computation time. The use of convolving function $q(m \cdot \Delta s)$ (formula (11)), presented in paper [6] by R.M. LEWITT, in this algorithm ensures that in UTT it is possible to reconstruct the object internal structure images of different contrast by controlling the value of parameter E within range $[0, 1]$ without the necessity of introducing other convolving functions.

The convolution and backprojection algorithm presented and optimized in this research can be applied directly to the UTT visualization of an object's internal structure as the distribution of local sound velocities in it, reconstructed on the basis of the mean times of passage of an ultrasonic wave through the object immersed in water, in a parallel ray projection geometry.

The method of fitting proposed here, scaling and correcting transition time measuring data before they are entered into the reconstruction algorithm, makes it possible to obtain accurate local sound velocities after the reconstruction. This method has been verified by simulation calculations and actual measurements, which have shown that quite an accurate tomographic image can be obtained already for half the number of rays which follows from the number-of-projections-to-number-of-rays criterion (formula (20)). As regards the reconstruction process itself, it is enough to satisfy this criterion to obtain good-quality tomographic images. It has been found that a cross-section of homogenous structure can be visualized by UTT with high accuracy using the convolution and backprojection algorithm, if $M \geq 51$ rays per cross-section's largest dimension and $N \geq 81$ projections are assumed and if we have error-free mean transition measurements obtained in a parallel ray projection geometry.

Number of rays M determines the resolution of an image, the accuracy with which the size of structures is imaged and the accuracy of the reconstruction of image point values. Number of projections N determines the image's dynamics and distortions: if it is too low, distortions in the form of streaks and glow, which extend the scale of reconstructed values downwards, appear.

Because of computation time and image blur, an optimum size of reconstruction grid $K \times L$ — according to the visualization criterion — should be chosen.

Acknowledgements

This research was carried out as part of grant no. 8 T11E 029 14 funded by KBN (Scientific Research Committee) in the years 1998–2000.

References

- [1] Y. CENSOR, *Finite series-expansion reconstruction methods*, Proceedings of the IEEE, **71**, 3, 409–419 (1983).
- [2] E.J. FARRELL, *Processing limitations of ultrasonic image reconstruction*, Proc. of 1978 Conf. on Pattern Recognition and Image Processing (1978).

-
- [3] T. GUDRA, K. OPIELIŃSKI and W. SELWESIUK, *Experimental setup for ultrasound transmission tomography* [in Polish], Proceedings of XLIII Open Seminar on Acoustics OSA'96, **1**, 259–264 (1996).
 - [4] A.K. JAIN, *Fundamentals of digital image processing*, Prentice-Hall, Englewood Cliffs, New Jersey 1989, p. 570.
 - [5] A.C. KAK and M. SLANEY, *Principles of computerized tomographic imaging*, The IEEE Inc., IEEE Press, New York 1988, p. 329.
 - [6] R.M. LEWITT, *Reconstruction algorithms: transform methods*, Proceedings of the IEEE, **71**, 3, 390–408 (1983).
 - [7] S.A. NIELSEN, K.K. BORUM and H.E. GUNDTOFT, *Verifying an ultrasonic reconstruction algorithm for non-destructive tomography*, Proc. Of The 1995 World Congress on Ultrasonics, 447–450 (1995).
 - [8] K. OPIELIŃSKI, *Computer model of ultrasound transmission tomography: reconstruction of images* [in Polish], Proceedings of XLIII Open Seminar on Acoustics OSA'96, **2**, 547–552 (1996).
 - [9] K. OPIELIŃSKI, *Imaging of object's internal structure by ultrasound transmission tomography (UTT) on the basis of computer simulation of acoustic parameters* [in Polish], Acoustics in Technology, Medicine and Culture — KBN Grant Projects carried out in the years 1993–1995, 215–220 (1996).
 - [10] K. OPIELIŃSKI, *Reconstruction of image of object's internal structure by ultrasound transmission tomography (UTT) on the basis of computer simulation of ultrasound velocity measurements* [in Polish], Molecular and Quantum Acoustics, **17**, 219–226 (1996).
 - [11] G.N. RAMACHANDRAN and A.V. LAKSHMINARAYANAN, *Three dimensional reconstructions from radiographs and electron micrographs: Application on convolution instead of Fourier transforms*, Proc. Nat. Acad. Sci., **68** (1971).
 - [12] L.A. SHEPP and B.F. LOGAN, *The Fourier reconstruction of a head section*, IEEE Trans. Nucl. Sci., NS-21 (1974).
 - [13] M. STAPPER and G. SOLLIE, *Ultrasound transmission tomography by means of a personal computer*, Ultrasonics International'85, 935–940 (1985).

THE TWO FACES OF AUDITORY MASKING

U. JORASZ

Institute of Acoustics
Adam Mickiewicz University
(61-614 Poznań, Umultowska 85, Poland)

B.C.J. MOORE

Department of Experimental Psychology
University of Cambridge
(Cambridge, United Kingdom)

The experiments are concerned with the comodulation masking release (CMR) and modulation discrimination interference (MDI) that can occur when modulated carriers are added to a target modulated sound at frequencies remote from the target frequency. The results are discussed in terms of the factors influencing the both effects.

1. Introduction

FLETCHER [2] suggested that the peripheral auditory system behaves as if it contained a bank of bandpass filters, with continuously overlapping passbands (now called “auditory filters”). Fletcher thought — and recent data are consistent with this point of view — that the basilar membrane inside the cochlea provided the basis for the auditory filters. When an observer is trying to detect a sinusoidal signal of a given frequency in a noise background, it has often been assumed that performance is based on the output of the single auditory filter that gives the highest signal-to-noise ratio. The centre frequency of this filter is usually the same as or close to the signal frequency. Threshold is assumed to correspond to a constant signal-to-noise ratio.

This model works very well in many situations [9] but it clearly fails in others. In some cases, the outputs of auditory filters tuned away from the signal frequency can be used to enhance signal detection, as in the phenomenon of comodulation masking release (CMR) [4]. CMR occurs when the task is to detect a signal centred in a narrow-band masker (the on-frequency band) that is amplitude modulated in some way. The addition of other components to the masker, remote from the signal frequency, can enhance signal detection, provided the extra components have a similar pattern of modulation to the on-frequency band. These extra masker components are sometimes called “flankers”.

In the majority of experiments demonstrating CMR, the on-frequency band and flankers have been modulated at the same depth. It is usually assumed that the flankers improve detection of the signal because the listener can make use of the disparity in modulation pattern at the outputs of different auditory filters; when the signal is absent, the pattern is similar for all filters, but when the signal is present the modulation pattern differs for filters tuned close to the signal frequency and filters tuned close to the flanker centre frequencies.

In other cases, the outputs of auditory filters tuned away from the signal frequency degrade signal detection. This degradation seems to happen mainly when the task of the observer is to discriminate changes in modulation depth of the signal or to detect a change in the modulation pattern of the signal [12]. In this case, the signal carrier frequency is often called the “target”. The ability to discriminate/detect these changes is adversely affected by the presence of other modulated sounds (also called flankers, but sometimes also called “interferers”), even when those sounds have centre frequencies well away from that of the target. We use the acronym MDI (modulation detection/discrimination interference) to describe this effect. The greatest MDI occurs when the target and “interfering” sounds are modulated at similar rates [7, 13]. In this respect, MDI resembles CMR, except that the remote components enhance detection in CMR and degrade it in MDI. MDI often occurs when the modulation depth of the target is small, but the modulation depth of the interferers is large.

In many ways, the conditions in which CMR and MDI occur are only a little different. Both CMR and MDI involve modulated stimuli. In the case of CMR, the signal is added to a modulated sound, and results in a change in the modulation pattern of that sound. The flankers make it easier to detect the change in modulation pattern. In the case of MDI, the signal is also a change in modulation of a target sound. But now, the flankers make it harder to hear the change.

A point of special interest of our experiments was to examine the factors that determine whether the flankers produce MDI or CMR. One difference between conditions giving CMR and those giving MDI concerns the relative modulation depths of the target and flankers; a second difference concerns the ability of subjects to detect a decrease or an increase in modulation depth. MOORE *et al.* [6] showed that stimuli that were otherwise very similar could give CMR when the task of subjects was to detect a decrease in modulation depth, and MDI when the task was to detect an increase. In the experiments reported here, we manipulated the relative modulation depth of the target and flankers and compared the ability to detect a decrease and an increase in modulation depth.

2. Conditions of the experiments

2.1. Stimuli

Thresholds were measured for detecting either an increase or a decrease in modulation depth of a sinusoidally amplitude modulated (SAM) target signal, with that signal

presented either alone, or with flankers. The following expression describes a SAM sound:

$$A(t) = A_o[1 + m \cos(2\pi f_m t + \theta)] \cos(2\pi f_c t + \phi),$$

where A_o is the amplitude envelope of the unmodulated carrier, t is time, f_c is the carrier frequency, f_m is the modulator frequency, m is the modulation depth, and θ and ϕ are terms determining the starting phases of the modulator and carrier, respectively. In our experiments, the value of θ for the target sound had a random value from one stimulus to the next; thus the phase of the modulation was random relative to the onset of the stimulus.

The target was a 1000-Hz carrier SAM at a 10-Hz rate with a modulation index m of 0.5. The flankers, when present, consisted of two carriers which were not harmonically related to the target. Their modulation depths were 0.0, 0.25, 0.5, or 0.75. The two carriers were always modulated at the same rate as each other, and they were modulated at the same rate as the target, and in-phase with the target. In one set of conditions, they were centred at 230 and at 3300 Hz. In a second set they were centred at 550 and 1550 Hz. Both sets were chosen to be well outside the passband of the auditory filter centred at the target frequency.

All carriers were presented at a level of 60 dB SPL. To prevent changes in intensity providing a cue for discrimination of modulation depth, carriers which were SAM were "intensity compensated" to eliminate changes in overall intensity with changes in modulation depth [10]. The time pattern of the sounds is illustrated in Fig. 1. The relatively long stimulus duration was chosen for two reasons: so that several cycles of modulation would occur during each stimulus; and to reduce the possible role of perceptual grouping caused by synchronous gating of the target and flankers. In one stimulus the 1000-Hz carrier was modulated at the reference modulation depth (0.5). In the other, the modulation depth was greater, or, in a separate set of trials, less. The order of the two stimuli was random.

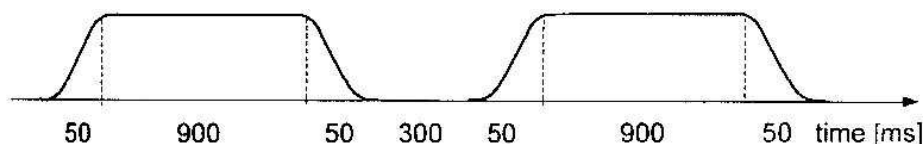


Fig. 1. Time pattern of the sounds. Each stimulus had a 900-ms steady-state portion and 50-ms raised-cosine rise/fall ramps. On each trial, two stimuli were presented, separated by a 300-ms silent interval.

All stimuli were generated using a Masscomp 5400 computer equipped with 16-bit digital-to-analogue converters. The sampling rate was 10 kHz, and stimuli were low-pass filtered at 4 kHz (-3 dB point) using a Fern Electronics EF16 filter with an attenuation rate of 100 dB/oct. The stimuli for each trial were calculated on line in the inter-trial interval.

Subjects were tested individually or in pairs in separate double-walled sound attenuating chambers. Stimuli were delivered via a manual attenuator to one earpiece of a Sennheiser HD414 headset.

2.2. Procedure

An adaptive 2AFC procedure was used to estimate the 79.4% correct point on the psychometric function. A run always started with a large change in modulation depth in the signal interval. After three successive correct responses the change in modulation depth was reduced while after each incorrect response it was increased. The modulation index was not allowed to be greater than 1.0 or less than 0. Initially, the step size for the change in modulation index was 5 dB in units of $20 \log(m)$. After four reversals, the step size was decreased to 2 dB and eight further reversals were obtained. The mean value of $20 \log(m)$ at last eight reversals was used to estimate the change in modulation index corresponding to threshold. At least four estimates were obtained for each condition, and the threshold was calculated as the geometric mean of the four. When the standard deviation of the log values exceeded 0.2, at least one further estimate was obtained and all estimates were averaged. The standard deviation of the log values was typically between 0.05 and 0.15. The standard error of the log values was never greater than 0.1 and was typically about 0.05. Correct-answer feedback was given after each trial by means of lights on the response box.

2.3. Subjects

Three subjects with a normal hearing at all audiometric frequencies were used. One was author UJ. The others were paid for their services. During initial training, performance in the reference condition (target sound alone) stabilised quite rapidly. Thresholds continued to decrease for some time in the conditions with flankers. All subjects found these conditions very difficult at first. They were given at least 15 hours of practice prior to collection of the data reported here.

3. Factors determining whether CMR or MDI occurs

3.1. The task of the subjects

The solid triangles in Fig. 2 (the results shown as open triangles will be discussed later (Subsec. 3.2)) show results for one subject (S3) from experiment 1, where all sounds were gated synchronously. For all subjects thresholds were consistent and very similar. Thresholds are expressed as the change in modulation index at threshold, divided by the reference modulation index (0.5), and are plotted as a function of the modulation depth of the flankers. The left-most points show thresholds in the reference condition (no flankers). These thresholds are consistent with those in the literature [8, 3, 11].

The unmodulated flankers raised thresholds somewhat. This effect may be partly caused by the synchronous gating of the target and flankers, a point we will return to later. However, modulated flankers produced more MDI, and the amount of MDI increased progressively as the modulation depth of the flankers was increased.

The pattern of results was similar for the two types of flankers (550 and 1550 or 230 and 3300 Hz), but the amount of MDI was slightly greater for the former. This could indicate that MDI is affected by the proximity in frequency of the target and flankers.

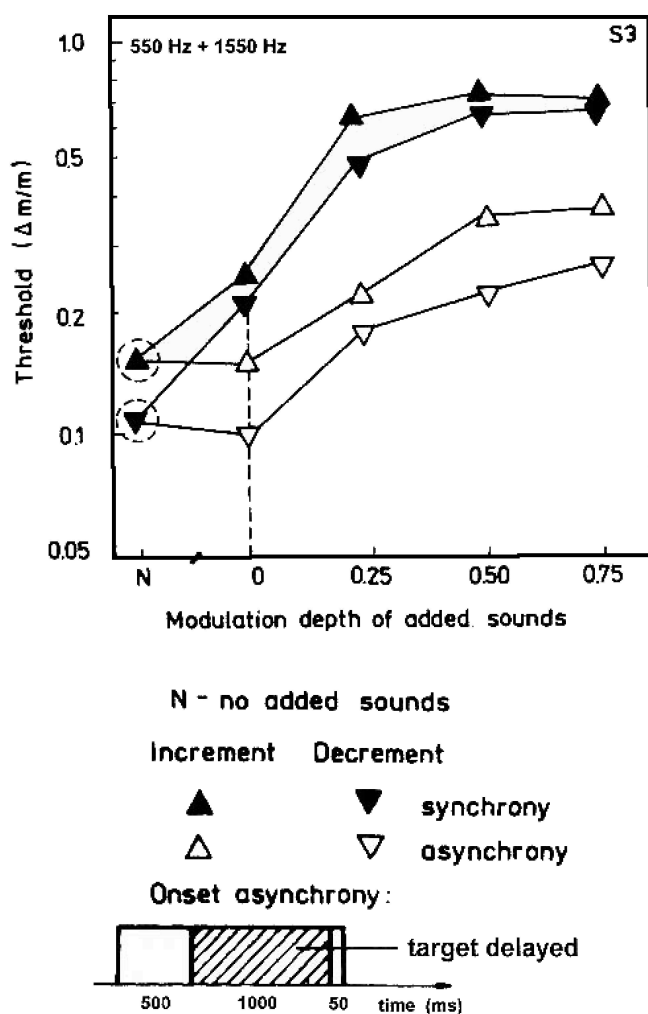


Fig. 2. The solid triangles show results from the first part of the experiment, where all sounds were gated synchronously. Thresholds are shown for detecting an increment in modulation depth (up-pointing triangles) or decrement in modulation depth (down-pointing triangles). Thresholds are expressed as a proportion of the modulation depth of the standard sound ($m = 0.5$) and are plotted as a function of the modulation index of the flankers. The open triangles show results when the onset of the target was delayed relative to the onset of the flankers.

However, the greater effect for the 550- and 1550-Hz sounds might reflect a small degree of interaction of the target and flankers in the peripheral auditory system.

Thresholds for detecting decrements in modulation depth were lower than those for detecting increments, but the difference was small. It may be asked why these data showed no sign of CMR, even in though there was a potential detection cue in at least one condition, where the flankers were modulated with the same depth, 0.5, as the reference sound)? We will try to provide the answer when considering our later experiments.

3.2. Onset asynchrony

Onset asynchrony is known to be a powerful factor in perceptual grouping. When a new sound is introduced after another sound has been on for some time, the new sound seems to “pop out” and to be perceived as a separate sound. It has been suggested that perceptual grouping processes play a role in both CMR and MDI [12]. One principle that operates in perceptual grouping is “common fate” [1]. Elements of a sound that change in the same way tend to be grouped and heard as a single stream. Two applications of this principle are relevant here: Elements that start and stop together tend to be perceived as a single sound; and elements that are modulated in similar way tend to be perceived as a single sound.

If MDI depends on perceptual grouping of the target and flankers, delaying the target sound relative to the flankers should result in a marked decrease in MDI. We also thought that the introduction of an onset asynchrony would increase the chances of obtaining CMR in the conditions of the experiment where the target and flankers had the same modulation depth as the target sound, and where the task was to detect a decrease in modulation depth.

The stimuli were essentially the same as those of the first part of experiment, except for the difference in time pattern (see the bottom of Fig. 2). The flankers were gated on 500 ms before and gated off 50 ms after the 1000-ms target sound. The subjects and procedure were the same as before. The standard error of the log values of the threshold estimates was never greater than 0.1 and was typically about 0.05.

The results are shown as the open triangles in Fig. 2. Now the unmodulated flankers did not produce MDI. This suggests that the MDI found with these sounds previously did not result from the interactions of the sounds in the peripheral auditory system. Rather, it may have been a consequence of perceptual grouping of the target and flankers caused by their synchronous gating. Onset asynchrony reduced the amount of MDI for all subjects. This fact suggests that perceptual grouping does play a role in MDI. However, even though the target sound was easily heard out, there was still no evidence for CMR.

3.3. The reference conditions

We consider now another difference between situations giving rise to CMR and those giving rise to MDI. This difference is related to the difficulty of signal detection in the condition with the on-frequency sound alone (the reference condition). Usually, large CMRs occur when there is a high degree of stimulus uncertainty in the reference condition, or when thresholds are high for some other reason. In contrast, in experiments demonstrating MDI, thresholds in the reference condition tend to be quite low. Thus, our failure to obtain CMR could have been a consequence of our use of too small a modulation depth in the reference condition, which gave rise to low thresholds. Hence, we decided to examine the effect of using greater modulation depths.

The following modulation depths of the target/flanking sounds were used: 0.75 and 0.75; 1.0 and 1.0; 0.75 and 1.0. Since the reference modulation indexes were high, it was not generally possible to measure thresholds for detecting increments in modulation

depth. Hence, thresholds were measured only for the detection of decrements in modulation depth. Thresholds were measured under three conditions: the reference condition (N – no flankers); with the target and flankers gated together (S – synchronous condition); and with the onset of the target delayed by 500 ms relative to the onset of the flankers (A). In all cases, the signal duration was 1000 ms.

To increase the chances of obtaining CMR, the two sets of flankers used earlier were combined, giving a set of flankers consisting of carriers at 230, 550, 1550, and 3300 Hz. The magnitude of CMR has been shown to increase with increasing numbers of flankers (for review, see [5]).

The results for the greatest modulation depth ($m = 1$) are shown in Fig. 3. The rest of results is very similar. In each triad of bars, the left-most bar shows results for subject 1, the middle bar for subject 2, and the right bar for subject 3. For all three subjects, the thresholds tended to be lower in all conditions when the flankers were modulated with $m = 1$ than when they were modulated with $m = 0.75$; increasing the modulation depth of the flankers produced a masking release. This contrasts with the results for first experiment, where thresholds tended to increase with increasing modulation depth of the flankers (Fig. 2), i.e. increasing the modulation depth of the flankers produced more MDI.

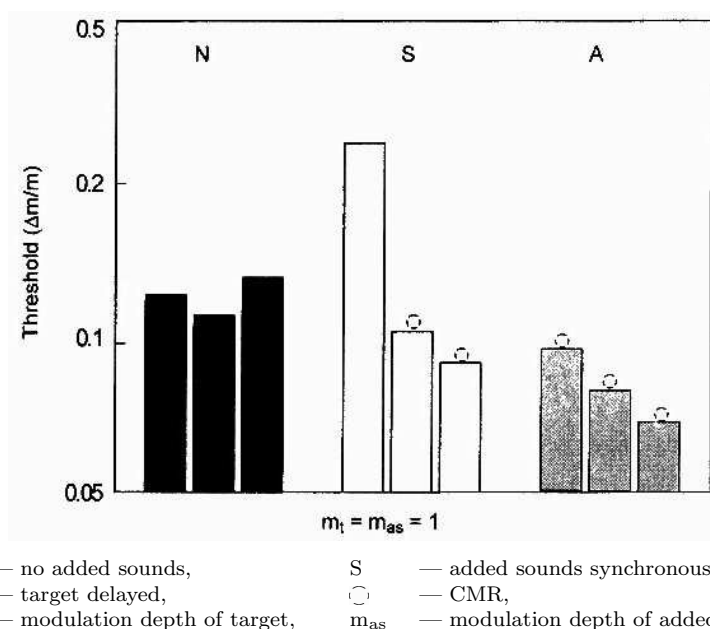


Fig. 3. Results of the experiment when the modulation depth was 1.0 for both the target and the flankers. In each group of three bars, the left bar shows results for subject 1, the middle bar for subject 2, and the right bar for subject 3.

In the introduction, it was pointed out that, in most experiments demonstrating CMR, the on-frequency and flanking bands have been modulated at the same depth. Our results suggest, however, that this is not critical; rather, the masking release can be

greater when the flanking bands have a greater modulation depth than the on-frequency sound.

It seems likely that our results reflect a balance between mechanisms producing MDI and those producing CMR. The higher modulation index of the target sound — the harder reference condition — created conditions more conducive to obtaining CMR. Now, the tendency for a greater modulation depth of the flankers to produce greater MDI was more than offset by the tendency for CMR to increase with increasing modulation index of the flankers. The balance between mechanisms producing MDI and those CMR varied across subjects. It seems that, under the conditions of this experiment, the most important factor affecting the balance between mechanisms producing MDI and those producing CMR was the onset asynchrony of the target sound.

4. Conclusions

Adding modulated carriers (flankers) at a frequency remote from the target frequency, sometimes impaired discrimination of modulation depth of the target (MDI) and sometimes improved it (CMR). When the modulation depth of the target sound was 0.5, the flankers always gave MDI rather than CMR. The amount of MDI generally increased progressively with increasing modulation depth of the flankers. The amount of MDI was markedly reduced, but not usually eliminated, by gating the target sound on after the flankers. This supports the suggestion that perceptual grouping mechanisms play a role in MDI; the asynchronous onsets of the target and flankers made the target appear to “pop out”, making it easier to discriminate changes in the target sound.

CMR occurs when both the target and flankers have a high modulation depth, and the signal is a decrease in modulation depth. It seems likely that a large amount of CMR only occurs when performance in the reference condition (target sound alone) is poor.

Acknowledgements

Preparation of this paper was supported by KBN. Grant 1H01FO8012.

References

- [1] A.S. BREGMAN, *Auditory scene analysis: The perceptual organization of sound*, MIT, Cambridge, MA 1990.
- [2] H. FLETCHER, *Auditory patterns*, Rev. Mod. Phys., **12**, 47–65 (1940).
- [3] D.W. GRANTHAM and S.P. BACON, *Detection of increments and decrements in modulation depth of SAM noise*, J. Acoust. Soc. Am. Suppl. 1, **84**, S140 (1988).
- [4] J.W. HALL, M.P. HAGGARD and M.A. FERNANDES, *Detection in noise by spectrotemporal pattern analysis*, J. Acoust. Soc. Am., **76**, 50–56 (1984).
- [5] B.C.J. MOORE, *Comodulation masking release: Spectro-temporal pattern analysis in hearing*, Brit. J. Audiol., **24**, 131–137 (1990).
- [6] B.C.J. MOORE, B.R. GLASBERG and G.P. SCHOONEVELDT, *Across-channel masking and comodulation masking release*, J. Acoust. Soc. Am., **87**, 1683–1694 (1990).

-
- [7] B.C.J. MOORE, B.R. GLASBERG, T. GAUNT and T. CHILD, *Across-channel masking of changes in modulation depth for amplitude- and frequency-modulated signals*, Q.J. Exp. Psychol., **43A**, 327–347 (1991).
- [8] E. OZIMEK and A. SEK, *AM difference limens for noise bands*, Acustica, **66**, 153–160 (1988).
- [9] R.D. PATTERSON and B.C.J. MOORE, *Auditory filters and excitation patterns as representations of frequency resolution*, [in:] Frequency selectivity in hearing, B.C.J. MOORE [Ed.], Academic, London 1986.
- [10] N.F. VIEMEISTER, *Temporal modulation transfer function based upon modulation thresholds*, J. Acoust. Soc. Am., **66**, 1364–1380 (1979).
- [11] G.H. WAKEFIELD and N.F. VIEMEISTER, *Discrimination of modulation depth of SAM noise*, J. Acoust. Soc. Am., **88**, 1367–1373.
- [12] W.A. YOST and S. SHEFT, *Across-critical-band processing of amplitude-modulated tones*, J. Acoust. Soc. Am., **85**, 848–857 (1989).
- [13] W.A. YOST, S. SHEFT and J. OPIE, *Modulation interference in detection and discrimination of amplitude modulation*, J. Acoust. Soc. Am., **86**, 2138–2147 (1989).

PERIPHERAL AND CENTRAL PROCESSES IN HEARING

U. JORASZ

Institute of Acoustics
Adam Mickiewicz University
(61-614 Poznań, Umultowska 85, Poland)

B.C.J. MOORE

Department of Experimental Psychology
University of Cambridge
(Cambridge, United Kingdom)

One of the important problem in contemporary psychoacoustics is what can be instrumental in eliminating a relatively wide gap between peripheral — within-channel — and central — across-channel — auditory processes. The authors argued that CMR and MDI — two forms of auditory masking — can be useful in clarifying this problem. The mechanisms involved in the both effects are peripheral and central as well.

1. Introduction

There is a relatively wide gap between what is known about very peripheral auditory processes (such as frequency analysis on the basilar membrane) and what is known about more complex central auditory processes (such as speech perception). Peripheral and central processes may differ in many ways. However, one possible way of characterising the difference is in terms of within-channel versus across-channel processes. In the auditory periphery, for example at the level of the auditory nerve, stimuli are represented in frequency “channels”, each responding to a limited range of frequencies. There is little interaction between channels with widely separated centre frequencies. However, at more central levels of the auditory system, neurones exist which combine information from different peripheral frequency channels.

If an aspect of auditory perception can be explained entirely by consideration of processes occurring within one frequency channel, then that aspect might reflect mainly peripheral processing. However, if an aspect of auditory perception can only be explained by processes that involve comparing or combining information across frequency channels, then those processes must occur relatively centrally, at a level higher than the auditory nerve. The phenomena known under acronyms CMR (comodulation masking release) and

MDI (modulation detection/discrimination interference) may be very useful in illustrating these aspects of peripheral and central processing in hearing.

It has often been assumed that, when an observer is trying to detect a sinusoidal signal of a given frequency in a noise background, performance is based on the output of the single auditory filter (the one peripheral channel) that gives the highest signal-to-noise ratio [15]. However, this assumption clearly fails in some situations. In the phenomenon of comodulation masking release (CMR) [4], the outputs of auditory filters tuned away from the signal frequency can be used to enhance signal detection. CMR occurs when the task is to detect a signal centred in a narrow-band masker (the on-frequency band) that is amplitude modulated in some way. The addition of other components to the masker, remote from the signal frequency, can enhance signal detection, provided the extra components have a similar pattern of modulation to the on-frequency band. These extra masker components are sometimes called “flankers”. CMR is usually assumed to reflect a relatively central across-channel process.

In the phenomenon of modulation detection/discrimination interference (MDI), the outputs of auditory filters tuned away from the signal frequency degrade signal detection. This degradation seems to happen mainly when the task of the observer is to discriminate changes in modulation depth of the signal or to detect a change in the modulation pattern of the signal [11, 12, 19]. The ability to discriminate/detect these changes is adversely affected by the presence of other modulated sounds (also called flankers, but sometimes also called “interferers”), even when those sounds have centre frequencies well away from that of the target. Again, MDI is usually assumed to reflect a relatively central across-channel process.

Results from CMR experiments were initially surprising, primarily because the paradigm used to measure the effect had previously been associated with highly successful within-channel explanations that were based upon peripheral auditory processes. If the initial results are viewed in the context of central auditory analyses, they are no longer so unexpected. In fact, the surprise may be that within-channel explanations based on the concept of the auditory filter can account so much data on auditory masking. But there may be another way of looking at this. If the within-channel model is so successful, perhaps peripheral, within-channel mechanisms contribute to CMR and MDI [18]. Exploration of the relative importance of within-channel and across-channel processes in CMR and MDI may shed light on the peripheral versus central nature of these processes.

2. Evidence for central across-channel processes

2.1. *Effects of monaural versus dichotic presentation*

Both CMR and MDI can occur when the flankers are presented dichotically, i.e. to the ear opposite that receiving the target sound. This clearly demonstrates that part of the CMR and MDI effects must depend upon central processes. These dichotic effects, however, have generally been less than those for monaural presentation [1, 17]. The difference between the monaural and dichotic effects may reflect contributions from peripheral, within-channel processes.

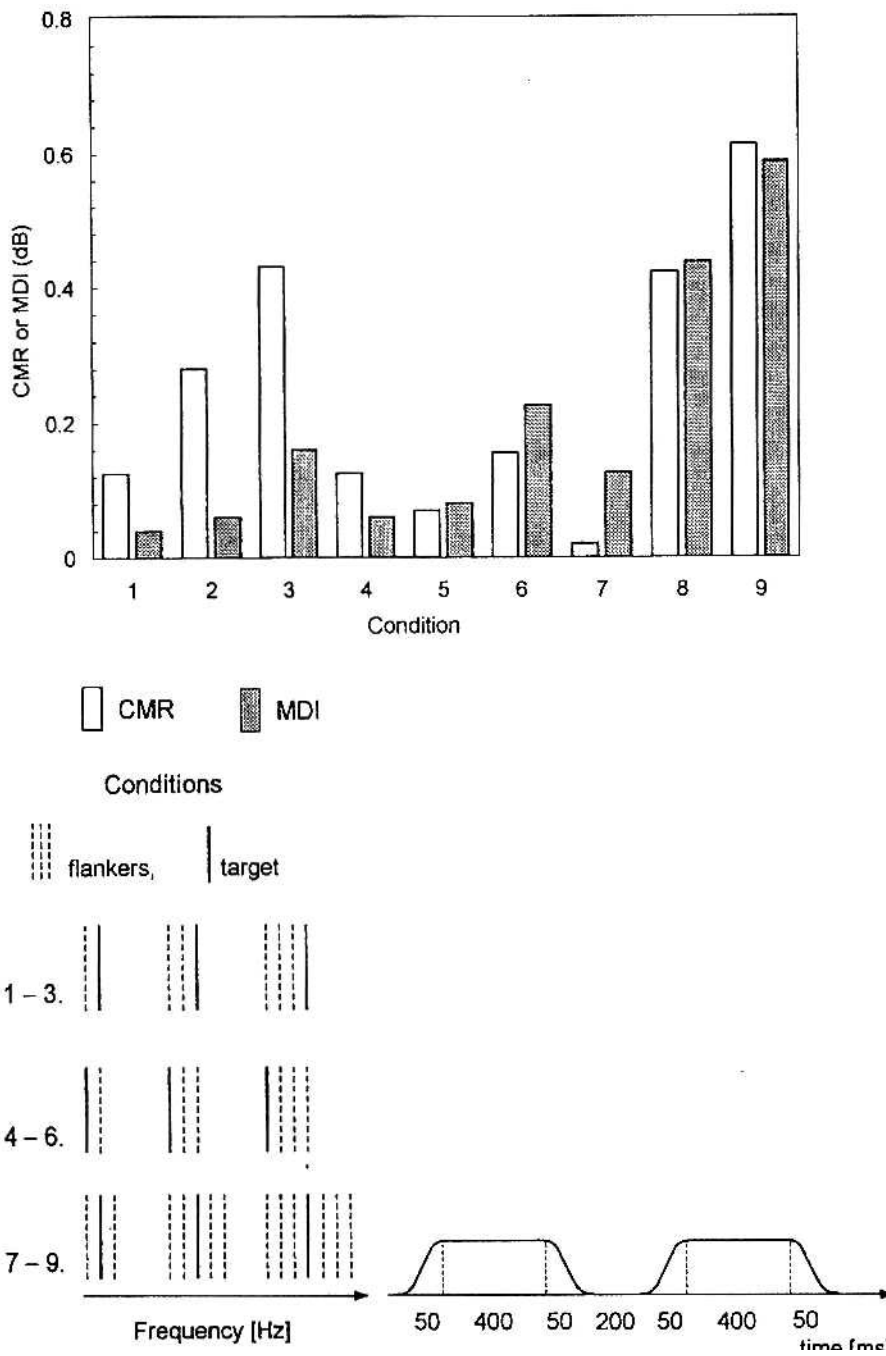


Fig. 1. The amount of CMR or MDI. The cartoons show schematically the spectra of the target and flankers for all conditions, time paradigm of signals, and their presentation in each forced-choice trial. Results shown are the average for three subjects (from [12]).

2.2. *Effects of the number and spectral location of the flankers*

One way of exploring the relative role of within and across-channel processes is to measure how the amount of CMR or MDI is influenced by the number of flankers and by the frequency separation of the flankers from the target. If CMR and MDI are mainly determined by within-channel processes, large effects should be produced by flankers close to the target frequency, and adding further flankers more remote from the target frequency should have little effect. MOORE and JORASZ [12] tested this prediction.

The target carrier frequency was 1000 Hz, and flanker carrier frequencies were: 416, 572, 765, 1301, 1670, and 2127 Hz. Both the target and the flankers were sinusoids which were amplitude modulated by narrow-band noise extending from 5 to 15 Hz. The overall intensity was held constant (level = 60 dB SPL per carrier) regardless of modulation depth. In one condition, called “comodulated”, the flankers were all modulated in the same way (i.e. with the same modulator) as the target. In a second condition, called non-comodulated, the flankers were all modulated in the same way as each other, but the target was modulated by an independent narrowband noise. For the CMR task, the subject was required to detect a 1000-Hz sinusoid added to the 1000-Hz noise-modulated carrier. The MDI task was to detect a decrease in modulation depth of the target. The target and masker carriers were gated together; in the CMR task, the signal was gated synchronously with the target and masker carriers.

Figure 1 shows schematic spectra of the stimuli (bottom left), the time pattern of the stimuli (bottom right) and the experimental results (top). Both MDI (filled bars) and CMR (open bars) increased with an increase in the number of flanking bands. In other words, adding flankers more remote from the target frequency led to larger effects. This suggests that both CMR and MDI are influenced by across-channel processes; the greater the number of channels involved, the larger are the effects.

2.3. *MDI and perceptual grouping*

In everyday life we often listen to several sound sources simultaneously. The auditory system is faced with the task of deciding which “elements” of the complex mixture arise from one source, and which from another. The process of doing this is often called “perceptual grouping” or “stream formation” [2]. The elements of the sound are grouped across-frequency and across time to form percepts of coherent streams each with its own loudness, pitch, timbre and location. Some researchers have suggested that MDI arises from a form of perceptual grouping of the target and the flankers; this presumably reflects a central process. When the target and flankers are perceptually grouped, it may be difficult to discriminate changes in the modulation of the target.

One principle that operates in perceptual grouping is “common fate”; components of a complex sound that change in a similar way over time tend to be grouped together and perceived as a single sound source. Two applications of this principle are relevant to MDI: elements that start and stop together tend to be perceived as a single sound; and elements that are amplitude modulated in a similar way tend to be perceived as a single sound. Several studies have examined the influence of these factors — similarity of amplitude modulation and synchrony versus asynchrony of onsets — on MDI [11, 19].

Figure 2 (data from the same experiment of MOORE and JORASZ [12]) shows a small but significant effect on MDI of whether the flankers were comodulated or non-comodulated (open or filled bars respectively) with the target; comodulated flankers usually gave greater interference, hence the greater amount of MDI. This effect was present when the amount of MDI was small (conditions 1–7). The lack of an effect for larger amounts of MDI might have been produced by a ceiling effect (the change in modulation index at threshold was close to the maximum possible value). Overall, the results suggest that similarity of modulation pattern does play a role in MDI, supporting that idea that central perceptual grouping processes play a role.

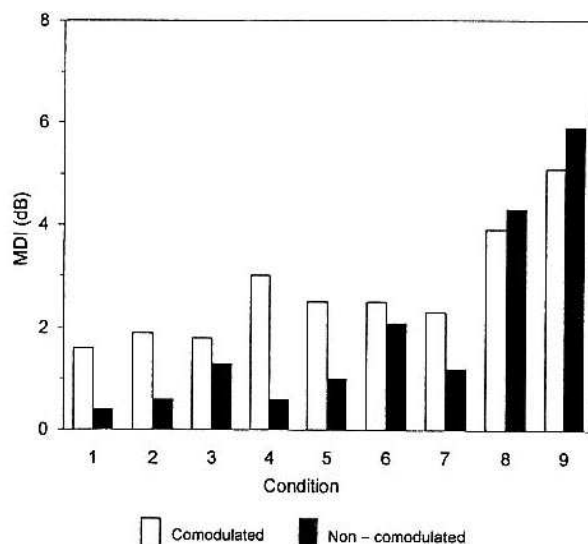


Fig. 2. The influence of comodulation of flankers on the amount of MDI. Conditions and the rest of data as Fig. 1 (from [12]).

Onset asynchrony is known to be a powerful factor in perceptual grouping; when a background sound has been on for some time, an added new sound seems to “pop out” and to be perceived as a separate sound [2, 9]. Thus, if MDI depends on perceptual grouping of the target and flankers, asynchrony of the target relative to the flankers should result in a decrease in MDI. MOORE and JORASZ [11] demonstrated that the amount of MDI was indeed markedly reduced by gating the target on after the flankers, a result which has also been found by others [3, 14].

3. Evidence for within-channel processes

So far we have argued that MDI and CMR are at least partly caused by central across-channel processes. There is, however, some evidence suggesting that within-channel processes influence both effects in some circumstances. The peripheral processes involve the flankers either masking part of the excitation pattern of the target or introducing ex-

tra modulation into part of the excitation pattern evoked by the target. This might be particularly important for flankers higher in frequency than the target, since changes in excitation level of the target are effectively magnified on the high-frequency side of the excitation pattern [20].

Consider the results shown in Fig. 1. There is a tendency for the amount of MDI to be greater for flankers centred above the target frequency (conditions 4–6) than for flankers centred below the target frequency (conditions 1–3). This is consistent with a role for within-channel processes. In addition, some studies have shown that the amount of MDI increases as the difference between the target and flankers carrier frequencies decreases [5, 11, 19]. This has been attributed partially to within-channel processes.

RICHARDSON *et al.* [16] studied MDI for users of cochlear implants. They found that thresholds for detecting amplitude modulation of signals applied to a single electrode were influenced by a masking modulation on a second electrode. In other words, a form of MDI occurred. For three of the four subjects, MDI increased with decreases in the spatial separation between the two electrodes. This presumably reflected an increasing overlap of the neural populations excited by the two electrodes.

In Fig. 1 we can see that CMR tends to be greater for multiple flankers centred below than above the target frequency. A possible explanation for this effect is as follows. To obtain maximum CMR, the coding of the target modulation may be more important than the coding of the modulation of any single flanker (provided that multiple flankers are present, to allow for some redundancy in the coding of the modulation of the flankers). When the flankers are all below the target frequency, the changes in excitation level produced by the target would be effectively magnified on the high-frequency side of the excitation pattern, and these magnified changes would not be affected by the flankers. This would lead to greater CMR than when the flankers are all above the target frequency. The effect in this case depends on both peripheral and central processes.

MOORE [8] has argued that CMR arises mainly from comparisons of the outputs of different auditory filters, but that these comparisons are made most effectively for filters that are reasonably closely spaced in centre frequency. If this is the case, it reflects an influence of peripheral processes on the central processes that lie at the heart of CMR.

4. Conclusions

It seems likely that MDI and CMR can be influenced both by peripheral within-channel processes and by central across-channel processes. The nature of these processes, and the way that they interact can be explored using relatively simple studies of the detection and discrimination of modulated sounds. We suggest that studies of MDI and CMR can be useful in clarifying the role of peripheral and central processes in hearing.

Acknowledgements

Preparation of this paper was supported by KBN. Grant 1HO1FO8012.

References

- [1] S.P. BACON and J.M. OPIE, *Monotic and dichotic modulation detection interference in practised and unpractised subjects*, J. Acoust. Soc. Am., **95**, 2637–2641 (1994).
- [2] A.S. BREGMAN, *Auditory scene analysis: The perceptual organization of sound*, The MIT Press, 1990.
- [3] J.W. HALL and J.H. GROSE, *Some effects of auditory grouping factors on modulation detection interference (MDI)*, J. Acoust. Soc. Am., **90**, 3028–3035 (1991).
- [4] J.W. HALL, M.P. HAGGARD and M.A. FERNANDES, *Detection in noise by spectro-temporal pattern analysis*, J. Acoust. Soc. Am., **76**, 50–56 (1984).
- [5] U. JORASZ, *Selektywność układu słuchowego*, Wydawnictwo Naukowe UAM, Poznań 1999.
- [6] U. JORASZ, *Wykłady z psychoakustyki*, Wydawnictwo Naukowe UAM, Poznań 1998.
- [7] L. MENDOZA, J.W. HALL and J.H. GROSE, *Within- and across- channel processes in modulation detection interference*, J. Acoust. Soc. Am., **97**, 3072–3079 (1995).
- [8] B.C.J. MOORE, *Across-channel processes in auditory masking*, J. Acoust. Soc. Jpn. (E), **13**, 25–37 (1992).
- [9] B.C.J. MOORE, *An introduction to the psychology of hearing* (4th ed.), London 1997.
- [10] B.C.J. MOORE [Ed.], *Hearing*, London 1995.
- [11] B.C.J. MOORE and U. JORASZ, *Detection of changes in modulation depth of a target sound in the presence of other modulated sounds*, J. Acoust. Soc. Am., **91**, 1051–1061 (1992).
- [12] B.C.J. MOORE and U. JORASZ, *Modulation discrimination interference and comodulation masking release as a function of the number and spectral placement of narrow-band noise modulators*, J. Acoust. Soc. Am., **100**, 2373–2381 (1996).
- [13] B.C.J. MOORE, A. SEK and M.J. SHAILER, *Modulation discrimination interference for narrow-band noise modulators*, J. Acoust. Soc. Am., **97**, 2493–2497 (1995).
- [14] B.C.J. MOORE and M.J. SHAILER, *Modulation discrimination interference and auditory grouping*, Phil. Trans. Roy. Soc. Lond. B, **336**, 339–346 (1992).
- [15] R.D. PATTERSON and B.C.J. MOORE, *Auditory filters and excitation patterns as representations of frequency resolution*, [in:] *Frequency Selectivity in Hearing*, B.C.J. MOORE [Ed.], Academic, London 1986.
- [16] L.M. RICHARDSON, P.A. BUSBY and G.M. CLARK, *Modulation detection interference in cochlear implant subjects*, J. Acoust. Soc. Am., **104**, 442–452 (1998).
- [17] G.P. SCHOONEVELDT and B.C.J. MOORE, *Comodulation masking release (CMR): Effects of signal frequency, flanking-band frequency, masker bandwidth, flanking-band level, and monotic versus dichotic presentation of the flanking band*, J. Acoust. Soc. Am., **82**, 1944–1956 (1987).
- [18] J.L. VERHEY, T. DAU and B. KOLLMEIER, *Within-channel cues in comodulation masking release (CMR): Experiments and model predictions using a modulation-filterbank model*, J. Acoust. Soc. Am., **106**, 2733–2745 (1999).
- [19] W.A. YOST and S. SHEFT, *Across-critical band processing of amplitude-modulated tones*, J. Acoust. Soc. Am., **85**, 848–857 (1989).
- [20] E. ZWICKER, *Masking and psychological excitation as consequences of the ear's frequency analysis*, [in:] *Frequency Analysis and Periodicity Detection in Hearing*, R. PLOMP, G.F. SMOORENBURG [Eds.], Sijthoff, Leiden 1970.

**THE EFFECT OF RATE CHANGES OF THE CONSTANT EXTERNAL
MAGNETIC FIELD ON THE COEFFICIENT OF ULTRASONIC WAVE
ABSORPTION IN POLYDISPERSIVE MAGNETIC FLUID**

A. JÓZEF CZAK, A. SKUMIEL and M. ŁABOWSKI

Institute of Acoustics
Adam Mickiewicz University
(60-769 Poznań, Jana Matejki 48/49, Poland)
e-mail: aras@amu.edu.pl

In this paper are presented experimental results of changes of the ultrasonic wave absorption coefficient as the function of external magnetic field intensity, for different rates of magnetic field changes in a polydisperse magnetic liquid EMG-605 based on water. Measurements were performed for two frequencies of ultrasonic wave: 3.6 MHz and 6.12 MHz, where the directions of propagation of ultrasonic wave and external magnetic field were mutually parallel and perpendicular. This paper presents also the radii of detected spherical clusters formed in magnetic fluid under the influence of magnetic field.

1. Introduction

A magnetic fluid is a colloidal suspension of polydisperse magnetic molecules, covered with a layer of surfactants in a liquid carrier [1]. This layer as well as thermal motions prevent the molecules from binding and their precipitation.

Influencing a polydisperse magnetic fluid, the external magnetic field changes some of its properties, among others its viscosity [2, 3], magnetic susceptibility [4], and the ultrasonic velocity in the magnetic fluids [7]. The reason for such changes is the binding, under the influence of a magnetic field, of single molecules and formation of spherical clusters [7, 8]. By measuring the changes of the ultrasonic wave absorption coefficient during the sweeps of magnetic field, it is possible to detect clusters formed in the magnetic fluid, as well as to determine their size by applying the resonance ultrasonic wave absorption [7].

The process of cluster formation in a magnetic fluid depends on the rate of changes of the external magnetic field [9]. The work presents experimental results of changes of the ultrasonic wave absorption coefficient as the function of external magnetic field intensity for different rates of magnetic field changes (different rates of “sweeping”). Besides, the sizes of spherical clusters formed in the magnetic field were also determined.

2. Resonance absorption of ultrasonic wave in a magnetic field

A spherical cluster formed in a magnetic fluid, of a magnetic moment m , placed in a magnetic field B , is subjected to the mechanical moment T aligning it with the direction of the magnetic field. This moment is balanced by the moment following from the Newton's second law for rotation:

$$T = mB \sin \varphi = -I \frac{d^2 \varphi}{dt^2}. \quad (1)$$

Thus we obtain:

$$\frac{d^2 \varphi}{dt^2} + \frac{mB}{I} \sin \varphi = 0, \quad (2)$$

but for $\varphi < 0.1$ radian, we may approximately assume that $\sin(\varphi) \approx \varphi$, and thus we obtain an equation of harmonic oscillator motion:

$$\frac{d^2 \varphi}{dt^2} + \omega_0^2 \varphi = 0, \quad (3)$$

where

$$\frac{\omega_0}{2\pi} = f_0 = \frac{1}{2\pi} \sqrt{\frac{mB}{I}}. \quad (4)$$

If the ultrasonic wave of the frequency f propagates in a magnetic fluid containing spherical clusters of the magnetic moment $m = VM_{cl}$ and the inertia moment $I = 2V\rho_{cl}r^2/5$, the energy of the wave is absorbed first by the translatory, and only then by the rotary degrees of freedom of the clusters.

If the magnetic fluid, in which an ultrasonic wave propagates, is subjected to a constant magnetic field of intensity changing from 0 to an undefined value, then at a certain value of magnetic induction B , the frequency of the ultrasonic wave f will be equal to the frequency of self-vibrations of clusters f_0 . This will result in ultrasonic resonance wave absorption by the rotary degrees of freedom, which is reflected by the maximum value of absorbancy. The formula of resonance cluster frequency is the following [7]:

$$f_0 = \frac{1}{2\pi r} \sqrt{\frac{5M_{cl}B}{2\rho_{cl}}}, \quad (5)$$

where M_{cl} — cluster magnetization, ρ_{cl} — cluster density, r — cluster radius. Using expression (5) we can determine the cluster radius in the form:

$$r = \frac{1}{2\pi f_0} \sqrt{\frac{5M_{cl}B}{2\rho_{cl}}}. \quad (6)$$

3. The measuring method

A diagram of the applied measuring system is shown in Fig. 1. The measurements of the changes of ultrasonic wave absorption coefficient were carried out by a pulse method using the MATEC instruments. The ultrasonic pulse propagating in the vessel

undergoes multiple reflections from the walls of the converters, due to which it is possible to record both the pulse and its subsequent echoes. So, two adjacent pulses are chosen, each following a different trajectory to reach the detector, from which signals proportional to their amplitudes are led to a logarithmic amplifier. A change of the initial intensity of the logarithmic amplifier is proportional to the changes of the coefficient of ultrasonic wave absorption of a given medium. A detailed description of this phenomenon is given in [7]. The system was lined up with a computer which at the same time performs the readout of the value of ultrasonic wave absorption coefficient and the value of the external magnetic field.

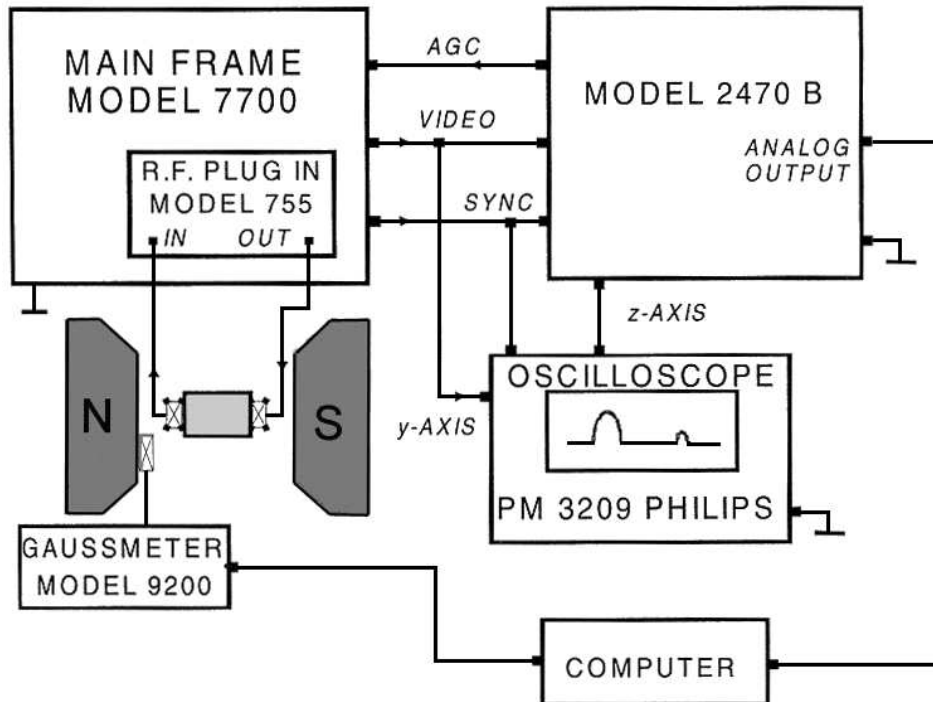


Fig. 1. A block diagram of the measuring system.

A slowly changing magnetic field was produced in the electromagnet which was controlled with a system of a programmed current generator. The system enabled automatic sweeps of a given range of a magnetic field at a given time.

4. Experimental results and their analysis

In our case, the studied medium was a magnetic liquid with a symbol of EMG-605 produced by Ferrofluidics Corporation. This liquid is based on water in which magnetite molecules of a 10 nm diameter, covered with layer of oleic acid, are suspended.

The measurements were carried out at the temperature of 20°C, for two frequencies of the ultrasonic wave: 3.6 MHz and 6.12 MHz. Experiments were performed for two cases: when the directions of propagation of the ultrasonic wave \mathbf{k} and external magnetic field \mathbf{H} were either parallel or perpendicular.

Figures 2 and 3 present the dependence of changes of the ultrasonic wave absorption coefficient as a function of external magnetic field intensity for different times t of sweeping of the magnetic field for frequencies 3.6 MHz and 6.12 MHz respectively, when the directions of ultrasonic wave propagation and external magnetic field overlap ($\mathbf{H} \parallel \mathbf{k}$). It follows from the figures that with the increase of intensity of the external magnetic field, the absorption coefficient increases too, and the character of the changes largely depends on the rate of changes of the magnetic field (the rate of sweeping t). For fast changes of magnetic field (a short rate of sweeping), the increase of absorption coefficient is probably caused by a classical processes, i.e. by changing viscosity of the ferroliquid. As the rate of the external magnetic field sweeping increases, the structure of fluid undergoes some changes too: in the magnetic field the clusters are formed, what is indicated by the appearance of maxima on the plots. For very slow changes, very clear maxima can be observed, which are a consequence of the resonance absorption of the ultrasonic wave by spherical clusters. For $f = 3.6$ MHz and $t = 50$ min, the average radius of the cluster $r = 210$ nm, while for $f = 6.12$ MHz and $t = 78.5$ min, $r = 98$ nm. The radii differ significantly, which indicates that in the magnetic field clusters of various sizes are formed. The above cluster radii were determined on the basis of formula (6).

Figures 4 and 5 are presenting the dependence of changes of the ultrasonic wave absorption coefficient in the function of external magnetic field intensity for different times t of sweeping of the magnetic field, for frequencies 3.6 MHz and 6.12 MHz respectively, when the direction of ultrasonic wave propagation is perpendicular to the direction of the external magnetic field ($\mathbf{H} \perp \mathbf{k}$). It can be noticed that, as in the previous case, with a decreasing rate of the changes of magnetic field the structure of liquid undergoes some changes, and for longer sweeping times the maxima appear as a result of resonance absorption of ultrasonic wave by spherical clusters. For $f = 3.6$ MHz and $t = 50$ min, the absorption should be attributed to clusters of the size ranging from 194–216 nm, while for the frequency $f = 6.12$ MHz and $t = 79.5$ — to the clusters of the average size $r = 92$ nm, as it follows from formula (6).

The revealed character of changes of the ultrasonic wave absorption coefficient as a function of external magnetic field intensity for perpendicular direction of ultrasonic wave propagation and magnetic field, differs from that observed for the parallel alignment. These results confirm the anisotropic character of magnetic fluid.

For a given frequency f and a given time t of the magnetic field sweeping and with the use of the method of resonance absorption of ultrasonic wave, spherical clusters of almost the same size (within the limit of an error) were found both for the perpendicular and parallel directions of propagation of ultrasonic wave and magnetic field. This confirms the effectiveness of the method presented in the paper [7].

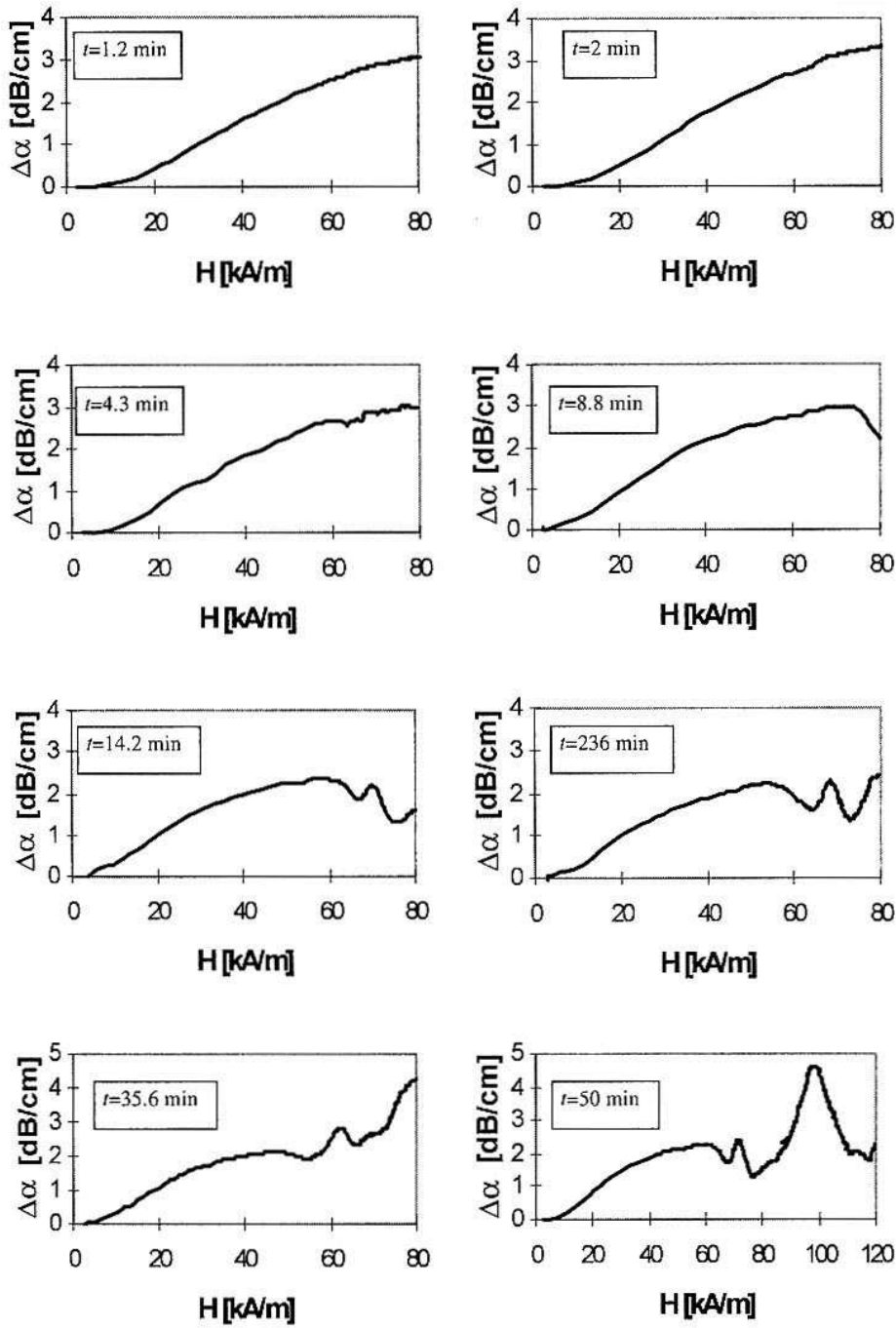


Fig. 2. Dependence of changes $\Delta\alpha$ of ultrasonic wave of the frequency $f = 3.6$ MHz as a function of magnetic field intensity H , where $H \parallel k$.

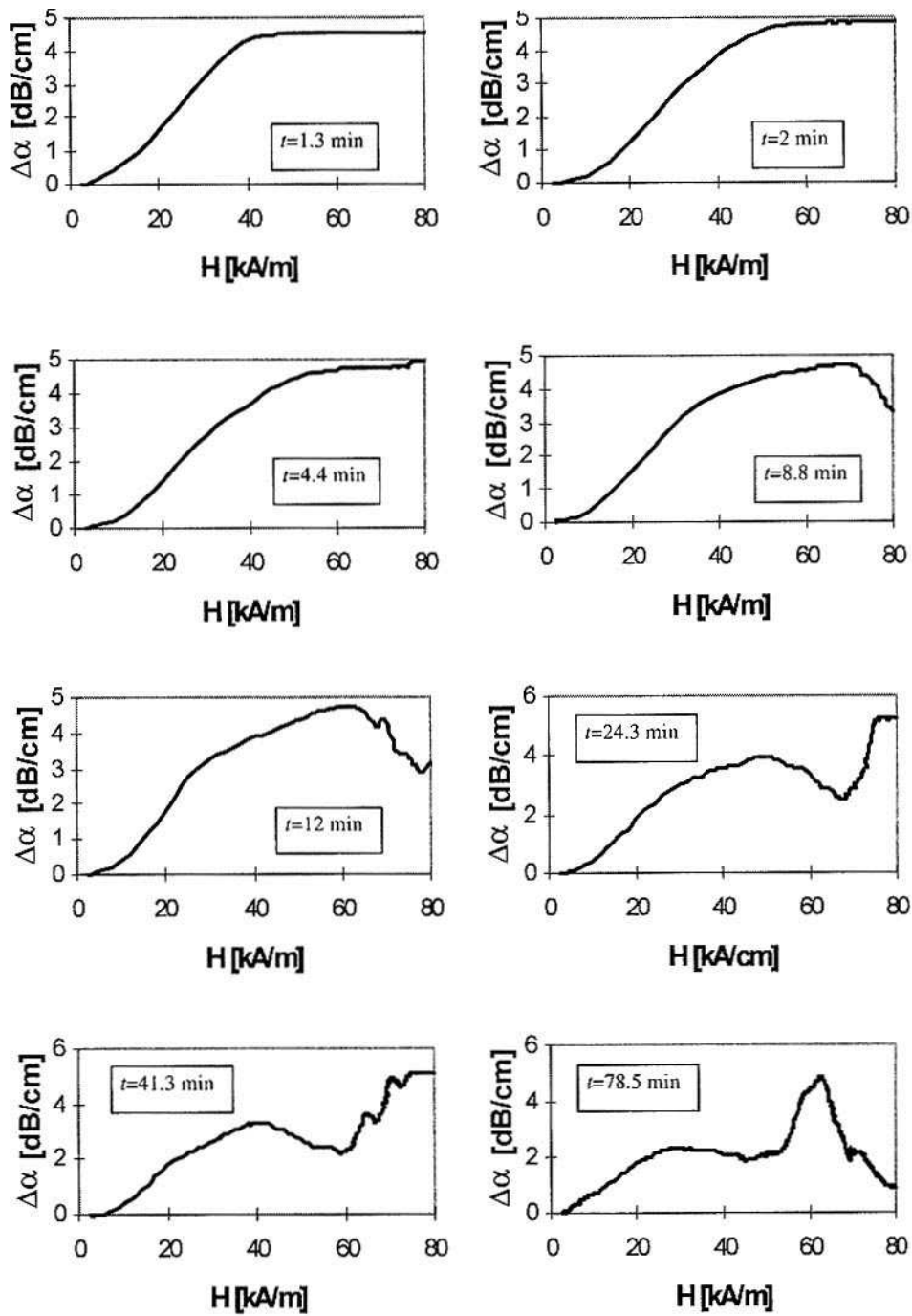


Fig. 3. Dependence of changes $\Delta\alpha$ of ultrasonic wave of the frequency $f = 6.12$ MHz as a function of magnetic field intensity H , where $H \parallel k$.

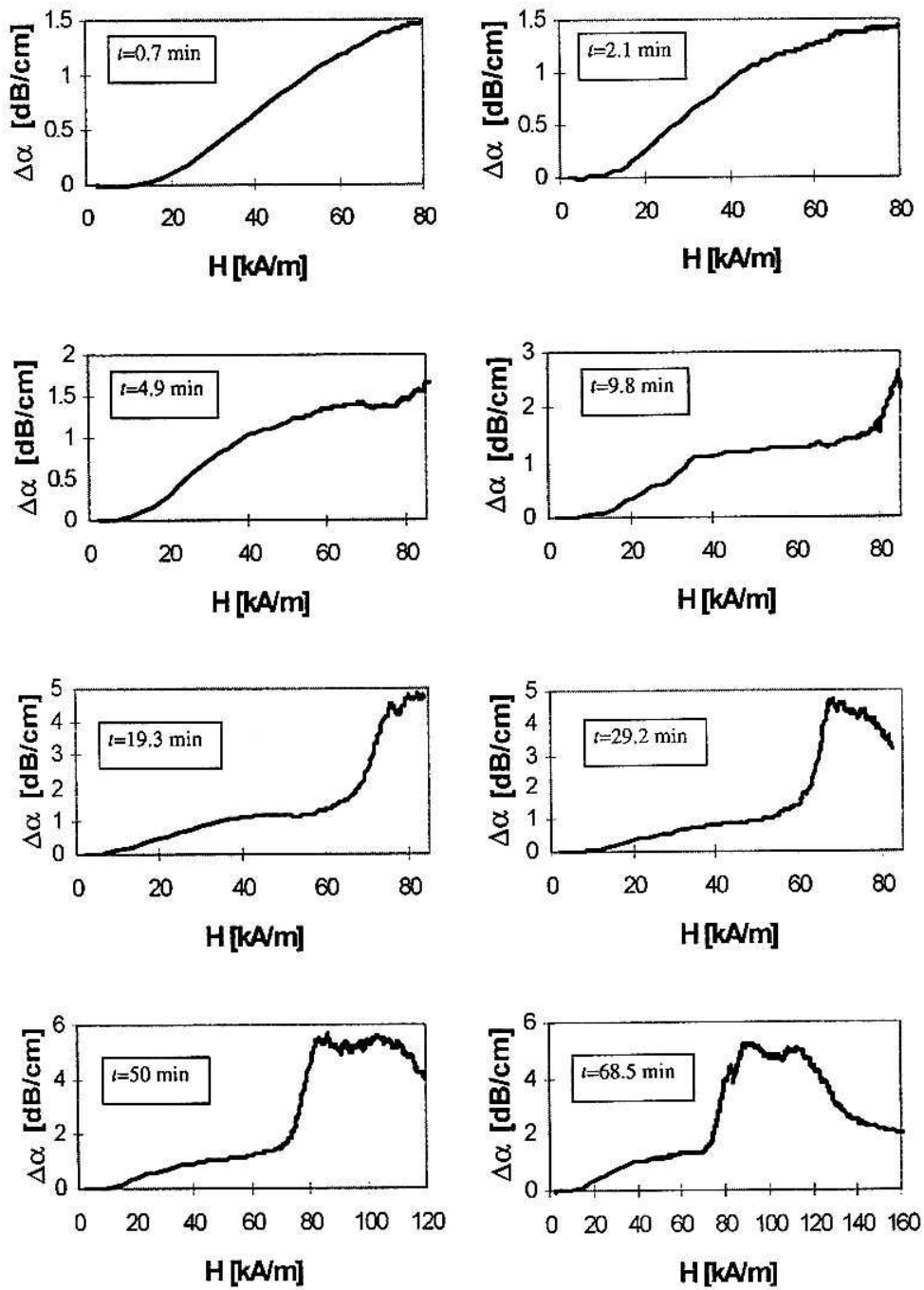


Fig. 4. Dependence of changes $\Delta\alpha$ of ultrasonic wave of the frequency $f = 3.6$ MHz as a function of magnetic field intensity H where $H \perp k$.

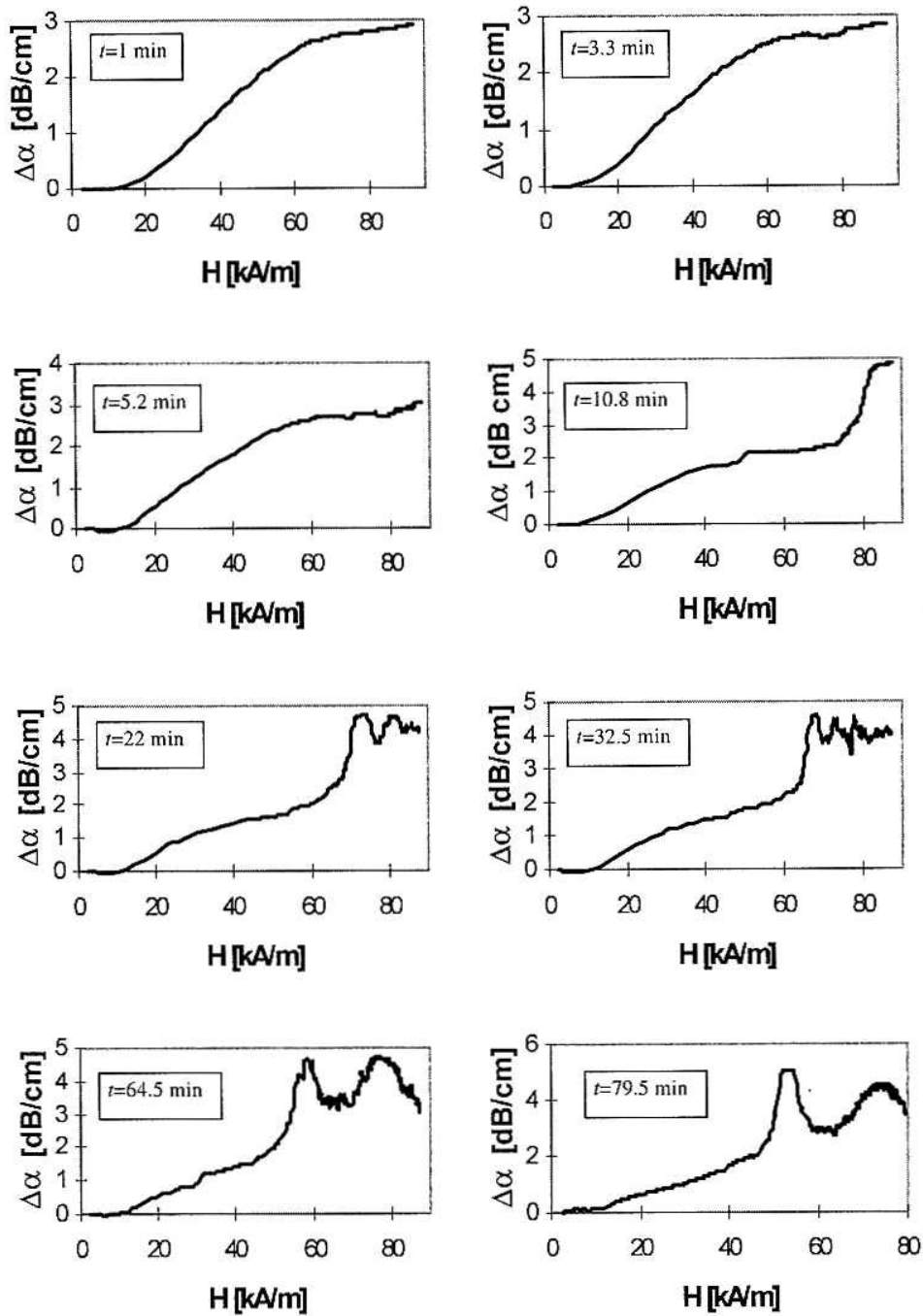


Fig. 5. Dependence of changes $\Delta\alpha$ of ultrasonic wave of the frequency $f = 6.12$ MHz as a function of magnetic field intensity H where $H \perp k$.

5. Summary

A polydisperse fluid is an anisotropic medium, the structure of which changes under the influence of a variable magnetic field. These changes depend on the rate of magnetic field changes: the slower are the changes of the magnetic field, the greater will be the transformations of the structure. This process was recorded in order to study the dependence of the coefficient of ultrasonic wave absorption as a function of the intensity of external magnetic field, for different rates of its sweeps.

When performing these measurements it was also possible to detect spherical clusters formed in the liquid as well as to determine their size. In the studied fluid, clusters of a radius ranging from 92–98 nm and 194–216 nm were found.

Acknowledgement

This work was supported by grant 2P03B 079 12 from the Polish Committee for Scientific Research.

References

- [1] R.W. ROSENSWEIG, *Ferrohydrodynamics*, Cambridge University Press (1985).
- [2] R.W. ROSENSWEIG, "Negative viscosity" in a magnetic fluid, *Science*, **271**, 614–615 (1996).
- [3] M.S. KRAKOV, *Damping ability of magnetic fluid shock-absorber*, Proceedings of the International Symposium on Hydrodynamics of Magnetic Fluids and its Applications, Sendai, 100–103 (1997).
- [4] P.C. FANNIN, B.K.P. SCAIFE and S.W. CHARLES, *The field dependence of the complex frequency-dependent susceptibility of magnetic fluids*, *J. Phys. D: Appl. Phys.*, **21**, 533–534 (1988).
- [5] D.Y. CHUNG and W.E. ISLER, *Ultrasonic velocity anisotropy in ferrofluids under the influence of a magnetic field*, *J. Appl. Phys.*, **49**, 1809–1811 (1978).
- [6] K. IMANO and H. INOUE, *Measurement of acoustic properties of magnetic fluid and its application to nondestructive evaluation*, *Jpn. J. Appl. Phys.*, **33**, 3208–3211 (1994).
- [7] A. SKUMIEL, M. ŁABOWSKI and A. JÓZEF CZAK, *Resonance absorption of ultrasonic waves in a magnetic fluid*, *Arch. Acoust.*, **23**, 195–210 (1998).
- [8] V.V. GOGOSOV, S.I. MARTINOV, S.N. TSURIKOV and G.A. SHAPOSHNIKOVA, *Ultrasound propagation in a magnetic fluid*, *Magn. Gidrodin.*, **2**, 19–27 (1987).
- [9] J. CERNAK and P. MACKO, *The time dependence of particle agglomeration in magnetic fluid layers*, *J. Magn. Magn. Mater.*, **123**, 107–116 (1993).

NONLINEAR DYNAMICS OF DIRECTED ACOUSTIC WAVES IN STRATIFIED AND HOMOGENEOUS LIQUIDS AND GASES WITH ARBITRARY EQUATION OF STATE

A. PERELOMOVA

Technical University of Gdańsk
(80-952 Gdańsk, G. Narutowicza 11/12, Poland)
e-mail: anpe@mifgate.gda.pl

A method of separating one-dimensional disturbances into components propagating upwards and downwards and the stationary one in a stratified medium was developed. The system of equations is split into three coupled nonlinear equations of interacting components. Weak nonlinear evolution formulae for the directed and stationary components of a medium with an arbitrary equation of state were obtained. The wave components treated by the numerical calculations keep their propagation direction, even for quite large initial amplitudes. The results of the numerical simulation are presented. The examples demonstrate a nonlinear evolution of the wave propagating downwards for both the models of the atmosphere: the exponentially stratified model and the homogeneous one.

1. The problem of separating the directed and stationary modes

The problem of separating gasdynamical field components comes from the adaptation and initialization problems in Geophysics [1–3]. The common way of separating is to share branches of the dispersion relation. In this way it is possible to separate, for example, acoustic, internal gravity and Rossby waves in the atmosphere. Every wave mode possesses a certain range of frequencies and corresponding group velocities [1, 2]. In the one-dimensional atmosphere model only acoustic wave modes can propagate.

Frequently, a particular direction of propagation is under consideration. This problem has many aspects, as for instance to separate the overall field into stationary and up- or down- moving components at any instant, or to choose initial conditions for one directed mode preferable generation and so on. The close problem is the transport of energy in one direction predominantly by a special selection of initial conditions.

The main aim of the linear problem is to pick up terms in the Fourier transformation corresponding to the signs of ω and k : the same signs for the down-moving component and opposite signs for the up-moving one (or left- and rightwards in a homogeneous medium, where the basic scheme looks quite simple). At first, we get connections between the independent variables (for example, p , ρ , v) in the (k, ω) -representation, and then we just obtain connections in the (r, t) -representation. For the stationary part, one should

treat the components with $\omega = 0$. In this way, the overall wave motion is separated into components of a chosen direction or a stationary one.

The problem can be solved exactly in the case of linear dynamics: the basic system leads to three independent evolution equations for every mode. In the nonlinear problem, the modes obviously interact and, in general, one can't separate strictly the directed components from the stationary one. Thus, the method of the weak nonlinear problem arises consisting in acting projectors to the basic nonlinear system and getting coupled nonlinear evolution equations for the "nearly" directed and stationary modes. These equations may be simplified under certain conditions, for example, in the case of self-action only, if one mode was previously excited. In this case, we go on to the evolution equation for any gasdynamical variable of the selected mode taking into account connections between (p, ρ, v) for this mode obtained before. This is a general scheme.

2. Inhomogeneous gas and liquid affected by gravity

2.1. The dispersion relation and connection equations

The basic system of equations contains: the second Newton's law and the equations of mass and energy conservation in the differential form with gravitational force being taken into account:

$$\begin{aligned} \partial v / \partial t + v \partial v / \partial r + (1/\rho) \partial p / \partial r + g &= 0, \\ \partial \varepsilon / \partial t + v \partial \varepsilon / \partial r + (p/\rho) \partial v / \partial r &= 0, \\ \partial \rho / \partial t + \partial(\rho v) / \partial r &= 0. \end{aligned} \quad (2.1)$$

The above equations should be completed with the caloric equation of state $\varepsilon = \varepsilon(p, \rho)$, where r -coordinate (height over the Earth surface), t — time, ρ , p , ε , v — mass density, pressure, internal energy per mass unit and velocity, respectively, g — the gravity acceleration. The problem is to exclude ε from the system (2.1). Let a small change of the energy density for any stratified media has the general form:

$$\begin{aligned} \rho_0(\varepsilon - \varepsilon_0) = A(p - p_0) + B(\rho - \rho_0) + A1(p - p_0)^2/p_0 + B1(\rho - \rho_0)^2/\rho_0 \\ + D(p - p_0)(\rho - \rho_0)/\rho_0. \end{aligned} \quad (2.2)$$

The undisturbed values are marked by zero. Let also the undisturbed medium be exponentially density stratified:

$$\rho_0(r) = \rho_{00} \exp(-r/h), \quad p_0(r) = p_{00} \exp(-r/h) = \rho_{00}gh \exp(-r/h),$$

where p_{00} and ρ_{00} are the values on the Earth surface, h is the scale height of the medium, $p_{00} = \rho_{00}gh$ is a consequence of the stationary equation $\partial p_0(r)/\partial r = -\rho_0(r)g$. The corresponding Fourier components for the perturbations in an exponentially stratified medium are written in the form:

$$\tilde{v}'(k) \exp(r/2h + \alpha r) \exp(i(\omega t - kr)),$$

$$\begin{aligned} &\tilde{p}'(k) \exp(-r/2h + \alpha r) \exp(i(\omega t - kr)), \\ &\tilde{\rho}'(k) \exp(-r/2h + \alpha r) \exp(i(\omega t - kr)). \end{aligned}$$

Here and later the disturbed values are primed. The way of the dispersion relation obtaining from the linear analogue of (2.1) is quite clear [4–6]; the final expressions are:

$$\begin{aligned} \omega^2 &= k^2(gh - B)/A + g^2(A + 1)^2/(4A(gh - B)) \quad \text{or} \quad \omega = 0, \\ \alpha &= -(Agh + B)/(2h(gh - B)). \end{aligned} \tag{2.3}$$

Both signs of the frequency roots and the zero solution yield the ability of three independent types of the linear wave motion. We propose to distinguish three independent modes: the up-propagating one, the down-propagating one, and the stationary one in the overall wave motion by the complete set of orthogonal projection operators. This is convenient from the physical point of view because the projection procedure may be performed by certain calculations at any moment of the evolution.

The main steps of the derivation of equations waves directed vertically are as follows from [5–7]. First of all, taking into account the dispersion relation (2.3), one can obtain equations connecting the Fourier-components of the perturbed variables

$$\begin{aligned} \tilde{p}'(k) &= \frac{-i\rho_{00} [g(ik + 1/2h - \alpha) - \omega^2]}{\omega(ik + 1/2h - \alpha)} \tilde{v}'(k), \\ \tilde{\rho}'(k) &= \frac{-i\rho_{00}(ik + 1/2h - \alpha)}{\omega} \tilde{v}'(k). \end{aligned} \tag{2.4}$$

Now, keeping in the Fourier-transformation of each gasdynamic variable the terms corresponding to the same (the upwards directed mode) or to different (downwards directed one) sign of ω and k or $\omega = 0$ (the stationary one), one can get the connection equations for each couple of variables in the (r, t) -representation.

Let

$$\tilde{\tilde{v}}'(k, t) = \tilde{v}'(k) \exp \left[i \sqrt{\frac{gh - B}{A} k^2 + \frac{g^2(A + 1)^2}{4A(gh - B)} t} \right].$$

Then

$$v'(r, t) \exp(-r/2h - \alpha r) = \int_{-\infty}^{\infty} \tilde{\tilde{v}}'(k, t) \exp(-ikr) dk + c.c.$$

is a common Fourier-transformation, which leads to the overall field disturbance that is presented as the sum of the upwards and downwards components, while the stationary component of the velocity equals obviously to zero. The expressions for the rightwards wave perturbations are as follows:

$$\begin{aligned} v_+(r, t) &\equiv v'_{\text{up}}(r, t) \exp(-r/2h - \alpha r) = \int_{-\infty}^{\infty} \tilde{\tilde{v}}'(k, t) \theta(k) \exp(-ikr) dk + c.c., \\ p_+(r, t) &\equiv p'_{\text{up}}(r, t) \exp(r/2h - \alpha r) = \int_{-\infty}^{\infty} \tilde{\tilde{v}}'(k, t) F1(k) \theta(k) \exp(-ikr) dk + c.c., \end{aligned}$$

$$\rho_+(r, t) \equiv \rho'_{\text{up}}(r, t) \exp(r/2h - \alpha r) = \int_{-\infty}^{\infty} \tilde{v}'(k, t) F2(k) \theta(k) \exp(-ikr) dk + \text{c.c.}, \quad (2.5)$$

$$F1(k) = \frac{-i\rho_{00} [g(ik + 1/2h - \alpha) - (k^2(gh - B)/A + g^2(A + 1)^2 / [4A(gh - B)])]}{(ik + 1/2h - \alpha) \sqrt{k^2(gh - B)/A + g^2(A + 1)^2 / [4A(gh - B)]}},$$

$$F2(k) = \frac{-i\rho_{00}(ik + 1/2h - \alpha)}{\sqrt{k^2(gh - B)/A + g^2(A + 1)^2 / [4A(gh - B)]}},$$

where

$$\theta(k) = \begin{cases} 1, & k > 0, \\ 0, & k \leq 0. \end{cases}$$

Therefore, only the components corresponding to different signs of ω and k are left. The dispersion relation (2.3) and the connections (2.4) have been taken into account.

Just the same formulae apply to the leftwards component with $\theta(-k)$ instead of $\theta(k)$. At last, an inverse connection should be used:

$$\tilde{v}'(k, t) = \frac{1}{2\pi} \int_{-\infty}^{\infty} v'(r, t) \exp(-r/2h - \alpha r) \exp(ikr) dk + \text{c.c.}.$$

After substitution this equation to (2.5), the final connections in the (r, t) -representation are obtained:

$$p_+ = L1v_+, \quad \rho_+ = L2v_+, \quad p_- = -L1v_-, \quad \rho_- = -L2v_-, \quad \rho_{\text{stat}} = L3p_{\text{stat}}. \quad (2.6)$$

For the stationary component a mass density or pressure should be designed since the velocity component equals to zero:

$$\tilde{\rho}' = \frac{(ik + 1/2h - \alpha)}{g} \tilde{p}'(k).$$

The integrodifferential operators $L1, L2, L3$ have the form:

$$L3 = (1 - 2\alpha h - 2h\partial/\partial r)/(2gh),$$

$$L1 = \rho_{00}/(\pi\sqrt{(gh - B)/A}) \int_{-\infty}^{\infty} dr' \left\{ -\frac{gh - B}{A} F_{AB}(r - r') \partial/\partial r' + \frac{g(A - 1)}{2A} F_{AB}(r' - r) \right\},$$

$$L2 = \rho_{00}/(\pi\sqrt{(gh - B)/A}) \int_{-\infty}^{\infty} dr' F_{AB}(r - r') \left\{ -\partial/\partial r' + \frac{g(A + 1)}{2(gh - B)} \right\},$$

$$F_{AB}(r) = \int_0^{\infty} \frac{\sin(kr) dk}{\sqrt{k^2 + \left[\frac{g(A + 1)}{2(gh - B)} \right]^2}} = \frac{\pi}{2} \left[I_0 \left(r \frac{g(A + 1)}{2(gh - B)} \right) - L_0 \left(r \frac{g(A + 1)}{2(gh - B)} \right) \right],$$

where I_0, L_0 — the modified Bessel function of zero order and the Struve function, respectively.

Then, using (2.6), from the first equation of (2.1) we also get the linear evolution equations for the upwards and downwards directed waves:

$$\partial v_{\pm} / \partial t \pm \sqrt{\frac{gh - B}{\pi^2 A}} \int_{-\infty}^{\infty} \left\{ v_{\pm r' r'} - \frac{g^2(A + 1)^2}{4(gh - B)^2} v_{\pm} \right\} F_{AB}(r - r') dr' = 0. \quad (2.7)$$

The evolution equations could be obtained for p_{\pm} and ρ_{\pm} from the second and third equations (2.1) and the relations (2.6); they look just the same. The acoustic field separation is mathematically unique and may be proceeded at any instant of the evolution.

2.2. Projectors

It seems more convenient to use variables $v'_s = v'(r, t) \exp(-r/2h - \alpha r)$, $p'_s = p'(r, t) \exp(r/2h - \alpha r)$, and $\rho'_s = \rho'(r, t) \exp(r/2h - \alpha r)$ instead of v' , p' , and ρ' . Following the relations (2.6), a matrix \mathbf{M} should be determined:

$$\begin{pmatrix} v'_s \\ p'_s \\ \rho'_s \end{pmatrix} \equiv \begin{pmatrix} v_+ + v_- \\ p_+ + p_- + p_{\text{stat}} \\ \rho_+ + \rho_- + \rho_{\text{stat}} \end{pmatrix} = \mathbf{M} \begin{pmatrix} v_+ \\ v_- \\ \rho_{\text{stat}} \end{pmatrix},$$

and also

$$\mathbf{M}^{-1} : \mathbf{M} = \begin{pmatrix} 1 & 1 & 0 \\ L1 & -L1 & L3 \\ L2 & -L2 & 1 \end{pmatrix}, \quad \mathbf{M}^{-1} = \begin{pmatrix} 1/2 & l1 & l2 \\ 1/2 & -l1 & -l2 \\ 0 & l3 & l4 \end{pmatrix},$$

from which the projectors follow immediately.

Now we present the new formulae taking into account the energy density decomposition (2.2):

$$\mathbf{P}_{\pm} = \begin{pmatrix} 1/2 & \pm l1 & \pm l2 \\ \pm L1/2 & L1l1 & L1l2 \\ \pm L2/2 & L2l1 & L2l2 \end{pmatrix}, \quad \mathbf{P}_{\text{stat}} = \begin{pmatrix} 0 & 0 & 0 \\ 0 & l3 & l4 \\ 0 & L3l3 & L3l4 \end{pmatrix}, \quad (2.8)$$

where

$$K_- = \int_{-\infty}^r dr' \exp \left[(r' - r) \frac{g(A + 1)}{2(gh - B)} \right],$$

$$K_+ = \int_r^{\infty} dr' \exp \left[-(r' - r) \frac{g(A + 1)}{2(gh - B)} \right],$$

$$l1 = 1 / \left(2\rho_{00}\pi\sqrt{(gh - B)/A} \right) \times \int_{-\infty}^{\infty} dr' F_{AB}(r - r') \left\{ -\partial/\partial r' + \frac{g(A + 1)}{2(gh - B)} \right\},$$

$$\begin{aligned}
l_2 &= -g / \left(2\rho_{00}\pi\sqrt{(gh-B)/A} \right) \times \int_{-\infty}^{\infty} dr' F_{AB}(r-r'), \\
l_3 &= \frac{Ag}{gh-B} K_-, \\
l_4 &= \frac{g}{A+1} K_+ - \frac{gA}{A+1} K_-, \\
L1l1 &= \frac{1}{2} - \frac{Ag}{2(gh-B)} K_-, \\
L2l1 &= \frac{A}{2(gh-B)} - \frac{A(A+1)g}{2(gh-B)^2} K_-, \\
L1l2 &= -\frac{g}{2(A+1)} K_+ + \frac{gA}{2(A+1)} K_-, \\
L2l2 &= \frac{Ag}{2(gh-B)} K_-, \\
L3l3 &= -\frac{A}{gh-B} + \frac{Ag(A+1)}{2(gh-B)^2} K_-, \\
L3l4 &= 1 - \frac{Ag}{(gh-B)} K_-;
\end{aligned}$$

$L1$, $L2$, $L3$ have been determined earlier. For the inverse matrix \mathbf{M}^{-1} and the projector element derivation, the equation

$$\int_{-\infty}^{\infty} F_{AB}(r'-r) \left(\frac{\partial^2}{\partial r^2} - \left[\frac{g(A+1)}{2(gh-B)} \right]^2 \right) F_{AB}(r-r'') dr = \pi^2 \delta(r'-r'')$$

was used.

The operators (2.8) obtained have the ordinary properties of projectors:

$$P_- + P_+ + P_{\text{stat}} = \tilde{\mathbf{I}}, \quad P_- P_+ = P_- P_{\text{stat}} = \dots = \tilde{\mathbf{0}}, \quad P_- = P_- P_- , \dots,$$

where $\tilde{\mathbf{I}}$ and $\tilde{\mathbf{0}}$ are unit and zero matrices. For example, in order to obtain the upwards propagating component at any instant, it is sufficient to apply P_+ on the total field:

$$P_+ \begin{pmatrix} v'(r,t) \exp(-r/2h - \alpha r) \\ p'(r,t) \exp(r/2h - \alpha r) \\ \rho'(r,t) \exp(r/2h - \alpha r) \end{pmatrix} \equiv P_+ \begin{pmatrix} v'_s(r,t) \\ p'_s(r,t) \\ \rho'_s(r,t) \end{pmatrix} = \begin{pmatrix} v_+(r,t) \\ p_+(r,t) \\ \rho_+(r,t) \end{pmatrix}.$$

One can see that the operators depend only on the coefficients A , B . It follows from the linearized caloric equation of state. This is quite clear because the operators are obtained in fact from linear gasdynamic equations. Let us stress, that the stratified medium is strongly dispersive, but the projectors are got explicitly in the dispersive linear problem. So, one can calculate every disturbance evolution without any restriction of its extent.

2.3. Nonlinear evolution of directed waves

By letting P_- , P_+ or P_{stat} act on the complete system of nonlinear equations (2.1) we obtain new evolution equations which account for the interaction between modes which is a generalization of (2.7). It will be useful to write on the system (2.1), separated into the linear left-hand side and the nonlinear right-hand side involving the second-order terms, only in (v'_s, p'_s, ρ'_s) -variables:

$$\begin{pmatrix} \frac{\partial v'_s}{\partial t} + \frac{(\partial/\partial r + \alpha - 1/2h)p'_s}{\rho_{00}} + \frac{g\rho'_s}{\rho_{00}} \\ \frac{\partial p'_s}{\partial t} + \rho_{00} \frac{(p_{00}/\rho_{00} - B)}{A} \frac{\partial v'_s}{\partial r} + \frac{\rho_{00} B v'_s}{Ah} \\ \frac{\partial \rho'_s}{\partial t} + \rho_{00}(\partial/\partial r + \alpha - 1/2h)v'_s \end{pmatrix} = \exp(r(\alpha + 1/2h))$$

$$\times \begin{pmatrix} -v'_s \left(\frac{\partial}{\partial r} + \alpha + \frac{1}{2h} \right) v'_s + \frac{\rho'_s}{\rho_{00}^2} \left(\frac{\partial}{\partial r} + \alpha - \frac{1}{2h} \right) p'_s \\ v'_s \left[\left(-\frac{\partial}{\partial r} + \frac{1}{2h} - \alpha + \frac{2A1B}{Agh} - A - D \right) p'_s + \frac{DB}{A} - \frac{B - 2B1}{Ah} \rho'_s \right] \\ - \frac{p'_s \left(\frac{2A1c^2}{gh} + D - 1 \right) + \rho'_s (B + 2B1 + c^2D + gh)}{A} \left(\frac{\partial}{\partial r} + \frac{1}{2h} + \alpha \right) v'_s \\ -v'_s \left(\frac{\partial}{\partial r} + \alpha \right) \rho'_s - \rho'_s \left(\frac{\partial}{\partial r} + \alpha \right) v'_s \end{pmatrix}. \quad (2.9)$$

Then, the projector (P_- or P_+) acting on both sides of (2.9) with the non-zero right side results in the non-zero nonlinear right-hand side of the evolution equation (2.7) for the corresponding directed mode. The evolution nonlinear equations for the upwards and downwards velocity are as follows:

$$\begin{aligned} \partial v_{\pm}/\partial t \pm \sqrt{\frac{gh - B}{\pi^2 A}} \int_{-\infty}^{\infty} \left\{ v_{\pm r' r'} - \frac{g^2(A + 1)^2}{4(gh - B)^2} v_{\pm} \right\} F_{AB}(r - r') dr \\ = (l/2 \pm l1 \pm l2) \exp(r(\alpha + 1/2h)) \end{aligned}$$

$$\times \begin{pmatrix} -v'_s \left(\frac{\partial}{\partial r} + \alpha + \frac{1}{2h} \right) v'_s + \frac{\rho'_s}{\rho_{00}^2} \left(\frac{\partial}{\partial r} + \alpha - \frac{1}{2h} \right) p'_s \\ v'_s \left[\left(\frac{\partial}{\partial r} + \frac{1}{2h} - \alpha + \frac{2A1B}{Agh} - A - D \right) p'_s + \frac{DB}{A} - \frac{B - 2B1}{Ah} \rho'_s \right] \\ \frac{p'_s \left(\frac{2A1c^2}{gh} + D - 1 \right) + \rho'_s (B + 2B1 + c^2 D + gh)}{A} \left(\frac{\partial}{\partial r} + \frac{1}{2h} + \alpha \right) v'_s \\ -v'_s \left(\frac{\partial}{\partial r} + \alpha \right) \rho'_s - \rho'_s \left(\frac{\partial}{\partial r} + \alpha \right) v'_s \end{pmatrix}. \quad (2.10)$$

Similar equations can be derived for the pressure and density. The nonlinear right-hand side can be further simplified, for example, by ignoring the upwards propagating and the stationary inputs of the nonlinear evolution of the “downwards directed” disturbances [7, 8]. That corresponds to the case of self-interaction only. The numeric calculations have been performed and proved that upwards and stationary modes caused by “downwards” initial disturbances are of a considerably smaller amplitude than that of the initial one. Thus, it is reasonable to use only the self-acting right-hand side for the approximate investigation of the concrete excited initially mode evolution.

But if the disturbance includes some modes of nearly equal amplitudes, one should take into account all terms of the right-hand nonlinear side. In this way the reciprocal influence of the generated modes on the initial one can be studied as well. Generally, the nonlinear evolution equations are coupled, because the nonlinear vector includes all inputs of the modes. There are three coupled nonlinear equations which could be written in any basic variables: ρ_+ , ρ_- , ρ_{stat} , for example, p_+ , p_- , ρ_{stat} or v_+ , v_- , ρ_{stat} .

3. Homogeneous media

3.1. Dispersion relation and connection equations

In the case of a homogeneous medium (liquid or gas), the formulae become quite simple. At first, the background pressure and density are constants now independent on r . The corresponding Fourier-components of the perturbations are presented as $\tilde{v}'(k) \exp(i(\omega t - kr))$, $\tilde{p}'(k) \exp(i(\omega t - kr))$, and $\tilde{\rho}'(k) \exp(i(\omega t - kr))$; the background pressure and density are equal to constants: $p_0 = p_{00}$, $\rho_0 = \rho_{00}$. Similarly, $\rho_{\pm} = \pm L2v_{\pm}$ and $p_{\pm} = \pm L1v_{\pm}$. The dispersion relation has the form: $\omega^2 = k^2((p_0/\rho_0) - B)/A$ or $\omega = 0$. There is no dispersion now, the group and phase velocities are equal to $c = (p_0/\rho_0 - B)/A)^{1/2}$ respectively. Expressions for the corresponding operators can be got directly from the previous formulae by going to the limits: $h \rightarrow \infty$, $g \rightarrow 0$, $gh \rightarrow p_0/\rho_0$, $\alpha \rightarrow 0$ which leads to $L1 = \rho_0 c$, $L2 = \rho_0/c$ and $l1 = 1/2\rho_0 c$, $l2 = 0$. A new connection of the stationary components takes place: $p_{\text{stat}} = L\rho_{\text{stat}} = 0$, thus $L = 0$. The

operator chosen in this way is inverse to $L3$. In the case of the homogeneous medium, it seems natural to consider the directed waves as propagating leftwards and rightwards.

Therefore, there exist only two pressure components in a homogeneous medium, the leftwards component and rightwards one, in contrast to the stratified medium. The three density components exist in both cases. One could also get the primitive linear evolutionary equations for the directed waves:

$$\partial v_{\pm} / \partial t \pm c \partial v_{\pm} / \partial r = 0.$$

Finally, v_{\pm} , p_{\pm} , ρ_{\pm} , ρ_{stat} are corresponding parts of the usual variables.

3.2. Projectors and nonlinear evolution of directed waves

Their elements are not integrodifferential operators, but numbers:

$$P_{\pm} = \begin{pmatrix} 1/2 & \pm 1/(2L1) & 0 \\ \pm L1/2 & 1/2 & 0 \\ \pm L2/2 & L2/(2L1) & 0 \end{pmatrix}, \quad P_{stat} = \begin{pmatrix} 0 & 0 & 0 \\ 0 & 0 & 0 \\ 0 & -L2/L1 & 1 \end{pmatrix}.$$

The common properties of orthogonal operators are retained, too. Let us put in this case an analogue of (2.9):

$$\begin{pmatrix} \frac{\partial v'}{\partial t} + \frac{\partial p' / \partial r}{\rho_0} \\ \frac{\partial p'}{\partial t} + \rho_0 c^2 \frac{\partial v'}{\partial r} \\ \frac{\partial \rho'}{\partial t} + \rho_0 \frac{\partial v'}{\partial r} \\ -v' \frac{\partial}{\partial r} v' + \frac{\rho'}{\rho_0^2} \frac{\partial}{\partial r} p' \end{pmatrix} = \begin{pmatrix} -v' \frac{\partial}{\partial r} p' + \frac{\partial v'}{\partial r} \frac{[p'(-1 + D + 2A1c^2 \rho_0 / p_0) + \rho'(p_0 / \rho_0 + Dc^2 + 2B1 + B)]}{A} \\ -v' \frac{\partial}{\partial r} \rho' - \rho' \frac{\partial}{\partial r} v' \end{pmatrix}.$$

The evolution nonlinear equation for the upwards and downwards velocity is:

$$\partial v_{\pm} / \partial t \pm c \partial v_{\pm} / \partial r = \begin{pmatrix} \frac{1}{2} & \pm \frac{1}{2\rho_0 c} & 0 \\ -v' \frac{\partial}{\partial r} v' + \frac{\rho'}{\rho_0^2} \frac{\partial}{\partial r} p' \\ -v' \frac{\partial}{\partial r} p' + \frac{\partial v'}{\partial r} \frac{[p'(-1 + D + 2A1c^2 \rho_0 / p_0) + \rho'(p_0 / \rho_0 + Dc^2 + 2B1 + B)]}{A} \\ -v' \frac{\partial}{\partial r} \rho' - \rho' \frac{\partial}{\partial r} v' \end{pmatrix}.$$

4. Applications of the theory

4.1. Application of the theory to gas and liquid dynamics

Since the equation of state is taken in the general form depending on the coefficients A , B , $A1$, $B1$, D of (2.2), the theory may be applied to both gases and liquids with an arbitrary caloric equation of state. Besides of these coefficients, the background values of pressure and mass density are needed. The right-hand nonlinear vector may be completed by viscous and dispersive terms of the order of nonlinear ones. Since the viscous term depends on temperature, a thermal equation of state (that decomposition looks like (2.2)) $T(p, \rho)$ should be involved in the basic system.

4.2. Homogeneous and exponentially stratified atmosphere

For an ideal atmospheric gas the problem becomes quite simple. In this case, $\varepsilon = p/(\rho(\gamma - 1))$, $A = 1/(\gamma - 1)$, $B = -gh/(\gamma - 1)$, $A1 = 0$, $B1 = -B$, $D = -A$, $\alpha = 0$, and the same can be applied in the stratified and homogeneous cases putting p_0/ρ_0 instead of gh . Here $\gamma = C_p/C_v$ is the ratio of specific heats.

Then, the evolution equations, by accounting only self-interaction, is:

$$\partial v_{\pm}/\partial t \pm c \partial v_{\pm}/\partial r + \frac{\gamma + 1}{2} v_{\pm} \partial v_{\pm}/\partial r = 0. \quad (4.1)$$

The evolution equation for the stratified atmosphere has a somewhat complicated form which can be obtained directly from (2.10) and the connecting equations (2.6).

The same can be obtained by the well-known method of slowly changing variables [9, 10]. An analytical solution of (4.1) is well-known, too. The proposed method, in contrast to the method of slowly changing variable, where only one directed mode is traced, allows to get coupled nonlinear equations. The upwards and downwards propagation of some types of initial disturbances are discussed in [5, 6, 8]. In this case, $\alpha = 0$, so that there is now an additional amplitude growth (or decrease). Both upwards and downwards-propagating modes retain their properties even for essentially large initial perturbation amplitudes, such as the velocity up to 150 m/s. The initial conditions were constructed using the linear equations and the numerical calculations were carried out by means of a nonlinear Lagrange finite-difference scheme [4–6].

4.3. Illustrations

Numerical simulations of equations (2.10) and (4.1) were carried out. Some peculiarities of the wave propagation in a stratified atmosphere caused by dispersion properties of medium and exponential dependence of nonlinear input on r are expected. We adopted the values $h = 1.033 \cdot 10^3$ m, $g = 9.8066$ m/s², and $\gamma = 1.4$, $A = 2.5$, $B = -2.533 \cdot 10^5$ J/kg.

Figure 1 presents the nonlinear evolution of a saw initial disturbance of velocity in the stratified and homogeneous atmosphere models. The influence of dispersion is clear: it widens the disturbance. For initial disturbances enough narrow, even additional

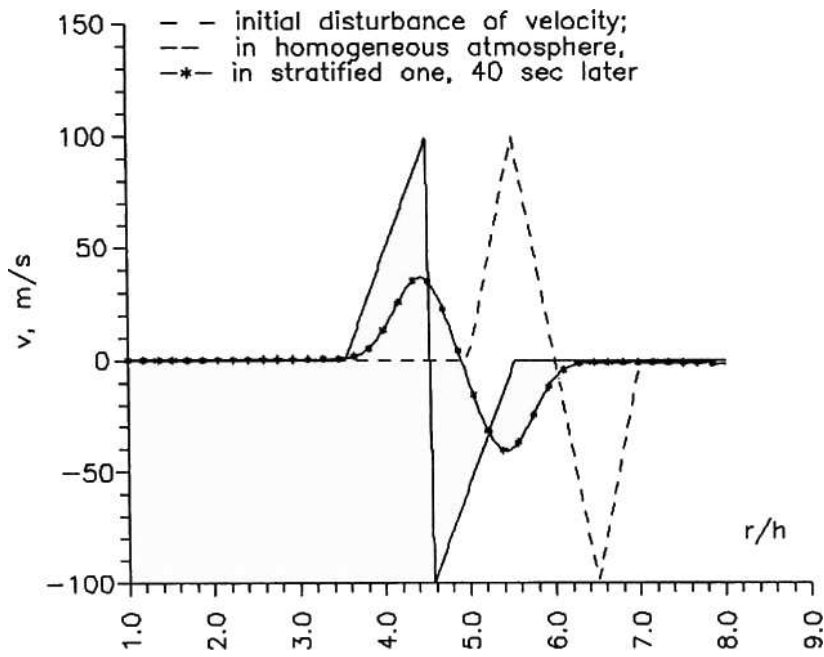


Fig. 1. Evolution of the initial disturbance of the velocity for the downwards directed wave in a stratified and a homogeneous gas.

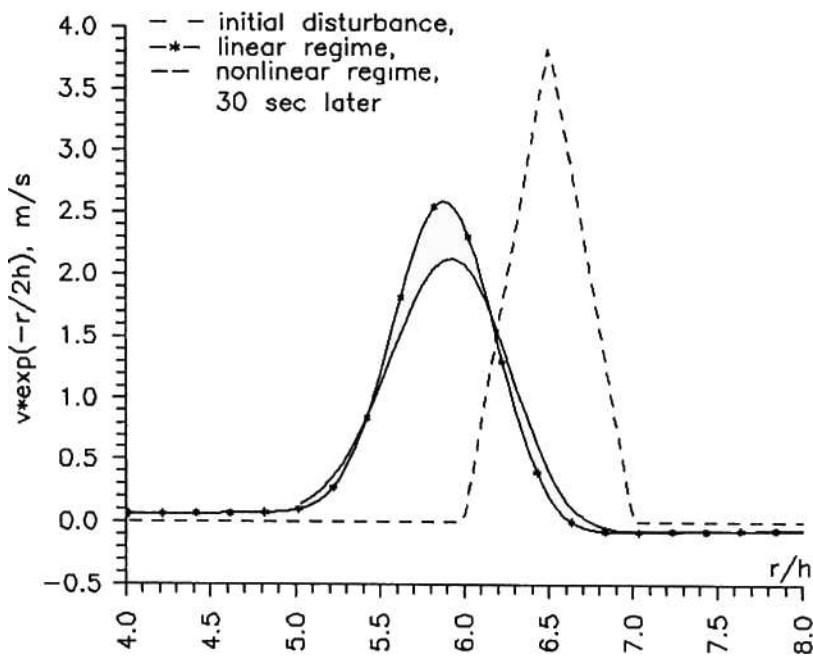


Fig. 2. Evolution of the initial disturbance of the velocity for the downwards directed wave in the linear and weak nonlinear regimes.

“hills” following the propagating disturbance appear. Evolution (4.1) of the disturbance in a homogeneous atmosphere gas is described by the known expressions [9, 10]. The amplitude of the wave in a stratified atmosphere seems to be much smaller than in a homogeneous one. The formulae for the directed wave were obtained for the variable $v \cdot \exp(-r/2h - \alpha r)$ instead of v in the homogeneous case (for an ideal gas $\alpha = 0$). The figure plotted for this variable shows that the propagating mode is more close to the initial one.

Figure 2 presents the evolution of the downwards directed wave in the stratified atmosphere with the account of the nonlinearity and without it. The initial amplitude of the velocity is about 100 m/s. Weak nonlinearity influences the wave shape in the same way as in the homogeneous atmosphere: points of larger amplitude move with a relatively smaller speed (for positive disturbances). This is in agreement with (4.1).

5. Conclusions

The projectors are written in a general form depending on the equation of state only both for the stratified and homogeneous models of a gas or liquid. The possibilities of the method are wide: nonlinear self-action or mutual interaction of the directed waves, generation of a mean field by the directed wave and so on. Generally, the coupled evolution equations obtained are suitable for the boundary regime problems as well as for the problems with initial conditions.

Thus, the projectors serve as an universal tool for the investigation of nonlinear evolution both in homogeneous and stratified gases and liquids. Moreover, the formulae for the projectors may be improved by applying of the perturbation theory.

Acknowledgements

I am thankful to prof. S.B. LEBLE for fruitful discussion.

References

- [1] A.S. MONIN and A.M. OBUKHOV, *The small oscillations of atmosphere and adaptation of meteorological fields* [in Russian], *Izv. AN SSSR, Geophysics*, **41**, 1360–1373 (1958).
- [2] V.A. GORDIN, *Mathematical problems of hydrodynamic weather prediction. The analytical aspects* [in Russian], Gydrometeoizdat, Leningrad 1987, p. 256.
- [3] L.M. BREKHOVSKICH and A.O. GODIN, *Acoustics of layered media*, Springer-Verlag, Berlin 1990, p. 141.
- [4] S.B. LEBLE, *Nonlinear waves in waveguides with stratification*, Springer-Verlag, Berlin 1990, p. 163.
- [5] A.A. PERELOMOVA, *Construction of directed disturbances in one-dimensional isothermal atmosphere model*, *Izv. RAN, Physics of Atm. Ocean*, **29**, 1, 47–50 (1993).
- [6] A.A. PERELOMOVA, *Generation conditions and nonlinear sound directed propagation in inhomogeneous medium*, EAA Symposium, Gdańsk–Jurata, 189–194 (1997).

-
- [7] YU.V. BREZHNEV, S.B. LEBLE and A.A. PERELOMOVA, *Nonlinear effects and one-dimensional sound propagation in inhomogeneous gas media*, Physical Express, **41**, 29–37 (1993).
 - [8] A.A. PERELOMOVA, *Nonlinear dynamics of vertically propagating acoustic waves in a stratified atmosphere*, Acta Acustica, **84**, 6, 1002–1006 (1998).
 - [9] M.B. VINOGRADOVA, O.V. RUDENKO and A.P. SUKHORUKOV, *Theory of waves* [in Russian], Nauka, Moscow 1979, p. 383.
 - [10] O.V. RUDENKO and S.I. SOLUYAN, *Theoretical foundations of nonlinear acoustics*, Consultants Bureau, Plenum, 1977, p. 287.

PROPAGATION PARAMETERS OF ULTRASONIC WAVES IN POLYMER COMPOSITES

L. RADZISZEWSKI

Kielce University of Technology
(25-314 Kielce, Al. 1000-lecia P.P. 7, Poland)

The non-contact ultrasonic technique of wave generation was used to test polymer composites. Transient elastic waves were generated with a Nd:YAG pulsed laser. Measurements aiming at the determination of the macroscopic parameters of propagation of bulk waves (amplitude, velocity and frequency distribution) were made in a unidirectional glass/epoxy (GFC) and isotropic polyvinyl chlorid plastic (PVC) thick plate. The influence of a constrained surface on the ultrasound parameters is discussed. The variations of the macroscopic parameters of propagation as functions of distance from the epicentrum were studied. PZT-ceramic standard ultrasound probes were used as receiver.

1. Introduction

There are many techniques that have been used for determining the macroscopic properties of materials or for detecting flaws and inhomogeneities. The use of active ultrasonic techniques for nondestructive materials evaluation has the advantage of a direct connection between the characteristics of the wave propagation and the mechanical properties of the material. The passive acoustic emission techniques are able to monitor the integrity of a large structure and to investigate dynamic failure processes in materials. Ultrasonic waves can be generated in a solid by many means corresponding to different dynamic loading of the specimen. These include ultrasonic plane-wave techniques which utilize a specific transducer excited by a burst pulse or continuous-wave excitations generating waves in the specimen. A recent alternative to the plane-wave technique is that utilizing transient signals generated by a source of small aperture. Transient elastic waves are generated on the surface of the specimen by broad band excitation sources which include a steel ball impact, a laser impact, a fracture of a capillary or a pencil lead, and a bombardment with electron beams. The advantages of this method include the possibility of determining the wave speeds of all the waveforms resulting in a solid from a single excitation pulse.

The focusing of a laser beam on the surface of a solid has been recognized recently to be a powerful mean for generating acoustic waves. The mechanism of the laser generation of an ultrasound has been shown by WHITE [1] to be thermoelastic at low laser energy densities; the source can be represented as a dipole strength parallel to the surface of the specimen. At a high power level, the laser source operates in the ablation regime by

vaporizing a small amount of the surface material. Thus it can be modelled by a force normal to the surface of the specimen. The radiated field of such a source resembles a monopole radiating strongly in all directions from a source point (HUTCHINS [2]). Using numerical solutions for the free-surface Green's function, SCRUBY [3] derived one of the first three-dimensional models for ultrasonic generation in solids. Despite an idealized point source approximation of the experimental illumination spot, this model predicts correctly the salient features of experimental waveforms. The analytic considerations of ROSE [4] about a point of dilation just below the surface of an elastic halfspace (due to thermoelastic mechanism) leads to a reasonable qualitative agreements with experiment, but do not relate all the relevant material and laser parameters to the displacement field. Later, SCHLEICHERT [5] described the optical generation of elastic waves in the thermoelastic regime taking into account the structure of different laser modes, the optical, thermal and elastic material properties as well as the finite area of a capacitance transducer. The theory of transient wave propagation in bounded isotropic materials has been established by SCRUBY [6]. The application of a laser point-source for the generation and detection of ultrasonic waves in thin platelike specimens has been described by HUTCHINS [7], NAKANO and NAGAI [8] and HURLEY [9]. These studies, were focused on measurements of the lowest-order symmetric and antisymmetric Rayleigh-Lamb wave modes in specimens which are elastically isotropic. The ultrasound velocities (with a resolution $\approx 2.5\%$) as a function of frequency were measured to determine the dispersion curve, from which the Young's modulus was deduced and their temperature dependences have been successfully measured up to 1500 K. Besides, some restrictions on using the lowest plate modes to extract the elastic modulus and thickness information of a thin plate were noted. Viscoelastic dissipation effects of the medium have also been considered by WAVER [10]. The methodology for measuring the intrinsic ultrasonic attenuation and dispersion within a broad frequency band (nearly 6 octaves) in different polymers using laser ultrasonic techniques has been presented by POUET [11]. He used the ablation mechanism for the ultrasound generation in order to obtain signals of high enough acoustic energy at the epicenter. This methodology enables the measurement of the frequency dependence of attenuation and phase velocity over a broad frequency band.

The ultrasound signals generated by a laser, such as the Q-switched lasers, are broadband signals in nature and do not display a clear central frequency. The selection and use of traditional narrow band ultrasonic sensors, such as the PZTs, is therefore questionable and the measurement of such broadband signals is susceptible to noise interference. Also, since broadband signals have no clear acoustic central frequency, it is difficult to ascertain the defect sizes that can be resolved. Modulated laser pulses can narrow the bandwidth of ultrasonic signal improving the signal-to-noise ratios by providing a direct control over the central frequency of the ultrasound. Both the spatial and temporal modulation of laser sources have been implemented experimentally using a variety of techniques for the bulk and surface wave modes. The purpose of modulation, whether spatial or temporal, is to create a clear spike in the signal frequency spectrum centered around some desired frequency so that a narrow band sensor, such as a PZTs one, can be readily used, and/or band pass filters can be used in the receiving electronics for the broadband sensor, such as interferometers, to improve noise rejection (SANDERSON [12]).

The extension of the laser ultrasound technique to measurements of elastic constants of anisotropic materials has been reported for composites by PICHE [13] and along the principal axes in germanium single crystals by AUSSEL [14]. In addition, a laser-generated ultrasonic bulk wave (CASTAGNEDE [15]) and a surface one (CHAI [16]) were also applied to the determination of elastic constants of anisotropic materials. SCRUDER [17] recorded waveforms at a series of positions along lines both parallel and perpendicular to the fibre axis in carbon/epoxy. Velocity profiles of major arrivals have been determined and shown to correspond to the group and phase velocities for quasi and pure bulk wave modes. A recent application of such measurements to characterize anisotropic materials has focused on inverting ultrasonic group velocities, obtained from pulse arrival time data, in signals that propagated in nonprincipal directions in an uncut specimen in order to obtain the matrix of its elastic stiffness. The determination of all the wave speeds from one detected waveform resulting from a single excitation pulse was described by KIM [18]. The determination of both longitudinal and shear wave speeds in an isotropic solid from the waveform detected by an arbitrary located sensor described was first. Then, measurements of the wave speeds made in various directions in silicon single crystal plates were analysed. The effect of the deviation of the propagation direction between the energy and phase bulk wave-mode fronts, detected by suitably positioned sensors in the anisotropic materials, was considered too. Angular amplitude directivity patterns of bulk waves in carbon/epoxy:unidirectional and cross-play, and the acoustic ray focusing was considered by CORBEL [19]. The scan images of very thin ($145\mu\text{m}$) graphite/epoxy laminates and silicon wafers, which represents the detailed spatial and temporal characteristics of the elastic wave field in a specimen, were obtained by VEIDT [20]. The features of such an image can be directly related to the material's anisotropy and macrostructure. Basing on laser generation and laser detection of acoustic waves, the stiffness tensor of a polymer matrix composite has been measured by GUILBAND [21]. The model developed predicts accurately the focusing effects caused by anisotropy and the spreading of the signals caused by the dispersion and attenuation. Despite the dispersion and echos overlapping, the stiffness coefficients are identified with good reliability from the group velocities of bulk waves. This work is concerned with transient acoustic radiation generated by a laser in a polymer matrix composite. This is motivated partly by the desire to understand how the acoustic emission transients caused by growing defects propagate in composites. This work is an extension of the work of previous authors [15–19] aimed at characterizing the material quantitatively by using the laser technique. However, not only the wave propagational effects, such as signal attenuation, dispersion and radiation must be known, but also the effects of the measurement system, particularly the sensor and its coupling to the specimen, so that a correct relationship between the measured signal amplitudes and the source-receiver separation can be established [22].

The purpose of the present work was to generate and detect ultrasonic bulk wave modes first in a quasi isotropic, homogeneous and uniform, viscoelastic material. Hence, a 20 mm thick polyvinylchlorid plastic (PVC) plate has been chosen. Secondly, an anisotropic heterogeneous, polymer matrix composite was considered, using a 17 mm thick composite plate made of unidirectional glass fibres impregnated in an epoxy matrix. For these two samples scan images have been measured and compared.

From these experiments an understanding of how the composite response evolves as a function of the source-receiver separation has been gained.

The knowledge obtained from the isotropic case is applied to identify the various wave arrivals in the waveforms of the anisotropic specimens. In contrast to the foregoing [17, 19], the focus is on the variation of the ultrasonic amplitude at an oblique orientation using data at the epicenter for comparison. Commercial sensors made of PZT-ceramic and the contact technique for receiving ultrasonic waves were applied. The purpose of the experiments in a thick PVC plate was to verify the wave modes, the wave velocity and the amplitude distribution of the ultrasound generated by a laser.

This paper is organized as follows: In Sec. 2 the measuring set and procedure are presented. The experimental results are described in Sec. 3. First, the amplitude distribution is discussed. Then, the results of measurements of velocity are discussed. At the end of the paper, in Sec. 4, the experimental results are compared and discussed.

2. Procedure: setting up and measurement

For the excitation of the ultrasound, a Q-switched Nd:YAG laser (with a built-in non-linear crystal) has been used. Laser pulses were emitted with a frequency equal to 2 Hz. An electromagnetic wave of length $\lambda = 532$ nm and energy — 1.7 mJ with a temporal width of 10 ns was focused down to a spot of 1.5 mm on the sample face. The pulse-to-pulse fluctuation of the laser energy was about 5%. The power density deposited on the tested sample surface was 10 MW/cm². Some ablation of the sample did occur leaving small pits in its surface.

Noncontact, capacitance or electromagnetic acoustic transducers, optical interferometric sensing systems available now are capable of detecting surface motions. Although they possess a broad frequency response, the sensitivity of such systems is at most by an order of magnitude higher than that provided by piezoelectric sensors. Furthermore, such an expensive instrument was not available for us. For this reason, piezoceramic contact transducers were used in this study to detect the ultrasonic signals. Piezoelectric ultrasonic probes were used to measure the deformation of the surface caused by the ultrasound wave. The measurements were performed using Panametrics standard ultrasonic probes; a probe for the measurement of AE with a resonance frequency of 160 kHz, and ultrasound broadband probes; 2.25 MHz of bandwidth of about 94.4%. The diameter of the transducers in all the probes was 12.7 mm. The medium which coupled the probe to the sample surface was an aqueous solution of glycerine or Panametrics resin. Additional details of the measurement system has been described previously [23]. The amplitude distribution and wave-front arrival times were measured in thick plates (for the PVC plate the distance from the source ($h \geq 20$ mm) was much larger than the acoustic wavelength $L \cong 3$ mm). Initially, we have to verify the wave modes which were generated by the laser in thick plates. Measurements of the arrival time by the transmission method, with the probe adhered to the sample surface in different positions (Fig. 1 b), were made to verify waves which propagate under the surfaces and in the bulk of the specimens. In a few experiments we have coupled a plexiglass plate on the surface between acoustic

source and the probe to eliminate surface waves. In this way it has been proved that the measured waves were bulk waves.

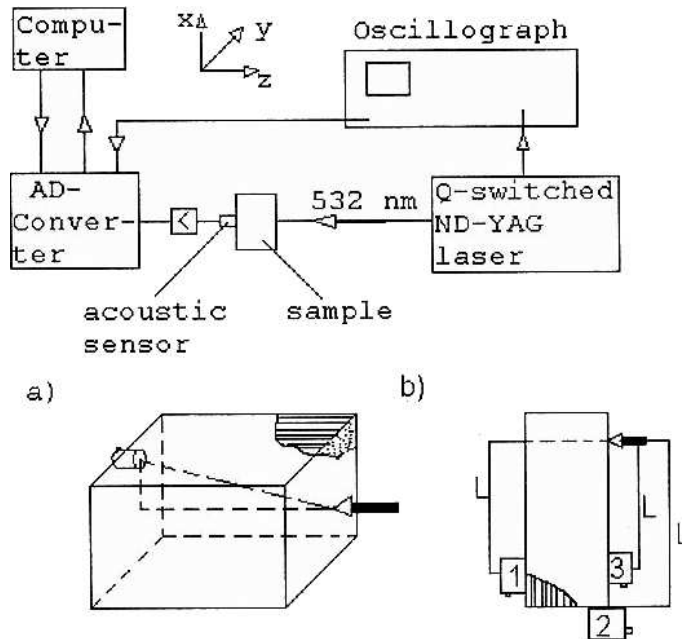


Fig. 1. Measuring stand with Nd:YAG laser; a) measurements in GFK-cuboid; b) measurement in GFK- or PVC-plate.

The amplitude distribution versus distance from the epicenter were deduced from the variations of peak to peak magnitude of each remote acoustic pulse. The measurements of the maximum amplitude of the first arriving pulse of the acoustic wave (longitudinal-L or shear-T) was performed every 0.1 mm within 4 seconds. A mean amplitude value from eight measurements at one point was established to be the result. The measurements in a PVC plate were made using a 2.25 MHz probe for the longitudinal (L-probe) or shear (T-probe) waves. The X-Z plane of measurements intersected first ($y = 0$) the epicenter of the acoustic source. During the amplitude distribution measurements, the probe moved in precise steps from its initial position in one X-Z plane along a straight line changing in this way the direction of the shortest path from the source to receiver (Fig. 1). For measurements with a shear probe, the probe was coupled by resin to the surface and the set plate-probe changed the distance to the laser illumination point in the same way as previously. The first pulse in the time window for a dilatation wave was recorder at the points of measurements. Next, a frequency spectrum was determined using a fast Fourier transformer. The mean value (for two measurements made at one point) of the frequency for the pulse of dilatation waves of maximum amplitude changes was taken as the result of the measurement. Both the control of the probe movement and the recording of the results were performed by a PC computer. The surface on which light falls was either free or constrained with a plexiglass plate and silicon oil.

When the measurements in one plane were finished, the probe was moved transversely 2 mm to a next plane (from position $y = 2 \cdot i$ to $y = 2 \cdot (i + 1)$ for $i = \pm 0, 1, 2, \dots, 10$). An area of $50 \text{ mm} \times 100 \text{ mm}$ was scanned in this way.

The velocity of wave was calculated as a sonic distance divided by time of flight. The arrival times of the wave packets that propagated through the medium at their energy velocity were measured directly on the digitized waveforms.

The experiments carried out concerned two materials: isotropic polyvinyl chloride plastic and epoxy resin reinforced unidirectional with glass fibre. The GFC specimens had the form of a thick plate (17 mm) or a cuboid, the dimensions of which were $31 \text{ mm} \times 60 \text{ mm} \times 70 \text{ mm}$.

3. Experimental results and assessments

3.1. Amplitude distribution in the PVC- and GFC-plates

The amplitude distribution in the PVC plate for the longitudinal and shear waves in the X-Z plane accrossing the epicenter is presented in Fig. 2. The amplitude of the longitudinal wave falls down nonlinearly, while the amplitude of the shear wave (the axis of the polarization direction of the T-probe was X-X) falls down linearly as a function of distance from the centre. When the axis of the polarization direction of the T-probe was Y-Y, the measured amplitudes were about 10 dB smaller but the measurement accuracy was rather poor.

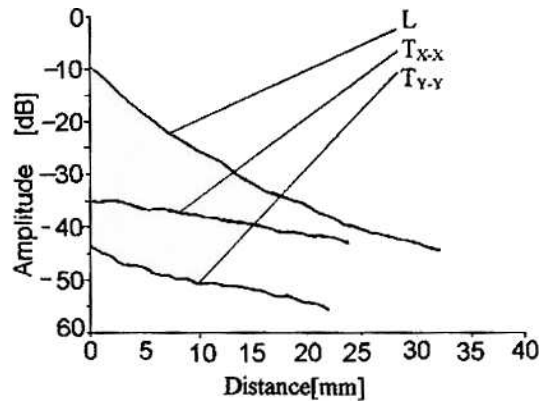


Fig. 2. Comparison of amplitude distribution of longitudinal (curve-L)- and shear (curves T_{X-X} , T_{Y-Y}) in one plane X-Z, $y = 0$) waves versus distance from the epicenter in the PVC plate, probe 2.25 MHz; T_{X-X} -direction of polarization X-X, T_{Y-Y} -direction of polarization Y-Y.

The amplitude of the longitudinal wave is greater than that of the shear wave in the whole measuring range; the differences are about 25 dB near the epicenter. The longitudinal wave is generated as a primary wave in the acoustic source. The shear wave is generated by the transformation of the longitudinal one during the reflexion at the surface where the laser beam incident. This transformation is accompanied by energy losses. This is one of the most important reasons of the amplitude differences. However

moving from the epicenter the differences quickly vanish. It is supposed to result from the fact that far from the epicenter the thermoelastic mechanism of wave generation is more effective as the ablation one. Secondly, for the set up configuration presented in Fig. 1 b (probe T in position 1, axis of polarization in the direction X–X) and the measurement procedure, the measured amplitude of the shear wave depends in any position on the attenuation and directivity pattern of the sound source. It appeared that the measured amplitude of the longitudinal wave depends additionally on the incident angle to the probe; this is probably the reason for the nonlinear relation in Fig. 2 (curve L).

The results of the amplitude distribution measurements with the probe 2.25 MHz coupled on the edge of the PVC-plate (see Fig. 1, probe in position 2) are presented in Fig. 3. This time, the amplitude of the shear wave (axis of polarization direction T-probe X–X) is greater than the longitudinal wave in the whole measuring range. It results from the amplitude directivity patterns of the sound source for the longitudinal and shear waves [3]. The amplitude of longitudinal wave falls down nonlinearly as function of the distance from the centre, but for the amplitude distribution of the shear wave we can write a linear relation. The nonlinear relation of the amplitude distribution of the longitudinal wave can be approximated by two linear equations. From this amplitude directivity pattern it is obvious that for $x \in (10 \text{ mm}, 15 \text{ mm})$ there should be a change of the dominating mechanism of the ultrasound generation from the ablation mechanism near the epicenter to the thermoelastic one far from the epicenter.

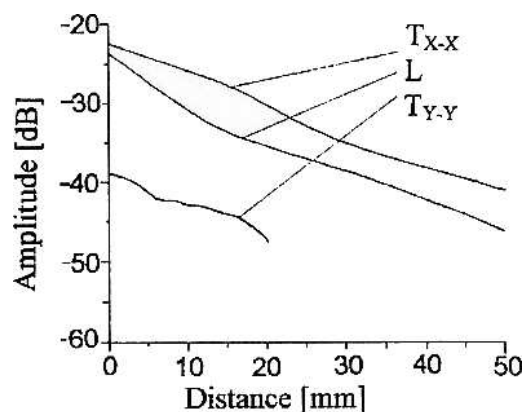


Fig. 3. Comparison of amplitudes of longitudinal (curve-L)- and shear (curves T_{X-X} , T_{Y-Y}) — wave distribution versus distance from epicenter, probe 2.25 MHz coupled on edge in PVC plate; T_{X-X} -direction of polarization X–X, T_{Y-Y} -direction of polarization Y–Y.

Figure 4 shows a 3-D scan of the amplitude distribution of a longitudinal wave in the PVC-plate. A maximum value of the amplitude occurs in the direction of the laser ray. It confirms once more that first of all we have to do with an ablation mechanism of the ultrasound generation. Although the material is isotropic, the amplitude falls by 6 dB in the range of angle $16^\circ < \alpha < 18^\circ$ but non-uniformly in the different directions of propagation. The reason for it is probably the nonsymmetric energy distribution in the acoustic source which results from the imperfection of the laser ray.

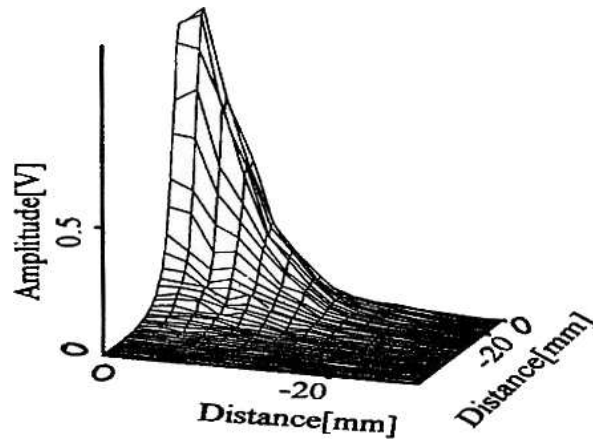


Fig. 4. The 3-D amplitude distribution of a longitudinal wave in the PVC plate measured by the 2.25 MHz probe.

The scan image of the amplitude distribution of the longitudinal wave was measured also for a GFC plate with a free surface (Fig. 1 b). The maximum value of the amplitude occurs in the direction of the laser ray. The amplitude falls by 6 dB in the range of the angle α (for path $y = 0$ or $x = 0$) which is illustrated in Table 1. It is well known that the properties of the GFC plate depends on the direction of investigation. The measurements of 6 dB fall ab of the amplitude using a 2.25 MHz-probe confirm it. However the same measurements with an AE-probe do not lead to such a conformation. The resonance frequency of the AE-probe was 160 kHz. For the ultrasound wave of that frequency, the investigated GFC plate (in the direction X-X or Y-Y near the epicenter) was almost homogenous.

Table 1. Amplitude distribution for the GFC plate.

	2.25 MHz sensor	AE sensor
Fibre direction (X-X)	$\alpha = 33^\circ$	$\alpha = 36.5^\circ$
Perpendicular to fibre (Y-Y)	$\alpha = 24.5^\circ$	$\alpha = 36^\circ$

After the normalization of the values of the amplitude in the epicenter (e.g. the amplitude for each experimental curve is for $\alpha = 90^\circ$ equal to 0 dB), we can compare this relation as shown in Fig. 5. First of all it is evident that the results of the amplitude distribution depends on the receiving probe. The amplitudes measured with AE transducers fall much slower than those measured with a 2.25 MHz probe.

The amplitude of a longitudinal wave in the Y-Z plane (isotropic plane, perpendicular to fibre, $x = 0$) is decreasing almost linearly with the angle $\beta = 90 - \alpha$ [deg] (see Fig. 5 a).

In the X-Z plane (in the fibre direction, $y = 0$), the amplitude of a longitudinal wave as function of the angle to fibre falls nonlinearly (see Fig. 5 b). However, these relations can be represented by two linear functions.

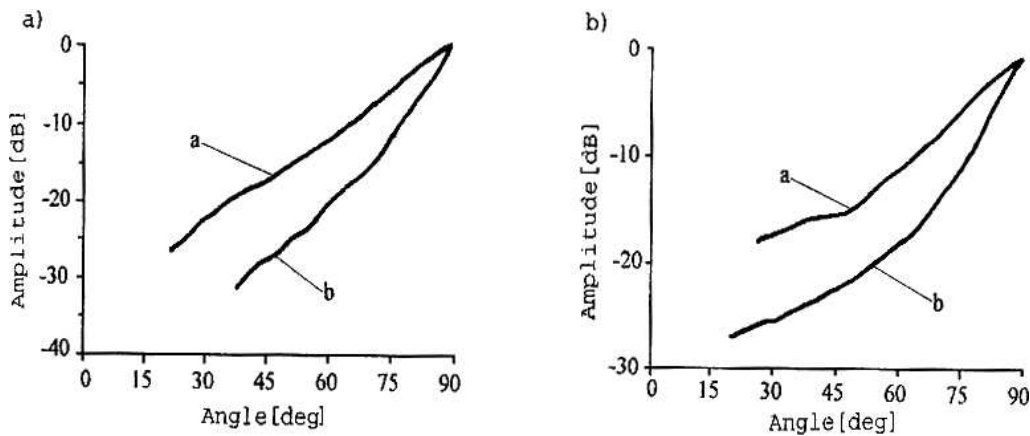


Fig. 5. 1-D amplitude distribution in a GFC plate; a) measurements perpendicular to fibres b) measurements in the fibre direction; a — curve measured with an AE-transducer, b — curve measured with a 2.25 MHz transducer.

From these relations it is evident that near the epicentrum (on the surface opposite to the source) the properties of the composite are not so strongly dependent on the direction of investigation. Figure 6 shows a 3-D scan of the amplitude distribution of a longitudinal wave in a GFC cuboid (see Fig. 1 a). The maximum value of the amplitude occurs in the direction of the laser ray (which is now parallel to the fibre, i.e. $\alpha = 0^\circ$). The amplitude falls by 6 dB in the range of the α angle; in the X-Z plane, $\alpha = 8^\circ$; in the Y-Z plane, $\alpha = 8.6^\circ$. This means that the energy flux is concentrated along the fibre. From another point of view we know that the elastic properties of composites are also strictly related

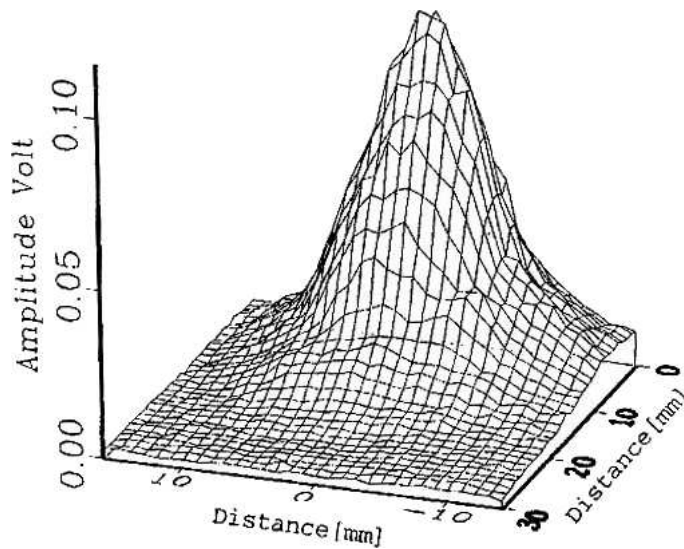


Fig. 6. The 3-D amplitude distribution of a longitudinal wave in the GFC cuboid measured with a 2.25 MHz transducer.

to the fibre direction. Moving a little away from fibre direction, there is a drastic fall of the amplitudes.

The surface of a composite appears to be never completely free from stresses. Usually, the composite surface has a protective resin coating. In our tests, the surface of the GFC plate was constrained additionally with silicon oil and a plexiglass plate. These constraining layers cause a 30 dB increase in the amplitude of a longitudinal wave launched near the epicentre. The amplitudes measured in the fibre direction are always higher than those measured in the direction perpendicular to the fibre. When, however, the surface is free, i.e. without a silicon oil or a plexiglass plate, the difference is less than 5 dB. In the case of a constrained surface, the amplitudes measured in the direction perpendicular to the fibre (in the Y-Z plane) fall much more rapidly as those measured in the fibre direction (in the X-Z plane). When the surface is constrained, the thermoelastic stresses in the acoustic source as well as the amplitude of the generated waves increase. Depending on the angle between the acoustic ray and the fibres, this increase of the amplitude is different. It is the greatest in the fibre direction. It should be mentioned that such an anisotropy occurs as well due to the application of the near-infrared laser. This laser provides the optical absorption localized on the glass fibres [19]. No such anisotropy occurs if the absorption takes place in the epoxy resin, as in the case of a CO₂ laser.

3.2. Measurements of the velocity and frequency

The measured velocity of longitudinal and shear waves in an isotropic PVC-plate depends on the position of the receiving probe; the differences of the results reaches 6%. When the probe was coupled to the surface opposite to the source, the velocity was $c_L = 2366$ m/s for the longitudinal wave and $c_T = 1064$ m/s for the shear one whereas for the probe coupled to the edge the velocities were $c_L = 2246$ m/s and $c_T = 1131$ m/s.

This means that the accuracy of the measurements of the velocity of the longitudinal or shear waves did not exceed 6%. For comparison the velocity of a wave was measured by transmitter-receiver probe of 2.25 MHz placed onto the PVC-plate. The velocity of the longitudinal wave was 2246 m/s and for shear one 1131 m/s. The velocity of the wave was calculated as the sonic distance divided by the time of travel. The position of the source in the X-Y surface was known quite exactly i.e. with a tolerance of ± 0.75 mm. The acoustic source excited by the laser is buried in the material. Thus, its position under the surface can be only approximated. In this work, we have taken into account that the acoustic source lies 0.3 mm under the surface. The sonic distance was the shortest path between the source and the receiver. However, the assumption that the probe is a point receiver was not valid since the diameter of the probe of 12.7 mm was too large. Thus, the shortest sonic path from the source to the receiver was measured very roughly when the probe was not in the epicenter. When the probe is coupled on the edge, such a problem does not exist and the accuracy is as high as for the transmitter-receiver method.

Figures 7 and 8 show the dependence of the longitudinal wave velocity on the angle between the wave and the fibre measured in a GFC plate (with free surface) by a 2.25 MHz transducer and an AE-transducer.

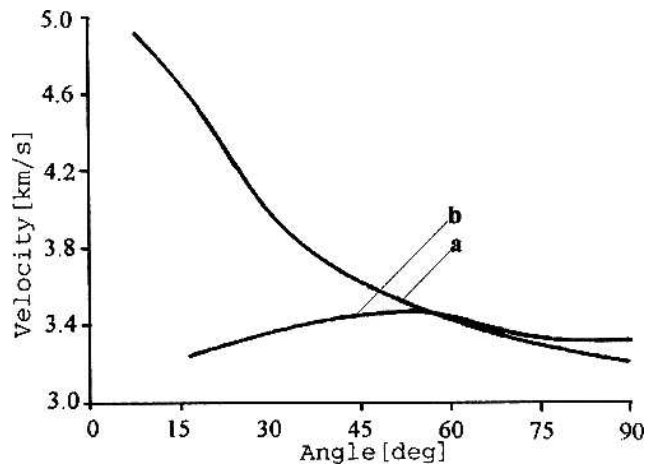


Fig. 7. Velocity of the longitudinal pulse in a GFC plate measured with a 2.25 MHz transducer. Curve a — measurement in the X-Z plane, curve b — measurement in the Y-Z plane.

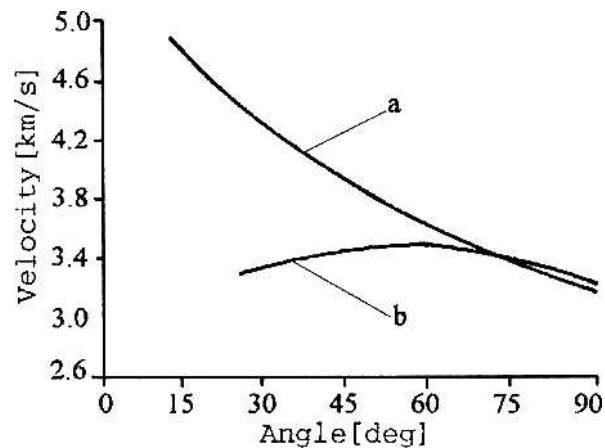


Fig. 8. Velocity of a longitudinal pulse in a GFC plate measured with an AE-transducer. Curve a — measurement in the X-Z plane, curve b — measurement in the Y-Z plane.

The velocity of a longitudinal wave measured in the X-Z plane depends nonlinearly on the angle β to the fibres. In the Y-Z plane perpendicular to the fibres (the isotropy plane), the measured velocity of a longitudinal wave has a local maximum for angle $\beta \cong 60^\circ$, but the phenomenon is difficult to explain. One possible reason is that the Y-Z plane may not be a perfectly isotropic one for this particular composite. However, the measurement accuracy is 6%, as found for the isotropic materials. From this point of view, the velocity in plane perpendicular to the fibre should be constant. There are differences between the results of velocity measurements obtained with a 2.25 MHz probe and an AE one. The differences are less than 10%. As it was supposed from the analysis of the amplitude distribution in the GFC cuboid, the energy flux should be concentrated

along the fibre. The results of the velocity measurements in the GFC-plate corroborate this conclusion. The velocity of longitudinal wave is the greatest in the fibre direction (over 5000 m/s) and falls rapidly to about 3400 m/s with increasing deviation from this direction.

The assumption that the pulses of a longitudinal wave of maximum amplitude measured with a 2.25 MHz transducer would vibrate with a frequency of about 2.25 MHz appeared not to be true.

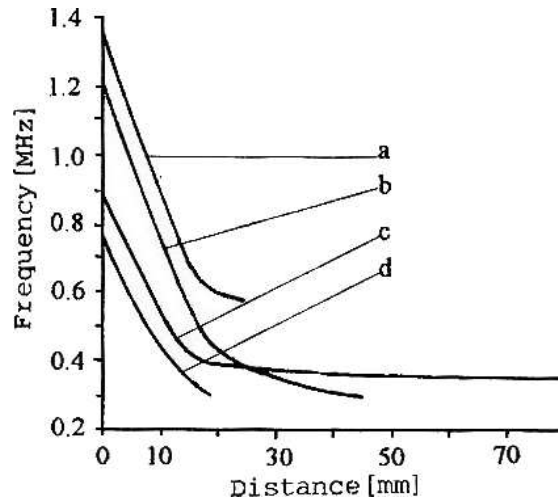


Fig. 9. Frequency distribution of a longitudinal wave: in a GFC plate with free surface measured in the direction perpendicular to fibres (curve a) or in the fibre direction (curve b); and in a GFC plate with constrained surface measured in the fibre direction (curve c) or in the direction perpendicular to the fibres (curve d).

The results of measurements in a GFC plate made with a 2.25 MHz probe shows that the vibration frequency of these pulses depends on the direction of investigation and the state of the surface. Figure 9 shows the frequency distribution of a longitudinal wave generated in a GFC plate by a laser. The vibration frequency in the epicentre is about 1.35 MHz for a free surface, whereas in the case of a constrained surface it is about 0.85 MHz. A vigorous decrease in the frequency up to 0.4 MHz near the epicentrum (distance up to 30 mm) is observed. When the distance from the epicentre increases, this decrease is systematic, probably because the flux of the wave energy is concentrated along the glass fibre. It should be mentioned that the measurement accuracy is rather low and equals to about 15%.

4. Conclusions

The investigation has shown that the laser light of a power density of 10 MW cm^{-2} when incident on the polymer surface causes the formation of an acoustic source, mainly due to the ablation mechanism and, to a small degree, to the thermoelastic mechanism.

The generation of an ultrasound by the ablation mechanism is more effective near the epicenter, whereas the thermoelastic mechanism is still present and makes it possible to measure the amplitude of the ultrasound waves far from the epicenter. The laser generated wave near the epicenter propagates with a frequency much higher than that of waves far from the epicenter. In isotropic materials, the amplitude directivity patterns are almost symmetrical in relation to the normal to the surface. The wavefronts generated by the laser in composite materials are more complex than the near-spherical wavefronts in isotropic polymers. The test results show the interdependence of the state of the test piece surface, anisotropy, anelasticity and the elastic wave propagation. The constraining layers cause a 30 dB increase in the amplitude of a longitudinal wave launched near the epicentre. The amplitude distribution and velocity of waves in composites depend on the direction of propagation. The measured velocity of a longitudinal wave refers to the group velocity rather than phase one. There are differences up to 10% between the results obtained with a 2.25 MHz-probe and an AE one. The measurements accuracy is: for the amplitude distribution 3% and for the velocity 6%. For measurements far from the epicenter the use of a probe of shear waves coupled with a resin to surface is very effective.

References

- [1] R.M. WHITE, *Generation of elastic waves by transient surface hitting*, J. Appl. Phys., **34**, 12, 3559–3567 (1963).
- [2] D.A. HUTCHINS, *Ultrasonic generation by pulsed laser*, W.P. MASON and R.N. THURSTON [Eds.], Academic, New York 1988.
- [3] C. SCRUBY and L. DRAIN, *Laser-ultrasonics*, Adam Hilger, Bristol 1990, Ch. 5, 263.
- [4] L.R.F. ROSE, *Point source representation for laser-generated ultrasound*, JASA, **75**, 723–732 (1984).
- [5] U. SCHLEICHERT, *Die Theorie der optischen Erzeugung elastischer Wellen in Festkoerpern*, Ph.D. Thesis, University of Kassel, 1989.
- [6] C.B. SCRUBY, *Quantitative acoustic emission techniques*, Research Techniques in Nondestructive Testing, vol. VIII, R.P. SHARPE, ed. Academic Press, London 1985, p. 141–210.
- [7] D.A. HUTCHINS, K. LUNDGREN and S.B. PALMER, *A laser study of the transient lamb waves in thin materials*, JASA, **85**, 4, 1441–1448 (1989).
- [8] H. NAKANO and S. NAGAI, *Laser generation of anti-symmetric Lamb waves in thin plates*, Ultrasonics, **29**, 230–234 (1991).
- [9] D.A. HURLEY, J.B., SPICER, R.J. CONANT and K.L. TELSCHOW, *Determination of the Optical Absorption Coefficient via Analysis of laser generated plate waves*, IEEE Ultrasonics, Ferro. Freq. Control., **44**, 4, 902–908 (1997).
- [10] R.L. WAVER and W. SACHSE, *Transient ultrasonic waves in a viscoelastic plate*, JASA, **85**, 6, 2255–2267 (1989).
- [11] B. POUET and N. RASOLOFOSAON, *Measurement of broadband intrinsic ultrasonic attenuation and dispersion in solids with laser techniques*, JASA, **93**, 1286–1292 (1993).
- [12] T. SANDERSON, CH. UME and J. JARZYNSKI, *A comparison of Q-switched and intensity modulated laser pulses for ultrasonic NDT*, J. of Nondestructive Evaluation, **17**, 4, 199–208 (1998).

-
- [13] L. PICHE, B. CHAMPAGNER and J.-P. MONCHALIN, *Laser ultrasonic measurements of elastic constants of composites*, Mater. Eval., **45**, 74–79 (1987).
- [14] J.-D. AUSSEL and J.-P. MONCHALIN, *Precision laser-ultrasonic velocity measurement and elastic constant determination*, Ultrasonics, **27**, 165–177 (1989).
- [15] B. CASTAGNEDE, K.Y. KIM, W. SACHSE and M.O. THOMPSON, *Determination of the elastic constants of anisotropic materials using laser-generated ultrasonic signals*, J. Appl. Phys., **70**, 1, 150–157 (1991).
- [16] J.-F. CHAI and T.T. WU, *Determinations of anisotropic elastic constants using laser generated surface waves*, JASA, **95**, 6, 3232–3241 (1994).
- [17] L.P. SCUDDER, D.A. HUTCHINS and I.T. MOTTRAM, *The ultrasonic impulse response of unidirectional carbon fibre laminates*, Ultrasonics, **32**, 5, 347–357 (1994).
- [18] K.Y. KIM, W. SACHSE and A.G. EVERY, *On the determination of sound speeds in cubic crystals and isotropic media using a broadband ultrasonic point source/point-receiver method*, JASA, **93**, 3, 1393–1406 (1993).
- [19] C. CORBEL *et al.*, *Laser generated elastic waves in carbon-epoxy composites*, IEEE Transaction, **40**, 6, 710–716 (1993).
- [20] M. VEIDT and W. SACHSE, *Ultrasonic point-source/point-receiver measurements in thin specimens*, JASA, **96**, 4, 2318–2326 (1994).
- [21] S. GUILBAND and B. AUDOIN, *Measurement of the stiffness coefficients of a viscoelastic composite material with laser-generated and detected ultrasound*, JASA, **105**, 4, 2226–2235 (1999).
- [22] X. LU, W. SACHSE and J. GRABEC, *Use of an automatic modeler and a small receiver array for acoustic emission source location*, Ultrasonics, **36**, 539–547 (1998).
- [23] L. RADZISZEWSKI, *On generating ultrasound by laser in polymers*, Archives of Acoustic, **19**, 381–393 (1994).

**FABRICATION OF THE MEMBRANES ON A SILICON BASE FOR THE
SENSORS WITH THE ULTRASONIC WAVES LAMBA-TYPE GENERATED
BY USING THE INTERDIGITAL TRANSDUCERS**

J. GOŁĘBIEWSKI

Technical University of Łódź
Institute of Theoretical Electrotechnics,
Metrology and Materials Science
(90-924 Łódź, Stefanowskiego 18/22, Poland)
e-mail: jacekgol@ck-sg.p.lodz.pl

The construction of the microsensor with the ultrasonic wave of Lamba-type as well as the conditions of the wave propagation are presented. The possibilities of the fabrication of multi-layer membranes on a silicon base using the microelectronics technologies are presented and discussed. The analysis of the usefulness of the processes mentioned for the production of thin membrane sensors was carried out taking into consideration intrinsic stresses. A summary of the experimental results is given and the most useful parameters of the membrane ultrasonic sensors are pointed out.

1. Sensor construction and conditions of Lamba wave propagation

The sensor membrane with the Lamba type ultrasonic wave consists of several layers of different thickness. For a membrane made of a silicon plate, the basic layer, which determines the elasticity properties of the whole membrane, is a monocrystalline silicon layer or a layer of silicon nitride or oxide. The others are piezoelectric and metallic layers. In the metallic layer, the interdigital electrodes are made of the piezoelectric transducers (IDT). A view of the transducers that are placed on the membrane surface as well as the contact fields (white field denotes the surface etched in the silicon — at the bottom) is presented in Fig. 1. The principle of the sensor work consists in the generation of an ultrasonic wave in the plane membrane by means of two interdigital transducers (IDT). One of them works as a transmitter and the other one as the receiver. The Lamba waves are determined as transverse waves which propagate in the plate plane. Their polarization plane is normal to the plane of the plate. These waves are symmetric and asymmetric in relation to the plane in the middle thickness of the membrane. Each of those waves can contain different numbers of the mode vibrations denoted by the indices 0, 1, 2. The velocity of the Lamba wave propagation depends on the wave frequency and the membrane thickness [2, 3].

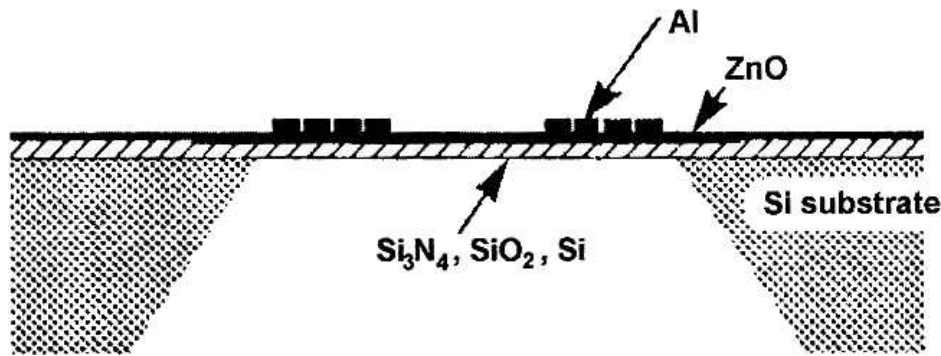


Fig. 1. The interdigital piezoelectric transducers (Al) on the surface of the sensor membrane.

For the symmetric wave it is possible to obtain lower phase velocities and a lower wave frequency in the sufficiently thin membrane. In order to obtain high sensitivities, in the application of membrane sensors as mass detectors, thin membranes should be used [1]. That is why for the following conditions should be fulfilled by the membrane: the maximum wave amplitude should be smaller than the thickness d , the wave length λ should be significantly larger than the membrane thickness ($\lambda \gg d$), the membrane width a and length b should be significantly larger than the thickness ($a \gg d, b \gg d$). The technologies of the production of thin elastic layers in the sensors' membranes are described below. The following layers are deposited on the base: a piezoelectric layer which is made of zinc oxide (ZnO) and a metallic one made of aluminium (Al) [4].

2. Fabrication of thin silicon membranes

The silicon membranes were obtained by anisotropic etching of the silicon. Wafers with the diameter of 3", made of the monocrystalline silicon one-sidedly polished with the orientation of $\langle 100 \rangle$ and a donor conductivity, phosphorus doped with resistivity of 1–2 Ωcm , were the basic material. The thickness of the wafers was 380 μm . The upper surface of the wafers was protected by silicon nitride against etching in potassium hydroxide (KOH). This layer was made by the LPCVD (Low Pressure Chemical Vapour Deposition) method in the reaction of dichlorosilane (SiH_2Cl_2) with ammonia (NH_3) at a temperature of 800° C; the ratio of SiH_2Cl_2 to NH_3 was 4 : 1. The thickness of the silicon nitride layer (Si_3N_4) was 20 nm [6]. The membrane shape on the bottom side of the silicon wafer was defined by a photolithographic process. The silicon nitride layer from the membrane area was etched off in a plasma process and then the photoresist was removed. Finally the wafer was etched in a aqueous solution of KOH. As the result of the anisotropic silicon etching, membranes with sizes of 2 × 2.5 mm and the thickness of 12–15 μm were obtained [5]. The cross-section of the sensor membrane with the silicon layer is shown in Fig. 2.

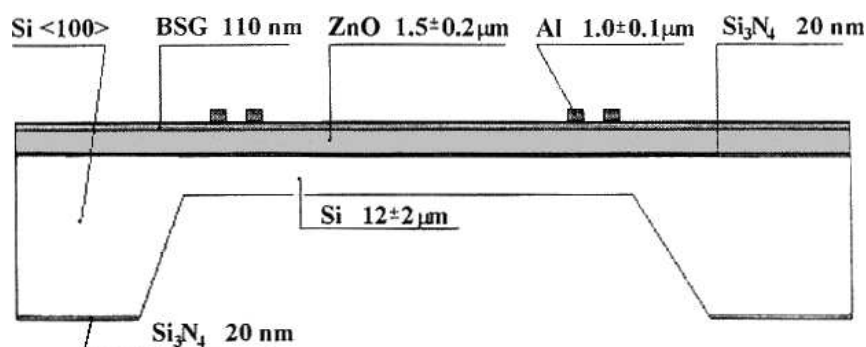


Fig. 2. The cross-section through the sensor membrane with the monocrystalline silicon layer: ZnO — the zinc oxide layer, Al — the aluminium layer, Si_3N_4 — the silicon nitride layer, Si — the wafer made of $\langle 100 \rangle$ monocrystalline silicon.

3. Fabrication of the silicon nitride membranes

The silicon nitride Si_3N_4 layer was made by the LPCVD method at a temperature of 800°C by the reaction of dichlorosilane (SiH_2Cl_2) with ammonia (NH_3) [11]. The ratio of the dichlorosilane to the ammonia was 4 : 1. The purity of the gases used in the process was “electronic grade”. Under the described conditions, the deposition rate of the Si_3N_4 layer was about 0.066 nm/s. The one-side polished silicon wafers with the diameter of 3" and thickness of $380\ \mu\text{m}$ were the substrate for the silicon nitride. They were made of monocrystalline silicon of *n*-type conductivity (phosphorus doped). The resistivity of the wafers and their crystallographic orientation were $1\text{--}2\ \Omega\text{cm}$ and $\langle 100 \rangle$, respectively. The silicon nitride layer of a thickness of about $1.3\ \mu\text{m}$ was deposited during 330 min. The thickness was measured by a reflectometer with accuracy of $\pm 20\ \text{nm}$. The refractive index of this layer was about 2.1. For the stoichiometry of the silicon nitride layer, the refractive index was equal to 2.0. The influence of the deposition conditions on the value of the refractive index in the silicon nitride layer is shown in Fig. 3.

As it can be seen, all the nitride layers obtained are not of the stoichiometric composition. The latter is Si_xN_y layer with $x > 3$ and $y < 4$. The parameters of the deposition process were chosen so as to minimize the stresses in the deposited layer. The total stresses, which are the sum of the thermal stresses and the intrinsic one, were lower than $8 \cdot 10^8\ \text{Pa}$ [7]. The photomasking process was done at the bottom side of the wafers and the Si_3N_4 was etched in a plasma process. Then, the wafers were etched in a KOH solution. From of the anisotropic silicon etching, membranes made of silicon nitride with sizes of $2 \times 2.5\ \text{mm}$ and a thickness of $1.3\ \mu\text{m}$ were obtained. In the membranes, however, too high intrinsic stresses were present. They caused cracking of the membranes. The dependence of the total stresses and the intrinsic one in the silicon nitride layer on the DCS/NH_3 ratio is shown in Fig. 4.

It was obvious that even for low values of the total stresses, which are the sum of the thermal stresses and intrinsic one, those components could reach high values. It is

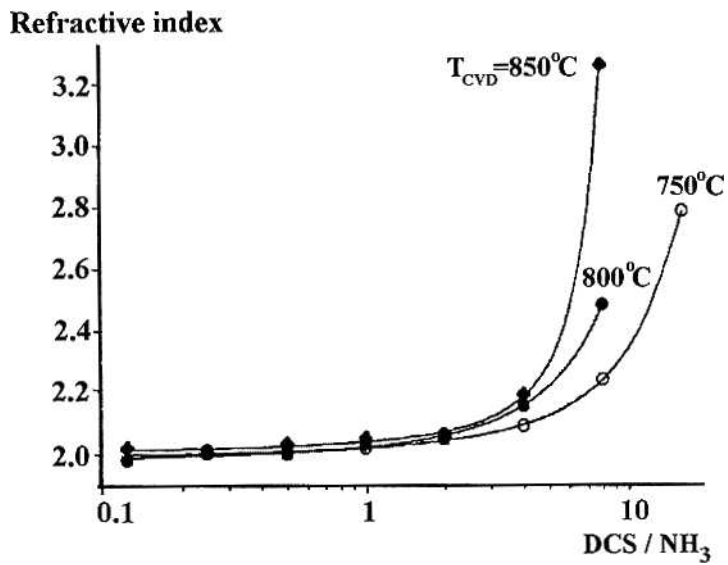


Fig. 3. The dependence of the refractive index on the DCS/ NH_3 ratio.

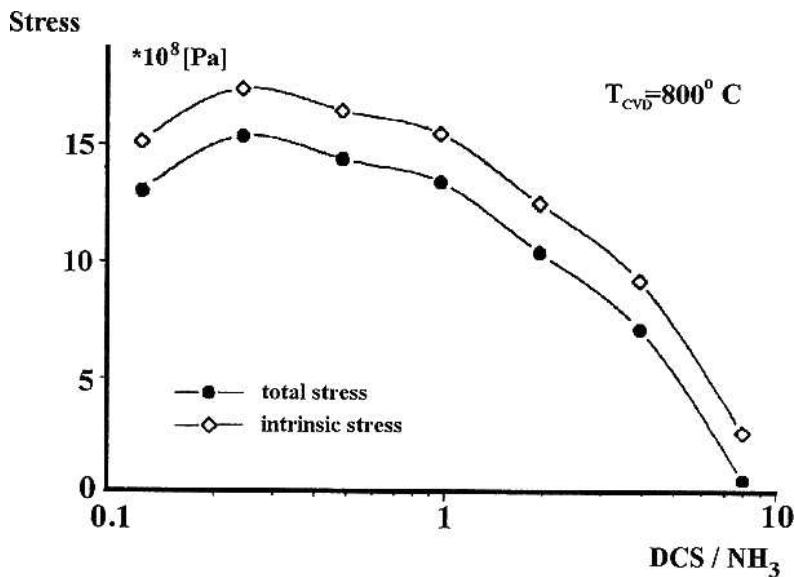


Fig. 4. The dependence of the total and intrinsic stresses on the DCS/ NH_3 .

the result of the existence of the stresses of different signs. Then, the silicon layer was removed in the etching process. The thermal stresses were removed during etching the silicon layer under a silicon nitride membrane. The remained intrinsic stresses were too high, thus they destroyed the thin silicon nitride layer.

A photograph of the membrane surface with silicon nitride is shown in Fig. 5. Traces of the cracks can be seen on the surface.

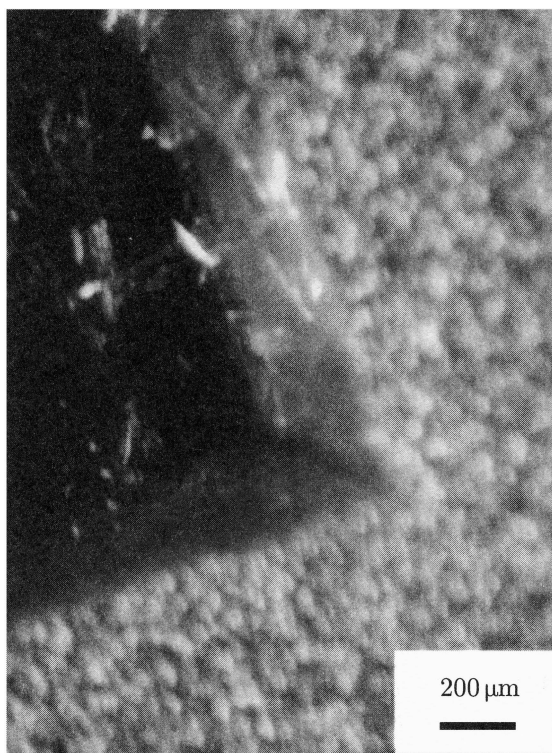


Fig. 5. Micrograph of the membrane surface with a silicon nitride layer (view from the etched surface side).

4. Fabrication of the Boron-Silicon-Glass membrane

The boron doped silicon dioxide layer (BSG-Boron Silicon Glass layer) was deposited by the APCVD (Atmospheric Pressure Chemical Vapour Deposition) method by the reaction of silane (SiH_4), boron hydride (B_2H_6) and oxygen at 300°C . The process of deposition was carried out in the VAPOX 5000 reactor at three different concentration of boron hydride in silane: 1, 2 and 3 percent. The volume ratio of oxygen to the mixture of silane and boron hydride was 2 : 1 [10]. There was atmospheric pressure in the deposition area. Under those conditions, the deposition rate of BSG was about 20 nm/s. The purity of the gases were of “electronic grade”. The thickness of the BSG layers obtained was $2.15\ \mu\text{m}$. The BSG layer was deposited on silicon wafers coated with a thin silicon nitride layer. The thickness of Si_3N_4 was 20 nm; it was deposited by the LPCVD method. Then the second silicon nitride layer 20 nm thick was deposited on the top of the BSG layer.

Silicon nitride layers deposited from both the sides of the BSG layer protected the latter during the silicon etching. The silicon nitride layers were very thin and, therefore, their influence on the BSG membrane deformation was insignificant. The thickness of the layers was measured by a reflectometer and ellipsometer. The photomasking process was performed on the bottom of the wafers and next the silicon nitride layer was etched by plasma. Finally, the silicon was etched in a KOH solution. Membranes of sizes of 2×2.5 mm and the thickness of about $2.1 \mu\text{m}$, consisting of a BSG and two Si_3N_4 layers, were obtained by the anisotropic etching. The dependence of total stresses in the BSG layer on the concentration of the boron doping is shown in Fig. 6. The membrane with the BSG layer is presented in Fig. 7.

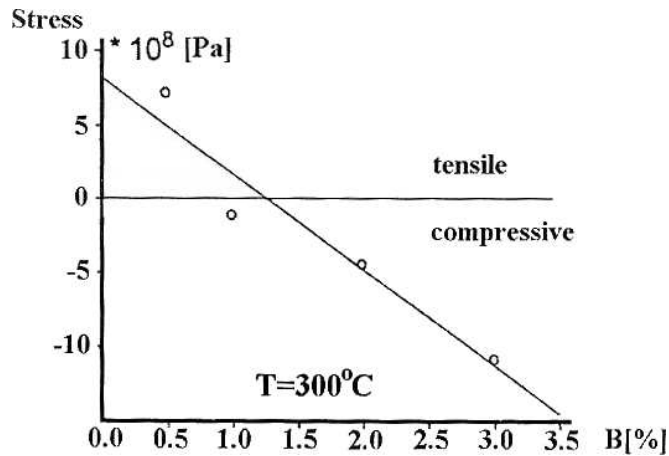


Fig. 6. The dependence of the total stresses on the concentration of the doped boron.

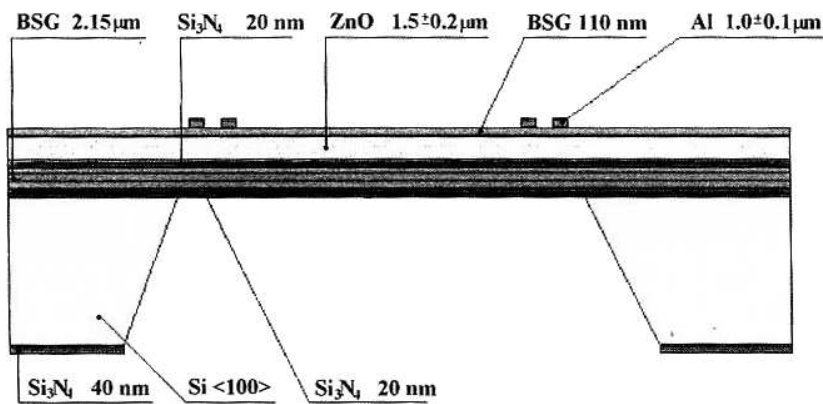


Fig. 7. The cross-section through the sensor membrane with the BSG layer: ZnO — zinc oxide, Al — aluminium, Si_3N_4 — silicon nitride, BSG — boron silicon glass, Si — monocrystalline $\langle 100 \rangle$ silicon.

A photograph of the membrane surface with a BSG layer with apparent surface deformations is shown in Fig. 8.

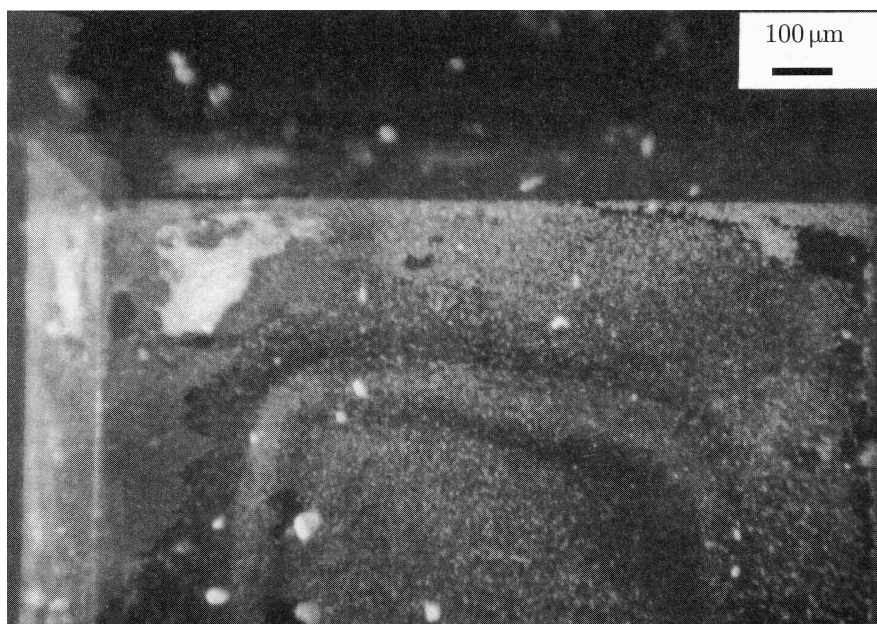


Fig. 8. The micrograph of the membrane surface with a BSG layer (view from the etched surface side).

5. Conclusions

The investigations of the fabrication of thin membranes made of monocrystalline silicon, silicon nitride and boron silicon glass lead to the following conclusions:

1. The rectangular silicon membranes with the sizes (length, width) of several millimetres (the membranes produced were 2.5×2 mm in size) and a thickness ranging from ten to nineteen micrometers meet the requirements of sensors with a Lamba wave. The ratio of the membrane thickness to its other sizes, however, is too low (1 : 150 – 1 : 250) to obtain high sensor sensitivities.

2. The rectangular silicon nitride membranes with the sizes (length, width) of several millimetres and the thickness ranging from one to several micrometers were damaged (cracked) because of the high intrinsic stresses. However, it is possible to obtain membranes of sizes (length, width) lower than one millimetre and a thickness below one micrometre. These small membranes can be applied in the sensors with Lamba wave. Thus allows the ranging of the ratio thickness to other sizes from 1 : 500 – 1 : 1500 and the obtaining of highly sensitive sensors. In this case the paths of electrodes in the IDT transducer should not exceed 3–5 μm.

3. It is possible to obtain rectangular boron silicon glass (BSG) membranes with sizes (length, width) of a few millimetres and thickness ranging from one to two micrometres. The lowest total stresses appear at a concentration of boron hydride in silane of about 1% (Fig. 5). However, surface deformations on some of the membranes were observed; those deformations disqualify them as membranes in sensors with Lamba wave. The production of BSG layers has not been worked out yet and needs further investigations.

Apart from the processes that were discussed in this paper, it is possible to manufacture thin membranes in a different ways, for example, by using etch-stop technique with diffusion or an epitaxial layer. These layers should have a high boron concentration in silicon (more than $8 \cdot 10^{19} \text{ cm}^{-3}$) [12].

Acknowledgements

This work was sponsored by the Polish State Committee for Scientific Research, grant No. 8T10C02216. The author also thanks Dr P. GRABIEC from Institute of Electron Technology in Warsaw for her help in carrying out the investigations.

References

- [1] J. GOŁĘBIEWSKI, *Silicon membrane sensors based on piezoelectric resonators*, Proceedings of the 6 MIXED Design of Integrated Circuits and Systems MIXDES'99, Kraków, 285–288 (1999).
- [2] R. WHITE, P.J. WICHER, S.W. WENZEL and E.T. ZELLERS, *Plate-mode ultrasonic oscillator sensors*, IEEE Trans. Ultrasonics Ferroelectr. Freq. Control, **34**, 162–171 (1987).
- [3] D.F.L. JENKIS, M.J. CUNNINGHAM, G. VELU and D. REMIENS, *The use of sputtered ZnO piezoelectric thin as broad-band microactuators*, Sensors and Actuators, **A63**, 135–139 (1997).
- [4] J. GOŁĘBIEWSKI, *Fabrication of piezoelectric thin film of zinc oxide in composite membrane of ultrasonic microsensors*, J. Mat. Sci., **34**, 19, 4661–4664 (1999).
- [5] R.T. HOWE and R.S. MULLER, *Stress in polycrystalline and amorphous silicon thin films*, J. Appl. Phys., **54**, 4674–4678 (1983).
- [6] M. CHANG, J. WONG and D.N.K. WANG, *Low stress, low hydrogen, nitride deposition*, Solid State Technology, **5**, 462–468 (1988).
- [7] E.A. IRENE, *Residual stress in silicon nitride films*, J. Electr. Mater., **5**, 287–297 (1976).
- [8] M. SEKIMOTO, H. YOSHIHARA and T. OHKUBO, *Silicon nitride single-layer x-ray mask*, J. Vac. Sci. Technol., **21**, 1017–1021 (1982).
- [9] A. MULLER *et al.*, *Dielectric membrane support*, European Semiconductor, **19**, 27–29 (1997).
- [10] J. GOŁĘBIEWSKI, T. BUDZYŃSKI, P. GRABIEC, J. JAŻWIŃSKI and J. KOSZUR, Proceedings of the Conference on “Optoelectronic and Electronic Sensors COE'98”, Jastarnia, Poland, 239–243 (1998).
- [11] B. FOLKMER, P. STEINER and W. LANG, *Silicon nitride membrane sensors with monocrystalline transducers*, Sensors and Actuators, **A51**, 71–75 (1995).
- [12] CH. BURRER and J. ESTEVE, *High-precision BESOI-based resonant accelerometer*, Sensors and Actuators, **A50**, 7–12 (1995).

PERIODIC CRACK-MODEL OF COMB TRANSDUCERS: EFFICIENCY AND OPTIMIZATION

E. DANICKI

Polish Academy of Sciences
Institute of Fundamental Technological Research
(00-049 Warszawa, Świątokrzyska 21, Poland)
e-mail: edanicki@ippt.gov.pl

A model for a comb transducer is investigated in which the comb-sample interface is modeled by a periodic system of cracks. Leaky interface crack waves are generated by a normal incident shear bulk wave beam or by an equivalent excitation of the comb teeth at the interface. The generation efficiency is analyzed in systems where both the comb and the sample halfspaces are from the same material, steel or aluminium, for different teeth width and period, and for the case of solid contact between the two halfspaces between cracks; the other case of sliding contact is discussed briefly. Numerical results show that up to 25% of the incident power can be transformed into interface crack waves by a comb tooth. Optimal number of comb teeth is estimated, and the transducer frequency response is discussed. Approximated relationships are presented that may help designing a comb.

1. Introduction

A model of comb transducer analyzed below was introduced in two earlier papers [1, 2]. They present the analysis of the bulk wave scattering by periodic cracks at the interface of two contacting elastic halfspaces (Appendix A). It has been shown that an interface “crack wave” can be excited by a normal incident bulk wave beam and that this is a leaky wave that sheds its energy back to bulk waves due to the interaction with periodic cracks.

In this paper we continue investigation of the crack wave generation using the convenient transfer function model developed in [2] (and shortly presented in Appendix B), that is applying indirect characterization of the incident bulk wave by certain equivalent excitation of comb teeth at the interface ($\hat{\mathbf{u}}_0$). This approach simplifies much the analysis and delivers sufficiently “flexible” tool for evaluation and optimization of the comb transducer parameters. For simplicity reasons, the same material is assumed for both the comb and the sample to which the comb is applied with solid contact between cracks. The incident wave is a normal propagating shear wave, characterized by a shear force at the comb teeth-sample contact area. (It is worth to note that in the considered

case, the normal stress at the interface vanishes [1] because both the contacting half-spaces vibrate accordingly in this direction. Thus the ‘solid contact’ means vanishing normal stress at the interface between two identical halfspaces. In the complementary case of sliding contact and vanishing shear stress, where the normal stress is applied at the interface, the resulting normal particle displacements of both halfspaces may overlap; this case requires cautious discussion, perhaps including nonlinear effects [3] which may prevent such transducer application in nonlinear investigation of materials [4]. This case is discussed only briefly at the end of this paper.)

The above mentioned relationship is

$$\bar{\mathbf{T}}_m = \mathbf{Y}_{m-n} \dot{\mathbf{u}}_n, \quad (1)$$

where $\bar{\mathbf{T}}_m$ is the total force exerted by the m -th comb tooth (placed at $x = m\Lambda$ where $\Lambda = 2\pi/K$ is the teeth, or crack period) onto the sample, $\dot{\mathbf{u}}_n$ is the equivalent excitation of the n -th tooth at the interface which interpretation is presented in Fig. 3 of [2]. It is sufficient here to describe it as an equivalent difference of displacement velocity of the comb tooth and the sample that accounts for the displacement velocity of the incident wave $\dot{\mathbf{u}}^I$. As concern \mathbf{Y} , its most important component discussed in this paper is that resulting from the propagation of crack waves along the interface and causing some distant teeth to respond to the excitation. In the considered case and the interface normal to y axis, $\dot{\mathbf{u}} = [\Delta\dot{u}_x, 0]$, $\bar{\mathbf{T}} = [\bar{T}_{yx}, 0]$, and \mathbf{Y} are all scalars.

We neglect the local bulk wave field around the excited tooth that vanishes much faster with distance $(n - m)\Lambda$ than the leaky interface crack waves do. The discussed part of the transfer function results from the residuum (at poles $\pm r_c$) of the discrete inverse Fourier transform integral presented below after [2]

$$\mathbf{Y}_k = \frac{1}{K} \int_{-K}^K \left(\frac{a}{r - r_c} + \frac{a}{r + r_c} \right) e^{-jrk\Lambda} \sin \pi \frac{r}{K} dr. \quad (2)$$

Note that in the considered systems ($|r_c| \approx 0$ with respect to K) the integration path can be extended to $\pm\infty$ within accepted accuracy and using the Cauchy theorem, the integral can be easily evaluated by residua (the Jordan’s lemma is satisfied).

Equation (1) allows us to evaluate 1) the delivered power from the excitation source $\dot{\mathbf{u}}_n$ directly to the crack interface waves, that is necessary in evaluation of the efficiency of the comb transducers, 2) how this efficiency depends on the comb/sample material, teeth width and period, 3) and how much power of interface wave can be achieved at the comb edge for long combs having many teeth, accounting for that some distant teeth contribute weakly due to the leaky nature of the interface crack waves causing them to decay along the propagation path. The above subjects are discussed details in this paper on the basis of extended numerical examples for steel and aluminium materials. The analysis is carried out for particular frequency (we apply $\omega = 10^6 \text{ s}^{-1}$ like in [1]), note however that varying K is equivalent to varying ω^{-1} at constant Λ as discussed in [1]. That means that the comb frequency characteristic can be figured out from the transducer efficiency dependence on K .

2. Approximation parameters

It is shown in [1] that the interface “free vibration” exists for certain wave number of cracks K_c , and the leaky interface crack waves exist for $K > K_c$. Thus the primary task is to find K_c for the considered system: crack width $2w$, the material of comb and sample (in this paper they are the same), and the type of contact between cracks (considered solid here). Figure 1 presents the results of computations carried out on the basis of theory presented in [1]. Note that the free vibrations correspond to $r_c = 0$ in Eq. (2), and that $a = 0$ in this case because, as was shown in [1], no normal incident bulk wave is able to excite them.

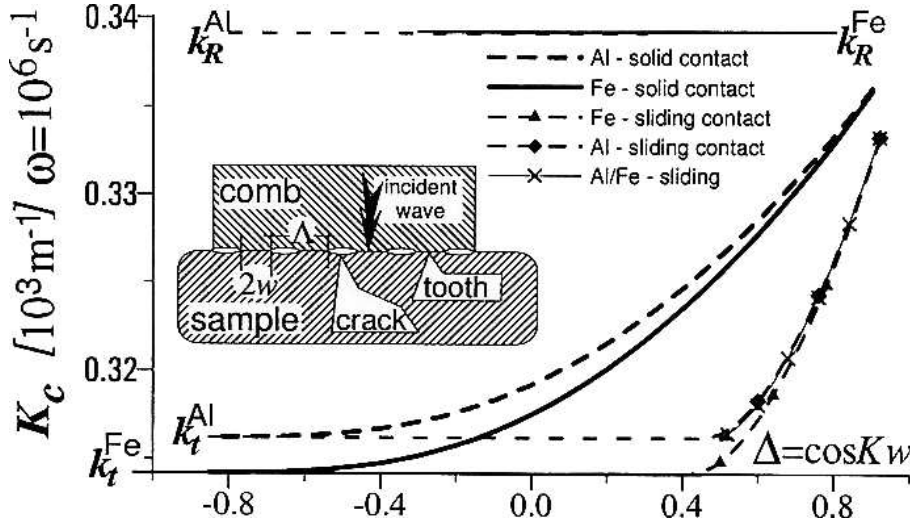


Fig. 1. “Free interface vibration” wave number K_c for cracks in steel (thick solid line) and aluminium (dash), for different crack width ($\Delta = \cos K_c w$). Thin lines with corresponding symbols present cases of sliding contact between the same or different halfspaces. Free vibrations, if exist, have their wave number between corresponding shear and Rayleigh wave numbers, k_t and k_R .

In Eq. (2), two parameters are introduced which must be evaluated numerically for the considered systems: the interface excitation strength a and the wave number r_c that is related to the wave number of the right propagating interface wave by $k_c = -r_c + K$. We apply r_c because conveniently $r_c^R = \text{Re}\{r_c\} > 0$ and $r_c^I = \text{Im}\{r_c\} > 0$. Naturally, $\text{Im}\{k_c\} < 0$ because the leaky wave propagating right, $\exp(j\omega t - jk_c x)$, decays at $x \rightarrow +\infty$ [2].

Starting from K_c , any higher K produces a and r_c different from 0, their evaluation is discussed in [2]. The results are presented in Fig. 2 for steel and aluminium, for several values of crack relative width characterized by $\Delta = \cos K w$ and for certain domain of $K > K_c$. The applied material data are for Al: $\rho = 2.7[10^3 \text{ kg/m}^3]$, $\mu = 27[10^9 \text{ Nm}^{-2}]$, $\lambda = 108[10^9 \text{ Nm}^{-2}]$ resulting in the shear wave number $k_t = .3162[1/\text{mm}]$, and for Fe: $\rho = 7.8$, $\mu = 79$, $\lambda = 112$, and $k_t = .3142$, in corresponding units.

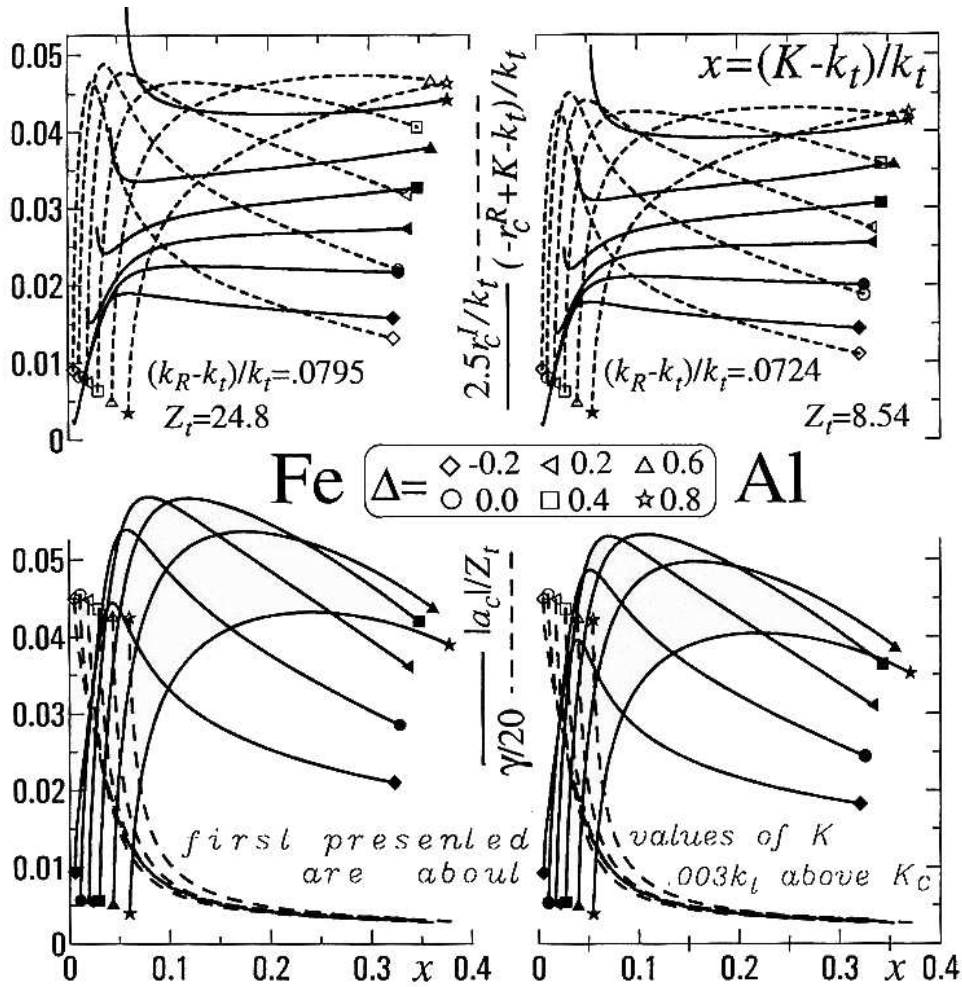


Fig. 2. Parameters of the spectral transfer function approximation, r_c and $|a_c|$, dependent on crack wave number K , for steel and aluminium and different Δ . Horizontal and vertical axes are nondimensional: $(k_c^* - k_t)/k_t$ (imaginary part of k_c^* is $2.5\times$ exaggerated) in the upper row, and a_c/Z_t in the lower. The interface wave number $k_c^R = K - r_c^R$ is little above k_t and almost constant for larger K , while its damping coefficient, r_c^I , has maximum at K close to k_t . If the difference $k_c - k_t$ is larger, then the interface wave field decays faster in depth of the body and thus is more similar and matched to Rayleigh waves propagating at free sample surface. Dash lines present a standing wave coefficient γ (actually $\gamma/20$ to match the scale) discussed in the last section.

3. Energy flow

Let's assume that only $\dot{\mathbf{u}}_0 \neq 0$, and the remaining $\dot{\mathbf{u}}_n$ are all zero accordingly to the solid comb/sample contact condition without existence of any incident bulk wave there (it means, within the interpretation of [2], that we consider a narrow incident wave beam of width constrained to a single comb period). Using Eqs. (1), (2), we easily obtain for

$m \neq 0$ on both sides of the excited tooth at $x = 0$

$$\overline{\mathbf{T}}_m = j\dot{\mathbf{u}}_0 \Lambda a_c e^{-jk_c |m|\Lambda}, \quad a_c = a \sin \pi r_c / K. \quad (3)$$

Neglecting unimportant phase, the total force exerted by m -th comb tooth on the contacting sample behaves like $|\overline{\mathbf{T}}_0| \exp(-r_c^I m \Lambda)$ where $\overline{\mathbf{T}}_0$ is a limit of $\overline{\mathbf{T}}_m$ as formally evaluated from Eq. (3) at $m \rightarrow 0$. This comb tooth/sample contact force results from the decaying leaky interface crack waves that spread the acoustic signal along the interface from the excited tooth to infinity in both directions. This was illustrated in figures presented in [2] in logarithmic scale producing easily recognizable linear dependencies with slope determined by r_c^I .

The above results deserves deeper discussion. For $r_c \sim 0$, the bulk wave reradiated due to the above mentioned leakage, propagates in almost normal direction to the interface. Moreover, the decaying is not very rapid so that we can consider this reradiated wave to be a planar wave, with different amplitude in different Λ -wide domains centered at $m\Lambda$. We know the total force in that domain, it is $|\overline{\mathbf{T}}_m|$, thus we may guess that the average stress in this Λ -wide domain is $\mathbf{T}_0 = |\overline{\mathbf{T}}_m|/\Lambda$. This average is the 0-th Bloch component of the interface stress distribution discussed detailedly in [1].

The surface stress \mathbf{T}_0 (this is a shear stress in the discussed system) excites shear bulk waves of power density $\Pi_y = |\mathbf{T}_0|^2/Z_t$ combined in both upper and lower halfspaces, where $Z_t = \sqrt{\rho\mu}$ is the acoustic impedance. (Exact evaluation of the wave field components and powers is presented in Appendix C.) The power reradiated into bulk in one Λ -wide domain is $\Lambda \Pi_y$ (the power per comb tooth), and the total reradiated (“leaking”) power on both sides of the excited tooth is

$$P^{\text{lk}} = \frac{2}{Z_t \Lambda} \sum_{m=1}^{\infty} |\overline{\mathbf{T}}_0|^2 e^{-2r_c^I m \Lambda}, \quad (4)$$

that must be equal to the total power of the generated interface waves in both directions, that is $2\Pi^c$ where Π^c is the right-propagating interface wave power.

Thus, on the strength of Eqs. (3), (4), we obtain important estimation

$$\Pi^c = \frac{1}{2r_c^I Z_t} \left| \frac{\overline{\mathbf{T}}_0}{\Lambda} \right|^2 = \frac{1}{2} \frac{|a_c|^2}{r_c^I Z_t} |\dot{\mathbf{u}}_0|^2, \quad (5)$$

for the crack wave power generated in one direction by a single tooth. It depends on the excitation strength $\dot{\mathbf{u}}_0$, and also on both spectral transfer function parameters discussed in previous section: r_c and a . (We apply notation of Π for the power flux density: $[\text{Wm}^{-2}]$ for bulk waves and $[\text{Wm}^{-1}]$ for interface waves, and P for total delivered power: Π multiplied by a beam width of bulk waves, for instance.)

In general, the parameter a in Eqs. (2), (3) has complex value. It describes the complicated phenomenon of crack wave generation by the excited comb tooth in presence of the bulk wave field that is excited simultaneously, and which field is described by the term const in Eq. (20) of [2]. This term is neglected in Eq. (2) of this paper; only terms describing interface waves alone are accounted for there. The resulting simplified approximation cannot be used for evaluation of the delivered power to the system through 1) evaluation

of the resulting force at the excited tooth $\overline{\mathbf{T}}_0$, and 2) applying it in the relation for the executed work $.5\text{Re} \{ \overline{\mathbf{T}}_0 \dot{\mathbf{u}}_0^* \}$, because $\overline{\mathbf{T}}_0$ is not the full force there.

There is another point of view however, by analogy to the similar problem for interdigital transducers [5]. We can apply another parameter a' in Eq. (2) instead of the original complex a , in order to evaluate the work on excitation of the *isolated* interface waves only, provided that 1) a' has imaginary value so that the power delivered to the system by far spectrum ($|r|$ large) vanishes (and vanishes if there are no poles at all), and 2) the excited wave field, in our case $|\overline{\mathbf{T}}_m|$, evaluated with a' is the same as that evaluated with a .

Both conditions are immediately satisfied by applying $a' = j|a|$. This makes the relation (2) to describe correctly the system supporting the isolated crack waves only, thus the evaluated force under the excited tooth can be used for evaluation of the executed power on *excitation* of interface waves, that is, the power delivered to crack waves alone

$$\overline{\mathbf{T}}_0' = \frac{\dot{\mathbf{u}}_0}{2K} \int_{-\infty}^{\infty} \left(\frac{|a|}{r - r_c} + \frac{|a|}{r + r_c} \right) (e^{jr\Lambda/2} - e^{-jr\Lambda/2}) dr. \quad (6)$$

Note that the Jordan lemma is satisfied either in lower or upper complex halfspaces of r . This yields $\overline{\mathbf{T}}_0' = j\Lambda|a| \exp(jr_c\Lambda/2)$, and finally the delivered power to the system

$$P^{\text{div}} = \frac{1}{2} \text{Re} \{ \overline{\mathbf{T}}_0' \dot{\mathbf{u}}_0 \} = \frac{1}{2} |\dot{\mathbf{u}}_0|^2 |a| e^{-r_c\Lambda/2} \sin \pi r_c^R / K, \quad (7)$$

which power must be equal to the earlier evaluated total power of both excited crack waves. This produces the relationship that is fairly well satisfied in the computed examples

$$|a| = Z_t r_c^I r_c^R |r_c|^{-2}. \quad (8)$$

Direct evaluation of the excited crack wave power that verifies the above estimation is presented in Appendices C and D; that evaluation is used primarily in the computed results presented below.

4. Transducer efficiency

It results from Eq. (22) of [2] that the incident wave of particle displacement velocity $\dot{\mathbf{u}}^I$ is modelled by $\dot{\mathbf{u}}_0 = 2\dot{\mathbf{u}}^I$ in Eq. (1). Using again the plane wave approximation to the incident shear wave beam of one period width, the estimated incident power is $P^I = .5\Lambda|\dot{\mathbf{u}}_0/2|^2/Z_t$. The one-sided generation efficiency of a single comb tooth (accounting for only the interface wave propagating in either right or left direction), can be defined as

$$\eta_1 = P^c/P^I = r_c^R \Lambda \frac{r_c^I r_c^R}{|r_c|^2}, \quad (9)$$

where we exploited Eqs. (7) and (8). This strikingly simple estimation is valid for close to normal incidence and small r_c , independently of the teeth width or period, but may be less accurate for larger values of $K - K_c$. The bulk to crack wave conversion coefficient is

twice that: $2\eta_1 \approx r_c^R A \text{Im} \{(r_c/|r_c|)^2\}$. Figure 3 presents the single comb tooth efficiency evaluated for aluminium and steel materials. Up to about 25% of the incident wave beam power can be transformed into the interface waves by a tooth in both left and right directions (Appendix E). This is equivalent to about 5% of the incident power in an interface wave in the sample alone and in one propagation direction.

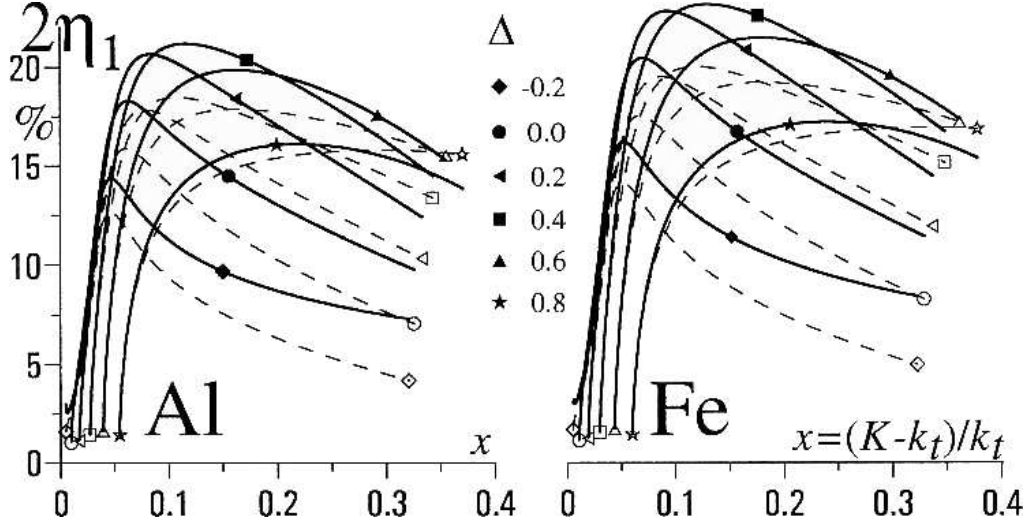


Fig. 3. A single tooth efficiency for aluminium and steel, for normal incident shear wave and solid contact between cracks, evaluated with help of Appendices A and B. Dash lines present the estimated values, Eq. (9). Maximum efficiency is achieved with comb teeth $\sim 30\%$ narrower than half teeth period ($\Delta \sim 0.4$).

It is interesting how much power can be transformed into an interfacial wave by direct tooth excitation, that is by applying $\dot{\mathbf{u}}_0$ neglecting how that can be done practically. This depends on how much bulk wave power is simultaneously generated by $\dot{\mathbf{u}}_0$. This depends on the neglected const in the approximation (2) to $\mathbf{Y}(r)$, see Eq. (20) of [2]. This const can be evaluated by applying small value of $r \ll r_c^R$ in Eq. (17) of [2]. The resulting Fig. 4 shows that this const = 0 for certain K_o . In this case the bulk wave radiation ceases; only interface waves are generated in both directions from the excited tooth. If there are many excited teeth, the evaluated interface wave field looks like these presented in Fig. 4. This figure computed using FFT like in the paper [2] shows that indeed at K_o , the interface wave field includes only the decaying crack waves, without bulk waves.

From practical point of view, more important is the maximum interface wave power that can be generated for given uniform excitation. Each of comb teeth contributes to the crack wave power. For $M = 2N - 1$ excited teeth, the resulting interface wave amplitude can be characterized by a force of the next to the last excited tooth in the system

$$|\bar{\mathbf{T}}_N| = \left| \dot{\mathbf{u}}_0 \sum_{l=1-N}^{N-1} \mathbf{Y}_{N-l} \right| \approx |\dot{\mathbf{u}}_0| \frac{A}{2} |a| |1 - e^{j r_c M \Lambda}|, \quad (10)$$

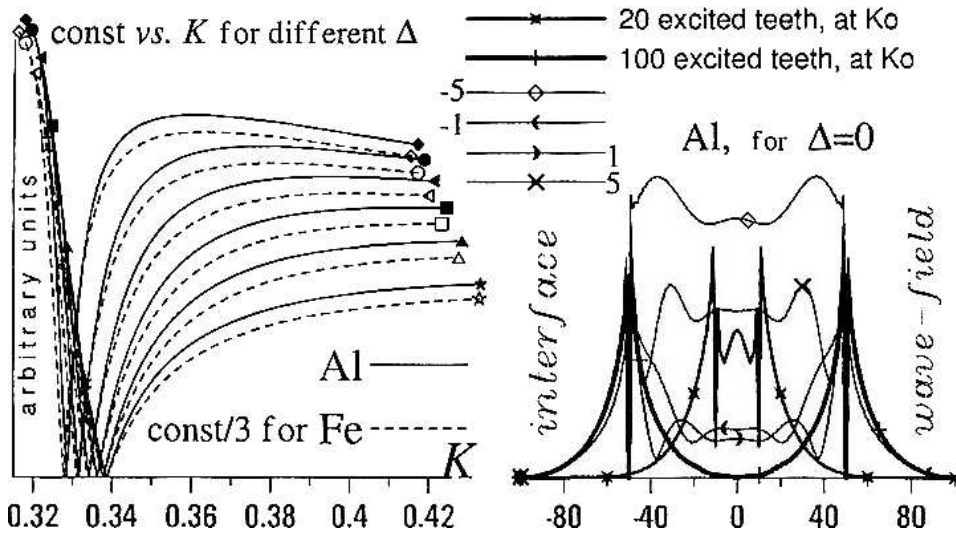


Fig. 4. The const part of $Y(r)$ that is responsible for direct bulk wave generation by the excited comb teeth, vanishes at certain K_0 . The wave-field exponential shape inside the uniform excitation domain of 100 teeth confirms well that there is almost exclusively an interface wave without a floor of bulk waves. This is not the case if $K \neq K_0$, shown here for comparison. This figure clearly shows that applying more teeth than optimal does not produce any higher interface wave amplitude: compare wave-fields outside the excitation domains of 20 and 100 teeth.

Its value is $|1 - e^{jr_c M \Lambda}| |2 \sin \pi r_c / K|^{-1}$ times greater from the earlier evaluated $|\bar{T}_1|$ for a single excited tooth, Eq. (3).

Applying this value for estimation of the crack wave power, Eq. (5) or the corresponding relations from Appendix C, we obtain that

$$\Pi^c = \Pi_\infty |1 - e^{jr_c M \Lambda}|^2, \quad \Pi_\infty = \frac{P^I}{2r_c^I \Lambda} |a/Z_t|^2, \quad (11)$$

where $P^I = .5Z_t \Lambda |\dot{u}^I|^2$ is the incident power per comb period. In the limit of infinite comb, $\Pi^c = \Pi_\infty$. The coefficient $g = \Pi^c / P^I$ shows how much times the crack wave power is greater than the incident bulk wave power per comb period. The transformation efficiency of comb transducer is g/M because the total incident power is $M P^I$. Example dependences of the generated interface wave power on a number of exciting comb teeth are shown in Fig. 5 (reminding the correspondence of ω and K^{-1} , this figure also represents the comb frequency response). There are local maxima resulting from certain interference of contributions of the edge comb teeth that ceases with growing M because of wave damping, $r_c^I > 0$. For given K , the first maximum appears at M where

$$e^{-r_c^I M \Lambda} \sin \phi = \sin(r_c^R M \Lambda + \phi), \quad \sin \phi = r_c^I / |r_c| \quad (12)$$

$(\pi - 2\phi < r_c^R M \Lambda < \pi - \phi)$. This M is an optimal number of teeth making the comb to produce the maximum power of an interface crack wave.

It depends on r_c how many teeth the comb must count to achieve the maximum crack wave power. In practice, the comb should have number of teeth evaluated for K produc-

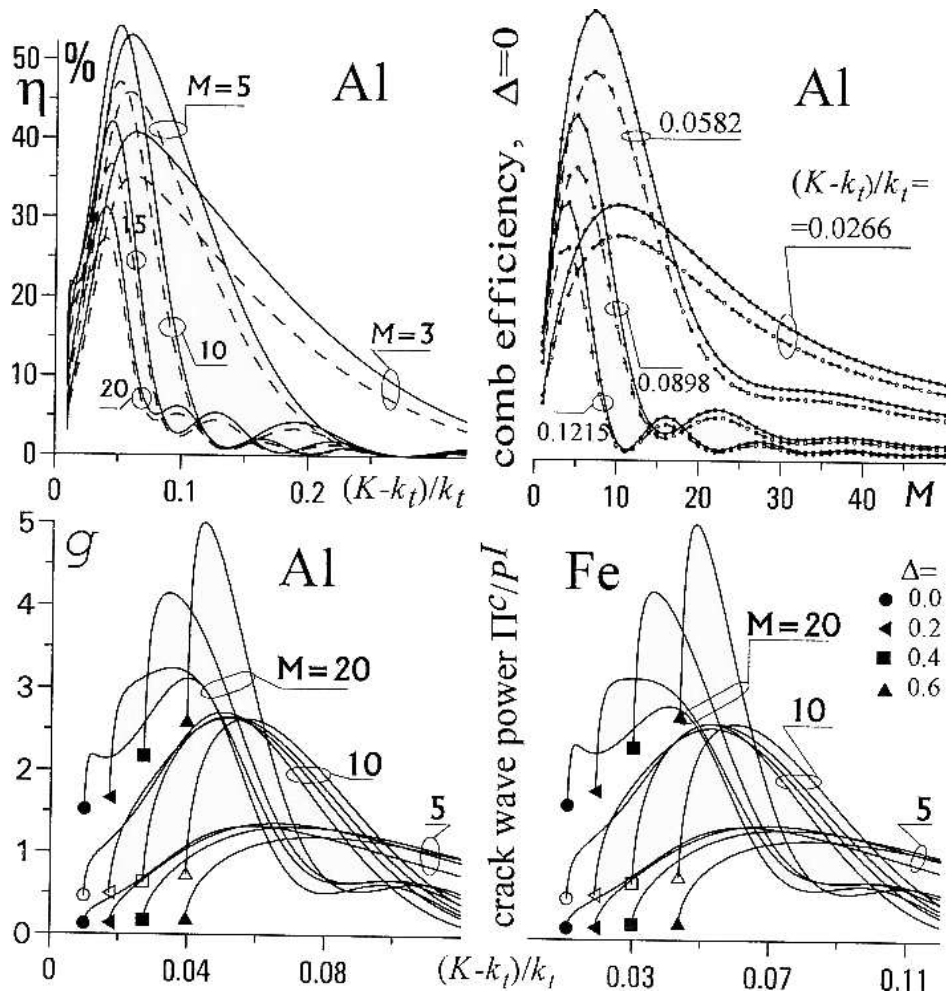


Fig. 5. Power conversion efficiency of combs with different teeth number M , as evaluated from the crack wave power (solid lines) and estimated (dash lines). Accounting for that $\omega \sim K^{-1}$ for given comb period, the frequency characteristic of comb can be figured out from the comb efficiency dependence on K . Figures show that, for reasonable values of M , the maximum efficiency is achieved at K not much higher from K_c , and that the efficiency is higher for narrower teeth, at cost of narrower passband, which relative width is generally smaller by half, than M^{-1} .

ing the highest interface crack power. Figure 6 presents the convenient dependency of maximum interface power on the optimal number of teeth, both evaluated for given K . This parametric dependence (with parameter K), is sufficient for the comb optimization: we seek the largest power possible within the required passband that is inversely proportional to the teeth number (Fig. 5).

In the discussed transfer function model, we neglected the term resulting from the unknown \mathbf{T}_0 in Eq. (B.1). Now we check the validity of this assumption. Figure 6 presents the interface wave field evaluated from the model and evaluated directly from

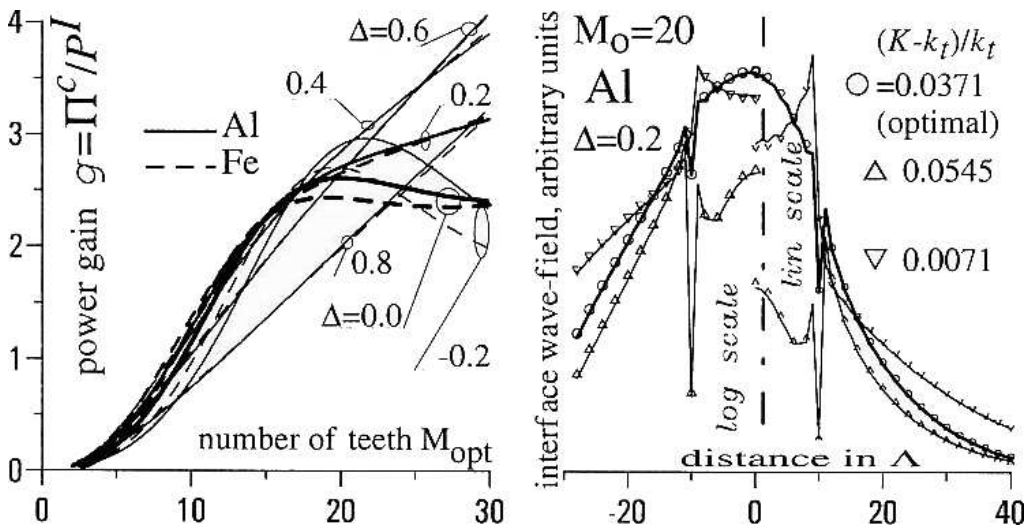


Fig. 6. A basis for comb optimization: the parametric dependence of maximum, with varying K , of the generated crack wave power on the teeth number M : for given K , an optimal M is evaluated and then the resulting crack wave power at the comb edge. Much higher power can be achieved with larger but not practical values of M resulting for lower K , and for narrower teeth width because of smaller crack wave leakage: smaller r_c^I at low $K - K_c$. Example interface wave-fields are shown for optimal value of $M_o = 20$ teeth assumed somewhat narrower than half period Λ ($\Delta = 0.2$), inside and outside the comb domain and for optimal, lower and higher values of K . They are evaluated using the model (lines), and by applying the “ $\sin x/x$ ” angular spectrum of incident wave beam $\mathbf{T}^I(r)$ in Eq. (A.1) (symbols). The overlapping results confirm the assumptions applied in modeling the teeth excitation (Appendix B).

Eqs. (A.1)–(A.5), by applying $\mathbf{T}^I(r) = M \sin(rM\Lambda/2) / \sin(r\Lambda/2)$: this is an approximated spectrum of uniform incident wave beam of width $M\Lambda$. The agreement is excellent.

5. A modified comb

Let’s consider a slightly oblique incidence, at angle α off normal. It results in the interface force having different phase at different comb teeth: $\dot{\mathbf{u}}_t = \dot{\mathbf{u}}_0 \exp(jl\Lambda k_t \sin \alpha)$. Neglecting the origin of these forces, whether resulting from an incident wave or from a direct teeth excitation, their spectral representation at the interface plane has the known “ $\sin x/x$ ” shape, $x = (r - k_t)M\Lambda/2$ where $M\Lambda$ is the excitation area.

For normal incidence considered in previous sections, this $\sin x/x$ function is centered at $r = 0$. The excited interface wave amplitude however, is evaluated from Eqs. (1), (2) at poles $\pm r_c \neq 0$. This means particularly that the interface waves are excited inefficiently by side, off-maximum spectral line of the excitation force, and can be near zero if r_c^R falls near zero of $\sin x/x$ (this depends on M). The remedy to this deficiency is discussed here. To place the maximum spectral line of the excitation force closer to r_c , we modify the comb transducer arrangement by applying oblique wave beam incidence. In order to stay within previously applied assumption of $T_{22} = 0$ at the comb/sample interface, two

oblique incident shear waves (with $\pm\alpha$ angle of incidence) should be generated by two piezoelectric slab transducers at the comb top. Their total normal power flux combined Π_y yields an equivalent teeth excitation $\dot{\mathbf{u}}_0 = \sqrt{2\Pi_y \cos \alpha / Z_t} \exp(\pm j k_I x)$ that is $\sqrt{\cos \alpha}$ times that of a single normal incident wave beam discussed earlier.

A pair of off-normal incident wave beams produces an interface excitation force having two spectral lines of $\sin x/x$ shapes with maxima placed at $\pm k_I$. We may assume that the left incident wave beam, producing spectral line at k_I , matches $r_c = K - k_c$ and produces only the left-propagating crack wave, and the right wave beam – the right interface wave only. For uniform excitation with variable phases, the amplitude of tooth force just right to the comb is

$$\begin{aligned} \bar{\mathbf{T}}_N &= \dot{\mathbf{u}}_0 \sum_l \int_{-K}^K \frac{a}{r + r_c} e^{j(r - k_I)(N-l)\Lambda} \sin \pi r / K \, dr / K, \\ |\bar{\mathbf{T}}_N| &\approx |a_c| |\dot{\mathbf{u}}_0| \Lambda \left| \frac{1 - \exp j(r_c - k_I)M\Lambda}{2 \sin(r_c - k_I)\Lambda/2} \right|, \end{aligned} \quad (13)$$

which $|\bar{\mathbf{T}}_N|$, like in all numerical results presented above, can be applied in equations of Appendices C, D in order to evaluate the interface power Π^c .

The maximum crack wave appears at $k_I = r_c^R$; this determines a center frequency of the structure. This maximum is $\sim M \exp(-r_c^I M \Lambda / 2)$ dependent on M , and there is optimal $M_o = 2/r_c^I \Lambda$ producing its largest value $\sim M_o/e$. The maximum value of $|\bar{\mathbf{T}}_N|/\Lambda$ is $|\dot{\mathbf{u}}_0| |a_c| M_o/e$ which value is used for the estimation of both generated interface waves power based on Eqs. (5) and (8).

$$2\Pi_{\max}^c \approx 8 \frac{\Pi_y \Lambda \cos \alpha}{r_c^I \Lambda} \left| a \frac{r_c \Lambda}{2Z_t} \right|^2 \frac{M_o}{e^2} \frac{2}{r_c^I \Lambda}, \quad (14)$$

it can be as high as $.5\Pi_y M_o \Lambda$. It results that almost 50% conversion can occur in an optimal case.

The structure is promising. Particularly, $r_c - k_I$ can have purely imaginary value at center frequency. Thus the maximum interface wave power is *independent* of how large the value of r_c^R is, allowing us to exploit the optimal case of large a and small r_c^I in the whole domain of K . With small r_c^I , we get large optimal wave beam width $M_o \Lambda$ that is large total incident power, and large part of it can be converted into crack waves at center frequency.

6. Incident longitudinal waves

The short discussion here concerns the case of normal incidence of longitudinal wave beam and sliding contact between cracks. The same materials are assumed for the comb and the sample. Therefore the interface stress $\mathbf{T} = [0, T_{yy}]$, particle displacements $\mathbf{u} = [0, u_y]$, acoustic impedance $Z_t = \sqrt{\rho(2\mu + \lambda)}$, and proper transfer function \mathbf{Y} should be applied in the theory that is otherwise similar to that presented above for incident shear wave. Here we present only numerical results in the domain of K where Eq. (8)

is satisfied with adequate accuracy. This means that the same physical interpretation of the results holds in both cases.

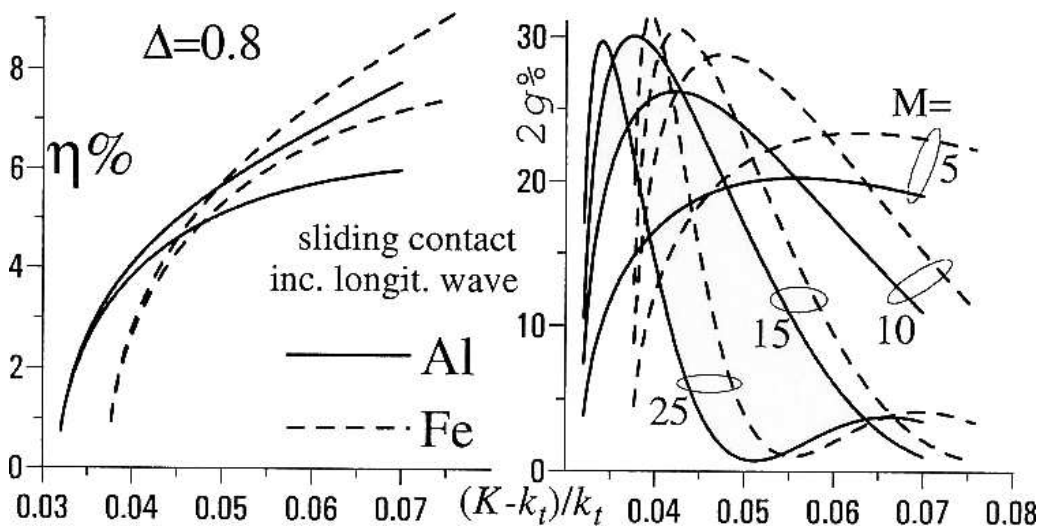


Fig. 7. Optimization figure for the case of incident longitudinal wave and sliding comb-sample contact. The efficiencies evaluated from the Bloch wave powers (higher values) and estimated, Eq.(9) (lower values), diverge at higher K indicating that the model losses its validity there. The comb efficiency is much lower than in the case of incident shear wave in the analogous domain of K and M .

We notice from Fig.1 that the free vibrations exist only for relatively wide crack and narrow teeth: below $\Lambda/3$ wide. Figure 7 presents the single tooth efficiencies, both evaluated from the energy flow of the generated wave-field, and from the approximation (8). Note that the efficiency is much lower than in the previously discussed case of solid contact in similar domain of K . This results in low efficiency of comb having practical $M < 25$ teeth; the generated power is much less than the incident power per comb period.

7. The edge phenomena

Above, we discussed the phenomenon of interface wave generation in infinite system of periodic cracks, that is the generation under an infinite comb attached to an infinite sample (albeit only finite number of teeth were insonified by the incident wave beam). The interface waves were assumed to propagate freely along the entire system. This assumption is correct for combs long enough with respect to the interface wave length $2\pi/k_c \approx \Lambda$, and is well satisfied for combs with near optimal number of teeth (10 or more, Fig. 6).

There is an edge however in any practical combs, where the crack waves can no longer propagate and thus the complicated phenomena of reflection, transformation into a Rayleigh wave existing outside comb, and scattering into bulk waves must be invoked.

It is far beyond the scope of this paper to cover adequately the resulting diffraction problem for semiinfinite periodic system (to focus attention on the single edge of a comb only). Instead, we will present a simplified model appropriate only for better physical understanding of comb transducers. We will consider only the wave field in the sample neglecting this part of the interface wave that propagating inside the comb, must fall on the comb walls and scatter. Moreover, we neglect the backward wave component of the interface waves.

The considered system is periodic, and thus the interface wave field is composed of series of Bloch components. Two of them, ± 1 st components carry energy along the interface: the 1st carries energy in positive direction with respect to the interface wave propagation, this is a forward propagating component, and the -1 st carries energy in opposite direction – this is a backward wave component. The power carried by an interface wave is the sum of both partial powers $\Pi^c = \Pi^{(1)} + \Pi^{(-1)}$, accounting for that $\Pi^{(-1)} < 0$. These two components may have quite different wave numbers: $k_c = k_1 = -r_c + K$ and $k_{-1} = -r_c - K$ respectively for the forward and backward components of a crack wave propagating right, and they decay quite differently in depth of the sample [1]. This makes the considered scattering phenomenon much more complicated than the corresponding phenomenon of interdigital transducers where both forward and backward components are only weakly perturbed Rayleigh modes [3] in which case the exploited simplification leads to the reflection/transmission problem only.

Examples of the standing wave coefficients $\gamma^2 = -\Pi^{(-1)}/\Pi^{(1)}$ in the considered structures are presented in Fig. 2, as yet another characterization of interface waves. We notice that $\gamma \rightarrow 1$ at $K \rightarrow K_c$; this explains why the interface “free vibrations” ($K = K_c$) do not transport energy along the interface: the energy carried back by backward Bloch component compensates perfectly the energy carried forward by the forward component. For greater K however, $\gamma < 1$ and the backward energy transport diminishes allowing some net energy to be transported along the interface; this is the interface wave power. In what follows, we will consider the case of small γ , allowing us to neglect the backward wave component. This simplifies the modeled wave scattering phenomenon. It is still however, much more complicated than that for interdigital transducers because of proximity of wave numbers k_c and k_t (the shear wave number). Due to the resulting significant difference in the penetration depths of crack and Rayleigh waves, much power is expected to be scattered into bulk waves.

Summarizing, the model of the scattering problem is the following. There is a semi-infinite comb where an interface wave propagates (only its forward propagating Bloch component is accounted for but its damping is neglected, $\text{Im}\{k_c\} \rightarrow 0$) towards the edge where it scatters producing the transmitted Rayleigh wave outside the comb, and also producing the reflected interface wave and bulk waves. We are interested mostly in the transmitted Rayleigh wave amplitude and also in the reflected interface wave because it can result in certain spurious “ringing” phenomenon in real finite combs. The problem is considered in detail in Appendix F with help of the Wiener-Hopf technique [6]. Figure 8 presents the computed examples. Generally, the interface wave to Rayleigh wave transformation depends strongly on k_c when $k_c \sim k_t$. In practical combs however, k_c does not change much with K (Figs. 2 and 3) and thus the transmission coefficient does not

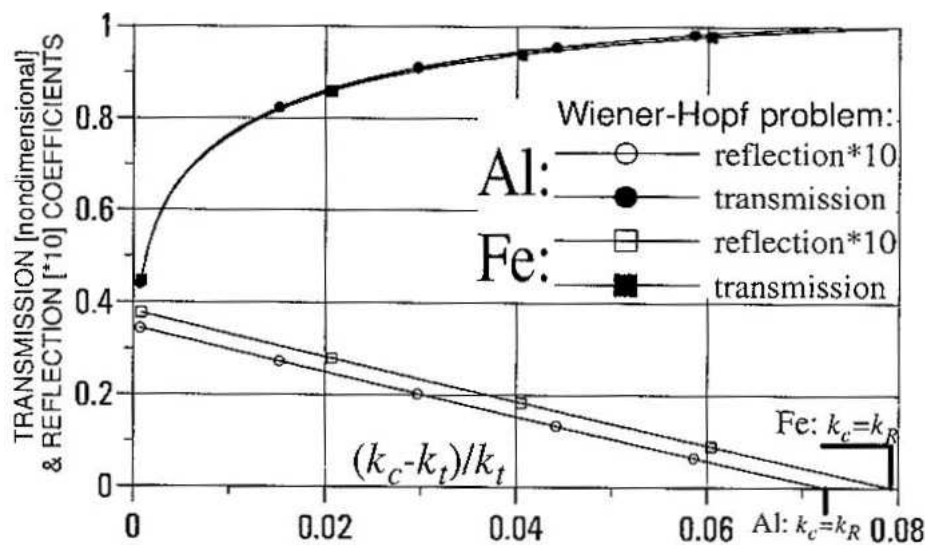


Fig. 8. An interface to Rayleigh wave transformation at the comb edge, estimated on the basis of the Wiener-Hopf diffraction problem: the incident and the reflected crack waves have wave numbers $\pm k_c$, the transmitted is the Rayleigh wave with wave number k_R . The transmission is low when k_c is close to k_t , and is full when $k_c \approx k_R$. Reflection coefficient is small, few percents, and can be neglected. The remaining part of the incident wave power is scattered into bulk waves.

change significantly with K : it is approximately 90%. The reflection coefficient can be neglected.

8. Conclusions

Comb transducers are rather complicated structures. The developed model is perhaps the simplest but powerful enough to figure out the transducer basic parameters: efficiency and frequency response, and can be used for certain optimization of the system. Moreover, the model reveals a number of wave phenomena involved in the bulk to Rayleigh wave transformation needed for better understanding the comb in practical use.

Summarizing the numerical results presented in this paper we conclude that the efficiency of comb transducers is not high; about 5% of the incident power (MP^I) is transformed into right-propagating Rayleigh wave in the sample only. The usefulness of comb relies however on using large P^I (incident power per comb period) to generate strong Rayleigh wave of power $\sim 2P^I$. The overall efficiency can be perhaps improved with the proposed modified comb (oblique incidence).

Surprisingly, the optimal number of comb teeth (~ 20) agree with practical applied combs [4] (they are usually glued to the sample with salol to make rather solid contact; practical comb teeth height is a fraction of comb period, and the crack model with infinitesimal teeth height seems acceptable). However, low expected efficiency of comb with longitudinal incident wave is rather disappointing.

Perhaps higher efficiency at smaller M and wider transducer passband can be achieved with different comb material of rather low acoustic impedance and especially optimized for given types of materials, e.g. steel or aluminium. Anisotropic or composite materials can also be analyzed within the developed technique.

Acknowledgments

Dr. Donna Hurley from NIST, Boulder, is acknowledged for sharing her experience with comb transducers, and also for her kind assistance in preparation of this paper. Financial support was provided by the Polish-US Maria Curie Skłodowska Joint Fund II under Grant No. PAN/NIST-97-300. This paper is dedicated to the memory of Maria Curie Skłodowska, a double Nobel laureate.

Appendix A: The scattering problem

An elastic halfspace $y > 0$ is characterized in spectral domain by a harmonic Green's relationship $\mathbf{u} = \mathbf{G}\mathbf{T}$, where \mathbf{u} and \mathbf{T} are surface particle displacement and stress; \mathbf{G} is the Green's matrix for the sample. The incident wave in comb material is characterized by $\mathbf{u}^I = \overline{\mathbf{G}}\mathbf{T}^I$. The scattering problem of bulk waves on cracks is described by a system of equations [1]

$$[\mathbf{g}_\infty S_{n-m} - \mathbf{g}(r + nK)]\mathbf{t}_m P_{n-m}(\Delta) = -\dot{\mathbf{g}}(r)\delta_{n0}\mathbf{T}^I(r), \quad (\text{A.1})$$

for n -th Bloch wave field component, $r \in (0, K)$. There is summation over $m \in [-N, N+1]$, P_ν is a Legendre function, and

$$\mathbf{g}(p) = -jp \left(\mathbf{G} + \overline{\mathbf{G}}^T \right), \quad \dot{\mathbf{g}}(p) = -jp \left(\overline{\mathbf{G}} + \overline{\mathbf{G}}^T \right). \quad (\text{A.2})$$

The applied method of solution allows us to constrain n to a finite domain: $n \in [-N, N]$, where $N \gg k_t/K$ (the domain of n is shifted left for $r \sim K$); we used $N = 3$ in computations.

The equation results from a contact condition between comb and sample

$$\overline{\mathbf{u}} = \frac{j\pi}{K \sin \pi r/K} \mathbf{g}_\infty (-1)^m \mathbf{t}_m P_{-m-r/K}(-\Delta) = 0 \quad (\text{A.3})$$

that closes the system.

Now, $\mathbf{t}_m(r)$ can be evaluated for any r and given spectrum of the incident wave $\mathbf{T}^I(r)$. For example, the n -th Bloch component of the interface stress is

$$\mathbf{T}_n = \mathbf{t}_m P_{n-m}(\Delta). \quad (\text{A.4})$$

and the spectral representation of a discrete interface force is

$$\overline{\mathbf{T}}(r) = \Lambda \mathbf{t}_m P_{-m-r/K}(\Delta), \quad (\text{A.5})$$

which inverse Fourier transform over domain $(0, K)$ yields $\overline{\mathbf{T}}_l$, the total force exerted by l -th comb tooth on the sample. This force may result directly from the incident wave

beam or, if l is outside the area of incidence $(-M/2, M/2)$, from the generated interface waves. In this case $\bar{\mathbf{T}}_{M/2+1}$ can be used for evaluation of the crack wave amplitude. This straightforward evaluation of the excited interface wave was applied in [2]. In this paper, we apply the transfer function model presented in Appendix B.

Appendix B: The model

Following the earlier development [2], the incident wave \mathbf{T}^I can be equivalently characterized by a direct teeth excitation $\dot{\mathbf{u}}$. Here, we present shortly how, and with what approximation, can this be done.

It is assumed here that r/K is small. This is reasonable if the normal incident wave beam is wide and thus its spectrum is narrow, see Eq. (A.1). In what follows, we will neglect small terms of an order of r . Noticing first that the right-hand side of the Eq. (A.1) at $n = 0$ is small ($\sim r$), we divide it by $-jr$ and add to Eq. (A.3) multiplied by $jK \sin(\pi r/K)/\pi \approx -jr$. This yields

$$-jr^{-1} \mathbf{g}_\infty [S_{-m} P_{-m}(\Delta) - (-1)^m P_{-m-r/K}(-\Delta)] \mathbf{t}_m = 2\mathbf{u}^I - [\mathbf{G} + \bar{\mathbf{G}}^T] \mathbf{T}_0, \quad (\text{B.1})$$

because $\dot{\mathbf{g}}\mathbf{T}^I = 2\mathbf{u}^I$. The other component on the right-hand side, $(\mathbf{G} + \bar{\mathbf{G}})\mathbf{T}^{(0)}$ is still unknown. We will have to check it *a posteriori* if this term can be neglected.

Note that the coefficients of above equation are of an order of r^0 , thus finite with $r \rightarrow 0$. Moreover, with the accepted accuracy, Eq. (A.1) at $n = 0$ becomes

$$\mathbf{g}_\infty S_{-m} \mathbf{t}_m P_{-m}(\Delta) = 0. \quad (\text{B.2})$$

It makes possible to neglect the first term of (B.1), and thus for $r \rightarrow 0$, the Eq. (A.1) and the above equations yield the following system that constitute the model

$$\begin{aligned} [\mathbf{g}_\infty S_{n-m} - \mathbf{g}(r+nK)] \mathbf{t}_m P_{n-m}(\Delta) &= 0, \\ j\omega \mathbf{g}_\infty (-1)^m \mathbf{t}_m P_{-m-r/K}(-\Delta) &= \dot{\mathbf{u}} \sin \pi r/K, \end{aligned} \quad (\text{B.3})$$

which $\dot{\mathbf{u}}(r) = 2\dot{\mathbf{u}}^I - j\omega(\mathbf{G} + \bar{\mathbf{G}})\mathbf{T}^{(0)}$. Using Eqs. (A.5) and (B.3), we evaluate the spectral transfer function $\mathbf{R}(r)$ involved in

$$\bar{\mathbf{T}}(r) = \mathbf{R}(r) \dot{\mathbf{u}} \sin \pi r/K, \quad \mathbf{R}(r) \approx \text{const} + \mathbf{Y}(r), \quad (\text{B.4})$$

as presented in [2]. Its inverse Fourier transform yields Eq. (1), neglecting the const term, unimportant for interface waves.

The unknown component in $\dot{\mathbf{u}}$ on the right-hand side of Eqs. (B.3) requires certain further interpretation. We attempt to replace the incident wave, the true source of interface waves, by certain *known* teeth excitation at the interface. This is like attempting to neglect the intrinsic impedance of an electric voltage source, replacing it by *known* voltage at the load port. Naturally, we need to correct this voltage *a posteriori*, accounting for the voltage drop due to the current flowing through the impedance.

Something similar, but more complicated is the case considered in this paper: the interface equivalent excitation $\dot{\mathbf{u}}$ depends on the unknown 0-order Bloch component of

the interface stress \mathbf{T}_0 . The same stress is responsible for the leakage of interface waves which is rather small, allowing the wave to propagate along the interface. This suggest that it can be indeed neglected.

Moreover it is worth to note here that the interface stress \mathbf{T}_1 is, in fact, responsible for resonant generation of the interface waves because both have the same wave number $-r_c + K = k_c$ (for right propagating waves). Thus we can define alternatively the equivalent $\dot{\mathbf{u}}$ that reproduces, at $r = -r_c = k_c - K$ and in a domain around it, the original \mathbf{T}_1 resulting from \mathbf{T}^I in Eq. (A.1).

To check the validity of the above introduced model, we may evaluate $\mathbf{Y}(r)$ and \mathbf{T}_1 in both cases, that is using 1) Eqs. (A.1) and (A.3) with \mathbf{T}^I given, and 2) Eqs. (B.3) with given *equivalent* $\dot{\mathbf{u}}$, solving these equations and evaluating the above mentioned functions of r . The numerical verification proves that the above mentioned equivalent characterization is very satisfactory in most important domain of spectral variable $|r - r_c| \leq |r_c|$, for any K discussed in this paper. In fact, this is also confirmed in Fig. 6. As such, it can be used for evaluation of both r_c and a , and the Eq. (1) can be indeed applied in our analysis of comb transducers.

Appendix C: Amplitudes and powers

Introducing notation for longitudinal and shear partial wave amplitudes F_l and F_t , it was shown in [1] that

$$\begin{bmatrix} \dot{u}_1 \\ \dot{u}_2 \end{bmatrix} = \frac{j}{\sqrt{\rho\omega}} \begin{bmatrix} p & -q_t \\ q_l & p \end{bmatrix} \begin{bmatrix} F_l \\ F_t \end{bmatrix}, \quad (\text{C.1})$$

which $F_{l,t}$ can be evaluated from stress $\mathbf{T} = [T_{21} \ T_{22}]^T$ at $y = 0$

$$\begin{bmatrix} F_l \\ F_t \end{bmatrix} = j \frac{\omega}{\mu} \frac{\sqrt{\rho\omega}}{D} \begin{bmatrix} 2pq_t & k_t^2 - 2p^2 \\ 2p^2 - k_t^2 & 2pq_l \end{bmatrix} \begin{bmatrix} T_{21} \\ T_{22} \end{bmatrix}, \quad (\text{C.2})$$

where p is the wave number $r + nK$ of n -th Bloch component of a wave field; $q_{l,t}$ are p -dependent wave numbers in depth of the body of corresponding partial waves, and

$$\Pi_2 = \text{Re} \{ q_l |F_l|^2 + q_t |F_t|^2 \} / 2 \quad (\text{C.3})$$

is the y -component of the Poynting vector. It can be used for evaluation of the power shed by the interface wave into bulk wave, particularly by its 0-order Bloch component, $p = -r_c$ for the right propagating interface wave.

To evaluate the x -component of Poynting vector, we need T_{11} . It must be evaluated from equations of motion of the body

$$T_{11,1} + T_{12,2} = -\rho\omega^2 u_1, \quad (\text{C.4})$$

which, using (A.1-2), yields $T_{11} = j\mu[(2q_l^2 - k_t^2)F_l + 2pq_t F_t]/(\omega\sqrt{\rho\omega})$ and thus

$$[T_{11} \ T_{12}] = \frac{j}{\sqrt{\rho\omega}} \frac{\mu}{\omega} [F_l \ F_t] \begin{bmatrix} 2q_l^2 - k_t^2 & -2pq_l \\ 2pq_t & 2q_t^2 - k_t^2 \end{bmatrix}. \quad (\text{C.5})$$

Taking into account that the wave field inside the body is $\exp(j\omega t - jpx - jq_{l,t}y)$, $y > 0$ for instance, the x -component of Poynting vector is $\Pi_1 = .5\text{Re} \{ \mathbf{T}\dot{\mathbf{u}}^* \}$, that is

$$\begin{aligned} \Pi_1(y) &= -\frac{1}{2}\text{Re} \{ k_t^{-2} [F_l \ F_t] \mathbf{X} [F_l^* \ F_t^*]^T \} \\ \mathbf{X} &= \mathbf{E} \begin{bmatrix} 2q_l^2 - k_t^2 & -2pq_l \\ 2pq_t & 2q_t^2 - k_t^2 \end{bmatrix} \begin{bmatrix} p^* & -q_t^* \\ q_l^* & p^* \end{bmatrix} \mathbf{E}^*, \end{aligned} \quad (\text{C.6})$$

where $\mathbf{E} = \text{diag}(e^{-jq_l y}, e^{-jq_t y})$.

For real $q_{l,t}$ this yields the y -averaged value analogous to (C.3)

$$\Pi_1 = \text{Re} \{ p|F_l|^2 + p|F_t|^2 \} / 2, \quad (\text{C.7})$$

but in our analysis, where both p and q 's are complex, the wave field decays in depth of the body and we need the total power carried in the domain $y \in (0, \infty)$. This requires integration of Eq. (C.6) term by term

$$\Pi_x = \int_0^\infty \Pi_1(y) dy \quad (\text{C.8})$$

(the resulting formula is too complex to be presented here). The above relations can be applied to any Bloch component of an interface wave under substitution $p = -r_c + nK$.

Appendix D: Low Bloch components

The boundary value problem for interface crack waves is closed in the homogeneous system (A.1), (A.3) taken with $\mathbf{T}^I = 0$, or equivalent system (B.3) taken with $\dot{\mathbf{u}} = 0$; its solution is then eventually applied in other equations to obtain corresponding wave field components, particularly \mathbf{T} , that may characterize the wave amplitude. For given \mathbf{T} , we use Eqs. (A.5) in place of (A.3) to evaluate \mathbf{t}_m and then the other wave field components, particularly the lower Bloch components of interface stress, $\mathbf{T}_{0,\pm 1}$ from Eq. (A.4) at $n = 0, \pm 1$. In the case of interface waves (no incident bulk wave, $\mathbf{T}^I = 0$), these are equal stresses on both sides of the contacting halfspaces that can be used in Eqs. (C.3), (C.8) in order to evaluate the corresponding power flux.

The most important are powers carried along the interface by ± 1 Bloch components: $\Pi^{(\pm 1)}$, and in depth of the body by 0-th component, Π_y . (The ± 1 components can carry comparable powers in opposite directions; this is a typical phenomenon in periodic systems [8]; the ratio $\gamma^2 = -\Pi^{(-1)}/\Pi^{(1)}$ describes the standing wave coefficient). These powers determine the total power carried by an interface wave along the interface, $\Pi^c = \Pi^{(1)} + \Pi^{(-1)}$ and the power shed into bulk due to the leakage phenomenon, Π_y . Both directly evaluated crack wave power and the total shed power agree perfectly in computations. One may thus conclude that the other Bloch components contribute negligibly to the energy transport in the system; this is also evident from Eq.(C.8) applied for wave components having large $p = -r_c + K$.

Appendix E: Maximum efficiency

THEOREM. $2\eta_1 \leq 1/2$ results from the system symmetry.

PROOF. In certain units, the interface wave power is $|a\mathbf{T}|^2$, while the incident power is $|\mathbf{T}^I|^2/Z_c$, and reflected and transmitted powers are $|\mathbf{T} - \mathbf{T}^I|^2/Z_c$ and $|\mathbf{T}|^2/Z_s$, respectively, see Eqs. (3) of [1] for stress in the upper and lower elastic halfspaces. We apply index c for the acoustic impedance Z of a comb, and s of a sample.

The energy conservation law states that

$$2|a\mathbf{T}|^2 + |\mathbf{T} - \mathbf{T}^I|^2/Z_c + |\mathbf{T}|^2/Z_s = |\mathbf{T}^I|^2/Z_c, \tag{E.1}$$

resulting in

$$|\mathbf{T}| = |\mathbf{T}^I| \frac{\cos \theta / Z_c}{a^2 + \alpha}, \quad \alpha = (Z_c^{-1} + Z_s^{-1})/2, \tag{E.2}$$

where θ is a possible phase shift between \mathbf{T} and \mathbf{T}^I . Substituted into expression for the interface wave power, this yields

$$\Pi^c/P^I = \frac{2}{Z_c} \frac{a^2 \cos^2 \theta}{(a^2 + \alpha)^2}, \tag{E.3}$$

which ratio has maximum at $a^2 = \alpha$, thus

$$2\Pi^c/P^I = \frac{\cos^2 \theta}{1 + Z_c/Z_s} \tag{E.4}$$

that is less than a half for the considered case of $Z_c = Z_s$. Only 50% of the incident power can be transformed into crack waves in both directions.

Making a digression, let's consider a bulk wave beam scattering on a solid surface with periodic grooves on it; this arrangement was proposed for generation of surface waves [8]. There is not transmitted bulk wave, thus the last term on the left hand side of (E.1) must be neglected, and we easily obtain that up to 100% of the incident power can be transformed into Rayleigh waves in this arrangement.

Appendix F: Edge scattering

Here we apply an approximation [9] to the planar harmonic Green's function of arbitrary elastic halfspace assuming that the normal stress vanishes at the body surface. For harmonic waves $\exp(j\omega t - jpx)$ on the surface, we have

$$u = \frac{1}{\sqrt{p^2}} \frac{\sqrt{p^2 - k_t^2}}{\sqrt{p^2 - k_t^2} - \alpha \sqrt{p^2}} T, \tag{F.1}$$

where $u = u_1$ and $T = T_{12}$, in certain units that are not important here. The approximation is valid in vicinity of k_t , but we apply it in the whole domain of spectral variable p ; this yields the simplest model of elastic halfspace supporting only shear bulk wave mode which is cut-off at $|p| = k_t$. The halfspace supports also a Rayleigh wave (for $T = 0$) having wave number $k_R > k_t$ at zero of denominator (F.1).

To model crack interface waves having wave number $k_c > k_t$ at another boundary conditions, we put an elastic layer on the halfspace described by $\Delta T = eu\sqrt{p^2}$ where ΔT is the stress difference on both sides of the layer (although it is considered infinitesimally thin). The stress on the top of the system is

$$T' = T + \frac{e}{\sqrt{p^2}}u = (1 + e)\frac{\sqrt{p^2 - k_t^2} - \beta\sqrt{p^2}}{\sqrt{p^2 - k_t^2} - \alpha\sqrt{p^2}}T, \quad (\text{F.2})$$

$\beta = \alpha/(1 + e)$. There is another surface wave for $T' = 0$,

$$k_R = k_t/\sqrt{1 - \alpha^2}, \quad k_c = k_t/\sqrt{1 - \beta^2}. \quad (\text{F.3})$$

The layer is semiinfinite, residing at $x < 0$, and its edge correspond to the edge of comb transducer; the rest of the body surface, $x > 0$, is free where a Rayleigh wave can propagate. We are going to consider a scattering problem with incident "interface" wave $\exp(j\omega t - jk_c x)$, $x < 0$, propagating from $-\infty$ towards the edge at $x = 0$ where it scatters producing the reflected interface wave $\exp(j\omega t + jk_c x)$, $x < 0$, and a transmitted Rayleigh wave $\exp(j\omega t - jk_R x)$, $x > 0$, and also the scattered bulk waves.

It is convenient to introduce certain Rayleigh ($x > 0$) and interface ($x < 0$) modal amplitudes F^+ and F^- , respectively, related to the mode powers by $.5|F^\pm|^2$. Equation (F.2) can be transformed into

$$F^- = \frac{1}{\sqrt{\xi}}\sqrt{\frac{\alpha}{\beta}\frac{1 - \beta^2}{1 - \alpha^2}}\frac{\sqrt{p^2 - k_t^2} - \beta\sqrt{p^2}}{\sqrt{p^2 - k_t^2} - \alpha\sqrt{p^2}}F^+, \quad (\text{F.4})$$

that is convenient for Jones' formulation of the Wiener-Hopf problem [6] where $1/(p - k_c)$ describes the incident wave,

$$F^- + \frac{1}{p - k_c} = A\frac{p^2 - k_R^2}{p^2 - k_c^2}\frac{G_\beta(p)}{G_\alpha(p)}F^+, \quad (\text{F.5})$$

$$G_a(p) = \frac{1}{1 + a}\left(1 + \frac{a\sqrt{p^2}}{\sqrt{p^2 - k_t^2}}\right) \rightarrow 1 \quad \text{at } |p| \rightarrow \infty,$$

which $G_a(r)$, $a = \alpha, \beta$, can be easily factorized into $G_a^+G_a^-$, a product of functions regular in either upper or lower complex halfplanes of p , $A^2 = [(1 - \alpha)/(1 + \alpha)][(1 + \beta)/(1 - \beta)]\alpha/\beta$.

The standard separation of functions regular in different complex halfplanes yields

$$F^- = \left[\frac{p + k_R}{p + k_c} \frac{G_\beta^-(p)}{G_\alpha^-(p)} \frac{2k_c}{k_c + k_R} \frac{G_\alpha^-(k_c)}{G_\beta^-(k_c)} - 1 \right] \frac{1}{p - k_c}, \quad (\text{F.6})$$

$$F^+ = \frac{1}{A} \frac{2k_c}{k_c + k_R} \frac{G_\alpha^-(k_c)}{G_\beta^-(k_c)} \frac{G_\alpha^+(p)}{G_\beta^+(p)} \frac{1}{p - k_R}.$$

An applied inverse Fourier transform would yield the solution, but we are interested only in the modal amplitudes which are determined by corresponding residua at poles $-k_c$ and k_R .

Both $k_{c,R} > k_t$, and this simplifies evaluation of the required factors of $G_a(p)$, $p = \pm k_{c,R}$

$$G_a^+(p) = \frac{j\sqrt{k_t}}{\sqrt{|p| - k_t}} \exp \left\{ \frac{a}{\pi} \int_0^{\pi/2} \frac{\ln(|p/k_t - \sin \eta|)}{\cos^2 \eta + a^2 \sin^2 \eta} d\eta \right\}. \quad (\text{F.7})$$

It is easy to check that for both $k_{c,R}$ sufficiently larger from k_t ,

$$F^- \approx \frac{k_R - k_c}{k_R + k_c}, \quad F^+ \approx \frac{2\sqrt{k_c k_R}}{k_R + k_c}, \quad (\text{F.8})$$

which power combined, approximately equals the incident power, and thus the scattering into bulk waves is weak. But for k_c close to k_t , both amplitudes of transmitted and reflected modes can be much smaller and large part of the incident power goes into bulk waves.

References

- [1] E.J. DANICKI, *Resonant phenomena in bulk wave scattering by in-plane periodic cracks*, J. Acoust. Soc. Am., **105**, 84–92 (1999).
- [2] E.J. DANICKI, *Periodic crack model of comb transducers: excitation of interface waves*, Arch. Acoust., **25**, 213–227 (2000).
- [3] S. HIROSE and J.D. ACHENBACH, *Higher harmonics in the far field due to dynamics crack-face contacting*, J. Acoust. Soc. Am., **93**, 142–147 (1993).
- [4] D.C. HURLEY, *Measurements of surface-wave harmonic generation in nonpiezoelectric materials*, J. Acoust. Soc. Am., **103**, 2923(A) (1998).
- [5] E.J. DANICKI, *Generation and Bragg reflection of surface acoustic waves in nearly periodic system of elastic metal strips on piezoelectric half-space*, J. Acoust. Soc. Am., **93**, 116–131 (1993); and further relations in: *Spectral theory for IDTs*, 1994 IEEE Ultras. Symp. Proc., 213–222 (1994).
- [6] R. MITTRA and S.W. LEE, *Analytical techniques in the theory of guided waves*, Ch. 3, Macmillan, New York 1971.
- [7] R.E. COLLIN, *Field theory of guided waves*, Ch. 9, McGraw-Hill, New York 1960.
- [8] R.F. HUMPHRYES and E.A. ASH, *Acoustic bulk-surface wave transducer*, Electr. Lett., **5**, 175–176 (1969).
- [9] E.J. DANICKI, *An approximation to the planar harmonic Green's function at branch points in wave-number domain*, J. Acoust. Soc. Am., **104**, 651–663 (1998).

C H R O N I C L E

Polish Seminar on Acoustics (OSA 2000)

XLVII OSA'2000 is a significant scientific forum for presenting the experience and achievements from basic fields of both the experimental and theoretical acoustics as well as its applications.

The seminar is an overview of the recent, mainly Polish, contributions to the development of research in the field. It is also an opportunity for public discussion and exchange of scientific views concerning such an important interdisciplinary science as acoustics. Last but not least, it plays a crucial role in integrating the scientists.

The papers presented at XLVII OSA'2000 have been divided into plenary papers and papers concerning different areas of acoustics.

Plenary papers (8)

are interdisciplinary in nature and comprise a wide range of issues:

- Acoustics at the Outset of the 20th Century;
- Nonlinear Acoustics and its Applications: A Historical Perspective;
- Fractals in Acoustics;
- International Co-operation in Control of Vibroacoustic Threats;
- Sound Intensity;
- Methods of Assessing the Quality of Speech Transmission;
- Modern Techniques in Ultrasonographic Imaging;
- Recent Progress in Automatic Recognition of Noise Sources.

Papers concerning different areas of acoustics (Contributed reports)

1. Underwater Acoustics (12 papers)

This area comprises a wide range of acoustical issues concerning liquid media. The research done refers to navigation, localisation of underwater objects, as well as acoustical properties of various media.

2. *General Linear Acoustics* (6 papers)

The papers refer to a linear description of different aspects of an acoustical field, and the problem of energy radiation of sound sources. The research methods are mainly analytical and can be applied in research in other fields of acoustics.

3. *Nonlinear Acoustics* (2 papers)

The papers take into consideration a nonlinear description of different phenomena, as well as a number of significant properties of real acoustical systems.

4. *Ultrasonics, Quantum Acoustics and Physical Effect of Sound* (20 papers)

The papers present methods and applications of ultrasonic technology in the: research on physical properties of different substances and components, technological processes in various fields of industry, measurements in the area of medicine and physics, and a precise localization of objects in different media.

5. *Bioacoustics* (9 papers)

The issues are interdisciplinary in nature and combine such disciplines as acoustics, biology and medicine. The research refers to diagnostics and treatment of diseases with the application of acoustical methods.

6. *Structural Acoustics and Vibration* (9 papers)

The papers concern the research done on vibration and mechanical values of different physical structures and their vibrations. Vibration attenuation achieved in various ways, and acoustical field generated by vibrating structures are analysed.

7. *Noise, its Effects and Control* (12 papers)

The papers take up an important issue of vibroacoustic threats and ways of fighting, minimising, and preventing them, as well as the issues concerning the elimination of the noise effects, and the measurement methods. The research results allow to design, for example, the work and public places, so that they fulfil health and safety requirements determined by the standards.

8. *Architectural Acoustics* (4 papers)

The issues refer to the research into sound systems, quality of sound, and the level of noise indoors.

9. *Transduction* (11 papers)

The papers deal with properties and quality of signal transmission by electroacoustic measurement and sound transducers. Some of the papers refer to sound power devices.

10. *Psychological and Physiological Acoustics* (9 papers)

The papers concern the research into hearing. The results have a lot of applications, for example processing the sound signals in such a way that the best perception of sound within the range of audibility is assured.

11. *Speech Production, Perception and Processing* (10 papers)

The papers refer to the analysis technique, processing and recognition of speech signal, the analysis of the acoustical modelling of Polish phonemes, as well as the acoustical analysis of lack of fluency in pathological speech.

12. *Music and Musical Instruments* (3 papers)

The papers present the results of the research into musical properties of both the hearing organ and musical instruments.

Plenary reports

Acoustics at the outset of XXI century

Ignacy MALECKI

Polish Academy of Sciences, Institute of Fundamental Technological Research
00-049 Warszawa, Świętokrzyska 21, Poland

Changes of the behaviour and importance of acoustics form a separate branch of physics related with audible sound to the generally recognised interdisciplinary science. The evolution of the role and development of the diverse fields of acoustics in the course of XX century are presented in the quantitative way on the tables. The proportional participation of the indicated field of acoustics to: 1. References in the international databases on contemporary papers on acoustics for the periods 1949–1958, 1959–1963, 1982–1983, 1996–1997; 2. The papers presented at the international congresses on acoustics (ICA) 1965, 1983, 1998, at Forum Acusticum 1996, 1999 and at the Meetings of Acoustical Soc. of America 1967, 1982, 1999; 3. Papers presented at the Open Seminars on Acoustics OSA (Poland) 1965, 1983, and 1999. The items on the tables correspond to the following fields of acoustics: 1 – Physical acoustics, 2 – Physiological and psychological acoustics, 3 – Electroacoustics and acoustic signals processing, 4 – Speech acoustics, 5 – Musical acoustics, 6 – Architectural acoustics, 7 – Noise control, 8 – Vibroacoustics and structural acoustics, 9 – Ultrasonic applications. 10 – Hydroacoustics. The recent key problems related with applications of acoustics: 1. The acoustic methods for investigation: the objects of nature and engineering, the living organisms, the technological materials and physical-chemical processes. 2. The control and utilisation of the acoustic energy: noise and vibration, applications in medicine and manufacturing. Sound as a main medium for perception and transmission of information: the objective (physical) and subjective (psychological) evaluation of speech and music, the new hearing ends, the bioacoustics. The consequences of computerisation: digital and quantum definition of the acoustic field, statistical approach, collection and analysis of large databases. The integration of the acoustics as an interdisciplinary science is aided by the activities of a number of the national acoustical societies and the authorities of the acoustical journals.

* * *

Nonlinear acoustics and its applications: A historical perspective

Leif BJØRNØ

Technical University of Denmark, Department of Industrial Acoustics
DK-2800 Lyngby, Building 425, Denmark, prof.lb@get2net.dk

The most important contributions to nonlinear acoustics since Euler's formulation of his equations of motion in 1755 and until 1960 are reviewed briefly in this paper. The review includes the works by Lagrange (1760), Poisson (1808), Stokes (1848), Earnshaw (1860), Riemann (1860), Rankine (1870), Hugoniot (1889), Rayleigh (1910), Taylor (1910), Fay (1931), Fubini (1935), Thuras, Jenkins & O'Neil (1935), Burgers (1948), Hopf (1950) and Cole (1951), and Beyer (1960). The development in the mathematical basis and in understanding of the physics behind nonlinear acoustics will be emphasised, and the potential applications of nonlinear acoustics will be discussed. The discussions have been restricted to nonlinear acoustics of fluids, and relations between nonlinear acoustics as an important discipline of acoustics, and fluid mechanics, are pointed out.

* * *

Fractals in Acoustics

Andrzej DOBRUCKI

Wrocław University of Technology, Institute of Telecommunication and Acoustics
50-370 Wrocław, Wybrzeże Wyspiańskiego 27, Poland, ado@zakus.ita.pwr.wroc.pl

The idea of fractals, fractal dimension and fractal measures have been presented. The examples of artificially constructed fractals and natural fractals have been given. The first are e.g. the Cantor set, Koch curve, Sierpinski carpet; the second ones are e.g. the line of the coast (the most characteristic for Norway). The relations between fractal and deterministic chaos have been defined. The acoustical and vibrating systems using fractals have been described. There are vibrations of the strongly nonlinear moving system of electrodynamic loudspeaker, with sound synthesis and composition of music, defects in materials under dynamic stresses and acoustic diffusors.

* * *

International cooperation in control of vibroacoustic threats

Zbigniew ENGEL

University of Mining and Metallurgy, Department of Mechanics and Vibroacoustics
30-059 Kraków, Al. Mickiewicza 30, Poland, engel@uci.agh.edu.pl

The paper presents international collaboration in vibroacoustical protections. International organizations, congresses and scientific conferences were presented. The papers present also the activity of Polish teams in this collaboration.

* * *

Sound Intensity

Finn JACOBSEN

Technical University of Denmark, Department of Acoustic Technology
DK-2800 Lyngby, Building 352, Denmark, fjac@dat.dtu.dk

The advent of sound intensity measurement systems in the beginning of the 1980s had a significant influence on the noise control engineering. Today, the sound intensity measurements are routinely used in the determination of the sound power of machinery and other sources of noise in situ. Other important applications of sound intensity include the identification and rank ordering of partial noise sources, visualisation of sound fields, determination of the transmission losses of partitions, and determination of the radiation efficiencies of vibrating surfaces. Sound intensity is also an important research tool. This paper summarises the basic theory of sound intensity and its measurement, and gives an overview of the state of the art in various areas of application, with particular emphasis laid on recent developments.

* * *

Methods of assessing the quality of speech transmission

Wojciech MAJEWSKI, Wojciech MYŚLECKI and Stefan BRACHMAŃSKI

Wrocław University of Technology, Institute of Telecommunication and Acoustics
50-370 Wrocław, Wybrzeże Wyspiańskiego 27, Poland, majewski@aipsa.ita.pwr.wroc.pl

This paper presents subjective and objective methods of speech transmission quality evaluation, with particular attention paid to the research carried out at the Institute of Telecommunications and Acoustics of the Wrocław University of Technology. Within subjective methods, a method of logatom intelligibility measurements is discussed together with its modified version worked out at the Institute.

* * *

The modern techniques in ultrasonographic imaging

Andrzej NOWICKI

Polish Academy of Sciences, Institute of Fundamental Technological Research
00-049 Warszawa, Świątokrzyska 21, Poland, anowicki@ippt.gov.pl

This paper reports the latest developments in the ultrasonic medical imaging. The review of the modern high-density, multi-elements linear array, phase array and annular array transducers will be

given. These new technologies benefit from the synthetic aperture and composite wide-band piezoelectric materials, opening a new era of a real time scanning of the biological structures with unprecedented quality. Flow velocity colour mapping, power Doppler, tissue Doppler, contrast agents echo enhancement and other new, exciting developments are discussed.

* * *

Recent Progress in Automatic Recognition of Noise Sources

Didier DUFURNET, François MAGAND and Adam ROZWADOWSKI
Villeurbane, 01dB, BP 1126, France, didier.dufournet@01db.com

The technique of automatic noise sources' identification had been first developed under the EU project called MADRAS (DG12). This technique enters today the domain of practical applications. The feedback from these new fields creates new needs and triggers some new interesting investigations. The paper presents the results of recent identification technique developments in two very different particular fields: environmental noise and vehicle noise. The environmental application focuses on a precise set of noise sources present in urban environment (street vehicles, planes, ...). A new way of detecting the acoustic events (which is the first step of the identification) is presented. It is based on the application of psychoacoustical criteria. Detection of relevant events leads only to a better correlation between the measured and detected sources and the perception of noise by urban population. The second application presented concerns the detection and the recognition of small disturbing (usually transient) noises in a passenger car, called squeaks and rattles. Although the signal characteristics of squeaks and rattles are significantly different from the urban sources, the modular and arborescent concept of the MADRAS technique allows an efficient processing in both cases. Finally, the paper presents the procedures under development and discusses some future issues.

Contributed reports

Underwater acoustics

Investigation of the pressure level changes of the fixed spectrum component of underwater ship noise

Anna BARANOWSKA

Naval Academy
81-103 Gdynia, Śmidowicza 69, Poland, abar@arnw.gdynia.pl

The aim of the paper was the analysis of the underwater ship noise spectrum. Investigations were connected with changes of the pressure level of the spectrum component of underwater ship noise equal to 25 Hz. This frequency is characteristic for ships and, first of all, it is connected with the work of a generating set. Method of measurement of underwater ship noise and the method of its analysis were described in the paper. The paper presents some examples of underwater ship noise spectrum calculated for fixed ship speeds and changes of the pressure level of spectrum component equal 25 Hz as a function of the distance and the ship speed.

* * *

Analysis of possibilities for experimental verification of sound agglomeration of gas bubbles in liquid

Henryka CZYŻ and Tadeusz GUDRA*

Rzeszów Pedagogical University
35-310 Rzeszów, Rejtana 16a, Poland, hczyz@atena.univ.rzeszow.pl

* Wrocław University of Technology, Institute of Telecommunication and Acoustics
50-370 Wrocław, Wybrzeże Wyspiańskiego 27, Poland, gudra@zakus.pol.wroc.pl

The aim of this paper is to present an analysis of the possibilities for examination of the effect of concentration of gas bubbles in liquid — in the planes of nodes or antinodes of an ultrasonic standing wave applied. The interaction of ultrasonic waves with dispersions can be used for separating the dispersed gas bubbles from the fluid. Under the influence of the ultrasonic standing wave, the gas bubbles existing in the liquid experience a certain characteristic displacement, referred to as the drift. The drift force depends on the position of a gas bubble in relation to the nodes of the standing wave, on the gas bubble size, on the parameters of the acoustic field, and on the fluid. The paper presents an idea of a system,

which may be used to analyse this effect experimentally. The main objective of the experiment is to verify the theoretical results obtained. The effect has been observed (the quantitative verification) so far, and measurements are to be conducted in the future (qualitative verification).

* * *

Comparative investigations of acoustic pressure generation of the ship propeller

Jerzy DOBRZENIECKI and Ignacy GŁOZA

Naval Academy

81-103 Gdynia, Śmidowicza 69, Poland, igloza@amw.gdynia.pl

Knowledge of the acoustic pressure level generated by a ship to the water environment is an important exploitation problem. It is connected with assessment of technical conditions of the ship mechanisms and the planned ship task.

* * *

Seabed-type recognition using decision tree

Tran Van DUNG and Andrzej STEPNOWSKI

Technical University of Gdańsk, Department of Acoustics

80-952 Gdańsk, Narutowicza 11/12, Poland, dung@dolphin.eti.pg.gda.pl, astep@pg.gda.pl

A decision tree classifier was developed for sea bottom recognition from the acoustic echoes. The decision-tree algorithm was derived and used to construct the decision-tree classifier operated on the data collected on 38 kHz and 120 kHz echosounder's frequencies. The system has been applied successfully to the task involving forty parameters retrieved from acoustic echoes, including the wavelet coefficients. The data have been acquired from acoustic surveys carried out on Lake Washington, using DT4000 echosounder of 38 kHz and 120 kHz operating frequencies.

* * *

Shaping the horizontal beam pattern of the high-resolution, ahead-looking sonar

Andrzej ELMINOWICZ

Marine Technology Centre

81-109 Gdynia, Dickmana 62, Poland, andrzeje@ctm.gdynia.pl

The paper discusses high angular and range resolution of ahead-looking sonars with a multi-stave transmitting-receiving linear array. By increasing the sonar's working frequency, the size of the array can be reduced; however, as the beam gets narrower, the number of array staves goes up. The result is a growing number of receiving channels and transmitting modules. The number of array staves can be reduced by increasing the spacing between the stave centres above 0.5λ . As a result, however, grating lobes are produced for receiving and transmitting the beam patterns. For both patterns the grating lobes always occur in the same directions. Narrowing the observation sector does not reduce the level of grating lobes of both patterns, neither does it change their position with respect of one another. The work shows that in order to reduce the level of grating lobes of transmitting and receiving beam patterns of the multi-stave array for $\lambda < d < 2\lambda$, the horizontal beam patterns of the staves should be shaped by increasing the size of the elements. For a stave whose element is $0.9d$ wide, the level of grating lobes of both central beam patterns is approximately -10 dB but for steered beam it goes up to -8 dB which is too high. Two methods of shaping the horizontal beam patterns of array staves are presented. The shaping is done by increasing the size of the element above d by mechanical coupling of the staves. Transmitting and receiving array beam patterns obtained by computer simulation are presented for d changing from λ to 2λ with grating lobes below -20 dB, which brings the level of grating lobes of the sonar below -40 dB.

* * *

On dispersion of sound beams in bubbly liquid

Sergey B. LEBLE* and Andrey SUKHOV**,**

* Technical University of Gdańsk, Theoretical Physics and Mathematical Methods Department
80-952 Gdańsk, Narutowicza 11/12, Poland, leble@mif.pg.gda.pl

** Kaliningrad State University, Theoretical Physics Department, Russia

The dynamics of a bubbly liquid with small volume concentration of bubbles is considered. Beam propagation at a heterogeneous medium is treated in parabolic approximation. For source extended in one

direction (strip-like source) the resulting equation is equivalent to KP-II equation. For focused sources with appropriate choice of boundary conditions, a cylindrical KP (Johnson) equation is derived. We study terms solutions that could be expressed in the elementary, functions interpreting the singularities of them as poles in a complex plane. The position of the poles is shifted from the real axis on account for viscosity and thermoconductivity.

* * *

Acoustical investigation of “stable” structure in water mixtures

Bogumił J. Linde* and Karolina KLIKAR

University of Gdańsk, Institute of Experimental Physics

80-952 Gdańsk, Wita Stwosza 57, Poland

* University of Warmia and Mazury, Chair of Physics and Biophysics

10-719 Olsztyn, Oczapowskiego 2, Poland

The velocity of ultrasound and density were measured in the mixture of diethylene glycol and water in the temperature ranges 283–308 K. From these results, the adiabatic compressibilities were calculated from the Laplace equation. The compressibility dependencies on the temperature and concentration are presented as a group of isotherms with one common point of intersection. Such relation between the adiabatic compressibility and concentration and temperature indicates the formation of a liquid stable structure which we tried to compare with the solid clathrate. This structure was suggested by Baumgarten and Atkinson as well as by Endo, although the interpretation was different. The first authors relate the formation of clathrate structure to the minima of the compressibility isotherms but according to Endo, the intersections of the compressibility isotherms are related to such a structure.

* * *

Fractal modelling of seabed backscattering

Zbigniew LUBNIEWSKI and Marek MOSZYŃSKI

Technical University of Gdańsk, Department of Remote Sensing and Monitoring System

80-952 Gdańsk, Narutowicza 11/12, Poland, lubniew@eti.pg.gda.pl

The numerical modelling of echosounder signals backscattering by a fractally corrugated sea bed surface is presented. In particular, the relations between fractal dimension describing the large scale roughness of sea bottom, and the received echo envelope shape, especially its complexity measured also by fractal dimension, were investigated. The fractal relief of seabed surface was generated assuming the power law form of the spatial frequency power spectrum, and subsequently applying the two-dimensional inverse FFT algorithm. In the second stage, the bottom echo waveform was calculated numerically as a sum of contributing echoes from all surface elements. For each element, the echo amplitude was calculated assuming the form of angular dependence of the bottom backscattering coefficient obtained previously for small-scale roughness by Kirchhoff approximation. The obtained results of simulations show that under some conditions, the seabed surface fractal structure is transferred onto the shape of its impulse response and the echo envelope. The empirical relation between fractal dimension of the fractal seabed surface and of the echo waveform was also found. The results are important in the context of newly developed algorithms for acoustical seafloor classification.

* * *

Determining of accuracy zones of hydronavigational system

Artur MAKAR and Krzysztof NAUS

Naval Academy

81-103 Gdynia, Śmidowicza 69, Poland, Artur.Makar@amw.gdynia.pl

In this paper, the method of accuracy zones determination of the hydronavigational system has been shown. This system works on the basis of time delay estimation between the underwater signals which descended from the moving underwater object. Analyse of accuracy zones allows to optimal place of receivers for secure the high accuracy of position determining in the designed zone.

* * *

The forward and side scan sonar images computer simulation

Aleksandra RAGANOWICZ, Lech KILIAN and Jacek MARSZAL

Technical University of Gdańsk, Acoustics Department

80-952 Gdańsk, Narutowicza 11/12, Poland, ragola@eti.pg.gda.pl

The generation of dynamic sonar images in simulators of new sonar's generation with computer processing and displaying is possible directly by a personal computer. The simulation could also include full signal processing as in the real sonar. The methods of computer generation of echo signals, reverberations and noise in the training simulator of forward and side scan sonars are presented in this paper. The effects of sonar's simulator setting changes and some remarks about simulator constructions and the special communication network with the computer "teacher's" station are also shown. Some examples of real and simulated displays (for forward and side looking sonar) are compared.

* * *

Distribution of assessment of fish resources in Solina Dam Reservoir monitored with an acoustic-cum-fishing method

Andrzej ŚWIERZOWSKI

The Stanisław Sakowicz Inland Fisheries Institute in Olsztyn, Department of Fishing Techniques

Poland, irs@uwm.edu.pl

The objective of the study was to determine spatial distribution and densities of fish inhabiting the water column of Solina Dam Reservoir, using the method of acoustic-cum-fishing monitoring. An attempt was made to determine the fish stock composition, biomass and numbers, and to find possible relationships between these values and the environmental parameters, both natural and anthropogenic. Acoustic monitoring was performed at daytime as well as at night. Two research echosounders were used: Simrad EY-M (70 kHz) and Simrad EY-500 (120 kHz). Altogether 104 acoustic profiles were made along the pre-established routes, totalling about 100 km. Fish densities along the monitored routes were calculated using the programme HADAS and EP-500. Interpolating the net of the data thus obtained, maps of fish distribution and surface fish densities were worked out and fish numbers were calculated. Mean fish density as monitored with an echosounder EY-M was 264.3 fish/ha, while the respective result obtained with EY-500 was 440.9 fish/ha. The highest densities were registered in the area where Solinka and San rivers flow into the reservoir, and in the region close to habitable areas and recreation sites. Fish densities in Solina Reservoir are from several to over 40 times lower than in Polish lakes. In order to identify the fish species and to verify size composition of the stock, control catches were performed with pelagic trawl and gill nets. Composition of these catches was: 44.5% of bleak, 23.7% of roach and 15.0% of bream. Fish biomass was estimated at from 38 kg/ha to 63 kg/ha, depending on the echosounder used.

* * *

The modern method of the digital synthesis of the broadband sounding pulses in echo ranging

Krzysztof ZACHARIASZ

Technical University of Gdańsk, Acoustics Department

80-952 Gdańsk, Narutowicza 11/12, Poland, zachar@eti.pg.gda.pl

The method of digital synthesis of the broadband sounding pulses in active sonars is presented. The method uses the digital modulators, which are applied in the modern telecommunication systems. The characteristic features of the method are discussed on the basis of the designed digital transmitter of the chirp pulses. The sample sounding pulse along with the signal at the output of the matched filter are also presented.

*General linear acoustics***Measuring the directional vibration of acoustic wave propagation caused by temperature gradients**

Jacek GAWRYSIAK

Technical University of Gdańsk

80-952 Gdańsk, Narutowicza 11/12, Poland

The article presents a fragment of measurements of acoustic intensity distribution taken in Wdzydze Lake. A source of the acoustic wave at a frequency of 220 kHz was placed near the shore and directed

horizontally towards the lake centre. Next, a motor boat was used to take measurements of the profiles of sound velocity and depth intensity distribution in several selected spots of the lake. The experiment was then repeated for new positions of the transmitting antenna, first inclined by 4 and then by 6 degrees towards the bottom of the lake.

* * *

Operations of symmetry for any set of coherent point sources of zero order

Anna SNAKOWSKA and Henryk IDCZAK*

Rzeszów Pedagogical University, Institute of Physics

35-310 Rzeszów, Rejtana 16a, Poland

* Wrocław University of Technology, Institute of Telecommunication and Acoustics

50-370 Wrocław, Wybrzeże Wyspiańskiego 27, Poland

Any set of coherent point sources radiated under the free field conditions, that is when all sources interact, can be considered as a simplex graph, so its properties can be analysed by means of the graph theory. The paper presents an attempt of such an analysis. It is assumed that the symmetry of any set of coherent acoustic sources means the invariance of its total acoustic power emitted when some operations on the system are carried out. These operations may concern the whole set of sources (transformation of the co-ordinate system, translation etc.) or only some of the sources (rearrangement of position, variation of phase etc.) and so we deal correspondingly, with global or local symmetry. The formula for the acoustic center (in analogy to the center of mass in mechanics) has been presented as an example of the global symmetry. The cases of sources being in phase ($\varphi_i - \varphi_j = 0$, φ_i — i -source phase) or in antiphase ($\varphi_i - \varphi_j = \pi$) have been considered. It allows to formulate the criterion of equivalence: sets of acoustic sources are equivalent when and only when they have the same acoustic center and they radiate the same acoustic power.

* * *

Some limiting transitions leading to the formulae for the sound power of a circular plate

Witold J. RDZANEK*, Zbigniew ENGEL** and Wojciech P. RDZANEK, Jr*

* Rzeszów Pedagogical University, Institute of Physics

35-310 Rzeszów, Rejtana 16a, Poland, rdzanek@atena.univ.rzeszow.pl

** University of Mining and Metallurgy, Department of Mechanics and Vibroacoustics

30-059 Kraków, Al. Mickiewicza 30, Poland

Several limiting transitions from the formulae describing sound radiation by a clamped annular plate to the formulae valid in the case of a clamped circular plate have been performed in this paper. The theoretical analysis of sample magnitudes, the active and reactive power of sound radiated by both the sources included, has been carried out. A good agreement of the results obtained herein with the result obtained by means of other analytical methods has been reached, which confirms the correctness of the research performed. The formulae describing sound radiation by a circular plate obtained by performing some limiting transitions is a confirmation of the greater generality of the formulae valid in the case of a clamped annular plate.

* * *

The sound pressure distribution of a clamped annular plate at Fraunhofer's zone

Wojciech P. RDZANEK, Jr*, Zbigniew ENGEL** and Witold J. RDZANEK*

* Rzeszów Pedagogical University, Institute of Physics

35-310 Rzeszów, Rejtana 16a, Poland, rdzanek@atena.univ.rzeszow.pl

** University of Mining and Metallurgy, Department of Mechanics and Vibroacoustics

30-059 Kraków, Al. Mickiewicza 30, Poland

In this paper, the acoustic field of vibrating clamped annular plate has been considered. The sound pressure at the Fraunhofer zone has been reached. The sound radiation directionality indicator has been computed for the source. The plate vibrates harmonically under external pressure of axis symmetric distribution under the plate surface. The plate model by Kelvin-Voigt has been used, which made it possible to consider the plate's internal friction forces. The influence of the air column above the plate on the plate vibration modes has also been taken into account. The results of an annular plate free vibration analysis have been used.

* * *

Approximation of the parabolic partial differential equation in studies of acoustic waves propagation in randomly inhomogeneous media

Eugeniusz SOCZKIEWICZ

Silesian Technical University, Institute of Physics

44-100 Gliwice, Krzywoustego 2, Poland, Soczkiewicz@gnom.matfiz.polsl.gliwice.pl

Propagation of acoustic waves in randomly inhomogeneous media has been considered in the approximation of the parabolic-type differential equation. Application of the Feynman path integrals to solution of the parabolic partial differential equations has been described. Attenuation of acoustic waves, resulting from scattering in randomly inhomogeneous medium has been estimated for various forms of the correlation function of the acoustic refractive index fluctuations. In the case of a turbulent medium with von Kármán correlation function of the medium inhomogeneities, the scattering coefficient of acoustic waves has been calculated as a function of the parameter ν of the von Kármán function.

* * *

The cutoff frequency of acoustic horns

Tomasz ZAMORSKI

Rzeszów Pedagogical University

35-310 Rzeszów, Rejtana 16a, Poland, tzamor@atena.univ.rzeszow.pl

The accurate calculation of the cutoff frequency of a horn is important in designing the acoustical systems with horns. However, generally the difference between the experimental and theoretical values of cutoff frequencies amounts to about 20%. The calculation method of the cutoff frequency of horns is analysed in this paper, especially for Salmon's horns, which are commonly used. It is assumed that a one-dimensional infinitesimal wave is propagating in the horn without any loss of energy. The wave reflected from the open end is neglected. In the analysis, a formal analogy between the reduced Webster pressure equation and the Schrödinger equation is used. It is stated that the wave-front shape approximation considerably influences the value of the cutoff frequency. The usually assumed plane wave approximation decreases the cutoff frequency value. The method of calculation of the cutoff frequency of horns in a spherical wave-front shape approximation is proposed. This method is based on a discussion of the wave equation of a horn without necessity of solving it.

Nonlinear acoustics

Field of nonlinear elastic wave of a focusing source in the post-focal region

Eugeniusz KOZACZKA, Grażyna GRELOWSKA and Ignacy GŁOZA

Naval Academy

81-103 Gdynia, Śmidowicza 69, Poland, ekoz@amw.gdansk.pl

The focused intense ultrasound has been used for many applications in medicine and technology. The most interesting phenomenon is observed in the focal area. There are also many interesting features connected with the nonlinear propagation in the post-focal area. The main goal of this paper is to present some of them on the basis of the numerical as well as experimental investigations.

* * *

Nonlinear evolution of acoustic wave in semi-ideal gas

Anna PERELOMOVA and Magdalena KUŚMIREK-OCHRYMIUK

Technical University of Gdańsk

80-952 Gdańsk, Narutowicza 11/12, Poland, anpe@mifgate.pg.gda.pl, magda@imp.gda.pl

A system of coupled nonlinear equations for interacting modes of acoustic waves is derived using the projection technique. Three independent modes: leftwards, rightwards propagating and the stationary one are obtained by a set of orthogonal projectors of the linear problem. The projecting method yields a coupled system of interacting modes in the nonlinear problem. The final system is equivalent to the basic one up to the third-order nonlinear terms. A fluid medium is considered, caloric equation of state was taken as the Taylor expansion of the general form and then applied to a semi-ideal gas. Acoustic mode is analysed for ideal and semi-ideal gas models, the velocities and nonlinear coefficients are evaluated and compared for the case of CO₂.

*Ultrasonics, quantum acoustics and physical effect of sound***The method of measurement of ultrasonic attenuation**

Ya. BOBITSKI and O. MOKRII*

Rzeszów Pedagogical University, Institute of Technology
35-310 Rzeszów, Rejtana 16a, Poland* The State University "Lvivska Polytechnika"
79013 Lviv, S. Bandery 12, Ukraine, mokol@polynet.lviv.ua

This paper describes a method for measurement of acoustic wave attenuation and velocity in the nearfield. The method is considered for the case of liquid media. It enables to investigate the medium with high ultrasonic attenuation the frequency area of new MEGC. Two transducers exciting acoustic waves in the medium are taken into account. These two waves are composed in the registration area in such a way that the compensation is achieved owing to adjustment of the frequency and amplitudes of the waves. The velocity of acoustic wave is found from the value of frequency while the attenuation from the value of amplitudes. In this paper, relations for determining the attenuation and velocity are derived. Conditions providing the maximum accuracy are revealed.

* * *

Piezoceramic transducers with high temperature stability of resonance frequencyDariusz BOCHENEK, Julian DUDEK, Evgeni G. FESENKO*, Svetlana V. GAVRILYACHENKO*,
Aleksandr V. LEYDERMAN** and Zygmunt SUROWIAKSilesian Technical University, Department of Technology
41-200 Sosnowiec, Śnieżna 2, Poland, surowiak@us.edu.pl* Rostov University, Institute of Physics
344-104 Rostov, Prospekt Stachki 194, Russia

** Puerto Rico University, 00680 Mayaguez, USA

Dependence of the relative change of the resonance frequency (Df_r/f_r) on the content of (x)PbTiO₃ in the solid solution Pb(Zr_{1-x}Ti_x)O₃ – PbMn_{2/3}M_{1/3}O₃ – PbW_{1/2}Mn_{1/2}O₃ — based piezoceramics has been investigated. The correlation between Df_r/f_r and internal friction (Q_m^{-1}) has been ascertained, as well as the relation between these quantities and the crystalline structure, which depends on concentration of (x)PbTiO₃ has been revealed. It was found that the smallest values of Df_r/f_r appear in the following two cases. Firstly, in case of piezoceramics with tetragonal structure (T) and mole fraction x within the range $0.53 < x < 0.63$; secondly, in case of piezoceramics with rhombohedral structure (Re) and mole fraction x within the range $0.20 < x < 0.30$. The smallest temperature stability, however, was found for piezoceramics with compositions from the morphotropic phase boundary region (Re+T) at small δ -parameter, which describes the degree of deformation of the regular elementary cell in a given phase, and at large η -parameter, which determines the degree of reorientation of the remanent domains different from 180° and caused by an electric field. It can be seen from Fig. 1 that decrease of the PbTiO₃ — mole fraction from the values typical for PZT morphotropic region (MR) is accompanied by structural phase transition, i.e. ceramics exhibits a rhombohedral phase. At the same time, an increase in stability of the resonance frequency (decrease in Df_r/f_r) and increase in mechanical quality Q_m (increase in internal friction Q_m^{-1}) can be seen. These changes are smaller as compared with transition from the morphotropic region to tetragonal phase, but they are conditioned by a strong decrease in the number of the domain walls (increase in h -parameter). As the PbTiO₃ mole fraction moves towards T-structure compositions, mobility of the domain walls decreases due to the increasing d -parameter.

* * *

Investigation of diffusion process using photoacoustic effect

Jerzy BODZENTA, Roman BUKOWSKI, Andreas CHRIST* and Jacek MAZUR

Silesian Technical University, Institute of Physics
44-100 Gliwice, Krzywoustego 2, Poland, bodzenta@polsl.gliwice.pl* Martin Luther University Halle-Wittenberg, Medical Faculty
Institute of Medical Physics und Biophysics, D-06097 Halle (Saale), Germany

Possibility of analysis of a drug penetration through membranes using photoacoustic effect is considered. Basing on the 2nd Fick's law, a problem of distribution of drug concentration in the membrane

in space and time is solved. The obtained solution allows to derive the distribution of heat sources arising in the membrane illuminated by modulated intensity light. Subsequently, the temperature of the illuminated membrane surface is analyzed numerically. This temperature is directly connected with a signal registered in photoacoustic measurement. Qualitative agreement between the calculated time-dependence of this temperature and the photoacoustic signal measured in the corresponding experiment is shown.

* * *

Investigations of the thermotropic liquid crystals in Epidian 3 by an application of acoustic methods

Adam DRZYMAŁA, Marian CIEŚLAK and Dariusz WILK

Rzeszów University of Technology

35-959 Rzeszów, Wincentego Pola 2, Poland

fajdrzym@prz.rzeszow.pl, cieslak@prz.rzeszow.pl, wilkdar1@prz.rzeszow.pl

The results of measurements in pentylicyanobiphenyl (PCB) liquid thermotropic crystal were used as a standard for investigations of Epidian 3. Studies of a sound speed and sound attenuation of the frequency of 2.5 MHz were performed with US-6 measurements set for high frequencies manufactured by IPPT PAN in Warsaw. These investigations were realized during the heating and cooling processes of a liquid crystal in a region of the phase transition: nematic-isotropic liquid, and also isotropic liquid-nematic in the constant magnetic field perpendicular or parallel to the direction of an ultrasonic wave propagation, and also without magnetic field. The obtained data are presented using the Fisher curve for liquid crystal in the nematic and in the isotropic liquid. On the basis of the graphs for critical parameters in a phase transition isotropic liquid-nematic, in the perpendicular or parallel magnetic field relating a direction of ultrasonic wave propagation some of these parameters were determined. Using these graphs, the temperatures of phase transitions were determined in the presence of magnetic field or without this field. Some differences between the temperatures of phase transition were observed during the heating and cooling process. The temperatures of a phase transition corresponding to an isotropic liquid-nematic are lower than those for a phase transition nematic-isotropic liquid. These differences are about 1 K. Investigations of the sound speed and sound attenuation for Epidian 3 were performed in an isotropic liquid at a temperature of the transition to glassy mesophase. The research project of physical properties for liquid litropic crystal has been started recently.

* * *

Hysteresis of changes of ultrasonic wave absorption coefficient caused by the magnetic field

Arkadiusz JÓZEF CZAK, Mikołaj ŁABOWSKI and Andrzej SKUMIEL

Adam Mickiewicz University, Institute of Acoustics

61-614 Poznań, Umultowska 85, Poland, aras@amu.edu.pl

The structure of ferrofluid changes under the influence of external magnetic field and does not return to the initial condition after turning off the magnetic field. Probably, the clusters remain in magnetic fluid. For this reason, the properties of ferrofluid depend on its magnetic history. This phenomenon was studied using the measurements of changes of the ultrasonic wave absorption coefficient.

* * *

Dependence of ultrasound velocities on heat-treatment and magnetic field of the Fe-Cu-Nb-Si-B 17 mm thick amorphous ribbons

Zbigniew KACZKOWSKI, Elżbieta MILEWSKA, Andrzej KRZYŻEWSKI and Antal LOVAS*,**

Polish Academy of Sciences, Institute of Physics

02-668 Warszawa, Al. Lotników 32/46, Poland

* Hungarian Academy of Sciences, Research Institute for Solid State Physics

1525 Budapest P.O.B. 49 (Konkoly Thege ut. 29-33), Hungary, lovas@power.szfk.kfki.hu

**Technical University of Budapest, Department of Mechanical Engineering Technology

1111 Budapest, Bertalan L. utca 2, Hungary

Ultrasound velocities as the functions of the bias magnetic field and the annealing temperature were investigated in the $\text{Fe}_{72.5}\text{Cu}_1\text{Nb}_4\text{Si}_{13.5}\text{B}_9$ amorphous ribbons. The samples were 50 mm long, 3 mm wide

and 17 mm thick. The strip samples were annealed in vacuum for 1 h in the temperature range from 200 to 700° C. The maximum changes were observed after annealing at the temperature of 500° C when the magnetomechanical coupling coefficient reached the maximum value ($k = 0.71$). The ultrasound velocities were changing from 3.0 to 5.2 km/s, depending on the magnetic bias field and the thermal-treatment history.

* * *

Sensitivity of ultrasonic hydrophone probes in frequency range 0.25–40 MHz

Peter A. LEVIN, Andrzej NOWICKI* and Grażyna ŁYPACEWICZ*

Drexel University, School of Biomedical Engineering and Health Systems and Department of Electrical and Computer Engineering

PA 19104, Philadelphia, USA, lewin@ece.drexel.edu

* Polish Academy of Sciences, Institute of Fundamental Technological Research
00-049 Warszawa, Świątokrzyska 21, Poland

This paper describes the development and implementation of acoustic measurement methods capable of determining absolute sensitivity of miniature ultrasonic hydrophone probes over a wide, 100 MHz bandwidth. Currently used calibration technology is usually limited to approx. 20 MHz and to address this issue, two wideband calibration techniques were developed. The techniques allow frequency responses of different PVDF polymer hydrophone probes, including bilaminar membranes and needle designs to be determined from 200 kHz to 100 MHz. The overall uncertainty of the measurement technique developed was estimated to be better than ± 1.5 dB in the frequency range 0.2 MHz–30 MHz and ± 2 dB between 30 and 40 MHz. Absolutely calibrated probes are needed to determine and monitor the acoustic output of ultrasound imaging devices. The results of this work are necessary to implement the procedures for adequate determination of the Mechanical Index (MI) of ultrasound imaging devices and in development of therapeutic procedures based on the use of High Intensity Focused Ultrasound (HIFU).

* * *

Evaluation of residual stress and textural anisotropy from ultrasonic measurements

Józef LEWANDOWSKI

Polish Academy of Sciences, Institute of Fundamental Technological Research

00-049 Warszawa, Świątokrzyska 21, Poland, jlewando@ippt.gov.pl

The texture of every polycrystalline aggregate and the presence of stress in the material contribute to the anisotropy of its macroscopic physical properties, e.g., they induce the dependence of the ultrasonic wave velocities on the directions of the wave propagation and polarization. In the paper, a proposal of ultrasonic measurements accompanied by analytical and computational analysis is presented and outlined, what enables us to determine separately each of the two contributions to the orthorhombic anisotropy of a polycrystal made of cubic crystals with the highest symmetry. The steps of utilizing this method are the following: In the first step, following Degtyar and Rokhlin [J. Appl. Phys. 78 (1995)], the initial stress is to be found simultaneously with the stress and texture-dependent effective stiffness moduli from inversion of the Christoffel equations. The measured angular dependencies of the velocities of ultrasonic bulk waves are used as the input. In the second step, following Lewandowski [Ultrasonics 3 (1995); Ndt&E International 32 (1999)], the use is to be made of the Jaynes principle of maximum Shannon entropy. In this way, it is shown that on the basis of the measurements of respectively chosen ultrasonic velocities, it is possible to find simultaneously the maximum-entropy distribution function of the crystallite orientation and the single crystallite stiffness moduli.

* * *

Acoustic anomaly in critical point — characteristic frequency of concentration fluctuations in critical binary mixture of nitroethane-isooctane

Dariusz MADEJ and Tomasz HORNOWSKI

Adam Mickiewicz University, Institute of Acoustics

61-614 Poznań, Umultowska 85, Poland, darek@spl.ia.amu.edu.pl

Sound propagation is a valuable tool in the investigation of dynamics of phase transitions in critical mixtures. All theoretical models of acoustic wave propagation in critical mixtures describe attenuation

and sound dispersion as a function of reduced frequency. Thus the first step in theoretical description of experimental results is to determine the amplitude of characteristic frequency of concentration fluctuations w_0 . The viscosity of nitoethane-isooctane mixture was measured using a H'oppler viscometer in temperature ranges from 31 to 52° C. The obtained value of characteristic frequency was $w_0 = 5.44 \cdot 10^{10}$ Hz.

* * *

Recognition of the shapes, sizes and position of objects in gas medium using ultrasonic methods

Krzysztof J. OPIELIŃSKI and Tadeusz GUDRA

Wrocław University of Technology
50-370 Wrocław, Wybrzeże Wyspiańskiego 27, Poland
popi@zakus.ita.pwr.wroc.pl

The work presents a new way of recognising the shapes, sizes and position of objects, based on a method used in ultrasound transmission tomography (UTT). The concept of UTT in a gas medium is close to the classical tomography. However, because of the measurement environment, the visualisation of the object's internal structure is not possible. What is possible is the imaging of the object's shape and size, and also its position in the space. If the dimensions of the object are larger than the wavelength, then for every measurement on the transmitter-object-receiver way, the ultrasonic wave is either reflected from the object air boundary or it reaches the receiver omitting the object. In the paper, the results of object's shape, size and position investigation applying the image reconstruction algorithm for parallel ray projection geometry are presented. The choice of the kind of geometry was bound up with the possibility to adapt the existing set-up research.

* * *

Influence exerted on electrochemical deposition by acoustic streaming

Paweł POĆWIARDOWSKI, Leif BJØRNØ* and Andrzej STEPNOWSKI

Technical University of Gdańsk, Remote Monitoring Systems Department
80-952 Gdańsk, Narutowicza 11/12, Poland, astep@pg.gda.pl

* Technical University of Denmark, Lyngby, Denmark

The paper describes the efficient method of improving diffusion of more noble metal through the barrier layer created during the electrochemical deposition process, by means of ultrasonic waves. Ultrasound was used to produce micro-edges, which transport an electrolyte at the wafer surface. The Schlichting streaming theory basically describes those micro-edges. The experiments have been carried out for Ni-Fe plating bath based on J. Horkans. The results indicate that by controlling the acoustic intensity, it is possible to change the edges angular velocity and thus to control the amount of liquid injected to the vicinity of cathode. In this way, apart from simple ion diffusion, the controlled migration inside the barrier layer can be accomplished and thus the inspection of the mass of more noble metal in the plated alloy is possible.

* * *

Evaluation by Acoustic Emission (AE) method the critical stress and the pseudo-plasticity effect of ceramic materials

Jerzy RANACHOWSKI, Ignacy MALECKI and Zbigniew RANACHOWSKI

Polish Academy of Sciences, Institute of Fundamental Technological Research
00-049 Warszawa, Świętokrzyska 21, Poland, zranach@ippt.gov.pl

The three-point-bending method was applied for the investigation of critical stress and pseudo-plasticity of structural ceramics. In the first case the cordierite was used for testing. The dependence between the acoustic emission counts sum during the last stage of materials destruction and its critical stress were measured and analysed. The thermal shocks ΔT in the range of temperature differences 0 to 320° C were used to cause several stages of destruction of ceramics. An empirical formula was established. The coefficient H_{AE} equal to the ratio of the AE counts sum for the defected sample to the AE counts sum for the "intact" sample is proportional to the H_m coefficient representing the squared ratio of critical stresses of "intact" and defected sample. In the second case, the effect of pseudo-plasticity was measured in the magnesite-oxide ceramics. The threshold stress when the uninterrupted acoustic

emission begins seems to be an adequate parameter to evaluate the influence of pseudo-plasticity on the reliability of ceramics. [Work supported by the State Committee for Scientific Research in Poland, Grant No. 7 T07B-03413].

* * *

Oxide nanostructures: formation, deposition and acoustics methods of monitoring

Jadwiga RZESZOTARSKA*, Jerzy RANACHOWSKI and Feliks REJMUND

Polish Academy of Sciences, Institute of Fundamental Technological Research
00-049 Warszawa, Świętokrzyska 21, Poland, freymund@ippt.gov.pl

* Warsaw University, Department of Chemistry
02-093 Warszawa, Pasteura 1, Poland

The paper reviews the methods of the oxide nanostructures formation and deposition. The velocity and attenuation measurements of ultrasonic waves were proposed to determine the specific properties of nanostructures such as high porosity, the real and imaginary parts of the complex moduli of elasticity, evaluation of the structure and mechanical strength of the medium. The acoustic emission method was used for continuous observation of the process of nanostructure creation. The properties of the processes appearing during generation of nanostructures cause that the acoustic methods can be a valuable source of information about the processes which are complementary to the microscopic methods. [Work supported by the Committee for Scientific Research in Warsaw, Grant No. 7-T07B04715].

* * *

Ultrasonic meter of blood hematocrit

Wojciech SECOMSKI, Andrzej NOWICKI, Jacek KALUCKI

Polish Academy of Sciences, Institute of Fundamental Technological Research
00-049 Warszawa, Świętokrzyska 21, Poland, wsecom@ippt.gov.pl

The possibility of the noninvasive estimation of the blood hematocrit is important for the medical diagnosis. At present, only one method is known and it is based on measurement of the speed of sound. It is mainly used during patient's dialysis. We propose a novel approach to solve this problem. The instrumentation developed is based on the dependence of the absorption of ultrasonic wave in blood. The instrument is based on pulsed Doppler ultrasonic blood flowmeter, operating at frequency 20 MHz. Doppler signal is simultaneously recorded in two gates at two distinct depths. The ratio of signal power at two gates depends on the hematocrit only. The preliminary measurements were done *in vitro* using porcine blood. The red blood cells and plasma were mixed to obtain hematocrit in the range from 1% to 65%. The Doppler signal was recorded in two gates separated by 1.2 mm and 3.6 mm. A good agreement of hematocrit values calculated from the Doppler signal with laboratory measurements was obtained: for sample volumes separated by 3.6 mm and 1.2 mm, the correlation coefficients were equal to 0.96 and 0.79, respectively, for $p < .001$. Further investigations of applying this method *in vivo* in the common carotid artery are conducted. [Work supported by grant KBN No. 8T11E02317].

* * *

Determination of structural parameters of viscous ferrofluid by acoustic and magnetic methods

Andrzej SKUMIEL, Mikołaj ŁABOWSKI and Andrzej JÓZEF CZAK

Adam Mickiewicz University, Institute of Acoustics
61-614 Poznań, Umultowska 85, Poland, skumiel@amu.edu.pl

In this paper, the authors have presented experimental results of the dispersion research and anisotropy research of magnetic susceptibility, as well as the anisotropy measurements of an ultrasound wave absorption coefficient in a viscous ferrofluid, subjected to the test by an external magnetic field. According to the suitable theories, one can determine some parameters describing the structure of such a medium, and it is possible to explain the mechanism of an ultrasound wave absorption during a propagation. On the basis of magnetic research, the quantities such as: relaxation time of a magnetic susceptibility, average radius of a spherical cluster as well as the value of magnetic field strength causing saturation were determined.

* * *

The velocity of sound in bcc ^3He crystals near absolute zero

Jerzy SMELA and Piotr GRONKOWSKI

Rzeszów Pedagogical University, Institute of Physics

35-310 Rzeszów, Rejtana 16a, jsmela@atena.univ.rzeszow.pl, gronk@atena.univ.rzeszow.pl

Very-low-temperature behaviour of all modes of the velocity of sound in solid bcc ^3He is briefly explained. Both for the transverse and longitudinal velocities of sound in isotropic solids, the general relation is derived. It appears that for the qualitative agreement with experimental data, the absolute zero limit of the Debye function and effective temperature has been used. In this paper we have dealt only with the possibility of a theoretical explanation of the behaviour of the sound velocity measurements near the absolute zero temperature.

* * *

Construction of a new NaCl pressure scale and a universal equation of state for solids

Jerzy SMELA and Piotr GRONKOWSKI

Rzeszów Pedagogical University, Institute of Physics

35-310 Rzeszów, Rejtana 16a, Poland, jsmela@atena.univ.rzeszow.pl, gronk@atena.univ.rzeszow.pl

Recently a revised scale of pressure for NaCl was proposed by J.M. Brown (1999) as an updated approach of the 30-year old work of D.L. Decker (1965). An alternative approach to the analysis was utilised in conjunction with more recent data. The zero-Kelvin compression curve was parameterised using local basis function (splines) and constrained by accurate pressure-volume-temperature data. Pressure as a function of volume and temperature was calculated and listed. Now, the new approximate theory aiming at describing the function $p = p(V, T)$ is proposed. It appears that theoretical results agree with experimental data within 0.2%.

* * *

Mechanical properties investigation of the PZT type piezoceramics by mechanical spectroscopy method

Radosław ZACHARIASZ and Jan ILCZUK

Silesian Technical University, Department of Technology

41-200 Sosnowiec, Żeromskiego 3, Poland, rzachari@us.edu.pl

Ferroelectric ceramics of the PZT-type obtained on the basis of multiple solid solution $\text{Pb}(\text{Zr}_{1-x}\text{Ti}_x)\text{O}_3$ is used in many devices and piezoelectric transducers. Possibilities of utilization of the piezoceramics in many branches of industry are connected with qualification of its basic values, both dielectric and mechanical. The present paper shows the research results concerning the mechanical properties of the PZT-type piezoceramic, obtained by two methods — of hot pressing and the conventional method in different circumstances. Acoustic frequencies relaxation of the RAK-2 type was used to carry on the measurements, making it possible to determine the temperature dependencies of internal friction and changes of the dynamic Young modulus. Application of the UMT-11 supersonic defectoscopy made it possible to measure the speed of propagation of longitudinal and transverse supersonic waves. Basing on the measurements, the basic mechanical properties, such as Young's modulus, elasticity modulus and Poisson's coefficient obtained in different conditions, were determined. The obtained results of the measurements contributed to the technological optimization process of producing piezoceramics and widening its practical usage in different branches of industry.

*Bioacoustics***The audiometric assessment of hearing abilities in 16–60 years old individuals**

Helena GAWDA and Irena ISKRZAK

Medical Academy of Lublin, Department of Biophysics

20-074 Lublin, Spokojna 1, Poland, Gawda@panaceum.am.lublin.pl

Audiometric investigations (AAD-80) of 160 individuals at the age of 16-60 years were carried out. It was found, that the greatest loss of hearing in the frequency range of 250–2000 Hz was in the group of adolescents. Moreover, the percentage of individuals with a loss of hearing was maximum in this

age group. Instead, at the age of 50–59 years, the loss of hearing was minimal with respect to the physiological norm for this age group.

* * *

Biological structure phantom for purposes of ultrasound transmission tomography

Tadeusz GUDRA, Krzysztof J. OPIELIŃSKI and Juliusz S. BEDNAREK

Wrocław University of Technology

50-370 Wrocław, Wybrzeże Wyspiańskiego 27, Poland

gudra@zakus.ita.pwr.wroc.pl

In ultrasound transmission tomography (UTT), one of the most important parameters which allows to image the internal biological structure of the investigated object is the sound velocity. To estimate the accuracy and correctness of biological structures reconstructed on the basis of ultrasound velocity measurements, it is necessary to possess a phantom of this structure. In the paper, the parameters of the ultrasound velocity of an ultrasonic wave for chosen healthy organs and tissues and those affected by tumour are presented. Pathology may concern cells as well as tissues and can manifest itself by changes of sizes, shapes and densities of particular tissues. Using the latest literature on tissue parameters (healthy or with morbid symptoms), a laboratory investigation of different materials which could be used for the phantom building, was carried on. The results of this work enable us to build the biological structure phantom imitating healthy and pathological tissues. This phantom allows us to determine diagnostic possibilities of the ultrasonic apparatus based on the UTT method for internal structure imaging. [Work supported by the Committee for Scientific Research in Warsaw, Grant No. 8 T11E 029 14].

* * *

Biological basis for hygienic standardisation of whole-body vibration

Part I: Experimental studies

Barbara HARAZIN

Institute of Occupational Medicine and Environmental Health,

Sosnowiec, Kościelna 13, Poland

b-harazin@imp.sosnowiec.pl

Experimental studies carried out with participation of young subjects in laboratory conditions in the 60s and 70s revealed the role of basic parameters of the whole body vibration in inducing biomechanical, psychophysical and physiological reactions of the human body. These studies determined the influence of the acceleration magnitude, frequency, direction of vibration and duration on the degree and character of the reaction of the body. It was observed that the transmissibility of vibration in the human body depends on the biomechanical properties of the body, which are modified by its different postures and positions. The results of the experimental studies were used to determine the threshold limit values of the whole-body vibration developed for the protection of the health of workers professionally exposed to vibration.

* * *

Biological basis for hygienic standardization of whole-body vibration

Part II: Epidemiological studies

Barbara HARAZIN

Institute of Occupational Medicine and Environmental Health

Sosnowiec, Kościelna 13, Poland

b-harazin@imp.sosnowiec.pl

Occupational exposure to the whole-body vibration may result in the development of unspecific diseases in many systems of the human organism. As scientific knowledge advances, the threshold limit values are updated. They are now more and more often associated with remote unspecific health effects observed in the exposed workers. The assessment of large groups of employees exposed to vibration indicates that the biggest changes are observed in the motor system. Less affected are the digestive system, the vestibulo-cochlear organ, the organs of senses and the peripheral circulatory system. The aim of this paper was to present the results of epidemiological examinations of the back pain of the workers occupationally exposed to the whole-body vibration. Medical examinations indicate that early changes

in the spine may occur, such as: discopathy and degenerative changes of discs and joints. This paper presents current data from the world literature on the relationship between the level of daily vibration dose as well as the period of occupational exposure and the probability of occurrence of disorders in the lumbar section of the spine. The results of the studies were used to develop national suggestions for the threshold limit values of the whole-body vibration.

* * *

Influence of surgery argon laser on electric function of ear cochlea

Wojciech MICHALSKI*, Krzysztof PREŚ, Wojciech DZIEWISZEK, Lucyna POŚPIECH

* Wrocław University of Technology,
Institute of Telecommunication and Acoustic
50-370 Wrocław, Wybrzeże Wyspiańskiego 27, Poland

In the field of medicine, the argon laser is known as a surgery tool. At first the laser was used in dermatology and ophthalmology, next, from the end of the 70 th, in ear microsurgery. Up to now, the side-effects of using the argon laser in stapedotomy are not exactly known. During stapedotomy, the side effects mainly concern ear cochlea and can appear by changes of its electric activity. In other words, changes of electric response of cochlea can be a measure of the side effects caused by laser irradiation of the one. Such possibility has been used by us to measure the changes of electric response (the cochlear potentials) of guinea pigs cochlea caused by the argon laser irradiation of the cochlea surface. Different laser pulse parameters were used in the experiment. Unlike electric responses of the cochlea have been described. Limits for safety argon laser irradiation of the cochlea surface have been initially formulated.

* * *

Influence of biostimulation CTL-1106 MJ laser on electric function of ear cochlea

Wojciech MICHALSKI*, Krzysztof PREŚ and Lucyna POŚPIECH

* Wrocław University of Technology,
Institute of Telecommunication and Acoustic
50-370 Wrocław, Wybrzeże Wyspiańskiego 27, Poland

Laser beam of appropriate wavelength affecting living tissue can stimulate different processes on the cell level. If laser beam power is less than about 500 mW, no photothermal effects take place in the target tissue. The aim of the experimental studies was to determine if and how far the biostimulation laser beam can change the electrical activity of ear cochlea of guinea pigs. The CTL-1106 MJ semiconductor laser produced by Laserinstruments (Warsaw) was used in the experiment. Fundamental parameters of the laser are the following: CW output power –100 mW, generated wavelength –810 nm. The experiment was performed on 10 pigmented animals. Very different responses of cochlea to laser exposure have been recorded. Lack of answer of the cochlea on the laser irradiation was observed in 20% of the cases examined.

* * *

Arteriosclerosis risk evaluation on the basis of non-invasive ultrasonic examinations of the common carotid artery wall stiffness

Tadeusz POWAŁOWSKI, Zbigniew TRAWIŃSKI and Lech HILGERTNER*

Polish Academy of Sciences, Institute of Fundamental Technological Research
00-049 Warszawa, Świętokrzyska 21, Poland
tpowal@ippt.gov.pl, ztraw@ippt.gov.pl

* Medical Academy, Department of General and Thoracic Surgery
Warszawa, Banacha 1a, Poland

The authors present the new classification method for determining the arteriosclerotic risk factor group by means of the non-invasive ultrasonic examinations of the human common carotid artery wall stiffness. The evaluations of the common carotid artery wall stiffness were based on measurements of the logarithmic stiffness coefficient α . The examinations were performed using ultrasonic wall tracking system VED elaborated in IFTR-PAS in Warsaw. The sensitivity of the proposed method is 66% and its specificity 79%.

* * *

Analysis of the input vascular impedance in the human common carotid artery on the basis of non-invasive ultrasonic examinations

Tadeusz POWAŁOWSKI, Lech HILGERTNER*, Zbigniew TRAWIŃSKI and Krzysztof KAŁUŻYŃSKI**

Polish Academy of Sciences, Institute of Fundamental Technological Research
00-049 Warszawa, Świętokrzyska 21, Poland,
tpowal@ippt.gov.pl* Medical Academy, Department of General and Thoracic Surgery
Warszawa, Banacha 1a, Poland** Warsaw University of Technology, Institute for Precision and Biomedical Engineering
Warszawa, Chodkiewicza 8, Poland

The authors present the results of the examinations of the input vascular impedance in the human common carotid artery for different degrees of stenosis of the internal carotid artery caused by arteriosclerosis. In analysis of the input impedance, a three-element model was applied. The examinations were based on simultaneous measurements of the blood flow and the blood pressure, using the ultrasonic Doppler and echo tracking methods. [Work supported by the Committee for Scientific Research in Warsaw, Grant No. 8T11E00316]

* * *

Application of acoustic emission method for plant tissue investigation

Artur ZDUNEK

Polish Academy of Sciences, Institute of Agrophysics im. B. Dobrzańskiego
20-290 Lublin, Doświadczalna 4, Poland
azdunek@demeter.ipan.lublin.pl

External loading causes cracking of structural elements of a plant tissue, e.g. cracking of cell's membranes and debonding of the cells. The aim of the present paper is to apply a method of acoustic emission to study the influence of turgor on the process of potato tissue cracking. The AE method has been used to determine the failure conditions as a critical strain and a critical stress for potato tuber tissue. The compression tests were carried out with constant strain rate for samples with different turgor. Increase in turgor causes decrease in the compressive strength and the critical stress. The turgor does not influence the critical strain and maximal strain. The experiment showed that there was a negative correlation between the total count sum, the total event sum and the compressive strength of the potato samples. The results show that the acoustic emission method can be used in investigation of cracking processes in plant tissues. [Work supported by the Committee for Scientific Research in Warsaw, Grant No. 5 P06 F01317].

*Structural acoustics and vibration***Transfer path analysis as the tool for energy-based approach to vibroacoustical analysis**

Jacek CIEŚLIK

University of Mining and Metallurgy, Department of Robotics and Machine Dynamics
30-059 Kraków, Mickiewicza 30, Poland

The paper focuses on the application of energy flow to the analysis of mechanical behaviour. There are several different methods used for investigation of sound and vibration energy in spatial structures consisting of beams, shells and plates. Among them, the Transfer Path Analysis (TPA), as a test-based procedure, is used to trace of vibro-acoustic energy flow from a source to receiver through the set of known structure-born sound pathways. The main aim of TPA is to evaluate the energy flow contribution of each pathway in the total energy transfer. This method is used in the hybrid method - combination of Finite Element Method (FEM) and experimental modelling, for vibro-acoustic optimisation of a design. The presented approach leads to faster and better performance in modelling and in the analysis of large mechanical systems. In the article are presented the results of the energy flow analysis obtained from TPA between the chosen subsystems. The practical application aspects are discussed. Although the helicopter fuselage and elements of tram carriage suspension were basically used in the analysis, the same technique can be applied in other large mechanical structures.

* * *

The influence of the radiation impedance on the resonance of the two-dimensional mechanical systems with losses

Andrzej DOBRUCKI and Romuald BOLEJKO

Wrocław University of Technology, Institute of Telecommunication and Acoustics
50-370 Wrocław, Wyspiańskiego 27, Poland, ado@zakus.ita.pwr.wroc.pl, rom@zakus.ita.pwr.wroc.pl

The vibrations of the two-dimensional mechanical system are affected by the medium in which it is immersed. The influence of the medium on the resonance depends on the shape of vibrating system and on the ratio of density of the mechanical systems and the medium. In the presence of the medium, the resonance frequency of vibrating body decreases due to the mass of medium load. Overall losses of the vibrating systems are the sum of mechanical and acoustical losses. In the paper, the influence of the medium on the vibration of a thin cellulose plate is investigated. The influence of the medium load on the resonance frequency of a thin cellulose plate is of the order of several percent for gas, and of the order of some scores percent for liquid. Overall losses of the thin cellulose plate immersed in gas are defined by mechanical losses due to predominance of the mechanical resistance.

* * *

Optimization of vibroacoustical energy flow in complex mechanical systems

Marek IWANIEC

University of Mining and Metallurgy, Department of Robotics and Machine Dynamics
30-059 Kraków, Al. Mickiewicza 30, Poland

The paper shows a new advantages of an optimization method for energy flow. As the first stage, the algorithm is presented which allows to investigate the influence of the wide range of constructional parameters on vibroacoustical energy flow in complex mechanical structures. As a basis of analysis, the SE.4 method is used. The SEA calculations results create a data base for further optimality calculation with the arbitrarily chosen aim function. Using the described algorithm, some results are presented showing the variation of acoustical energy radiation with plate and stiffeners parameters for several stiffening configurations.

* * *

An Analytical and Experimental Comparison of Optimal Actuator and Error Sensor Location for Vibration Attenuation

Nicole KESSISSOGLOU

James Cook University, Mechanical Engineering
Qld 4811, Australia, Nicole.Kessissoglou@jcu.edu.au

Feedforward active control of the plate flexural waves in a finite plate has been analytically and experimentally investigated. The plate under consideration is simply supported along two parallel edges, and free at the other two edges. Point forces were used to generate the primary and secondary plate excitation. The error sensor is optimally located in order to achieve the best control performance.

* * *

Directional characteristic of free-edge circular plate

Lucyna LENIOWSKA

Rzeszów Pedagogical University, Institute of Technology
35-310 Rzeszów, Rejtana 16a, Poland, lleniow@atena.univ.rzeszow.pl

In this paper, the problem of determining the directional characteristic for a free-edge circular plate is considered. It was assumed that the axially-symmetric plate vibrations are forced by an external pressure, sinusoidally variable in time, acting on the central part of the plate surface with radius a_0 . The dynamic influence of the waves emitted by the plate on its vibration velocity distribution as well as the losses in the plate material were neglected. Applying the well-known solution of the plate equation of motion and considering the continuity and boundary conditions, the system of six equations was obtained. Solving this system by computer methods, an expression allowing to determine the directional characteristics was found. [Work supported by the Grant 7T07B05118 from Committee for Scientific Research of Poland].

* * *

Application of laser measurement technology for determination of vibration amplitude of free-edge circular plate

Lucyna LENIOWSKA, Jerzy PISAREK*, Stanisław SZELA and Andrzej SZUMIŁO

Rzeszów Pedagogical University, Institute of Technology
35-310 Rzeszów, Rejtana 16a, Poland, lleniow@atena.univ.rzeszow.pl* Technical University of Częstochowa, Institute of Mechanics and Machine Design Fundamentals
42-200 Częstochowa, Dąbrowskiego 73, Poland

This paper presents 3D plots of vibration velocity distribution of free-edge circular plate prepared on the basis of a mathematical model. These plots have been compared with the pictures of a vibrating plate obtained by experimental method, with the use of the laser measurement technology. Applying the holographic method of the time mean [2], the amplitude of plate vibration at chosen cross-section lines has been calculated. The photo of the (1,1) mode of a circular plate taken by the laser-method as well as corresponding diagrams of vibration amplitude for sample cross-sections have been enclosed. [Work supported by the Grant 7T07B05118 from Committee for Scientific Research of Poland].

* * *

Application of trigonometric spline function to modelling the resonance vibration

Ryszard LENIOWSKI

Technical University of Rzeszów
35-959 Rzeszów, Wincentego Pola 1, Poland, lery@ewa.prz.rzeszow.pl

This paper presents a short introduction to the new original innovation of finite element method (FEM), very useful for vibration analysis of complex dynamical systems. The characteristic feature of the proposed innovation is application of the modified trigonometric splines (ZTFS) as a shape function in FEM model instead of the Hermite polynomials. The set of trigonometric splines has all the advantages of cubic polynomials. These splines have no limits in case of n -order differentiation. Therefore the finite element method with ZTFS can be made automatically with the use of symbolic computations. The example of the innovated FEM method showing its effectiveness is enclosed. [Work supported by the Grant 7T07B05118 from Committee for Scientific Research of Poland].

* * *

Experimental study of vector field around flat structures inside acoustic flow field

Stefan WEYNA

Technical University of Szczecin, WTM
71-065 Szczecin, Al. Piastów 41, Poland, weyna@shiptech.tuniv.szczecin.pl

Most of the acoustic vector fields encountered in practice are too complicated to be precisely modelled mathematically. This is one of the reasons why the experimental investigation fields using sound intensity technique are a useful tool for the vector field distributions. In the article, the author presents the application of sound intensity technique to graphic presentation in 2D and 3D image of the spatial distribution of the acoustic energy flow over a hard disc and a rectangular plate. This description of acoustic vector field fully explains the physical meaning of wave phenomena and makes it possible to consider the mechanisms of propagation, radiation, diffraction or scattering on the obstacles.

* * *

Prediction of sound transmission loss of crane cab using SEA

Jerzy WICIAK, Bogdan STOLARSKI* and Ryszard PANUSZKA

University of Mining and Metallurgy, Department of Robotics and Machine Dynamics
30-059 Kraków, Al. Mickiewicza 30, Poland, wiciak@uci.agh.edu.pl* Technical University of Kraków
31-864 Kraków, Jana Pawła II 37, Poland, stolarsk@graf.mech.pk.edu.pl

The paper presents some results of calculations of transmission losses for a crane cab. Calculations were performed using Statistical Energy Analysis Method and compared with the results obtained by means of classical methods. This method of calculation allows to create the conditions of acoustic comfort in lift cabs according to the acoustic field conditions in industrial halls.

*Noise, its effects and control***Resonance sound absorbing elements adapted for high hygienic requirements**

Jan CZUCHAJ*, Antoni ŚLIWIŃSKI, Krzysztof ŚRODECKI and Stanisław ZACHARA

University of Gdańsk, Institute of Experimental Physics
80-952 Gdańsk, Wita Stwosza 57, Poland, fizas@univ.gda.pl

* ACE SOFT, 81-852 Sopot, Kasprzowicza 12, Poland

In special industrial application, e.g. in food or pharmacological factories where high hygienic requirements are necessary, no usual acoustical absorbing systems and materials can be used. In extremely wet or chemically active environmental conditions, only resonance systems of stainless steel, aluminium or hardy plastics may be applied. In the paper, some calculations of the absorption coefficient of some Helmholtz resonators used as elements for constructing absorbing coffer systems were performed. Some models were constructed and their absorbing properties were measured using the impedance tube.

* * *

Traffic noise at crossroads

Ryszard JANCZUR, Elżbieta WALERIAN and Mieczysław CZECHOWICZ

Polish Academy of Sciences

Institute of Fundamental Technological Research

00-049 Warszawa, Świętokrzyska 21, Poland, rjanczur@ippt.gov.pl

Acoustical climate dependence on urban structure and traffic parameters could be efficiently tested by computer simulation programs. Here, the PROP5 program is used to investigate the sound level along façades of buildings in the vicinity of a crossroad. The investigated urban structure has a form of a canyon-street of a given width. The dependence of the sound level at the ground floor and the sound level distribution along the building façade on parameters of the road as a noise source has been presented. These parameters are: the number of lanes and their positions in a canyon, concerning the road geometry, and vehicle streams parameters. The vehicles divided into classes are represented by the equivalent point sources of a given elevation above ground and the power spectrum. Their streams on a lane are characterised by the average speed and flow rate. The sound level distribution along the façades shows relatively smooth decrease with elevation. The decrease amounts to 3 dB(A) for the twelve-floor building. The addition of two lanes to the road results in the sound level increase of 2.5 dB(A), what is in agreement with the previously obtained results for a single canyon. Such details as the difference in the sound level, resulting from asymmetry of the crossroads, are also observed.

* * *

Noise protection in low frequency range

Anna KACZMARSKA, Danuta AUGUSTYŃSKA and Zbigniew ENGEL*

Central Institute for Labour Protection

00-701 Warszawa, Czerniakowska 16, Poland, ankac@ciop.waw.pl

* University of Mining and Metallurgy, Department of Robotics and Machine Dynamics
30-059 Kraków, Al. Mickiewicza 30, Poland

The papers presents a method of noise reduction in a control cabin in low-frequency noise. The models of sound absorber with Helmholtz resonators were described. Results of experimental investigations in low frequency range are included.

* * *

Investigations of changes in protection properties of hearing protectors due to duration of use — preliminary results

Ewa KOTARBIŃSKA and Janusz P. MNICH

Central Institute for Labour Protection

00-701 Warszawa, Czerniakowska 16, Poland, ewkot@ciop.pl, jamni@ciop.pl

The paper presents the results of one-year-long investigations of changes in hearing protector's protection properties due to duration of use. Four comparable patterns: two Polish ones — Faser N1, Opta OS-5N and two Swedish ones — Bilsom Loton 2401 and Peltor H9A, were investigated. Investigations

were performed at real conditions in four factories. Measurement results of sound attenuation, insertion loss and headband force for each of the tested patterns are presented. Also presented are the changes of protection parameters H, M, L and SNR, compared to catalogue values and changes of insertion loss and headband force after one-year use. [Work supported by the Committee for Scientific Research in Warsaw, realized in the framework of the National Strategic Program "Occupational Safety and Health Protection in the Working Environment" – SPR 03.7.20].

* * *

Acoustic and mechanical properties of level-dependent ear-muffs

Ewa KOTARBIŃSKA*, Zbigniew PUSŁOWSKI*, Dariusz PUTO* and Mariusz SIEK

* Central Institute for Labour Protection

00-701 Warszawa, Czerniakowska 16, Poland, ewkot@ciop.waw.pl

Technical University of Warsaw

00-658 Warszawa, Nowowiejska 15/19, Poland

The aim of the paper is to present the methods and some results of acoustic and mechanical measurements of four prototypes of level-dependent ear-muffs. The acoustic tests include measurements of sound attenuation of level-dependent ear-muffs in their passive mode, and criterion levels H, M, L with the electronic system in operation at full gain. The acoustic tests include testing of headband force, cushion pressure, adjustability and cup rotation. All the tests have been carried out according to the requirements of prEN 352-4:1999.

* * *

Validation of selection anti-vibration gloves procedure for vibratory tools

Jolanta KOTON, Piotr KOWALSKI and Janusz SZOPA

Central Institute for Labour Protection

00-701 Warszawa, Czerniakowska 16, Poland, jokot@ciop.pl, pikow@ciop.pl, jaszo@ciop.pl

Occupational exposure to hand-transmitted vibration can cause many kinds of disorders in the human body. One of the methods of reduction of the risk of vibration damage is using antivibration gloves (AV) by vibratory tool users. However, positive classification of a glove as an AV one, does not mean that this glove will be equally efficient in case of using it by workers handling various vibratory tools. That is why the procedure of selection AV gloves for vibratory tools was elaborated. In this procedure it was established that the glove efficiency in reducing vibration produced by a particular vibratory tool will be characterised by two protection efficiency indices (PEI). These indices depend on the visco-elastic properties of the glove as well as on the vibration spectra of a particular tool. The results of validation of the procedure, obtained by comparing the calculated indices and achieved by "in-situ" measurements, is presented in this paper. [Work supported by the Committee for Scientific Research in Warsaw, Project 03.8.7 realized in the frame of the National Strategic Program "Occupational Safety and Health Protection in the working environment"].

* * *

Influence of amplitude and frequency of excitation signal on vibration transmission from tool handle into the operator hand

Piotr KOWALSKI

Central Institute for Labour Protection

00-701 Warszawa, Czerniakowska 16, Poland, pikow@ciop.pl

The influence of amplitude and frequency of the excitation signal on the vibration transmission from the tool handle into the operator hand was investigated. The results obtained from these investigations are presented in this paper. The analysis of results achieved during examinations produced the data which constituted a basis to define proposals of the forms of two indices typical for transmission of vibration in the "operator's hand – manual tool" system. [Work supported by the Committee for Scientific Research in Warsaw, Project 02.4.8 realized in the frame of the National Strategic Program "Occupational Safety and Health Protection in the working environment"].

* * *

Determination of the sound power level of the reference sound source using engineering and sound pressure survey methods in different test conditions

Witold MIKULSKI and Piotr TADZIK

Central Institute for Labour Protection

00-701 Warszawa, Czerniakowska 16, Poland, wimik@ciop.pl, tadek@ciop.pl

The sound power level of the reference sound source using an engineering method (PN-EN ISO 3744) and a sound pressure survey method (PN-EN ISO 3746) were determined to check the precision of these methods for determination of L_w expressed as a standard deviation of reproducibility. It was made in two rooms and in a free field.

* * *

Acoustic assessment of machines on the basis of emission sound pressure levels

Dariusz PLEBAN and Aleksander GAWLIK*

Central Institute for Labour Protection

00-701 Warszawa, Czerniakowska 16, Poland, daple@ciop.pl

* University of Mining and Metallurgy, Department of Robotics and Machine Dynamics

30-059 Kraków, Al. Mickiewicza 30, Poland

The European Standards series EN ISO 11200 specifies the methods for determining the emission sound pressure levels at a workstation and at other specified positions. According to the Machinery Directive 98/37/EC, the emission sound pressure level must be taken into consideration, together with the sound power level, in carrying out the acoustic assessment of machines. The results of the experimental tests have proved a great consistence of the values of the emission sound pressure levels determined by using different methods specified in the European Standards series EN ISO 11200. However, the acoustic assessment of the machine, carried out only according to the requirements of the Directive 98/37/EC, does not enable a complete assessment. In this connection, an acoustic assessment of the machine using an emission index is proposed. The value of the emission index is calculated on the basis of the value of the emission sound pressure level.

* * *

Evaluation of the long term sound pressure level from power lines based on measuring under fair weather conditions

Tadeusz WSZOLEK

University of Mining and Metallurgy, Department of Mechanics and Vibroacoustics

30-059 Kraków, Al. Mickiewicza 30, Poland, twszolek@uci.agh.edu.pl

The corona noise depends strongly on weather conditions hence, according to Polish Standard PN-N-1339, it is necessary to perform measuring under fair and bad weather conditions. Although, because of some technical difficulties in taking measurement under bad conditions (rain, fog, etc.) as well as temporary character of those conditions and, on the other hand, steady state corona noise level (independent of the other reasons such as airborne substances, scratches etc.), an attempt was made to evaluate a long-term corona noise level (for one year period) based only on the measurement results. In that case the corona noise level in practice depends only on geometry of the transmission line layout and technical conditions, and its value can change by more than 10 dB. In order to estimate the corona noise level under bad conditions, an empirical model was used which was fitted according to the measurement results in the vicinity of 400 kV transmission lines in different parts of Poland. The long-term corona noise level was evaluated using algorithms known from the standard mentioned earlier.

* * *

Noise level in the vicinity of road junction

Zbigniew WOŹNIAK, Maria RABIEGA and Andrzej JAROCH

Wrocław University of Technology, Institute of Telecommunication and Acoustics

50-370 Wrocław, Wybrzeże Wyspiańskiego 27, Poland, maran@zakus.ita.pwroc.pl

The computer-aided model for equivalent noise level near the road junction is presented in the paper. Acoustical parameters such as sound power level and directivity index for accelerating and decelerating

vehicle were determined on the basis of time history recorded at a reference point near the road. A distance as well as a speed of a single vehicle at the beginning and in final phase of motion were known. The computer model written in Delphi3 was tested and showed that it is the phase of acceleration which causes an increase of noise level in the vicinity of road junction in comparison with that for freely flowing traffic. The model was verified in traffic conditions in Wrocław for several road junctions with traffic lights and showed a good agreement between calculated and measured data.

* * *

Hearing protectors: Attenuation of peak sound pressure of acoustic impulses

Jan ŻERA

Central Institute for Labour Protection
00-701 Warszawa, Czerniakowska 16, Poland, jazer@ciop.waw.pl

Peak sound pressure attenuation introduced by a hearing protector for acoustic impulses was measured for a sample of 23 protectors made by different manufacturers. The impulses were generated in the laboratory with the use of a foil blaster or a steel plate which was hit by a hammer. Their peak levels ranged from 130 to 155 dB. The peak pressure level attenuation was compared with the protector parameters H, M, L, and SNR. The investigation revealed that attenuation of a hearing protector measured for peak pressure of impulses with a short rise is usually smaller than the attenuation measured for steady-state noise signals (H, M, L, and SNR values). For the impulses used in the experiment, the M, L and SNR values were in better agreement with the peak sound attenuation than the H values.

Architectural acoustics

The sound reinforcement systems of sports halls

Bohdan W. KULESZA and Witold RYSZKOWSKI*

Wrocław University of Technology, Institute of Telecommunication and Acoustics
50-370 Wrocław, Wybrzeże Wyspiańskiego 27, Poland, bwkul@zakus.ita.pwr.wroc.pl

* Solski Academy of Theatre, 53-333 Wrocław, Powstańców Śląskich 22, Poland

The specific properties of sound reinforcement systems of multiple functions sports halls are presented in this paper on the examples of the sound reinforcement systems of Hala Ludowa and "Orbita" hall in Wrocław and the sports hall in Chełm Lubelski designed by the authors. The systems are well suited for operation with the following usage variants: sports events, competitions, training, fairs, exhibitions, stage performances, meetings. Factors influencing the quality of sound reinforcement systems are described starting with room acoustics, through electroacoustic circuits, to properties of loudspeakers and their distribution within the hall.

* * *

The influence of stage house and diffusion modeling on the theatre reverberation time

Piotr KOZŁOWSKI and Krzysztof RUDNO-RUDZIŃSKI

Wrocław University of Technology
50-370 Wrocław, Wybrzeże Wyspiańskiego 27, Poland, peterek@zakus.ita.pwr.wroc.pl

In the paper are presented two topics dealing with the computer modeling of theatre acoustics. In the modeling the Raynoise simulator has been used. The influence of the diffusive reflection and the method of the stage house modeling on the reverberation time were examined. The modeling results were compared with the measurement results of the existing theatre – Bogusławski Hall at National Theatre in Warsaw. With the creation of complete model of the theatre, with a hall and a stage house, a conformity of measurements and modeling has been obtained. Taking diffusive reflection into consideration, the reverberation time in the frequency of diffusive reflection was made shorter.

* * *

Measurement and evaluation of noise in buildings according to new European standard

Marianna MIROWSKA

Institute of Building Technology
02-656 Warszawa, Ksawerów 21, Poland, akustyka_itb@zigzag.pl

In the paper, a brief description of the noise measurement method proposed in the standard pr EN ISO 16032 is given. The problems of measurement and assessment methods are discussed. The results

of noise measurement in dwellings carried out according to pr EN ISO 16032 and PN-87/B-02156 are compared.

* * *

Direction of arrival algorithms for sound reinforcement systems

Krzysztof PASSELLA and Piotr ŁABNO

Wrocław University of Technology, Institute of Telecommunication and Acoustics
50-370 Wrocław, Wybrzeże Wyspiańskiego 27, Poland, kpas@il.wroc.pl

The paper concerns one of the possible directions in the development of sound reinforcement systems. The main topic is connected with the use of adaptive algorithms, in particular with the development of determination of the direction of arrival of acoustic wave finding (DOA Algorithms). The authors present the role of the DOA algorithms in sound reinforcement systems, which are a method of analysing the original acoustic field. This study examines the construction of the microphone-loudspeaker system, in which we can apply an adaptive steering for an acoustic panorama. The electroacoustic system also enables the possibility of synthesis in the first reflections of a listening space. This type of system solution is referred to as an "artificial" acoustic reinforcement system.

Transduction

Model of spatial impulse response of loudspeaker

Ireneusz CZAJKA, Henryk ŁOPACZ and Ryszard OLSZEWSKI

University of Mining and Metallurgy
30-059 Kraków, Al. Mickiewicza 30, Poland
ghczajka@cyf-kr.edu.pl, lopacz@agh.edu.pl, gholszew@cyf-kr.edu.pl

In this paper we describe our investigations of the model of spatial impulse response of a loudspeaker. We try to obtain the impulse response of source in a given direction, based on the impulse response on main axis of the sound source.

* * *

Psychoacoustic criteria for digital loudspeaker equalization

Paweł DZIECHCIŃSKI and Maurycy J. KIN

Wrocław University of Technology, Institute of Telecommunication and Acoustics
50-370 Wrocław, Wybrzeże Wyspiańskiego 27, Poland
pdziehc@zakus.ita.pwr.wroc.pl, mjk@zakus.ita.pwr.wroc.pl

One of the problems to be solved at digital equalization filters is to limit its dynamic range if the frequency response of the corrected object which has large irregularities. In the paper, the preview of knowledge on the perception of peaks and notches of the frequency response is presented. Application of this information in the design process can allow to remove unperceived irregularities from the response, making the dynamic range higher. The real-time filtering makes also these filters more expensive, so a compromise between the order of filter and the quality of equalization is needed. The threshold values connected with linear distortion also allows to define a minimal speed of signal processor which should be used for the equalization, making the corrected irregularities unperceived. This paper also presents analytical equations describing the different frequency scales which may be helpful for the defining the l parameter connected with the warped filters.

* * *

Microphone systems vs. perception of the sound source

Maurycy J. KIN and Małgorzata TETERUK

Wrocław University of Technology, Institute of Telecommunications and Acoustics
50-370 Wrocław, Wybrzeże Wyspiańskiego 27, Poland, mjk@zakus.ita.pwr.wroc.pl

In the paper, the basic aspects of perception of the sound source position resulting from the recordings made by various microphone systems, are discussed. The previously obtained results (theoretical and experimental ones) were the start point for research on the relations between the perceived sound source

position coming from a particular microphone system, and theoretically defined stereo imaging. In the course of modelling, it has been found that the sound source position depends strongly on the system used for the recording. The results have been discussed from the points of view of cohesion and spaciousness of the recording.

* * *

Secondary breakdown of transistors in high power audio amplifiers with enlarged output voltage

Marek KUKAWCZYŃSKI, Zygmunt MUSIAŁOWSKI and Józef STANCLIK

Wrocław University of Technology

50-370 Wrocław, Wybrzeże Wyspiańskiego 27, Poland, mak@zue.ita.pwr.wroc.pl

This paper deals with the secondary breakdown of output stage bipolar transistors of high power audio amplifiers. The amplifiers' output voltage is larger than that delivered by the applied integrated circuit alone. Therefore such amplifiers are particularly endangered to a failure. The worst conditions of the transistors' operation with respect to the secondary breakdown occur when the amplifier is loaded by a loudspeaker device model. Particularly critical transistor operating conditions occur at the frequency of 10 Hz, when the phase of loudspeaker device impedance equals 40°. Secondary breakdown is a destructive failure and its laboratory tests are difficult, time-consuming and expensive. Therefore computer simulation is an effective and convenient way to investigate this problem. However, for a computer simulation, the circuit element models are necessary. In order to fulfil this conditions, the relevant models of bipolar transistor, high-power audio amplifiers and loudspeaker device are used. The model of the transistor is a behavioral one and takes into account the dynamics of the secondary breakdown. It makes the calculations more effective and convenient. The obtained simulation results, using the PSpice computer program, confirm the serviceability of the proposed circuit element models.

* * *

Virtual acoustic objects

Henryk ŁOPACZ

University of Mining and Metallurgy

30-059 Kraków, Al. Mickiewicza 30, Poland, lopacz@agh.edu.pl

Convolution of the testing signal and impulse response of the object or loudspeakers can improve the quality of listen-oriented tests and make them easier. The described hardware and software solutions have been developed and evaluated since several years. They are implemented on DSP 5630xx, 9600x and ADSP 2106x processors and also on IBM PC compatible computers. In PC-solutions, a sound card is used as an I/O device and convolution calculations are realized by a system processor. It is possible to realize real-time testing signal convolution with minimal pre-delay using multiprocessor devices and an algorithm based on divided impulse response. With the aid of PIII processors calculation power and multitask possibilities, the software based on minimal cost algorithm was built. It is possible to build virtual rooms using this software. Using such virtual rooms it will be possible to evaluate more precisely the transmission quality of acoustic signal in real or model rooms.

* * *

Dispersive delay lines with nonlinear frequency modulation

A. MILEWSKI^o, S. GAWOR^{*}, P. MILEWSKI^{**} and M. BASZUN^{***}

^o Tele and Radio Research Institute

03-450 Warszawa, Ratuszowa 11, Poland

^{*} Agricultural Technical Academy

85-791 Bydgoszcz, Kaliskiego 7, Poland

^{**} Polkomtel S.A., 02-001 Warszawa, Al. Jerozolimskie 81, Poland

^{***} Technical University of Warsaw

00-665 Warszawa, Nowowiejska 15/19, Poland

A comparison between dispersive delay lines with linear and nonlinear frequency modulation is presented. Using nonlinear frequency modulations makes it possible to obtain low sidelobes level without using the amplitude weighting in the compressor. It allows to eliminate the receiver mismatch loss (in the linear frequency-modulated signals the mismatch losses are about 1.4 dB).

* * *

The influence of acting signal on the creation of NARMAX model of dynamic loudspeaker

Piotr PRUCHNICKI

Wrocław University of Technology, Institute of Telecommunication and Acoustics
50-370 Wrocław, Wybrzeże Wyspiańskiego 27, Poland, misio@zakus.ita.pwr.wroc.pl

In the case of linear object modelling, the choice of acting signal is not a critical step, because the important requirement is that this signal should have equal and wide spectrum. The choice of the signal is more important for NARMAX model because it is a nonlinear model. In the paper, the influence of the kind of acting signal on the accuracy of the dynamic loudspeaker NARMAX model, is presented. The noise with the uniform and Gaussian distribution, MLS signal, Chirp and rectangular impulse were the investigated signals. [Work supported by Polish State Committee for Scientific Research, Grant: 8 T11D 026 15].

* * *

Optimization of NARMAX model for dynamic loudspeakers

Piotr PRUCHNICKI

Wrocław University of Technology, Institute of Telecommunication and Acoustics
50-370 Wrocław, Wybrzeże Wyspiańskiego 27, Poland, misio@zakus.ita.pwr.wroc.pl

In modelling the nonlinearities with the NARMAX-method, the polynomial representation of this model is used very often. This allows to obtain the coefficients in a more effective and simple manner. However, the high number of them and the fact that nonlinear representation is not known, make the obtained model inaccurate. Implementation of the optimisation method of NARMAX model based on the choice of significant coefficients, is presented in the paper. The algorithm has been tested on the mathematical models and measurement results of a dynamic loudspeaker. [Work supported by Polish State Committee for Scientific Research, Grant: 8 T11D 026 15].

* * *

Modification of high power operational amplifier macromodel for computer-aided design of audio high-power amplifiers

Józef STANCLIK

Wrocław University of Technology
50-370 Wrocław, Wybrzeże Wyspiańskiego 27, Poland, jstan@zue.ita.pwr.wroc.pl

Efficiency of computer-aided design of electronic circuit depends on the models of applied circuit components. It particularly deals with modelling of integrated circuits, usually replaced by their macromodels. Power audio amplifiers can be built using high-power operational amplifiers which capable of delivering maximum output current of large value (up to 15 A). Macromodels of such amplifiers are known, but modelling of their saturation voltage is not accurate enough. In the paper, a macromodel modification of integrated high-power operational amplifiers including FET transistors in the input stage is presented. The modification improves the model accuracy (the saturation voltage of integrated circuit with respect to the output current is modelled). It results in a wider operating area, where the macromodel maintains a satisfactory accuracy. Furthermore, the structure and the manner of choosing the macromodel parameters and elements modelling the amplifier saturation voltage versus its output current are proposed. Improved macromodel accuracy has been obtained without using additional macromodel elements. As an example, a macromodel of the OPA502 integrated circuit and its accuracy estimation are given.

* * *

Compatibility of stereo imaging taken with different microphone systems

Małgorzata TETERUK and Maurycy J. KIN

Wrocław University of Technology, Institute of Telecommunications and Acoustics
50-370 Wrocław, Wybrzeże Wyspiańskiego 27, Poland, mjk@zakus.ita.pwr.wroc.pl

The basic amplitude-phase patterns for different microphone systems used in concert and studio recording are described in the paper. These patterns have been obtained first by theoretical considerations, and next they have been measured practically. The subjects of research were: MS, XY and two AB systems (with cardioid and omnidirectional capsules). It turned out that large differences appeared in

the comparison of the model and real systems. They were caused by the fact that “theoretical” systems did not take into consideration all the aspects of the receiving of the acoustic signal. In addition, full compatibility of particular systems does not exist what has been confirmed experimentally. For example, the MS system is not compatible with the others, both in the amplitude and phase domains.

* * *

The influence of the enclosure on loudspeaker nonlinear distortions

Bronisław ŻÓŁTOGÓRSKI

Wrocław University of Technology, ITA
50-370 Wrocław, Poland, brz@zakus.ita.pwr.wroc.pl

Variation of the equivalent stiffness (stiffness of moving system suspensions and the air closed in the enclosure) and electromechanical coupling coefficient B_l with displacement of the moving system are assumed to be the main sources of nonlinear effects at low frequencies around the basic resonant frequency. The mechanical system of lumped parameters and the corresponding electric equivalent circuit governed by the set of two ordinary differential equations of second order are the basis of investigations with the use of MATHCAD worksheet. The multi-parameter model takes into consideration the loudspeaker moving system parameters, dimensions of the vented or closed enclosure and acoustic coupling of loudspeaker diaphragm and vent orifice. The distorted period of the acoustic pressure at the given point, the Fourier spectrum of that period, the magnitude of the nonlinear distortion coefficient as well as the frequency characteristics of the on-axis pressure and the nonlinear distortion coefficient, are the results of calculations. The research shows that it is possible to design the loudspeaker enclosure with respect of nonlinear distortions level. For this purpose, the nonlinear characteristics of suspensions and magnetic field should be known.

Psychological and physiological acoustics

The problem of sample size in the 2AFC procedure

Elżbieta ARANOWSKA, Piotr ROGOWSKI

The Chopin Academy of Music, Laboratory of Musical Acoustics
00-368 Warszawa, Okólnik 2, Poland, pro@chopin.edu.pl

Statistical evaluation of the data sets from psychophysical experiments carried out with the 2AFC procedure is given. The procedure presented can be used in proper planning of the experimental algorithm with reference to the number of subjects and number of replications. It can be also used for estimation of statistical reliability of the results obtained.

* * *

Examining the influence of visual cues on perception of sound localization in home theatre systems

Andrzej CZYŻEWSKI, Bożena KOSTEK, Piotr ODYA and Sławomir ZIELIŃSKI

Technical University of Gdańsk, Acoustics Department
80-952 Gdańsk, Narutowicza 11/12, Poland, kid@sound.eti.pg.gda.pl

The presented study deals with the analysis of the influence of visual cues on sound localization in home theater systems. In order to develop the concepts how to record and mix the multichannel sound for the purpose of TV presentations, one should examine in which way and how the visual context interferes with the surrounding sound. Therefore, one of the purposes of experiments is to associate properly the surrounding sound with digital video presented at the TV screen. This problem will be examined with the application of fuzzy logic to the processing of subjective test results. [Work supported by the Committee for Scientific Research in Warsaw, Grant No. 8 T11D 00218]

* * *

The peripheral and central processes in hearing

Urszula JORASZ

Adam Mickiewicz University, Institute of Acoustics
60-615 Poznań, Umultowska 85, Poland

It is assumed that the peripheral auditory system contains a bank of overlapping bandpass filters called auditory filters. The detection and discrimination of narrowband signals has traditionally been

explained by considering just one auditory filter at a time, this one which gives the highest signal-to-masker ratio. Although this model works well in many situations, it clearly fails in others. In some cases, the outputs of auditory filters tuned away from the signal frequency can be used to enhance signal detection as in CMR (comodulation masking release). In other cases such as in MDI (modulation detection/discrimination interference), the outputs of auditory filters tuned away from signal frequency degrade the signal detection. It seems likely that CMR and MDI can be produced by both peripheral within-channel processes and central cross-channel processes. The postulate is that CMR and MDI play a specific role in the analysis of auditory scene: the bridge between the peripheral and central processes in hearing.

* * *

Masking in the amplitude modulation rate domain

Joanna LEMAŃSKA and Aleksander P. SĘK

Adam Mickiewicz University, Institute of Acoustics
60-615 Poznań, Umultowska 85, Poland, olekse@main.amu.edu.pl

This paper is concerned with masking in the amplitude modulation domain. AM detection threshold was determined for 4-kHz sinusoidal carrier signal, modulated by a simple tone at frequencies: 2, 4, 8, 12, 16, 20, 24, 28, 32, 40 Hz in the presence of one of the two masking modulators. 16-Hz tone and 8-Hz width low-noise noise centred at 16 Hz were masking modulating signals producing clearly audible amplitude fluctuation. The most effective masking was observed in the frequency range close to the masking signal frequency. It seems that results of this experiment are consistent with a hypothesis of the modulation filter bank in the auditory system.

* * *

Binaural perception of two-tone complexes

Edward OZIMEK and Jacek KONIECZNY

Adam Mickiewicz University, Institute of Acoustics
60-614 Poznań, Umultowska 85, Poland

The study deals with the binaural perception of two-tone complexes with determined physical parameters. The psychoacoustic experiment revealed that the binaural interaction of those signals creates the auditory sensation close to that of an AM signal. The measured modulation depth (m) of the signals under investigation suggest a mechanism of a linear interaction of those signals, but only for small values of m . For higher values of m , the perceived modulation depth decreases when m increases.

* * *

Effect of modulator spectral structure on the AM detection thresholds

Ewa B. SKRODZKA and Aleksander P. SĘK

Adam Mickiewicz University, Institute of Acoustics
61-614 Poznań, Umultowska 85, Poland, afa@main.amu.edu.pl, olekse@main.amu.edu.pl

This paper is concerned with measurements of AM thresholds of 4-kHz tone modulated by means of harmonics complex consisting of three sinusoids of equal amplitudes. The experiment tested the effect of relative modulator phase and component frequency on the detection of the multi-tone modulator applied to the sinusoidal carrier. The RMS value of the modulator was the only factor determining the AM detection. AM detection thresholds were found to be independent of the relative modulation phase and of the frequency spacing of the components. This pattern of the results suggests that a second stage of filtering in the auditory system, if there is any, is not a simple analogue to the first stage of filtering where the auditory filters act.

* * *

Examining properties of acoustical elements of the hearing aid using physical modelling

Grzegorz SZWOCH and Bożena KOSTEK

Technical University of Gdańsk, Acoustics Department
80-952 Gdańsk, Narutowicza 11/12, Poland, greg@sound.eti.pg.gda.pl

The aim of this paper is to present a new method of examining the properties of the acoustical system. A physical model of the acoustical element is designed and implemented. Next, this model is

used to perform computer simulations, in which the influence of the parameters of the model and on its transfer function are examined. Results of the experiments are presented and discussed. An application of this method to the process of fitting the acoustical elements of the hearing aid to the individual needs of the patient is proposed. [Work supported by the Committee for Scientific Research in Warsaw, Grant No. 8 T11E 034 15].

* * *

Computer simulation of the dynamic range control system in hearing aids

Grzegorz SZWOCH and Bożena KOSTEK

Technical University of Gdańsk, Acoustics Department
80-952 Gdańsk, Narutowicza 11/12, Poland, greg@sound.eti.pg.gda.pl

In this paper, a computer model of the hearing aid dynamic range control system is presented. In this model, dynamic range of the signal is controlled in six independent frequency bands. Two-threshold dynamic range blocks are used in each frequency band. Thus, the high speech quality in hearing aid may be obtained by means of accurate shaping of the dynamic range of the signal. [Work supported by the Committee for Scientific Research in Warsaw, Grant No. 8 T11E 034 15].

* * *

Model of the binaural perception of FM frequency deviation

Andrzej WICHER and Edward OZIMEK

Adam Mickiewicz University, Institute of Acoustics
61-614 Poznań, Umultowska 85, Poland, awakzy@amu.edu.pl, ozimaku@amu.edu.pl

Model of the binaural perception of FM frequency deviation has been considered in this paper. The model combines elements of the generally accepted function model of the auditory periphery, elements of Zwicker's model and principles of the auditory grouping. The results of the model simulation when the range of average values of the relative neural activity correlate well with the psychoacoustic experimental data.

Speech production, perception and processing

Methods of enhancement of noisy speech signal

Stefan BRACHMAŃKI and Christoph M. MUSIALIK*

Wrocław University of Technology, Institute of Telecommunication and Acoustics
50-370 Wrocław, Wybrzeże Wyspiańskiego 27, Poland, brach@aipsa.ita.pwr.wroc.pl
* Algorithmix GmbH, 79-761 Waldshut-Tiengen, Klettgaustr. 21, Germany, cmm@algorithmix.com

This paper presents a review of methods of enhancement of signals degraded by noise, with special consideration to the program Sound Laundry for enhancement of speech corrupted by acoustic noise. The efficiency of enhancement of speech by the Sound Laundry is presented.

* * *

An analysis of the individual pitch change range in Polish

Grażyna DEMENKO

Adam Mickiewicz University, Institute of Acoustics
61-251 Poznań, Międzychodzka 5, Poland, lin@amu.edu.pl

With a view to evaluating the inter-subject variability concerning fundamental frequency contours, a statistical analysis of pitch changes in the productions by 40 speakers (male and female voices) was carried out. The input text material (based on railway timetable information) included statements, wh-questions, yes/no questions, and instructions (over 2000 semantically diversified speech items altogether). The statistical analyses have shown the possibility of normalisation for pitch changes on the basis of the individual minimum fundamental frequency value and a variable register (defined by a changeable mean value). The results of the research can be used both in the evaluation of the applicability of fundamental frequency distribution statistical parameters for voice identification, and in the verification of an intonational phrase model which assumes pitch changes on three levels: L (Low), M (Medium)

and H (High). [Work supported by the Committee for Scientific Research in Warsaw, Grant No. 8 T11E 022 17].

* * *

A collection of comparative data base for the investigations of vocal canal pathologies

Helena GAWDA, Jan WARCHOŁ and Jolanta DOROBK

Medical Academy of Lublin

20-074 Lublin, Spokojna 1, Poland, janwar@panaceum.am.lublin.pl

The work concerns the collection of comparative data base for future investigations of a vocal canal and its pathologies. The investigations were carried out using the portable device type MiniDisc (Sony) and the sound analyser SVAN 912 (Svantek). The data base is collected on the basis of subtle acoustic spectra of Polish vowels of persons without any speech abnormalities. The results may be useful for setting the postoperative treatment and for diagnosis of a vocal organ.

* * *

Statistical modeling of Polish phonemes

Stefan GROCHOLEWSKI

Technical University of Poznań

60-965 Poznań, Piotrowo 3a, Poland, stefan.grocholewski@cs.put.poznan.pl

In the paper the results of modelling the Polish phonemes are presented. Starting with acoustic modelling for Polish, we began with standard CDHMMs (context-dependent phones) and standard front-end (cepstral coefficients and their derivatives). The acoustic models have been created on the basis of the fully annotated first speech database for Polish. Similar acoustic states have been tied by using tree-based clustering to ensure that all state distributions can be robustly estimated. The preliminary results of the detailed analysis of the obtained models are presented from the phonetic point of view. [Work supported by the Committee for Scientific Research in Warsaw, Grant No. KBN 8 T11E 022 17].

* * *

Wavelet packets transform for stop consonants classification

Ewa ŁUKASIK

Poznań University of Technology, Institute of Computing Science

60-965 Poznań, Piotrowo 3a, Poland, lukasik@put.poznan.pl

It was proved that the traditional DFT based methods of feature generation are not well suited for classification of non-stationary acoustic signals. Stop consonants are the examples of such signals. Wavelet packets transform (WPT) has been used to generate a feature set for context-independent recognition of three classes of unvoiced stop consonants: /p/, /t/, /k/. WPT is the generalized version of wavelet transform. It is redundant and the choice of the orthogonal base may be arbitrary. The best features base for classification has been sought, as well as the method of features space reduction providing the highest interclass separability. Two reduction strategies have been used. Features selection by the Local Discriminant Basis search algorithm (LDB) provides a choice of the best subset of features according to a given criterion. Features projection by Principal Components Analysis (PCA) results in creating the best combination of features enabling the most efficient clustering of data. Classification has been performed using NN. Classification rate for WPT-PCA features set is the highest in comparison with the other methods of features generation and reduction examined.

* * *

Application of automatic speech recognition system with parametric noise reduction for speech intelligibility measurements

Wojciech MYŚLECKI and Piotr ŁABNO

Wrocław University of Technology, Institute of Telecommunication and Acoustics

50-370 Wrocław, Wybrzeże Wyspiańskiego 27, Poland

The article includes the results of investigation of automatic speech recognition system application for objective assessment of speech transmission quality, made in the Institute of Telecommunication and

Acoustics of Wrocław University of Technology. These investigations are a continuation and development of previous ones, the results of which were presented in 1996 and 1998. The investigations were aimed at construction of automatic system enabling objective evaluation of speech quality according to the subjective measurements results and independent of the kind of telecommunication channel. Parametric noise reduction unit was added to the applied limited-state memoryless automatic system for isolated phrases recognition in order to obtain the results consistent with the subjective measurements.

* * *

The concentration of CO₂ in the air exhaled during speaking and the fluency of speaking

Barbara RACZEK, Bogdan ADAMCZYK and Anna PATRZYLAŚ

Curie-Skłodowska University, Institute of Physics

20-032 Lublin, Pl. M. Curie-Skłodowskiej 1, Poland, barbracz@tytan.umcs.lublin.pl.

We present results of an experiment, which is a continuation of our research series on correlation between the concentration of CO₂ in the air exhaled during speaking and the speech fluency. The experiment had a simulated character. The subject was one person, who repeated a test 10 times, which consisted of reading and 5 simulations of clonic stuttering and 5 simulations of tonic stuttering at various degrees of speech disfluency. The obtained results indicate that there exists a firm correlation between an absolute increment of the CO₂ concentration in the air exhaled during speaking, related to the level of the CO₂ registering during free respiration, and the degree of speech disfluency expressed as a number of errors made during utterance. For simulation of clonic stuttering, a ratio of correlation $r = -0.97$ was obtained, and for simulations of tonic stuttering a ratio $r = 0.83$ was obtained.

* * *

Recognising vowels in continuous speech

Elżbieta SMOLKA, Wiesława KUNISZYK-JÓŹKOWIAK and Waldemar SUSZYŃSKI

Curie-Skłodowska University, Institute of Physics

20-032 Lublin, Pl. M. Curie-Skłodowskiej 1, Poland, esmolka@tytan.umcs.lublin.pl

The presented results are a part of a research programme aimed at preparing a new visual-feedback-based method of stutterers' therapy. An animated image of mouth steered with speech signals and shown on a computer screen is to be employed, the recognised sounds in the utterance being vowels only. First the correctness was examined using our method of vowel classification realised in isolation as well as CVC and CVCV syllables. On the basis of the obtained results, identification maps were made separately for the groups of male, female and childish voices. At present, with the use of the maps, vowels are being recognised for male (stutterers') voices in a typical fragment of continuous speech, in which the vowel frequency has been set on the level characteristic of the Polish language. The percentage was evaluated of correctly identified vowels in the situations of individual reading and reading chorally with the echo. For 5 analysed voices, 74% correct recognitions were made. What was also examined is the significance of vowel's position (middle or end) in words in correct identification. For middle position, 77% correct identifications were achieved, and for end position — 67%.

* * *

Acoustical analysis of the disfluencies in stutterers' speech

Waldemar SUSZYŃSKI, Wiesława KUNISZYK-JÓŹKOWIAK and Elżbieta SMOLKA

Curie-Skłodowska University, Institute of Physics

20-032 Lublin, Pl. M. Curie-Skłodowskiej 1, Poland, biker@tytan.umcs.lublin.pl

In stutterers' utterances disfluent fricatives and plosives frequently occur at the beginnings of words. In the article, the results of spectrographic analyses of these disfluencies have been presented. The examined subjects read a text in two situations: with SAF (simultaneous auditory feedback) and with echo. Analyses have been made with the use of 1/3 octave filters in time intervals of 0.02 s. The prolongations of the fricatives are characterised by an increase in the sound intensity level within the range of higher frequencies as well as by extending the spectrum towards the high frequencies. The disfluent plosives are characterised by very short impulses occurring in significant time intervals with components within the range of high frequencies, which do not occur in fluently realised sounds, as well as by an infrequently significant reduction of the spectrum within the range of frequencies which are characteristic of fluent

utterances. The acoustic analysis of disfluencies in stutterers' utterances is a step towards objective diagnosing and greater possibilities for therapy of this disorder.

* * *

The evaluation of effectiveness of various neural network types in pathological speech analysis

Wiesław WSZOLEK and Ryszard TADEUSIEWICZ

University of Mining and Metallurgy

30-059 Kraków, Al. Mickiewicza 30, Poland, wwszolek@uci.agh.edu.pl, rtad@biocyb.ia.agh.edu.pl

In the present paper, partial results are described of a study concerning the utility of artificial intelligence methods, and in particular the neural network techniques, in the analysis and evaluation of pathological speech. In many problems of medical diagnosis, as well as in therapy and rehabilitation, an evaluation is required of the pathological speech signal quality. While in the typical problems concerning speech recognition the goal is to reveal (by selected parameters) the semantic aspects of the statement, in the tasks of medical diagnosis based on the speech signal analysis, the semantic contents of the statement is totally irrelevant (and it should be even regarded as interfering). In such problems the standard methods of speech signal processing and classification, used in the speech or voice recognition, totally fail. Also the standard parameterization techniques, like linear prediction coefficients or cepstral coefficients, cannot satisfactorily describe the pathological speech, because of its acoustic and phonetic structure, which is considerably different from the correct speech signal, and because the aim of the recognition process is completely different for such problems. In the paper, an application of three classes of neural networks (error backpropagation, resonant and Kohonen networks) is presented in the tasks of analysis and evaluation of pathological speech, and their utility in selected problems is discussed.

Music and musical instruments

Gap detection thresholds in 1/3-octave white noise centred at 4 kHz in young musicians with normal hearing and with very high frequency sloping hearing loss

Antoni JAROSZEWSKI, Anna JAROSZEWSKA and Piotr ROGOWSKI

Fryderyk Chopin Academy of Music

00-368 Warszawa, Okólnik 2, Poland, pro@chopin.edu.pl

Gap detection thresholds in 1/3-octave white noise centred at 4 kHz were determined in young musicians with normal hearing preserved and with very high frequency sloping hearing loss. The thresholds were determined in the control group of 20 with normal hearing, i.e. flat audiogram up to 16 kHz, and in the experimental group of 15 with high frequency sloping hearing loss exceeding 30 dB at 12 kHz or at 16 kHz, the so-called peculiar hearing loss. A group of 7 older subjects exhibiting also peculiar hearing loss was included for comparison. The results show the gap detection thresholds in the normal hearing subjects ranging from 1 ms to 6 ms which are in good agreement with the earlier data obtained by the present authors. However, few examples of higher gap detection thresholds (11, 26 ms) in normal hearing were also observed. For the experimental group with high frequency sloping hearing loss at 12 kHz or at 16 kHz, the gap detection thresholds found were on the average significantly higher, ranging from 6 ms to 26 ms. In the group of older subjects, the gap detection thresholds were on the average still significantly higher.

* * *

The measurement of pitch strength by the method of adjustment and by absolute magnitude estimation

Andrzej RAKOWSKI, Andrzej MIŚKIEWICZ and Piotr ROGOWSKI

Fryderyk Chopin Academy of Music

00-368 Warszawa, Okólnik 2, Poland, rakowski@chopin.edu.pl

Pitch strength of musical sounds was investigated by the method of adjustment and by absolute magnitude estimation. When adjustment was employed, the subjects' task was to adjust the frequency of a comparison pure tone to make the tone equal in pitch to the sound investigated. For most sounds, distribution of the comparison tone frequencies obtained in 72 adjustments (9 subjects ' 8 series of adjustments) was polymodal. The measure of pitch strength was defined as reciprocal of the measure of dispersion of frequencies belonging to the lowest mode, called the main mode, multiplied by the factor of monochromaticity. The highest values of pitch strength were obtained for the xylophone, the vibraphone,

the violin, and the marimba. The lowest values of pitch strength were found for the bass drum and the triangle. The values of pitch strength derived from pitch adjustments were in agreement with those obtained by absolute magnitude estimation. [Work supported by the Committee for Scientific Research, Grant No. T07B 023 14].

* * *

Hearing thresholds of children age 7–10 years

Piotr ROGOWSKI, Antoni JAROSZEWSKI and Teresa ROŚCISZEWSKA

Fryderyk Chopin Academy of Music

00-368 Warszawa, Okólnik 2, Poland, pro@chopin.edu.pl

Resting hearing thresholds were measured in 107 children aged 7-10 years, from primary schools in Warsaw. The children were recruited regardless of priority of these in which problems with hearing acuity were observed or expected. The measurements were performed with the use of tonal audiometry with intermittent 250/250 ms signal, in the frequency range 100–16000 Hz. In the children with deeper hearing loss, both air and bone conduction procedures were used. In the tested group, normal hearing within ± 10 dB was found in only 13% of the children. In the rest of the group, hearing loss of various nature was found, i.e.: wide-band (8%), high-frequency (24%), selective v-dip type (36%), low-frequency (54%) and other (16%). In the fraction with low-frequency hearing loss, often the conductive hearing loss was found, whilst in the case of high-frequency hearing loss, bone conduction audiometry indicated sensorineural type of hearing loss. Hearing loss in excess of 20 dB was found in 25% of the children tested. In the fraction with deep hearing loss in 25% of the children tested, hearing loss of approximately 40 dB was found.